THERMO-ELASTIC RESPONSE OF THIN FUNCTIONALLY GRADED BEAMS UNDER VARIOUS HEAT LOADS – THEORETICAL STUDIES AND EXPERIMENTAL VALIDATION

Thesis

Submitted in partial fulfilment of the requirement for the degree of

DOCTOR OF PHILOSOPHY

by

MALIK PRAVIN VITHAL

DEPARTMENT OF MECHANICAL ENGINEERING

NATIONAL INSTITUTE OF TECHNOLOGY KARNATAKA

SURATHKAL, MANGALORE – 575025

OCTOBER, 2017

DECLARATION

by the Ph.D. Research Scholar

I hereby *declare* that the Research Thesis entitled **Thermo-Elastic Response of Thin Functionally Graded Beams Under Various Heat Loads – Theoretical Studies and Experimental Validation** which is being submitted to the National Institute of Technology Karnataka, Surathkal in partial fulfilment of the requirements for the award of the Degree of **Doctor of Philosophy** in **Department of Mechanical Engineering** is a *bonafied report of the research work carried out by me*. The material contained in this *Research Thesis* has not been submitted to any University or Institution for the award of any degree.

Malik Pravin Vithal

Reg. No. 123031ME12P08

Department of Mechanical Engineering.

Place: NITK - Surathkal.

Date:

CERTIFICATE

This is to *certify* that the Research Thesis entitled **Thermo-Elastic Response of Thin Functionally Graded Beams Under Various Heat Loads – Theoretical Studies and Experimental Validation** submitted by **Malik Pravin Vithal (Reg. No. 123031ME12P08)** as the record of the research work carried out by him, is *accepted as the Research Thesis submission* in partial fulfilment of the requirements for the award of degree of **Doctor of Philosophy**.

Dr. RAVIKIRAN KADOLI
Research Guide and Professor,
Department of Mechanical Engineering,
National Institute of Technology Karnataka, Surathkal.

Chairman - DRPC,
Department of Mechanical Engineering,
National Institute of Technology Karnataka, Surathkal.

| | Shri Sateri, Mahalaxmi, Kudneshwar Prassana | |

| | Om Shri Ganeshaya Namaha:| |

| | Om Sai Ram | |

In dedication to the loving memory of my father

for making me who I am,

my mother, my daughters, my loving wife for supporting all

the way long

and

my Teachers who gave me the wealth of knowledge.

ACKNOWLEDGEMENTS

First and foremost, I would like to express my sincere gratitude and profound thanks to my research guide **Dr. Ravikiran Kadoli**, Professor, Department of Mechanical Engineering, for his invaluable guidance and support throughout the research work. His eternal supervision helped me in understanding the subject better and successful completion of this report. Working with him for my research work was a great experience. The time I have spent with him will be remembered and cherished all through the life.

I express my sincere thanks to RPAC members, Dr. K. Swaminathan, Department of Civil Engineering, NITK Surathkal and Dr. Srikanth Bontha, Department of Mechanical Engineering, NITK Surathkal for their valuable feedback during the research work. I express my sincere thanks to Dr. Narendranath, Prof. and Head, Department of Mechanical Engineering for providing the facalities in the department. I express my sincere gratitude and profound thanks to Dr. K. V. Gangadharan, Professor and former Head, Department of Mechanical Engineering for his advice and guidance accorded in carrying out the experimental work and providing the facilities in Solve Lab – Centre for System Design, NITK Surathkal. I extend my thanks to Dr. Pruthviraj, Department of Applied Mechanics and Hydraulics, NITK Surathkal, for providing thermal imaging camera to carry out experimental work. I extend my sincere thanks to Prof. A. O. Surendranathan and HOD, Department of Metallurgical and Materials Engineering for providing ball milling and SEM facilities. I thank, Strength of Materials laboratory staff from Department of Applied Mechanics & Hydraulics for providing UTM facilities to compact powder metallurgy samples. I am thankful to Dr. Sharnappa Joladarashi, Department of Mechanical Engg., NITK, Surathkal for his valuable inputs during the research work.

I will like to acknowledge the funds provided by the Ministry of Human Resource and Development (MHRD), Govt. of India, to NITK, Surathkal in order to carry out the research work.

The days I spent with many of my fellow research scholars are difficult to forget. I extend my regards to my fellow M.Tech. research scholars Maruthi M D and Jagadish P for their support in carrying out the experimental work. The time spent together in the college will be remembered and cherished all through the life.

I am thankful to N L Vhatte, AVP, Vedanta Limited, Goa for giving me sabbatical leave to attend course work of my research work.

Finally, I am thankful to my parents, wife, daughters, brother, sister and other family members for giving me endless encouragement and support for the success of my study.

PRAVIN MALIK

ABSTRACT

Suitability of functionally graded materials (FGMs) as structural members in modern industrial applications such as mechanical, aerospace, nuclear engineering and reactors are being explored vehemently. Considering the potential applications in thermal environment, functionally graded material structures may undergo various types of heat loads such as sudden heating or step heating, moving heat load, gradual heating, point heat load and or shock load, periodic and aperiodic thermal loads. The research related to fabrication of FGM structures and their theoretical modeling is very scarce. Researchers are exploring the manufacturing techniques to produce FGM structures with varying percentages of constituent materials. In the view of this fact, present work attempts to study the static deflection, free vibration and response to thermal loads of functionally graded beams numerically and validate them experimentally. The functionally graded SUS316-Al_2O_3 beams with ceramic content varying from 0 to 40% are prepared by plasma spraying technique while the functionally graded Al-Al_2O_3 beams with ceramic content varying from 0 to 50% are prepared using powder metallurgy process. A microstructure study is carried out using SEM to understand the distribution of various elements in the plasma sprayed and powder metallurgy process FGM beam samples. Nonlinear finite element analysis accounting the von Kármán strain is used to obtain static deflection and free vibration of a clamped free and clamp-simple support functionally graded beam. The results are experimentally validated with the functionally graded SUS316-Al_2O_3 and Al-Al_2O_3 beam. The numerical results had an error of 4.05-12.91% for the deflection and 2.02 to 14.31 % for the fundamental frequency in case of SUS316-Al_2O_3 beam and more than 50% for deflection and fundamental frequency in case of Al-Al_2O_3 beam with respect to experimental results. The porosity plays an important role and governs the Young's modulus of the sintered material which directly effects the deflection and free vibration frequency results. The commonly used and accepted theoretical models for Young's modulus with porosity effect available in the literature were used to obtain the theoretical results. 24-31% reduction in error was observed for pure aluminium beam while the error reduced by

13% for Al-Al_2O_3 FGM beam. ANSYS 3D 20 noded structural solid element is used to study the role of shear deformation of the FGM samples on displacements and natural frequencies. The first mode of vibration obtained from numerical approach and ANSYS 3D element are much closer to experimental results. However, the nonlinear finite element FGM code provide poor results for higher modes compared to ANSYS 3D element.

The nonlinear thermo-elastic analysis of thin functionally graded SUS316-Al_2O_3 beam accounting the von-Kármán strain and temperature dependent material properties under different heat loads and structural boundary conditions is also attempted. A two dimensional Lagrangian rectangular finite element is used to obtain the temperature distribution on the transverse plane of the beam. The significance of geometric nonlinearity is illustrated through numerical exercise. As the thermal load increases, the thermal deflection of FG beam are higher compared to linear analysis. Furthermore, the power law index also has a pronounced role. The numerical results of the static deflection of FG beam, in general, depends on power law index. Apart, the deflection produced by linear and nonlinear approach are considerably different. Thermo-elastic deflection and thermal stresses are evaluated for various structural and thermal boundary conditions. Thermo-elastic oscillations along with deflection are observed in case of beams subjected to step, concentrated line and shock heat load whereas thermo-elastic deflection is observed for beams subjected to moving heat load. In case of shock heat load, irrespective of the power law index, the time for maximum temperature rise of the beam material is same, whereas the maximum elastic deflection occurs either after or before the maximum temperature rise depending on the power law index. The thermo-elastic deflection increase continuously irrespective of the power law index for line heat source. When FGM beams are subjected to moving heat source the time for maximum deflection depends on the power law index whereas the time for maximum temperature rise is independent of the power law index. In general, temperature dependency of material properties influence the amplitude of thermal oscillations. High thermal stresses are induced in beams with pin-pin and clamp-pin boundary condition as compared to hinge-hinge beam.

Thermal analysis is carried out on SUS316-Al_2O_3 and Al-Al_2O_3 FGM beam with heat source at one end. The temperature distribution is simulated using ANSYS and is validated with the experimental results. The temperature profile from ANSYS simulation results are in good agreement with experiment the with an error of 17% near the heat source while the maximum error 5.65% is observed 50mm away from heat source. Thermal vibration and induced thermal deflection studies have been carried out on the SUS316-Al_2O_3 FGM beam sample under clamp free boundary condition with heat applied at clamp end using electric heating coil. The response of the 2 FGM beams and pure SUS316 beam are studied at various heat loads varying from 2.925 W to 23.9 W. Theoretical model is validated with experimental results for SUS316-Al_2O_3 FGM beam sample-1. The experimental results are in close comparison with the theoretical results.

Keywords:

Thermal induced motion; Non-linear finite element; Thermo-elastic response; Geometric non-linear thin beam; Functionally Graded Material; Surface heating; Shock thermal load; Moving line heat source; Plasma spray; Powder metallurgy; ANSYS 3D solid element; Experimental validation.

TABLE OF CONTENTS

ACKNOWLEDGEMENT **i**

ABSTRACT **iii**

TABLE OF CONTENTS **vii**

LIST OF FIGURES **xiii**

LIST OF TABLES **xxvii**

NOMENCLATURE **xxxi**

CHAPTER - 1 1

INTRODUCTION 1

1.1 Thermo-elastic response 1

1.2 Functionally Graded Materials 2

1.3 Application of Functionally Graded Materials 3

1.4 Oraganisation of Dissertation 4

CHAPTER - 2 9

LITERATURE SURVEY 9

2.1 Introduction 9

2.2 Literature survey on thermally induced vibrations of structures 9

2.3 Literature survey on Functionally Graded Material (FGM) 14

2.3.1 Functionally Graded Material Beams: 15

2.3.2 Functionally Graded Material Plates and Shells: 18

2.3.3 Fabrication of functionally graded materials 23

2.4 Motivation 24

2.5 Objectives of the present study 25

CHAPTER - 3 27

NONLINEAR FINITE ELEMENT FORMULATION FOR THIN FUNCTIONALLY GRADED BEAMS UNDER THERMAL LOADS 27

3.1 Introduction 27
3.2 Material gradation through thickness of functionally graded beam 28
3.3 Formulation of heat transfer problem 31
3.3.1 Formulation of the heat conduction equation with convection 32
3.4 Finite element discretization in one dimension for heat transfer problem ... 34
3.5 Finite element discretization in two dimension FOR heat transfer problem 36
3.6 Finite difference solution of heat transfer problem in time 41
3.7 Governing equations for non-linear thermo-elastic vibration analysis of FGM beams 44
3.7.1 Displacement field and nonlinear strains for Euler Bernoulli beam 44
3.7.2 Virtual work statement 47
3.7.3 Euler-Lagrange equations 48
3.7.4 Beam Finite element model 51
3.7.5 Solutions of nonlinear equations 56
3.8 Determination of dynamic stresses 58
3.9 Solution of the FGM equation of motion for thermal load 59
3.10 Summary 59

CHAPTER - 4 61
FABRICATION OF FUNCTIONALLY GRADED BEAMS USING PLASMA SPRAY AND POWDER METALLURGY PROCESS 61
4.1 Introduction 61
4.2 The FGM beam 61
4.3 Fabrication of FGM beam samples by plasma spray process 64
4.3.1 Powder preparation 64
4.3.2 Substrate preparation 64
4.3.3 Plasma spraying process 65
4.4 Fabrication of FGM beam samples by powder metallurgy process 68
4.4.1 Die fabrication 68
i. Die design 68

ii. Material selection for die 68
iii. Die machining 69
4.4.2 Powder mixing 70
4.4.3 Powder compaction 71
4.4.4 Sintering process 72
4.4.5 Steps in powder metallurgy sample preparation 73
4.5 Microstructural studies of powder mixtures and FGM beams 76
4.5.1 Principle of Scanning Electron Microscope (SEM) 76
4.5.2 Procedure for SEM analysis of powder mixtures 77
4.5.3 Procedure for SEM analysis of FGM beam samples 77
4.5.4 Discussion on SEM analysis of powders 77
4.6 Energy Dispersive X-ray Spectrometry (EDS) Analysis 85
4.7 Summary 87

CHAPTER - 5 89
EXPERIMENTAL VALIDATION OF STATIC DEFLECTION AND FREE VIBRATION ANALYSIS OF FUNCTIONALLY GRADED BEAMS 89
5.1 Introduction 89
5.2 Experimental setup 90
5.2.1 Static response measurements of FGM beam 90
5.2.2 Dynamic response measurements of FGM beam 90
5.3 Verification of central deflection for Euler Bernoulli beam 91
5.4 Validation of non-linear analysis using experimental studies on SUS316-Al_2O_3 FGM beam 94
5.4.1 Calculation of density of SUS316-Al_2O_3 FGM beam sample 94
5.4.2 Transverse bending of SUS316-Al_2O_3 FGM beam 95
5.4.3 Free vibration response of SUS316-Al_2O_3 FGM beam 102
5.5 Static deflection and free vibration analysis of Al-Al_2O_3 FGM beam and aluminium beam samples – Theoretical analysis and experimental validation 108

5.5.1 Static deflection studies of Aluminium and Al-Al_2O_3 FGM beam 110

5.5.2 Free vibration analysis of Aluminium and Al-Al_2O_3 FGM beam 116

5.6 Summary 119

CHAPTER - 6 121
RESULTS AND DISCUSSION - LINEAR FINITE ELEMENT ANALYSIS OF THIN FUNCTIONALLY GRADED MATERIAL BEAMS SUBJECTED TO STEP HEATING 121

6.1 Introduction 121

6.2 Numerical results and discussion on linear analysis of FGM beam subjected to step heating 121

6.2.1 Verification of Simply supported FGM beam subjected to step heating ... .122

6.2.2 Verification of free vibration characteristics of Simply Supported FGM Beam 125

6.2.3 Influence of temperature dependent and temperature independent material properties on thermal vibration of FGM Aluminium-Zirconia beam. .127

6.2.4 Effect of thermo-physical properties of material and physical boundary conditions on thermally induced vibrations of beams subjected to step heating 129

6.2.5 Effect of natural convection on thermally induced vibrations of FGM beam subjected to surface heating 133

6.3 Summary 137

CHAPTER - 7 139
RESULTS AND DISCUSSION - NONLINEAR FINITE ELEMENT ANALYSIS OF THIN FUNCTIONALLY GRADED MATERIAL BEAMS UNDER THERMAL LOADS 139

7.1 Introduction 139

7.2 Numerical results and discussion for nonlinear formulation of FGM beam subjected to various heat loads 140

7.2.1 Convergence for 2D thermal analysis 140

7.2.2 Verification problem, simply supported FGM beam subjected to step heating 141

7.2.3 Effect of material grading index and physical boundary conditions on nonlinear thermo-elastic vibrations of beams subjected to various heat loads .. 144

7.2.4 Beam moving under heat source 172

7.2.5 Nonlinear displacement field of FGM beam for various heat loads ... 176

7.2.6 Thermal effect on mechanical properties of FGM Beams..... 185

7.3 Nonlinear stresses in FGM beams 189

7.3.1 Step heating..... 190

7.3.2 Shock heating..... 193

7.3.3 Moving heat source 197

7.3.4 Concentrated line heat source 202

7.4 Summary..... 205

CHAPTER - 8 207

EXPERIMENTAL VALIDATION OF THERMAL ANALYSIS AND THERMO-ELASTIC DEFLECTION OF FUNCTIONALLY GRADED BEAMS..... 207

8.1 Introduction..... 207

8.2 Transient thermal analysis of SUS316-Al_2O_3 FGM beam with heat source at one end of beam..... 207

8.2.1 Experimental setup for thermal analysis of FGM beam..... 208

8.2.2 Results and discussion on thermal analysis of SUS316-Al_2O_3 FGM beam 209

8.2.3 Results and discussion on thermal analysis of Al-Al_2O_3 FGM beam . 211

8.3 Thermal vibration of SUS316-Al_2O_3 FGM beam..... 212

8.3.1 Experimental setup for thermal vibration of SUS316-Al_2O_3 FGM beam 212

8.3.2 Results and discussion on thermal vibration of SUS316-Al_2O_3 FGM beam 214

8.4 Summary 217

CHAPTER – 9 219
CONCLUSIONS AND SCOPE FOR FUTURE WORK 219
Scope for future work 223

REFERENCES 225

APPENDIX – I 239

APPENDIX – II 243
a. Introduction 243
b. Experimental setup to conduct free vibration test of FGM beams 243
c. Mounting arrangement for beam. 244
d. Impact hammer 245
e. Laser displacement sensor 246
f. RS422 / USB converter 248
g. ILD1402 DAQ software 248
h. FFT analyser 249
i. Accelerometer - 8730A (Kistler) 250
j. Procedure to measure free vibration natural frequency of beam samples. 252
k. Procedure to measure transverse deflection of beam samples. 254

APPENDIX – III 258

APPENDIX-IV 262

APPENDIX-V 263

Biodata 269

List of Publications 269

LIST OF FIGURES

Figure	Title	Page no.
Fig.3.1	Configuration of simply supported FGM beam subjected to step heating.	29
Fig.3.2	Variation of volume fraction of ceramic based on power law scheme.	31
Fig.3.3	Generalised work domain for heat transfer problem.	32
Fig.3.4	Finite element idealization of beam for one dimensional thermal analysis.	35
Fig.3.5	FGM beam subjected to moving line heat source	37
Fig.3.6	Finite element idealization of beam for two dimensional thermal analysis.	37
Fig.3.7	A simple rectangular element.	38
Fig.3.8	An approximation for $T(a)$ given $\partial T/\partial t$.	42
Fig.3.9	Kinematics due to transverse load on the simply supported Euler–Bernoulli beam.	45
Fig.3.10	The external forces applied on the two ends of a beam.	48
Fig.3.11	Finite element idealization of beam for structural analysis.	51
Fig.3.12	One-dimension beam bending element and nodal degrees of freedom	51
Fig.4.1	Geometry of typical 3 layer FGM made of SUS316 and Al_2O_3.	62
Fig.4.2	Powders used for FGM fabrication (a) Aluminium powder–200 mesh (Al) (b) Al_2O_3 powder – 15/45 micron (c) SUS316 powder – 63micron size.	62
Fig.4.3	Schematic representation of 5 layer functionally graded beam.	63
Fig.4.4	Planetary Ball Mill (PM-100) for mixing powders (Metallurgical and Materials Engineering Department, NITK, Surathkal).	64
Fig.4.5	SUS316 substrate preparation for plasma spraying.	65
Fig.4.6	The plasma spray process.	66
Fig.4.7	FGM samples prepared using plasma spray process.	68
Fig.4.8	(a) Final assembly of machined die, (b) Assembly of base and middle die and (c) figure showing top die, base and middle die in FGM die assembly.	69
Fig.4.9	Variation of volume fraction of alumina, V_c with respect to thickness coordinate, z .	70

Fig.4.10 Powder mixtures with different composition (a) 98.75%Al - 1.25% Al_2O_3 (b) 97.5%Al - 2.5% Al_2O_3 (c) 95%Al - 5% Al_2O_3 (d) 90%Al - 10%Al_2O_3 (e) 80%Al - 20%Al_2O_3 and (f) 50%Al - 50% Al_2O_3. 71

Fig.4.11 Unidirectional compacting of die filled with layer wise powder mixture in Universal Testing Machine (Strength of materials laboratory, NITK Surathkal). ..72

Fig.4.12 Sintering furnace with sintering temperature set at 650^0C (Heat treatment laboratory, NITK Surathkal).....73

Fig.4.13 SEM micrographs of (a) aluminium powder (b) aluminium oxide (Al_2O_3) powder and (c) SUS316 powder. 78

Fig.4.14 SEM micrographs of powder mixtures of different compositions (a) 98.75%Al-1.25%Al_2O_3 (b) 97.5%Al-2.5%Al_2O_3 (c) 95%Al-5%Al_2O_3 (d) 90%Al-10%Al_2O_3 (e) 80%Al-20%Al2O3 and (f) 50%Al-50%Al_2O_3.....79

Fig.4.15 SEM micrographs of SUS316-Al_2O_3 powders. 80

Fig.4.16 SEM micrographs of FGM beam sample no. 3 showing (a) variation of composition of Al – Al_2O_3 along thickness (b) interface of 50%Al-50%Al_2O_3 and 90%Al-10%Al_2O_3 and (c) interface of 90%Al-10%Al_2O_3 and 98.75%Al-1.25%Al_2O_3. 81

Fig.4.17 SEM micrographs of FGM beam sample no. 10 showing (a) variation of composition of Al – Al_2O_3 along thickness (b) interface of 90%Al-10%Al_2O_3 and 95%Al-5%Al_2O_3 and (c) interface of 95%Al-5%Al_2O_3 and 98.75%Al-1.25%Al_2O_3. 82

Fig.4.18 SEM micrographs of FGM beam sample no. 12 showing variation of composition of Al –Al_2O_3 along thickness.....82

Fig.4.19 SEM micrographs of FGM beam sample no. 2 showing variation of composition of SUS316-Al_2O_3 along thickness. 83

Fig.4.20 SEM micrographs of FGM beam sample no. 2 showing interface and defects of SUS316-Al_2O_3 FGM along thickness. 84

Fig.4.21 SEM micrographs of FGM beam sample no. 3 showing variation of composition SUS316-Al_2O_3 FGM along thickness. 85

Fig.4.22 SEM micrographs of FGM beam sample no. 3 showing interface of SUS316-Al_2O_3 along thickness. 85

Fig.4.23 SEM-EDX of Al-Al_2O_3 FGM Sample - 20 and its corresponding atom profiles. 86
Fig.4.24 SEM-EDX of pure Al Sample - 4 and its corresponding atom profiles. .. 87

Fig.5.1 Schematic diagram of experimental set-up for static response measurement. 90
Fig.5.2 Schematic diagram of experimental set-up for natural frequency measurement. 90
Fig.5.3 Transverse deflection versus distance along the length of a pinned–pinned Euler Bernoulli beam (a) Homogeneous (b) Functionally graded material. 92
Fig.5.4 Transverse deflection versus distance along the length of a pinned–pinned Euler Bernoulli functionally graded material beam (linear and nonlinear – present method). 93
Fig.5.5 Experimental setup for transverse bending analysis of cantilever beam. 95
Fig.5.6 Theoretical and experimental (a) deflection v/s load plot and (b) static deflection profile for 0.981 N tip load on pure SUS316 beam (sample-9) under clamp free boundary condition. 96
Fig.5.7 Theoretical and experimental deflection v/s load plot (a) and static deflection profile at 1.275 N tip load (b) for SUS316-Al_2O_3 FGM beam (sample-1) under clamp free boundary condition. 97
Fig.5.8 Theoretical and experimental deflection v/s load plot (a) and static deflection profile at 0.685 N tip load (b) for SUS316-Al_2O_3 FGM beam (sample-2) under clamp free boundary condition. 98
Fig.5.9 Theoretical and experimental deflection v/s load plot (a) and static deflection profile at 1.275 N tip load (b) for SUS316-Al_2O_3 FGM beam (sample-3) under clamp free boundary condition. 99
Fig.5.10 (a) Deflection v/s load plot and (b) static deflection profile for 0.981 N tip load on SUS316-Al_2O_3 FGM beam (sample-4) under clamp free boundary condition. 100
Fig.5.11 Experimental setup for transverse bending analysis of clamp-simple support beam. 101

Fig.5.12 Deflection v/s load plot for SUS316-Al_2O_3 FGM beam (sample-1) under clamp-simple support boundary condition. 101
Fig.5.13 Deflection v/s load plot for SUS316-Al_2O_3 FGM beam (sample-3) under clamp-simple support boundary condition. 102
Fig.5.14 Experimental Setup for free vibration analysis (a) View at 30^0 to vertical (b) View from top. 103
Fig.5.15 Natural frequencies of three-layer SUS316-Al_2O_3 FGM beams under cantilever boundary condition – Sample 1. 104
Fig.5.16 Mode shapes for SUS316-Al_2O_3 FGM sample-1 in ANSYS. 107
Fig.5.17 Mode shapes for SUS316-Al_2O_3 FGM sample-2 in ANSYS. 107
Fig.5.18 Mode shapes for SUS316-Al_2O_3 FGM sample-3 in ANSYS. 107
Fig.5.19 Deflection v/s load plot for pure extruded aluminium beam under clamp free boundary condition. 111
Fig.5.20 Deflection v/s load plot for pure sintered aluminium beam (sample-4) under clamp free boundary condition. 112
Fig.5.21 Static deflection profile for pure sintered aluminium beam (sample-4) under clamp free boundary condition at 1.275 N load.....112
Fig.5.22 (a) Deflection v/s load plot (L=120mm) and (b) static deflection profile at 1.275 N load (L=130mm) for Al-Al_2O_3 FGM beam (sample-19) under clamp free boundary condition. 112
Fig.5.23 (a) Deflection v/s load plot (L=120mm) and (b) static deflection profile at 1.275 N load (L=130mm) for Al-Al_2O_3 FGM beam (sample-20) under clamp free boundary condition. 113
Fig.5.24 Deflection v/s load plot for pure sintered aluminium beam (sample-4) under clamp free boundary condition. 115
Fig.5.25 (a) Displacement versus time and (b) magnitude versus frequency plots for Al-Al_2O_3 FGM beam sample 20 in clamped-free boundary condition. 117
Fig.5.26 (a) Displacement versus time and (b) magnitude versus frequency plots for pure Al beam sample 4 in clamped-free boundary condition. 118
Fig.5.27 (a) Displacement versus time and (b) magnitude versus frequency plots for pure Al (extruded) beam in clamped-free boundary condition. 118

Fig.6.1 (a) Close form solution (Eq.3.8) and (b) Solution of temperature variation across the thickness of the beam as referred from Boley (1956) for B=1(present method). 123
Fig.6.2 Non dimensional dynamic mid-span deflection of simply supported beam for B=1. 124
Fig.6.3 Convergence study for number of homogeneous layers for FGM beam. . 125
Fig.6.4 Dynamic mid-span deflection of simply supported Al-ZrO_2 FGM beam for $B=1$ (a) temperature independent material properties (b) temperature dependent material properties. 128
Fig.6.5 Dynamic mid-span deflection of simply supported SUS304-Al_2O_3 FGM beam for L/h=100. 130
Fig.6.6 Dynamic mid-span thermal moment of simply supported SUS304-Al_2O_3 FGM beam for L/h=100. 131
Fig.6.7 Dynamic mid-span deflection of clamped-simply supported SUS304-Al_2O_3 FGM beam for L/h=100. 132
Fig.6.8 Dynamic mid-span thermal moment of clamped-simply supported SUS304-Al_2O_3 FGM beam for L/h=100. 132
Fig.6.9 Dynamic mid-span deflection of clamped-free SUS304-Al_2O_3 FGM beam for L/h=100. 133
Fig.6.10 Dynamic mid-span thermal moment of clamp-free SUS304-Al_2O_3 FGM beam for L/h=100. 133
Fig.6.11 Simply supported beam subjected to step heating on one side and convection on other side. 134
Fig.6.12 Temperature distribution of SUS304-Al_2O_3 FGM Simply Supported beam with convection at bottom for n=400 (L/h=100). 134
Fig.6.13 Difference in temperature for SUS304-Al_2O_3 FGM Simply Supported beam with insulation at bottom and convection at bottom for n=400 (L/h=100)..... 135
Fig.6.14 Dynamic mid-span deflection of simply supported FGM beam for L/h=100 with sudden heating on top surface and convection on bottom surface. 135

Fig.6.15 Dynamic mid-span thermal moment of simply supported FGM beam for *L/h*=100 with sudden heating on top surface and convection on bottom surface. 136
Fig.6.16 Comparison of simply supported beam dynamic mid span deflection for *n*=100 (insulated v/s convection). 136

Fig.7.1 Non dimensional dynamic mid-span deflection of simply supported (H-H) beam. 141
Fig.7.2 Comparision of nonlinear thermo-elastic deflection for simply supported beam with step heating. 143
Fig.7.3 Temperature distribution at centre with respect to time for FGM beam subjected to step heating. 144
Fig.7.4 Different heat source condition at t=0.01s. 146
Fig.7.5 Pin-pin FGM beam subjected to step heating. 147
Fig.7.6 Dynamic mid-span axial force for pin-pin FGM beam subjected to step heating. 148
Fig.7.7 (a) Dynamic mid-span deflection (b) thermal moment for hinge-hinge FGM beam subjected to step heating. 149
Fig.7.8 Dynamic mid-span axial force for hinge-hinge FGM beam subjected to step heating. 149
Fig.7.9 (a) Dynamic mid-span deflection (b) thermal moment for clamped-pin FGM beam subjected to step heating. 150
Fig.7.10 Dynamic mid-span axial force for clamp-pin FGM beam subjected to step heating. 150
Fig.7.11 Temperature distribution at centre with respect to time for FGM beam subjected to shock heating. 151
Fig.7.12 (a) Thermo-elastic mid-span deflection (b) dynamic thermal moment for pin-pin FGM beam subjected to shock heating. 152
Fig.7.13 Dynamic mid-span axial force for pin-pin FGM beam subjected to shock heating. 153
Fig.7.14 (a) Thermo-elastic mid-span deflection (b) Dynamic thermal moment for HH FGM beam subjected to shock heating. 153

Fig.7.15 Dynamic mid-span axial force for HH FGM beam subjected to shock heating. 154
Fig.7.16 (a) Thermo-elastic mid-span deflection (b) Dynamic thermal moment for clamp-pin FGM beam subjected to shock heating. 154
Fig.7.17 Dynamic mid-span axial force for clamp-pin FGM beam subjected to shock heating. 155
Fig.7.18 Temperature distribution for FGM beam subjected to line heat source of 100 W at centre. 156
Fig.7.19 (a) Thermo-elastic mid-span deflection (b) Dynamic thermal moment for Pin-pin FGM beam subjected to concentrated line heat source at center. 157
Fig.7.20 Dynamic mid-span axial force for pin-pin FGM beam subjected to concentrated line heat source at center. 157
Fig.7.21 (a) Thermo-elastic mid-span deflection (b) Dynamic thermal moment for HH FGM beam subjected to concentrated line heat source at center..... 158
Fig.7.22 Dynamic mid-span axial force for HH FGM beam subjected to concentrated line heat source at center..... 158
Fig.7.23 (a) Thermo-elastic mid-span deflection (b) Dynamic thermal moment for clamp-pin FGM beam subjected to concentrated line heat source at center..... 159
Fig.7.24 Dynamic mid-span axial force for clamp-pin FGM beam subjected to concentrated line heat source at center. 159
Fig.7.25 Geometry of typical FGM made of SUS316 and Al_2O_3 with moving heat source. 161
Fig.7.26 Temperature distribution at the centre of the pin-pin beam for various values of n at velocity of 2m/s. 162
Fig.7.27 Temperature distribution at the start-centre-end of the pin-pin beam for $n=1$ at velocity of 2m/s..... 162
Fig.7.28 Temperature distribution across thickness of the pin-pin beam for $n=1$ at velocity of 2m/s. 163
Fig.7.29 (a) Thermo-elastic deflection at centre (b) dynamic thermal moment for pin-pin FGM beam subjected to moving line heat source for various values of n at velocity of 2m/s. 164

Fig.7.30 Dynamic mid-span axial force for pin-pin FGM beam subjected to moving line heat source. 165
Fig.7.31 (a) Thermo-elastic deflection at centre (b) Dynamic thermal moment for hinge-hinge FGM beam subjected to moving line heat source for various values of n at velocity of 2m/s. 165
Fig.7.32 Dynamic mid-span axial force for hinge-hinge FGM beam subjected to moving line heat source. 166
Fig.7.33 (a) Thermo-elastic deflection at centre (b) Dynamic thermal moment for clamp-pin FGM beam subjected to moving line heat source for various values of n at velocity of 2m/s. 167
Fig.7.34 Dynamic mid-span axial force for clamp-pin FGM beam subjected to moving line heat source. 167
Fig.7.35 Thermo-elastic deflection at centre of pin-pin beam for various values of n at velocity of 0.5m/s. 168
Fig.7.36 Thermo-elastic deflection at centre of pin-pin beam for various values of n at velocity at 4m/s. 168
Fig.7.37 Thermo-elastic deflection at centre of pin-pin beam at different values of velocities of heat source. 169
Fig.7.38 Temperature distribution at the centre of the pin-pin beam at different velocities of heat source. 169
Fig.7.39 Thermo-elastic mid-span deflection for pin-pin FGM beam subjected to moving heat load of various magnitude at 2 m/s. 170
Fig.7.40 (a) Thermo-elastic mid-span deflection and (b) Temperature distribution for various heat source at 0.01 s for pin-pin boundary condition. 171
Fig.7.41 Typical illustration of beam moving under heat source for surface treatment. 172
Fig.7.42 Temperature distribution for FGM beam subjected to shock heat of 100 W for 0.1 s. 173
Fig.7.43 Thermo-elastic mid-span deflection for pin-pin FGM beam subjected to shock heating. 174

Fig.7.44 Thermo-elastic mid-span deflection for pin-pin FGM beam subjected to shock heating of various magnitude. 175
Fig.7.45 Thermo-elastic mid-span deflection for hinge-hinge FGM beam subjected to shock heating. 175
Fig.7.46 Thermo-elastic mid-span deflection for clamp-pin FGM beam subjected to shock heating. 176
Fig.7.47 Displacement field for pin-pin beam subjected to step heating of 100W (time=0.05 s). 178
Fig.7.48 Comparison of linear and nonlinear displacement field for pin-pin beam subjected to step heating for n=1.0 (time=0.05 s). 179
Fig.7.49 Comparison of displacement field of FGM beam subjected to step heating of 100 W for various structural boundary conditions (time=0.05 s). 180
Fig.7.50 Comparison of displacement field for pin-pin FGM beam subjected to various heat loads of 100 W for n=1.0 (time=0.05 s). 182
Fig.7.51 Location of the neutral plane for various values of power law index and corresponding axial displacement for pin-pin beam subjected to step heating (time=0.05 s). 183
Fig.7.52 Axial displacement across the thickness for pin-pin beam subjected to step heating (time=0.05 s) for various values of power law index. 184
Fig.7.53 Effect of L/h ratio on the thermo-elastic vibration of hinge-hinge beam subjected to step heating 184
Fig.7.54 Temperature distribution through thickness of the beam due to step heat load of 6000 W. 185
Fig.7.55 Material properties through thickness of the beam. 186
Fig.7.56 Extensional stiffness, extensional-bending coupling stiffness and bending stiffness of FGM beam for different power-law index, n 188
Fig.7.57 Comparison of dynamic mid-span deflection for pin-pin FGM beam subjected to step heating with TDMP and TIMP. 189
Fig.7.58 Temperature distribution through the thickness of the beam due to step heat load of 100 W. 190

Fig.7.59 Dynamic thermal stress on left end of pin-pin FGM beam subjected to step heating. 191
Fig.7.60 Dynamic thermal stress along the length of pin-pin FGM beam subjected to step heating at t=0.05 s. 191
Fig.7.61 Dynamic thermal stress on left end of hinge-hinge FGM beam subjected to step heating. 192
Fig.7.62 Dynamic thermal stress along the length of hinge-hinge FGM beam subjected to step heating at t=0.05 s. 192
Fig.7.63 Dynamic thermal stress on left end of clamp-pin FGM beam subjected to step heating. 193
Fig.7.64 Dynamic thermal stress along the length of clamp-pin FGM beam subjected to step heating at t=0.05 s. 193
Fig.7.65 Dynamic thermal stress on left end of pin-pin FGM beam subjected to shock heating. 194
Fig.7.66 Dynamic thermal stress along the length of pin-pin FGM beam subjected to shock heating at t=0.05 s. 194
Fig.7.67 Dynamic thermal stress on left end of hinge-hinge FGM beam subjected to shock heating. 195
Fig.7.68 Dynamic thermal stress along the length of hinge-hinge FGM beam subjected to shock heating at t=0.05 s. 195
Fig.7.69 Dynamic thermal stress on left end of clamp-pin FGM beam subjected to shock heating. 196
Fig.7.70 Dynamic thermal stress along the length of clamp-pin FGM beam subjected to shock heating at t=0.05 s. 196
Fig.7.71 Dynamic thermal stress on left end of pin-pin FGM beam subjected to moving heat source. 197
Fig.7.72 Dynamic thermal stress on right end of pin-pin FGM beam subjected to moving heat source. 198
Fig.7.73 Dynamic thermal stress along the length of pin-pin FGM beam subjected to moving heat source at t=0.05 s. 198

Fig.7.74 Dynamic thermal stress on left end of hinge-hinge FGM beam subjected to moving heat source. 199
Fig.7.75 Dynamic thermal stress on right end of hinge-hinge FGM beam subjected to moving heat source. 199
Fig.7.76 Dynamic thermal stress along the length of pin-pin FGM beam subjected to moving heat source at t=0.05 s. 200
Fig.7.77 Dynamic thermal stress on left end of clamp-pin FGM beam subjected to moving heat source. 200
Fig.7.78 Dynamic thermal stress on right end of clamp-pin FGM beam subjected to moving heat source. 201
Fig.7.79 Dynamic thermal stress along the length of clamp-pin FGM beam subjected to moving heat source at t=0.05 s. 201
Fig.7.80 Dynamic thermal stress on left end of pin-pin FGM beam subjected to concentrated line heat source. 202
Fig.7.81 Dynamic thermal stress along the length of pin-pin FGM beam subjected to concentrated line heat source at t=0.05 s. 203
Fig.7.82 Dynamic thermal stress on left end of hinge-hinge FGM beam subjected to concentrated line heat source. 203
Fig.7.83 Dynamic thermal stress along the length of hinge-hinge FGM beam subjected to concentrated line heat source at t=0.05 s. 204
Fig.7.84 Dynamic thermal stress on left end of clamp-pin FGM beam subjected to concentrated line heat source. 204
Fig.7.85 Dynamic thermal stress along the length of clamp-pin FGM beam subjected to concentrated line heat source at t=0.05 s. 205

Fig.8.1 Experimental setup for thermal analysis of FGM beam. 208
Fig.8.2 Temperature variation along the length of the beam from t=30 s to 180 s for SUS316-Al_2O_3 FGM sample-5. 210
Fig.8.3 Experimental temperature variation along the length of the SUS316-Al_2O_3 FGM beam sample-5 from t=0 to 300 s. 210

Fig.8.4 Experimental temperature variation along the length of the Al-Al_2O_3 FGM beam sample-20 from *t*=0 to 300 s. 211
Fig.8.5 Schematic diagram of experimental set-up for thermal vibration. 212
Fig.8.6 Experimental setup for thermal vibration analysis. 213
Fig.8.7 Temperature distribution on SUS316-Al_2O_3 FGM beam sample-1. 215
Fig.8.8 Natural frequency of three-layer SUS316-Al_2O_3 FGM beam sample 1 under cantilever boundary condition after 300 s is 48.622Hz. 216
Fig.8.9 Frequency verses time and temperature verses time plot for SUS316-Al_2O_3 FGM beam sample 1. 216
Fig.8.10 Comparision of theoretical and experimental thermal deflection profile of the SUS316-Al_2O_3 FGM beam sample 1 after *t*=306 s. 217

Fig.I.1 Schematic 2D drawing of the die components and die assembly. 240

Fig.II.1 Schematic diagram of experimental setup to measure free vibration natural frequency of beams in clamped – free condition. 243
Fig.II.2 Actual test setup to measure free vibration natural frequency of beams in clamped – free condition. 244
Fig.II.3 Schematic representation of mounting of beam sample in the mounting arrangement. 245
Fig.II.4 PCB piezotronics make impact hammer. 245
Fig.II.5 Micro epsilon make laser displacement sensor (model: optoNCDT 1402-10). 247
Fig.II.6 RS422/USB converter (micro epsilon make). 248
Fig.II.7 User interface window of ILD 1402 DAQ tool. 249
Fig.II.8 FFT analyser tool dialogue box of origin pro 8 software. 250
Fig.II.9 Geometry and mounting details of the accelerometer. 251
Fig.II.10 Details of thermal imaging camera. 257

Fig.III.1 Natural frequencies of three-layer SUS316/Al_2O_3 FGM beams under cantilever boundary condition – Sample 2. 258

Fig.III.2 Natural frequencies of three-layer SUS316/Al_2O_3 FGM beams under cantilever boundary condition – Sample 3. 259
Fig.III.3 (a) Displacement versus time and (b) magnitude versus frequency plots for Al-Al_2O_3 FGM beam sample 8 in clamped-free boundary condition. 259
Fig.III.4 (a) Displacement versus time and (b) magnitude versus frequency plots for Al-Al_2O_3 FGM beam sample 13 in clamped-free boundary condition. 260
Fig.III.5 (a) Displacement versus time and (b) magnitude versus frequency plots for Al-Al_2O_3 FGM beam sample 15 in clamped-free boundary condition. 260
Fig.III.6 (a) Displacement versus time and (b) magnitude versus frequency plots for Al-Al_2O_3 FGM beam sample 18 in clamped-free boundary condition. 260
Fig.III.7 (a) Displacement versus time and (b) magnitude versus frequency plots for Al-Al_2O_3 FGM beam sample 19 in clamped-free boundary condition. 261
Fig.III.8 Displacement versus time and magnitude versus frequency plots for pure Al beam sample 2 in clamped-free boundary condition. 261
Fig.III.9 Displacement versus time and magnitude versus frequency plots for pure Al beam sample 3 in clamped-free boundary condition. 261

Fig.IV.1 Convergence study for number of elements in axial direction for FGM beam ……264

Fig.V.1 Temperature distribution on SUS316-Al_2O_3 FGM beam (sample-1-trial 2) (a) temperature variation along the length of beam at different time intervals (b) temperature variation with respect to time at various points on the beam.... 263
Fig.V.2 (a) Displacement versus time and (b) magnitude versus frequency plots for three-layer SUS316-Al_2O_3 FGM beam sample 1 (trial 2) under cantilever boundary condition after 300 s. 263
Fig.V.3 Thermal deflection profile of the SUS316-Al_2O_3 FGM beam sample 1 after t=320 s. 264
Fig.V.4 Temperature distribution on SUS316-Al_2O_3 FGM beam (sample-3-trial 1) (a) temperature variation along the length of beam at different time intervals (b) temperature variation with respect to time at various points on the beam. ... 265

Fig.V.5 (a) Displacement versus time and (b) magnitude versus frequency plots for three-layer SUS316-Al_2O_3 FGM beam sample 3 (trial 1) under cantilever boundary condition after 50 s.....265

Fig.V.6 Temperature distribution on SUS316-Al_2O_3 FGM beam (sample-3-trial 2) (a) temperature variation along the length of beam at different time intervals (b) temperature variation with respect to time at various points on the beam. ...266

Fig.V.7 (a) Displacement versus time and (b) magnitude versus frequency plots for three-layer SUS316/Al_2O_3 FGM beams under cantilever boundary condition – Sample 3.....267

Fig.V.8 Temperature distribution on SUS316 beam (sample-9) (a) temperature variation along the length of beam at different time intervals (b) temperature variation with respect to time at various points on the beam. 268

Fig.V.9 (a) Displacement versus time and (b) magnitude versus frequency plots for pure SUS316 beam (sample 9) under cantilever boundary condition. 268

LIST OF TABLES

Table **Title** **Page no.**

Table 4.1: Details of the thermally sprayed SUS316-Al_2O_3 functionally graded beam samples. 63
Table 4.2: Plasma spraying setup parameters for sample manufacturing. 67
Table 4.3: History of the process parameters of powder metallurgy process during preparation of Al-Al_2O_3 FGM beam samples. 75
Table 4.4: History of the process parameters of powder metallurgy process during preparation of pure aluminium beam samples. 76

Table 5.1: Comparison of analytical and FEM solution for non-dimensional centre deflection of simply supported homogeneous beam under uniform load for EBT. 92
Table 5.2: Measured and rule of mixture theoretical densities of SUS316-Al_2O_3 FGM samples. 94
Table 5.3: Theoretical and experimental tip deflection for clamped-free SUS316-Al_2O_3 FGM and pure SUS316 beam samples. 98
Table 5.4: Theoretical and experimental tip deflection for clamped-simple support SUS316-Al_2O_3 FGM beam samples. 102
Table 5.5: Theoretical and experimental damped natural frequencies for a clamped free SUS316-Al_2O_3 FGM beam samples. 106
Table 5.6: Deviation in displacement as function of time for SUS316-Al_2O_3 FGM beam samples - Theoretical and experimental for clamped-free boundary condition. 106
Table 5.7: Theoretical damped frequencies (second mode) for SUS316-Al_2O_3 FGM beam samples for clamped-free boundary condition. 106
Table 5.8: Details of the mode shapes obtained from ANSYS. 108
Table 5.9: Material properties of the Al and Al_2O_3. 108
Table 5.10: Layer-wise material composition of Al-Al_2O_3 FGM beam samples used in free vibration experimental setup for clamped free boundary condition. 109

Table 5.11: Dimension of Al-Al_2O_3 FGM beam and pure aluminium beam samples used in free vibration experimental setup for clamped free boundary condition. 109
Table 5.12: Actual, Archimedes and theoretical density of Al-Al_2O_3 FGM and pure aluminium beam samples. 110
Table 5.13: Theoretical and experimental tip deflection for clamped-free Al-Al_2O_3 FGM beam samples without porosity effect.....111
Table 5.14: Theoretical and experimental tip deflection for clamped-free Al-Al_2O_3 FGM beam samples considering porosity effect. 116
Table 5.15: Experimental and theoretical natural frequencies for Al-Al_2O_3 FGM and aluminium beam samples for clamped-free boundary condition without porosity effect. 117
Table 5.16: Free Vibration Analysis of Pure Aluminum and Al-Al_2O_3 FGM beam sample considering porosities. 119

Table 6.1: The first dimensionless frequency parameters λ for different material distribution.....126
Table 6.2: Temperature dependent coefficients for SUS316 and Al_2O_3. 130

Table 7.1: Convergence of temperature for moving heat source for different mesh size.....140

Table 8.1: Temperature at different times for SUS316-Al2O3 FGM beam sample-5.....213

Table I.1 Different materials, their chemical composition and applications for selecting material for die fabrication.....241
Table I.2 Volume fraction details, thickness and photographs of various physical sample.....243
Table II.1 Technical specifications of PCB piezotronics make impact hammer (Source: product manual, PCB piezotronics).....248
Table II.2 Technical specifications of optoNCDT 1402 laser displacement sensor

(Source: instruction manual, optoNCDT 1402)……..…249

Table II.3 Technical Data for Type 8730A accelerometer……..…..254

Table IV.1 Sample data for axial convergence plot in Fig.IV.1……...264

Table V.1 Details of reduction in frequency with time for SUS316-Al_2O_3 FGM beam sample 1 – trial 2……..…..266

Table V.2 Details of reduction in frequency with time for SUS316-Al_2O_3 FGM beam sample 3 – trial 1…….…….268

Table V.3 Details of reduction in frequency with time for SUS316-Al_2O_3 FGM beam sample 3 – trial 2……..……269

NOMENCLATURE

P_{eff}	Effective material property like E_{eff} , G_{eff} , ρ_{eff} , ν_{eff} , α_{eff} , k_{eff} , $c_{p_{eff}}$
P_m	Material property of metal
P_c	Material property of ceramic
V_m	Volume fraction of metal
V_c	Volume fraction of ceramic
P_i	Temperature coefficients in the cubic fit unique to each property of the material constituent.
n	Power law index
E	Young's modulus, N/m^2
G	Shear modulus, N/m^2
ρ	Mass density, kg/m^3
ν	Poisson's ratio
α	Coefficient of thermal expansion, $/ {}^0C$
k	Thermal conductivity of material, W/mK
c_p	Specific heat, J/kg^0C
h_c	Natural convective heat transfer coefficient, $W/m^2 {}^0C$
$\dot{q}_{vol}$	Internal heat generation rate per unit volume, W/m^3
q_h	Heat loss by convective heat transfer, W/m^2
Q	Heat flux, W/m^2
t	Time
T	Total time
dx	Small element length
x	Position along x-axis
l	Element length, m

L	Length of the beam, m
h	Total thickness of the beam, m
b	Width of the beam, m
S	Perimeter of boundary surface, m
A^e	Elemental area exposed to heat transfer, m^2
A	Elemental area for struatural problem, m^2
dw_0/dx	Slope of beam axis w.r.t horizontal.
u	Axial deflection in the x direction, m
w	Transverse deflection in the z direction, m
u_0	Axial deflection at centrodial plane in the x direction, m
w_0	Transverse deflection at centrodial plane in the z direction, m
N_j^L	Linear Lagrange interpolation functions
N_J^H	Hermite cubic interpolation functions
$\mathbf{K}_{\text{comb}}^e$	Elemental conduction and/or convection matrix
$\mathbf{K}_{\text{cap}}^e$	Elemental capacitance matrix
$\bar{\mathbf{F}}_Q^e$	Elemental thermal force vector
$\mathbf{K}$	Stiffness matrix
$\mathbf{M}$	Consistent mass matrix
$\mathbf{F}$	Force vector
$\hat{\mathbf{T}}$	Tangent stiffness matrix
$\mathbf{C}$	Damping matrix
T	Temperature of surface, ^{0}C
T_∞	Ambient or free air stream temperature, ^{0}C
T_T	Temperature on top surface of beam, ^{0}C
T_B	Temperature on bottom surface of beam, ^{0}C

T_1, T_2	Nodal temperatures, ^{0}C
ΔT	Change in temperature, ^{0}C
$f(x)$	Distributed axial load per unit length, N/m
$q(x)$	Distributed transverse load per unit length, N/m
M	Bending moment produced by the applied forces, Nm
M_T	Thermal bending moment, Nm
$F(t)$	Forcing function due to thermal moment, Nm
$\mathbf{F_T}$	Total force vector
m_T	Non dimensional thermal moment
I	Moment of inertia of beam cross section, m^4
c	Velocity of propagation of longitudinal waves
σ_{xx}	Dynamic stress, N/m^2
ε_{xx}	Total nonlinear strain
ε_{xx}^0	Axial strain
ε_{xx}^1	Transverse strain, beam curvature
N_{xx}	Stress resultant
M_{xx}	Moment resultant
N_{xx}^T	Stress resultant due to thermal load
M_{xx}^T	Moment resultant due to thermal load
Q_{ii}	Stiffness coefficient for FGM
A_{xx}	Extensional coefficient of the beam element
B_{xx}	Extensional-bending coefficient of the beam element
D_{xx}	Bending stiffness coefficient of the beam element
ω	Natural frequency, rad/s

κ	Thermal diffusivity
τ	Non dimensional time
ζ	Damping ratio
W	Concentrated load at the free end or centre of the cantilever and clamp-simply supported beam respectively.

CHAPTER - 1

INTRODUCTION

1.1 THERMO-ELASTIC RESPONSE

Determination of the thermal deflections of structural elements like beams and plates is very important in engineering design. Evaluation of thermal strain and stresses are integral part of design activity for gas turbines, nuclear, aerospace, chemical reactors, electronic circuit boards and many other fields. When structural elements are subjected to surface heating, a temperature difference exists through the cross-section of the structures. These high thermal gradients cause thermal distortion of thin-walled structures. The problem of coupled thermo-elastic vibrations of structural parts are common in high-speed aircraft, rockets and turbines. In these structures, the mechanical and thermal applied loads could lead to small amplitude high frequency nonlinear vibrations. The structures made with composite materials are more sensitive and vulnerable to temperature change as compared to their isotropic counterpart. This is due to the difference in the thermal expansion coefficients of different constituents of the material resulting in high stresses due to temperature changes from the surrounding environment. Traditionally, researchers used to attempt this problem separately to avoid the fully-coupled thermo-elasticity problem. The heat conduction problem is solved first for the thermal field and later the one-way coupled thermoelastic problem for the structure under a prescribed thermal field. Today's challenge for engineers and researchers is how to solve these coupled problems. In recent years, functionally graded materials (FGMs) have gained wide importance and are being developed extensively due to their excellent mechanical and thermal properties. FGMs are microscopically inhomogeneous composite materials. One of the major advantage of these materials is, they are able to withstand high temperature environments while maintaining their

structural integrity. Hence, study of the thermo-elastic problem becomes a challenge for FGM structures to meet the design requirements of today's emerging technology.

1.2 FUNCTIONALLY GRADED MATERIALS

The idea of functionally graded materials (FGMs) was advanced substantially in the early 1980's in Japan, where this new material concept has been proposed to increase adhesion and to minimize the thermal stresses in metallic ceramic composites developed for reusable rocket engines (with outside temperature of 2000 K and inside temperature of 1000 K across less than 10 mm thickness). Meanwhile, FGMs concepts have triggered world-wide research activity and have been applied to metals, ceramics, and organic composites to generate improved components with superior physical properties. FGMs have been characterized by gradual spatial changes in their composition and consequently in their properties. These materials do not contain well distinguished boundaries or interfaces between their different regions as in the case of conventional composite materials. Because of this, such materials possess good chances of reducing mechanical and thermal stress concentration in many structural elements, which can be developed for specific applications. After development of functionally graded material in 1984 by group of scientists in Japan, researchers have started focusing on FGM as one of the potential material as substitute in applications requiring high temperature sustainability and high strength. Researchers have started studying thermo-mechanical properties of FGM and materials response to thermal and structural loads. During last 5-10 years, researchers have focused on control mechanism for vibration attenuation of functionally graded material structures by using piezoelectric and magnetostrictive actuators. The structures are not simply inhomogeneous, but their heterogeneity is usually typical in one direction for the entire volume of material. The application of this concept to metal matrix composites (MMCs) leads to the development of materials and corresponding components designed with the purpose of being selectively reinforced only in regions requiring increased modulus, strength and/or wear resistance.

There are different kinds of fabrication processes for producing functionally graded materials. Functionally graded materials can be divided into two broad groups namely:

thin and bulk FGM. Thin FGM are relatively thin sections or thin surface coating, while the bulk FGM are volume of materials which require more labour intensive processes. Thin section or surface coating FGM are produced by physical or chemical vapour deposition (PVD/CVD), Plasma Spraying, Self-propagating High temperature Synthesis (SHS), etc. Bulk FGM are produced using powder metallurgy technique, centrifugal casting method, solid freeform technology, etc. As the fabrication process is improved, cost of powder is reduced and the overall process cost is reduced, hence expanding the application of FGM. Owing to the importance of FGM, there are lots of research efforts at improving the material processing, fabrication processing and properties of the FGM.

1.3 APPLICATION OF FUNCTIONALLY GRADED MATERIALS

Broad areas that requires use of functionally graded materials are listed by Mahamood et al. (2012) are as follows:

A. Aerospace : Functionally graded materials can withstand very high thermal gradient, hence make them suitable for use in structures and space plane body, rocket engine component, etc.

B. Medicine : Proper combination of materials and gradation could be a choice for orthopaedic application such as teeth and bone replacement.

C. Defence : One of the most important characteristics of functionally graded material is the ability to inhibit crack propagation. This property makes it useful in defence application, as a penetration resistant materials used for armour plates and bullet-proof vests.

D. Energy : FGM are used in energy conversion devices. They also provide thermal barrier and are used as protective coating on turbine blades in gas turbine engine.

E. Optoelectronics : FGM also finds its application in optoelectronics as graded refractive index materials and in audio-video discs magnetic storage media.

Other areas of application of FGM are: plasma facing materials, propulsion system of planes, cutting tool insert coating, engine exhaust liners, aerospace skin structures, incinerator linings, thermal barrier coatings of turbine blades, thermal resistant tiles, and directional heat flux materials are all examples where materials have to operate in

extremely high temperature transient environments. The list is endless and more application is springing up as the processing technology, cost of production and properties of FMG improve. Temperature dependency on material properties is one of the important criterion to be accounted when modeling FGM structures designed for high-temperature applications.

From structural point of view, many researchers have attempted problems on static deflection, stresses, buckling, free vibration, dynamic response, for beams and plate like structures. Most of the studies concentrate on theoretical analysis of these structures and very little work is devoted on fabrication and experimental validation of theoretical results. Literature studies revealed that, experimental studies along with theoretical investigations on the static deflection, free vibration and thermo-elastic deflection has not been attempted rigorously. In the present work, plasma or thermal spray and powder metallurgy techniques have been adopted to synthesis functionally SUS316-Al_2O_3 and Al-Al_2O_3 beam respectively. Nonlinear finite element formulation has been presented which accounts for geometric nonlinearities, thermal load and temperature dependent material properties to obtain numerical results on static deflection, natural frequencies and thermo-elastic deflection. Detail studies are presented on nonlinear thermo-elastic deflection and thermal stresses for various structural and thermal boundary conditions such as step, concentrated line, shock heat and moving heat load.

1.4 ORAGANISATION OF DISSERTATION

This dissertation consists of nine chapters, four appendices and a list of references. Chapter one and two are the introduction and literature survey, chapter three discusses the finite elements suitable to solve the temperature field and displacement field of functionally graded material beam, chapter four is on SUS316-Al_2O_3 and Al-Al_2O_3 FGM beam sample preparation using thermal spray and powder metallurgy process respectively for experimental work while chapter five is on the experimental free vibration and transverse deflection studies of SUS316-Al_2O_3 and Al-Al_2O_3 FGM beam sample. Chapter six and seven deals with the theoretical analysis on linear thermal induced vibration, nonlinear thermo-elastic deflection and nonlinear stresses of SUS316-Al_2O_3 FGM beam when the beam is subjected to various heat loads and

structural boundary conditions. Chapter eight deals with experimental thermal analysis of SUS316-Al_2O_3 and Al-Al_2O_3 FGM beam sample and theoretical validation of thermo-elastic deflection for SUS316-Al_2O_3 FGM beam. Summary for each chapter is presented below.

Chapter two reviews the structural analysis of functionally graded elements and associated manufacturing processes. This chapter summarizes the past work on thermally induced vibrations of structures such as beams and plates, Functionally Graded Material (FGM) and its application for structures like beams, plates and shells, and the techniques and processes/methods for fabrication of functionally graded material.

Chapter three presents basic equation for material gradation through thickness of functionally graded beam. Further, it discusses on the formulation of the heat conduction problem in one and two dimension with convection and discretization of this problem using finite element method. The chapter also discusses on finite difference solution of heat transfer problem in time. In the second part, chapter three presents the governing equations for non-linear thermo-elastic vibration analysis of FGM beams using Euler Bernoulli theory followed by the equation of the motion to develop the weak forms using the principle of virtual displacements and the associated finite element model.

Chapter four includes a detailed description on the fabrication of the functionally graded material beam using thermal spray and powder metallurgy process. The various parameters used while preparing the FGM and pure aluminium beam samples are also discussed in the chapter. Lastly, the microstructure studies of FGM powder mixtures and beam samples by using scanning electron microscope (SEM) and SEM-EDX are discussed.

Chapter five discusses the nonlinear analysis of FGM beams accounting the vonKármán nonlinearity and its experimental validation for the static deflection and natural frequencies. The effects of the material grading index and the nonlinearity on

the displacement fields under clamped-free and clamp-simple support boundary conditions are discussed. The results are validated with the functionally graded material SUS316-Al_2O_3 beam fabricated using the plasma spraying and Al-Al_2O_3 FGM beam manufactured using powder metallurgy process for the transverse deflection and natural frequencies under clamped-free and clamp-simple support boundary conditions. Studies using ANSYS 3D 20 noded structural solid element have been presented to understand the role of shear deformation of the SUS316-Al_2O_3 FGM samples on displacements and natural frequencies. Effect of porosity encountered in the fabrication of beam samples using powder metallurgy process is also discussed in this chapter.

Chapter six presents detailed investigation on the thermal induced vibration of a functionally graded material beam when subjected to a step thermal load. The study considers one surface of the beam subjected to heat load with opposite surface being thermally insulated or subjected to convective heat transfer. Under step heat load, for various structural boundary conditions, results of the FGM beam in terms of time dependent deflection and thermal moment are discussed.

Chapter seven is on the investigation of thermo-elastic response of the FGM beam. The structural response of the FGM beam is discussed for various types of heat loads (step, concentrated line, shock and moving heat) under various structural boundary conditions considering 2-dimensional temperature distribution with one surface of the beam subjected to heat load with opposite surface being thermally insulated. Effect of temperature dependent and temperature independent material properties on thermal deflection is also discussed. The chapter also discusses on the parametric studies conducted to examine the influences of the various involved parameters. In the second part, the analysis of nonlinear dynamic stresses in SUS316-Al_2O_3 FGM beam subjected to various types of heat loads is discussed. The stresses are evaluated considering the temperature dependency of material properties and 2-dimensional temperature distribution across the transverse plane of the beam.

Chapter eight presents transient thermal analysis of SUS316-Al_2O_3 and Al-Al_2O_3 FGM beam using ANSYS and its experimental validation with heat source at the end of beam.

Free vibration study is presented on the FGM beam sample when heated under clamp free boundary condition. Thermal vibration study is also carried out for SUS316-Al_2O_3 FGM cantilever beam with heat source at clamp end and a comparision of theoretical results with experimental results are discussed.

The conclusions of the dissertation and the scope for the future work have been presented in chapter nine.

The list of the cited references is provided after chapter eleven. Five appendixes are provided. These five appendixes contain details on die design, history of various process parameters involved in the various Al-Al_2O_3 samples prepared using powder metallurgy process and detail procedure for sample preparation, description of the experimental setup and instruments used for deflection, natural frequency and temperature measurement and experimental results for static deflection and free vibration for various FGM samples, respectively.

CHAPTER - 2

LITERATURE SURVEY

2.1 INTRODUCTION

Thermally induced structural vibrations have been studied since 1950s. This chapter discusses in detail the availability of literature on thermally induced vibration of beams, plates, shells and spacecraft booms which are subjected to radiant heating and other means. It is seen that most of the fundamental investigations on the thermally induced vibration of beams and plates was carried out during the period of 1950–1970. Later on during 1960-1970, the work was more focused on the thermally induced vibrations of spacecraft booms and from 1990 onwards solar arrays panels was the topic of study. The study in the area of thermally induced vibrations of internally heated beam was carried out in 1936 and recently in 2001 and 2007. After development of functionally graded material in 1984 by Japanese scientists, researchers have started focusing on FGM in applications requiring high temperature sustainability and high strength. Researchers have started studying thermo-mechanical properties of FGM and their response to thermal and structural loads.

2.2 LITERATURE SURVEY ON THERMALLY INDUCED VIBRATIONS OF STRUCTURES

Pioneering research by Boley (1956), Boley and Barber (1957) and Boley (1972) on thermally induced vibrations of beam provides a detailed inter-relation of time dependent temperature variation on the structural vibrations. Boley (1956) considered the problem of lateral vibration of a thin beam with simple supports and subjected to rapid heat flux on the upper surface and thermally insulated condition on the bottom. Boley (1956) proved that the time dependent thermal moment acts as a forcing function

to induce a structural deformation and for thicker beams the inertia effect can be neglected and the dynamic solution approaches the static solution. After establishment of this original work in 1956, other researchers were motivated to probe thermally induced vibrations in other structures and with different thermal and mechanical boundary conditions. Considering the presence and absence of the inertial effects, Boley and Baber (1957) investigated the dynamic displacement of beams and plates when subjected to step heat input. The role of inertia was found to be important for rapidly applied heat input and for thin plates. In a similar article, Boley (1972) describes an approximate method to study the thermally induced vibrations in an axially loaded beams and plates under the influence of damping. Researches of Boley (1956, 1972) and Boley and Barber (1956) reveal that the occurrence of thermally induced vibrations depends on a non-dimensional parameter B which is the ratio of the thermal response time of the structure to the structural response time. Further, it is shown that the existence of thermally induced vibrations depends only on B and as this parameter increases, inertia forces disappear. Manolis and Beskos (1981) have worked on the problem attempted by Boley (1956) using Laplace Transform and discussed the effects of axial load, internal viscoelastic damping and external viscous damping on thermal vibrations of simply supported beam subjected to rapid heating. Dynamic stresses and deformations were evaluated by Stroud and Mayers (1971) for a rapidly heated rectangular plate using the dynamic thermo-elastic variational principle. Kraus (1966) has presented numerical results on the quasi-static response and dynamic response as a function of inertia parameter for simply supported thin non-shallow spherical shells whose inside surface is insulated and suddenly applied heat flux on to its outer surface. Seibert and Rice (1973) have carried out studies on thermally induced vibration of a simply supported beam using Euler-Bernoulli and Timoshenko beam theory with heat input on one surface using one dimension as well as two dimension heat conduction equation. They showed that L/h ratio in conjunction with one and two dimension heat conduction play an important role on the amplitude of the thermal vibration. For short beams of $L/h \leq 5$ the temperature boundary condition in both the length and thickness direction has the greatest effect on the deflection in case of Timoshenko beam. For beam with $L/h \geq 500$ the two dimensional effect becomes essentially one dimensional.

Das (1983) has investigated vibration of elastic plates due to thermal shock through use of complex variable theory. He inferred that inertia plays an important role in vibration of elastic plate when subjected to thermal shock. Chang and Wan (1986) have presented analytical method for the analysis of large amplitude thermo-mechanically coupled vibrations of rectangular elastic plates with various boundary conditions. Finite element analysis on the transient behaviour of aluminium and graphite epoxy plates subjected to an instantaneously imposed heat flux has been reported by Chang et al. (1992). Kidawa-Kukla (1997, 2003) has carried out studies on thermally induced vibration of uniform simply supported beam heated by laser beam. The laser heat source moves harmonically over a fixed point on the beam. The transverse vibrations of a beam induced by a mobile heat source are studied considering the external and internal damping of the beam material. Ootao and Tanigawa (2005) carried out theoretical analysis of the multilayered magneto-electro-thermoelastic strip due to unsteady and non-uniform heat supply in the width direction by the methods of Laplace and finite sine transformations. Tran et al. (2007) have studied the thermally induced vibration and its control for thin isotropic and laminated composite plates using the finite element method for different material orientations and boundary conditions when heat flux is suddenly applied at the top surface of the plate. Amabili and Carra (2009) have studied the effects of thermal variations on nonlinear forced vibrations and post-buckling of isotropic rectangular plates in the frequency range around the first resonance. Calculations and experiments show that nonlinear vibration of very thin clamped plates is largely affected by temperature variations of the order of 1^0C. The effect of temperature variation decreases with plate thickness.

Hong has presented chronologically the research reports on use of the generalized differential quadrature (GDQ) method to study the vibrations of thermal sleeve, laminated plate and shell, and magnetostrictive plates. Hong (2009) studied the thermal vibration of laminated shells under rapid heating. The GDQ solutions were obtained for the time response of axial, circumferential and normal displacements. Hong et al. (2005) have used the generalized differential quadrature (GDQ) method to obtain the numerical results of thermal vibrations for two layer cross-ply laminated tubes used for piping components in the electric power industry which have to resist the thermal

fatigue cracking. Hong and Jane (2003) have studied the interlaminar stresses and deflections in a cross-ply laminated rectangular plate during thermal vibration using the GDQ method involving the effect of shear deformation.

Apart from structures which are subjected to radiant or surface heating, structures undergoing internal heating may also experience thermally induced vibrations. The non-uniform heat transfer results from differences in convection heat transfer over the surface of the structure. The heat transfer at the surfaces is a combination of both natural and forced convection, but the forced convection is responsible for causing a temperature difference across the specimen. As a result of temperature difference a time dependent thermal moment comes into play. The thermal and structural analyses are coupled through the forced convection. Thermal moment can be employed to calculate the forcing function when substituted in to the equation of motion and hence drives the structural vibration of an internally heated beam. It is observed that the amplitude of the vibrations increase initially to reach a maximum value and then decay slightly. The major concern is the variation of the thermal moment over the time and how it causes the vibration amplitude to increase. Literature survey indicates that when the thermal moment and velocity profiles for a specimen are compared, it is observed that the thermal moment is maximum when the velocity is zero and vice versa. The coupling between these two causes the amplitude to increase. The steady state amplitude is independent of the initial displacement. Thus these vibrations can be classified as self-sustained vibrations, a sub class of self-excited vibrations. A self-sustained vibration is a self-excited vibration whose steady state is independent of initial amplitude provided it is greater than zero. In case of specimen undergoing internal heating, according to Baker (1933) the vibrations were "excited by forces between the air and the specimen due to the thermal action of the moving hot specimen on the surrounding air". In fact the temperature difference between the opposite faces is the reason for these vibrations, which results due to asymmetric cooling at the specimen surface. Blandino and Thornton (2001) have carried out a detailed study on the thermally induced vibration caused by internal heating. The analysis showed that the natural frequency of the beam was more important than the heating rate in determining if vibrations occur. The steady-state vibration amplitude is reached when

the internal heating is balanced by convection from the beam surface. Malik et al. (2007) reported their findings related to the effect of boundary conditions on thermally induced vibrations of isotropic beam subjected to internal heating and convective heat loss. It was observed that the boundary conditions influence the magnitude of dynamic displacement and dynamic thermal moment. A sustained thermally induced motion is observed with progress of time when the temperature gradient being evaluated is dependent on the forced convection generated due to beam motion.

During 1960-1970, research was more focused on the thermally induced vibrations of spacecraft booms and from 1990 onwards solar array panels was the topic of study. It was observed that when a spacecraft makes an orbital eclipse transition as it exits from or enters into the Earth's shadow, vibrations may develop because of rapid changes in the thermal loading of appendages. Due to the unexpected displacements or accelerations, the spacecraft appendages may degrade system operations. Practically, interaction of structural deformations and incident heating may induce unstable vibrations of the appendages, which may result in spacecraft failure. Consequently, stability problems such as thermal flutter have been investigated by the use of thermally induced bending or torsional vibrations for the booms and solar arrays. Beam (1969) of NASA Ames demonstrated unstable thermally induced oscillations in the laboratory. The boom-mass system was observed to be stable for small amplitude motions but unstable for large amplitudes with an eventual limit cycle oscillation in a coupled bending torsion mode. Yu (1969) has reported his work on thermally induced vibration and flutter of a flexible boom (cantilever beam) without twisting. The analysis showed that bending oscillations were stable if the boom was pointed away from the sun and unstable if it was pointed towards the sun. Thornton and coworkers have presented chronologically the research reports on thermally induced vibration with applications to spacecraft [Thornton and Foster (1992), Thornton and Kim (1993), Murozono and Thornton (1998), Thornton et al. (1995), Gulick and Thornton (1995), Johnston and Thornton (1996, 2000)].

The research work published by Bachschmid et al. (2007) suggest that occurrence of thermal vibrations is not just limited to only spacecraft's but can also occur as a result of rotor-to-stator rub in real rotors. The effect is caused by combined effect of contact

forces which introduces heat as a result of which, a thermal bow is produced. It is interesting that thermally induced vibrations are also observed in the case of Carbon Nano-tubes. Cao et al. (2005) have studied the thermo-mechanical properties of carbon nanotubes to explore the thermal vibration and thermal contraction behaviors of single walled carbon nanotubes.

2.3 LITERATURE SURVEY ON FUNCTIONALLY GRADED MATERIAL (FGM)

During last two decades, materials with gradation in properties are being developed and one such material is functionally graded material (FGM), typically like the one that caters to high temperature, good wear resistance, in conjunction with high strength and toughness. FGMs were proposed in Japan during 1984-1985 for the space plan project. FGMs are a class of composites that have a continuous variation of material properties from one surface to another. The smooth transition between metallic and ceramic components reduces thermal stresses, residual stresses and stress concentration factors found in laminated composites. Functionally graded material beams, plates and sandwich plates are being proposed as potential structural elements for automotive, ship building, space vehicles, aircrafts, nuclear reactors, astronautical vehicles, biomedical, optoelectronics, industrial, residential buildings and civil structures (Gupta and Talha (2015)). FGMs are composite materials which are fabricated with combination of two or more materials with continuously varying material composition to obtain material properties suitable for specific application (Naebe and Shirvanimoghaddam (2016)). FGMs possesses number of advantages, such as enhanced thermal properties, potential reduction of in-plane and transverse through-the-thickness stresses, improved residual stress distribution, higher fracture toughness, reduced stress intensity factors, good wear resistance, and good corrosion resistance (Tounsi et al. (2013), Zidi et al. (2014)). Birman and Byrd (2007) presented the FGM reviews for development, design and applications. Some of the special problems and examples of applications of FGM structures that have recently been reported (Birman and Byrd, 2007) include: (i) functionally graded prosthesis joint, (ii) functionally graded polyester-calcium phosphate materials for bone replacement, (iii) functionally graded thermal barrier coating (TBCs) for combustion chambers, (iv) functionally graded layer between the

Cr–MO shank and ceramic tip of a cutting tool improving the thermal strength, (v) functionally graded piezoelectric actuators, (vi) FGM metal-ceramic armor, (vii) functionally graded thermal protection systems for spacecraft, hypersonic, and supersonic planes, (viii) functionally graded heated floor systems. Yet another application of FGM is thin-walled members like plates and shells, which are used in reactor vessels, turbines and other machine parts that are susceptible to instabilities due to buckling load and large amplitude deflections, or excessive stresses induced by thermal or combined thermo-mechanical loading. Considering these wide material variations and applications of FGMs, it is important to study the static and dynamic characteristics of functionally graded material structures, such as beams, plates and shells. The accuracy of response of FGM structures is dependent on both the kinematic modelling as well as the correctness of estimated material properties.

2.3.1 Functionally Graded Material Beams:

The elasticity solutions of a transversely loaded simply supported Euler-Bernoulli FGM beam were obtained by Sankar (2001) assuming exponential variation of Young's modulus, thermal expansion coefficient, and constant Poisson's ratio over the thickness. Sankar and Tzeng (2002) showed that the thermoelastic properties of beam can be tailored to reduce the thermal residual stresses for a given temperature distribution which can be accomplished by varying the thermoelastic constants in a manner opposite to the gradation of temperature through the thickness. Kadoli et al. (2008) have evaluated transverse deflection of metal-ceramic FGM beam numerically using higher order shear deformation theory. Using a third order zigzag theory, Kapuria et al. (2008) have validated through experiments the static and free vibration response for layered functionally graded beams. Thai and Vo (2012); and Sina et al. (2009) have analytically investigated the effects of boundary conditions, volume fraction and shear deformation on natural frequencies, and mode shapes on the bending and free vibration of FGM beams. Under the influence of a moving harmonic load, Simsek and Kocaturk (2009) analysed free vibration characteristics and dynamic behaviour of a FG simply supported beam. The system of equations of motion were derived using Lagrange's equation under the assumptions of Euler-Bernoulli beam theory. It was observed that the effects of different material distribution, velocity of the moving harmonic load and

excitation frequency play very important role on the dynamic behaviour of the FGM beam. Wattanasakulpong et al. (2011) analysed the linear thermal buckling and vibration characteristics of thick FG beams and found that the fundamental frequency decreases with the increase in temperature and tends towards minimum point closing to zero at the critical temperature while in the post-buckling region, the fundamental frequency increases with the increase of temperature.

Recently, Alshorbagy (2013) and Alshorbagy et al. (2011) have studied the effect of slenderness ratio, material distribution and boundary conditions on the free vibrational characteristics of a FG beam by using finite element method. The equation of motion of FG beam has been derived using Euler-Bernoulli beam theory and virtual work principle. Based on Euler-Bernoulli beam theory and Timoshenko beam theory, Anandrao et al. (2012) have studied free vibration of FGM beams for various structural boundary conditions and length to thickness ratios. They showed that transverse shear significantly affects the fundamental frequency and mode shape for lower length to thickness ratios of FGM beams. Based on first order shear deformation theory for axially constrained FGM beam subjected to uniform through thickness temperature, Anandrao et al. (2013) showed that with the increase in the temperature, the natural frequencies show a decreasing tendency. The natural frequencies predicted by considering the temperature independent (TID) material properties are higher than those predicted using the temperature dependent (TD) material properties. Simsek et al. (2013) analysed the influence of volume fraction index, material properties, length scale parameter, aspect ratio and Poisson effect on the static bending behaviour of FGM beams and showed that the deflections of the microbeam by the classical beam theory are always larger than those by the modified couple stress theory. Kiani and Eslami (2013) showed that elasticity modulus of the constituent materials have significant effect on critical buckling temperature of FGM beam and show different behaviors when subjected to in-plane thermal loading as compared to isotropic beam. Based on Timoshenko beam theory, the dynamic response of functionally graded multi-walled carbon nanotube polystyrene nanocomposite beams subjected to multi-moving loads was investigated by Heshmati and Yas (2013). Based on the classical and first order shear deformation beam theories using Rayleigh–Ritz method, Pradhan and

Chakraverty (2013) have studied free vibration analysis of FGM beams subjected to different sets of structural boundary conditions. Considering the effects of material property distribution and porosity volume fraction, Wattanasakulpong and Ungbhakorn (2014) have used differential transformation method to solve linear and nonlinear vibration responses of FGM beams with different kinds of elastic supports. They have proposed the modified rule of mixture for FGM with porosity volume fraction evenly distributed among the metal and ceramic. The imperfect FGM beam is assumed to have porosities evenly spreading within the beam cross-section due to defect during production. In case of nonlinear vibration analysis, they showed that irrespective of the boundary condition, the nonlinear frequency ratios are higher when the volume fraction of porosity increases. Based on Timoshenko beam theory, Kien et al. (2016) have studied the dynamic response of a simply supported FGM porous beam with varying cross section subjected to multiple moving forces. They have used the model proposed by Wattanasakulpong and Ungbhakorn (2014) and showed that porosity volume fraction plays an important role in the study of dynamic response of the beam. The buckling of two-dimensional functionally graded material Timoshenko beams with different boundary conditions has been investigate by Simsek (2016) assuming that the material properties of the beam vary in both axial and thickness directions according to the power-law form. Wang and Wu (2016) have studied the dynamic response of an axially functionally graded material beam subjected to a moving harmonic load under thermal environment using classical beam theory and Timoshenko beam theory.

Based on Euler-Bernoulli beam theory and von Kármán geometric nonlinearity, Ke et al. (2010) have shown that nonlinear frequency of FGM beam increases with increase in vibration amplitude. Frequency response of FGM beam at super harmonic and subharmonic resonances and the effects of different parameters on the frequency-response were studied by Shooshtari and Rafiee (2011). Governing equations for Euler–Bernoulli and Timoshenko beams have been developed by Reddy (2011) using von Kármán nonlinear strains for functionally graded beam and an analytical solution has been presented for linear case. Nonlinear finite element models of functionally graded beams considering the von Kármán geometric nonlinearity, power-law variation of material through the beam height, and microstructure length scale parameter have been

developed by Arbind and Reddy (2013) for the Euler–Bernoulli beam and the Timoshenko beam. Considering all thermo-mechanical properties to be temperature and position dependent, geometrically non-linear thermally induced vibrations of thick section FGM beams subjected to rapid heating was analyzed by Ghiasian et al. (2014). Based on Euler-Bernoulli beam theory and von Karman geometric nonlinearity Taeprasartsit (2015) has presented free vibration analysis of thin FGM beams with immovably supported ends.

Thermo-mechanical buckling and post-buckling deformations of a FGM Timoshenko beam resting on linear elastic foundation have been studied by Sun et al. (2016). FGM beams resting on elastic foundation and subjected to thermal loads were investigated for large amplitude nonlinear vibration, nonlinear bending and thermal post buckling by Shen and Wang (2014). They found that the foundation stiffness has a significant effect on the nonlinear vibration characteristics, the nonlinear bending behaviors, and the thermal post buckling behaviors of the beam. Analysis of FGM Timoshenko beam subjected to sudden uniform temperature rise resting over a conventional three-parameter elastic foundation has been studied by Ghiasian et al. (2015).

2.3.2 Functionally Graded Material Plates and Shells:

Reddy and Chin (1998) have analysed numerically the thermomechanical behaviour of FGMs under abrupt thermal loading conditions for different volume fractions of the constituents and combinations of different constituent materials. They have listed the temperature coefficients in the cubic fit unique to each property of the material constituent such as Young's modulus, Poisson's ratio, thermal conductivity, specific heat and so on for various materials in order to calculate the effective temperature dependent thermo-mechanical properties for FGM. Praveen and Reddy (1998) investigated the nonlinear response of functionally graded ceramic–metal plates using the first order plate theory subjected to uniformly distributed static loading and suddenly applied uniform dynamic loading under temperature field. Reddy and Cheng (2001) have studied the three-dimensional thermomechanical deformations of simply supported, functionally graded rectangular plates using an asymptotic method with effective material properties estimated by the Mori–Tanaka scheme. The temperature, displacements and stresses of the plate are computed for different volume fractions of

the ceramic and metallic constituents. Woo and Meguid (2001) used the classical plate theory for static bending response of FGM plates, using a power law variation for the volume fractions in order to compute all the effective material properties. Yang et al. (2003) have investigated the large amplitude vibration of initially stressed FGM laminated rectangular plates with thermo-electro-mechanical loading and demonstrated that the linear and nonlinear vibration behaviour of the pre-stressed laminated plates is greatly influenced by the various factors such as vibration amplitude, material composition, etc. The thermal shock strength of a FGM was evaluated theoretically by Wang et al. (2004) for a plate containing a surface crack wherein it is found that FGM with high metal content exhibits significant resistance to crack growth from the ceramic side to the metal side. Yang et al. (2006) have carried out post-buckling analysis of cylindrical panels made of functionally graded materials with temperature-dependent material properties graded in thickness direction according to a simple power law distribution. Chi and Chung (2006) studied and presented the closed-form solution for the mechanical behavior of FGM plate under transverse load. They found that the solutions of FGM plates are similar to homogeneous plates, except for the bending stiffness. Na and Kim (2006) have analyzed three-dimensional thermal buckling and postbuckling of functionally graded materials subjected to uniform or non-uniform temperature rise by using finite element method. Navazi and Haddadpour (2007) have investigated aero-thermoelastic stability margins of functionally graded panels. The structural formulation is based on the Classical Plate Theory (CPT) and the aerodynamic loading is formulated using piston theory to model quasi-steady aerodynamic loading. A simple power-law and the Mori–Tanaka scheme are used for estimating the effective material properties. Yang and Huang (2007) have studied nonlinear transient response of simply supported imperfect functionally graded plates in thermal environments subjected to a temperature field uniform over the plate surface but varying along the thickness direction. Sohn and Kim (2008) analysed static and dynamic stabilities of FG panels under supersonic air flows considering temperature and volume fraction changes and showed that FG panels are more stable than the isotropic metal panel, in terms of thermal post-buckling characteristics. To study the static deflection and transverse stresses, Nguyen et al.(2008) have proposed first-order

shear deformation plate models with shear correction coefficients for modelling structures made of functionally graded materials. The material properties are considered to be isotropic varying through the thickness according to a power law distribution. Zhao et al. (2009) have investigated buckling behaviour of functionally graded plates under uniaxial mechanical and thermal loading using first-order shear deformation plate theory, in conjunction with the element-free kp-Ritz method. The displacement field is approximated in terms of a set of mesh-free kernel particle functions. A stabilized conforming nodal integration approach is employed to evaluate the plate bending stiffness while the direct nodal integration method is used to estimate the shear and membrane terms to eliminate the shear locking effects of very thin plates. Sadowski et al. (2009) have carried out thermal analysis of thin layered functionally graded circular plate subjected to a sudden cooling process (thermal shock) at the upper surface. Lee et al. (2010) have presented postbuckling analysis of functionally graded ceramic–metal plates under edge compression and temperature field conditions using first-order shear deformation plate theory and the element-free kp-Ritz method. Chen et al. (2011) have presented thermal buckling analysis of hybrid functionally graded plates with an arbitrary initial stress including the effect of transverse shear deformation. Dogan (2013) has studied nonlinear dynamic responses of the FGM plates under random mechanical and thermal loading by using the classical plate theory. Malekzadeh and Shojaee (2013, 2014) have studied in detail dynamic response of beams and plates subjected to moving thermal load. They showed that under the influence of moving heat source, the amplitude of centre deflection decreases by increasing the velocity of heat source and convective heat transfer coefficient. Hamid et al. (2015) have developed simple sinusoidal plate theory that can accurately and efficiently evaluate the thermomechanical behavior of functionally graded sandwich plates. Yahia et al. (2015) studied wave propagation in order to compare different shear theories and porosity solutions in FGM plates. Pandey and Pradyumna (2017) have presented finite element formulation based on higher-order layerwise theory to study thermally induced vibration of FGM sandwich panels subjected to thermal shock.

The thermal vibrations of plates with or without piezoelectric actuators subjected to the combined action of thermal and electrical loads was studied by Shen (2007). He

revealed that the width-to-thickness ratio of a plate, plate aspect ratio as well as the volume fraction distribution have a significant effect while control voltage has a minor effect on the nonlinear thermal bending response of FGM plates. Deschilder et al. (2006) have carried out analytical study to solve the large deflection analysis of unsymmetrical cross ply laminates under cylindrical bending using the von-Karman geometrical nonlinearity. Yang and Shen (2003) have used the refined third order theory with an assumed power law variation for Young's modulus, thermal expansion coefficient and density, and a constant Poisson's ratio for static and dynamic response of FGM plates under thermal loading. Chakraborty et al. (2003) used the same material model to present a first order shear deformation theory (FSDT) based shear locking free element for FGM beams. Functionally graded, ZrO_2-Ti-6Al-4V, rectangular plates were imposed with transverse uniform and sinusoidal load under thermal environment for studying the nonlinear bending behavior by Shen (2002). Huang and Shen (2004) have studied nonlinear free and forced vibration of functionally graded plates in thermal environments with temperature-dependent material properties. Analytical solutions were presented using an improved perturbation technique.

The four variable refined plate theory developed by Tounsi et al. (2013) accounting for quadratic variation of the transverse shear strains across the thickness of the plate has been used by Bouderba et al. (2013) and Zidi et al. (2014) to study the bending response of FGM plate subjected to thermo-mechanical loading and hygro-thermo-mechanical loading resting on elastic foundation. Under various structural boundary conditions, Meziane et al. (2014) develop an efficient and simple refined shear deformation theory for the bucking and vibration analyses of FGM sandwich plates supported on elastic foundations. Belabed et al. (2014) developed a new higher order shear and normal deformation theory with only five unknowns for the bending and free vibration analysis of simply supported FGM plates. Bennoun et al. (2016) developed a new five-variable refined plate theory for the free vibration analysis of a multilayer FGM system-symmetric and unsymmetric FGM sandwich plates. For the bending and free vibration analysis of functionally graded plates, Hebali et al. (2014) have presented a new quasi-three-dimensional hyperbolic shear deformation theory accounting for both transverse shear and normal deformations without using shear correction factor. Mahi et al. (2015)

developed a new hyperbolic shear deformation theory for buckling and vibration of FG sandwich and laminated composite plates. Analytical solutions for deflection and stresses are obtained using Navier-type procedure. The thickness stretching effect is ignored. It accounts for parabolic variation of transverse shear strains and shear stresses through the thickness of the plate.

Based on the classical shell theory, using volume fraction and rule of mixture with temperature independent material properties, Nemat-Alla (2003) has theoretically demonstrated two dimensional functionally graded materials and inferred that thermal stresses are less when compared to the thermal stresses in conventional functionally graded material. Qatu et al.(2010) have reviewed more than 200 research papers in the area of dynamic analyses of composite shells from 2000-2009 to emphasis on the type of testing or analysis performed (free vibration, impact, transient, shock, etc.), complicating effects in material (damping, piezoelectric, etc.) and structure (stiffened shells, etc.), and the various shell geometries (cylindrical, conical, spherical and others). A general discussion of the various theories (3D, thick and thin shell, higher order shear deformation, layer wise shell and non-linear) is also presented. Naj et al. (2008) presented the thermal buckling analysis of FGM truncated conical shells made by the mixture of metal and ceramic based on first-order shell theory under a number of thermal and mechanical loads. Based on FSDT, Tornabene (2009) presented the generalized differential qradrature (GDQ) solution for the free vibration analysis of FGM conical and cylindrical shells and annular plates. Sepiani et al. (2010) have investigated the free vibration and buckling of a two-layered cylindrical shell made of inner functionally graded and outer isotropic elastic layer, subjected to combined static and periodic axial forces. Cinefra et al. (2012) presented the Finite Element Method (FEM) solutions for the static analysis of FGM plates and shells subjected to mechanical load. Zhang et al. (2012) presented the numerical results for the nonlinear dynamics analysis of FGM shells, included the first-order shear deformation theory (FSDT) and two edge clamped conditions. Sheng and Wang (2013) have presented a new simplifying model of functionally graded cylindrical shells based on Hamilton's principle, Von Kármán non-linear theory and the first-order shear deformation theory when subjected to thermal and axial loads.

2.3.3 Fabrication of functionally graded materials

Thermal Spray and powder metallurgy processes are ideally suited for fabricating gradient materials because of the excellent microstructural control and the versatility in these techniques. Limited literature is available on the fabrication of functionally graded material using these process with alumina and stainless steel as constutients of functionally graded material. Lambros et al. (1999) have presented a novel technique for the fabrication and fracture testing of large-scale polymeric based Functionally Graded Materials (FGMs). The technique generates a continuously inhomogeneous property variation by taking advantage of the susceptibility of a polyethylene carbon monoxide copolymer (ECO) to ultraviolet irradiation. The resulting FGMs exhibit a varying Young's modulus, usually in a linear fashion, from approximately 160 MPa to 250 MPa over 150 mm thick specimens. Mahamood et al. (2012) have presented an overview of fabrication processes, area of application, some recent research studies on FGM. Sobczak and Drenchev (2013) have systematically reviewed the basic production techniques for manufacturing metal based functionally graded materials by compiling several unpublished results. They showed that with the developments in manufacturing processes, special varying gradients can be achieved to suit various goals of engineering applications.

Several studies have been reported on the fabrication of ceramic-metal gradient materials considering alumina as ceramic material by different plasma spray methods. Ctibor et al. (2009) have fabricated composite coatings from a mixture of powders of alumina based ceramic and stainless steel using plasma spray process. They have used two different techniques, gas-stabilized plasma spray process (GSP) and water stabilized plasma spray process (WSP) which both belong to family of procedure known as atmospheric plasma spraying (ASP). Functionally graded ZrO2-NiCrAlY coatings were prepared by plasma spray process by Gu et al. (1997) using pre-mixed spheroidized powders as feedstock. Pre-mixed powders helped them to achieve chemical homogeneity and uniform density along the graded layers. Microstructure of series of composites produced by air plasma sprayed (APS) alumina were tested by Amsellem et al. (2007). Zhang and Kobayashi (2005) have studied the corrosion resistance properties of Al_2O_3+ZrO_2 composite coatings sprayed on stainless steel

substrate using gas tunnel type plasma spraying process. Li and Sun (2003) have studied the properties and microstructure of Al_2O_3 coating deposited using a novel microplasma torch of hollow cathode.

Kapuria et al. (2008) have fabricated Al-SiC FGM beam samples with three and five layers using the powder metallurgy route following consolidation of powder stack with cold isostatic pressing (CIP) followed by sintering. Five-layered Ni-Al_2O_3 beam samples were also prepared using combustion powder thermal spray process. Zhau et al. (2001) have developed ZrO_2-NiCr functionally graded material by powder metallurgical process and studied their mechanical properties and shrinkage effect. They have carried out detail microstructure studies of the FGM material to understand metal-ceramic interface and observed stepwise constitutional gradation. Erdemir et al. (2015) have studied microstructure characterities and mechanical properties of functionally graded Al2024-SiC composites prepared by powder metallurgy techniques. They showed that the increase in microhardness values and intermetallic formation play a major role on the improvement of mechanical properties of the composites. Bhattacharyya et al. (2008) have prepared multilayered FGM Al-SiC and Ni-Al_2O_3 beams using powder metallurgy route and thermal spraying technique respectively. Microstructural studies, porosity content and microhardness were determined. They have also studied bulk properties such as effective flexural strength, thermal fatigue behavior and thermal shock resistance. Wattanasakulpong et al. (2012) have developed theoretical model using third order shear deformation theory to study free vibration of layered Al_2O_3-Epoxy FGM beams prepared using multi-step sequential infiltration technique. Discrepancies between theoretical and experimental results were observed because of porosities which arises due to imperfect infiltration and approximation in the material model.

2.4 MOTIVATION

While literature on the vibrations induced by rapid heating in isotropic homogeneous and composite structures is available, a survey reveals that most of the researchers have focused on thermal induced vibration when top surface is exposed to sudden heat source and diametrically opposite surface is insulated. Also the geometric non-linearity and

temperature independent and temperature dependent material properties have not been considered together. Investigation on thermal vibrations due to temperature gradient in FGM structures with combined structural and thermal boundary conditions is also unattempted. Most of the studies are concentrated on theoretical analysis of structures and very little work is devoted on fabrication and experimental validation of theoretical results. Also, no results have been reported till date for FGM beams accounting the von-Kármán nonlinearity under different heat loads and structural boundary conditions. In this study, a functionally graded through-thickness beam with the von Kármán nonlinear strains is considered. This study aims to investigate the effects of the material grading index and the nonlinearity in the displacement fields (geometric nonlinearity) under various thermal loads and structural boundary condition. To validate the theoretical model, experimental studies are carried out on the FGM samples prepared using plasma spray and powder metallurgy process. The thermal analysis is carried out on the FGM samples to study the thermal response. The structural response is studied through static deflection and natural frequency analysis under clamped free and clamp-simple support boundary conditions.

2.5 OBJECTIVES OF THE PRESENT STUDY

The main objective of the present work is on the investigation of the thermo-elastic response of a FG beam when subjected to various thermal load on one surface with opposite surface being insulated or subjected to convective heat loss and experimental validation of the theoretical model with regards to static deflection and free vibration study.

From the foregoing review of literature, the detail objectives of the present work are outlined as follows:

- Thermo-elastic response of functionally graded material Euler Bernoulli beam – geometrically linear and nonlinear analysis.
    a) One and two dimensional finite element formulation for the evaluation of temperature distribution in a functionally graded beam.

b) Derivation of the nonlinear governing equation of motion considering thermal load. Deriving the associated finite element equation of motion to study the structural response to thermal load.

c) Evaluate the effect of volume fraction ratio, L/h ratio, heat transfer boundary conditions and structural boundary conditions on thermo-elastic response of beams.

d) To evaluate effect of temperature dependence of FGM material properties on thermo-elastic response of beams.

❍ Experimental validation of thermal vibration of functionally graded material beams.

a) Sample preparation of SUS316-Al_2O_3 FGM beam using plasma spray process.

b) Sample preparation of Al-Al_2O_3 FGM beam and pure Al beam using powder metallurgy process.

c) Theoretical analysis and experimental validation for transverse deflection and free vibration response of SUS316-Al_2O_3 and Al-Al_2O_3 FGM beam.

d) Study the effect of porosity on the transverse deflection and free vibration response of pure Al and Al-Al_2O_3 FGM beam.

e) Thermal analysis of SUS316-Al_2O_3 and Al-Al_2O_3 FGM beam subjected to heat source at one end.

f) Study of free vibration response and thermo-elastic deflection of SUS316-Al_2O_3 FGM clamp free beam with heat source at the clamped end.

CHAPTER - 3

NONLINEAR FINITE ELEMENT FORMULATION FOR THIN FUNCTIONALLY GRADED BEAMS UNDER THERMAL LOADS

3.1 INTRODUCTION

Beams are the most common type of structural component, widely useful in civil, mechanical, and aerospace engineering. The primary function of the beam is to support transverse load and carry it to the supports. A beam resists transverse loads mainly through bending action. The beam may undergo stretching, if it is constrained to move at the end supports. Similarly, beams may be subjected to thermal load which gives rise to thermal moment due to temperature difference on either sides of beam. Keeping in mind the prime application in thermal environment, structural elements are subjected to various types of heat loads such as sudden heating or step heating, moving heat load, gradual heating, point heat load and or shock load. The operation of gas turbine blades is one example wherein the gas temperature exceeds the melting point of blade material. Efficient cooling system is one approach to allow material to operate at temperature that exceed material temperature. Apart functionally graded material or functionally graded thermal coating is also the alternate possible approach for turbine blades. All modes of heat transfer are generally present in varying degrees in a real physical problem. The important aspects in solving heat transfer problems are identifying the significant modes and deciding whether the heat transferred by other modes can be neglected. The solution to the isotropic beam subjected to heat load is straight forward. Either the one or two dimensional problem can be solved for temperature across the thickness or along the length wherein the material properties are constant and do not

vary with temperature. In case of functionally graded material, the material properties vary across the thickness or along the length depending on the material gradation. Also the material properties are dependent on the temperature and vary as temperature of the beam increases.

In this chapter, a review of the differential equation for heat conduction in one dimension and two-dimension is presented. Both one- and two-dimensional finite element formulation of the heat transfer problem are considered. A one dimensional linear element is used to discretize across the thickness of the beam while a two dimensional Lagrangian rectangular finite element is used to discretize the transverse plane of the beam. Further, a finite difference solution of heat transfer problem in time domain is briefed. When the loads applied on the beam are quite large, the linear load-defection relationship is no longer valid because the beam develops internal forces that resist deformation (Reddy, 2004). The magnitude of internal forces increases with the loading as well as the deformation. In this context, the theoretical formulation for nonlinear load-defection response of straight beams will be dealt. The nonlinear formulation of straight beams is based on assumptions of large transverse displacements, small strains and small to moderate rotations (Bathe, 1996). The theoretical formulation is derived for Euler–Bernoulli beam accounting for the von-Kármán nonlinearity under different thermal and structural boundary conditions neglecting the transverse shear strains. First we begin with an assumed displacement field for the beam and compute strains that are consistent with the kinematic assumptions of the theory. Later the equation of motion are derived to obtain the weak forms using the principle of virtual displacements and the associated finite element model.

3.2 MATERIAL GRADATION THROUGH THICKNESS OF FUNCTIONALLY GRADED BEAM

Researchers have shown immense interest in studying the causes of thermal vibrations and the conditions under which the thermal vibrations will occur for various material models. Some of the material models listed by Kapuria et al.(2008) include, the self-consistent model of Hill, the mean field micromechanics models of Mori and Tanaka

and Wakashima and Tsukamoto, the simple rule of mixtures, the modified rule of mixtures and the unit cell model which provide simple and convenient ways for predicting overall response of two phase composite materials.

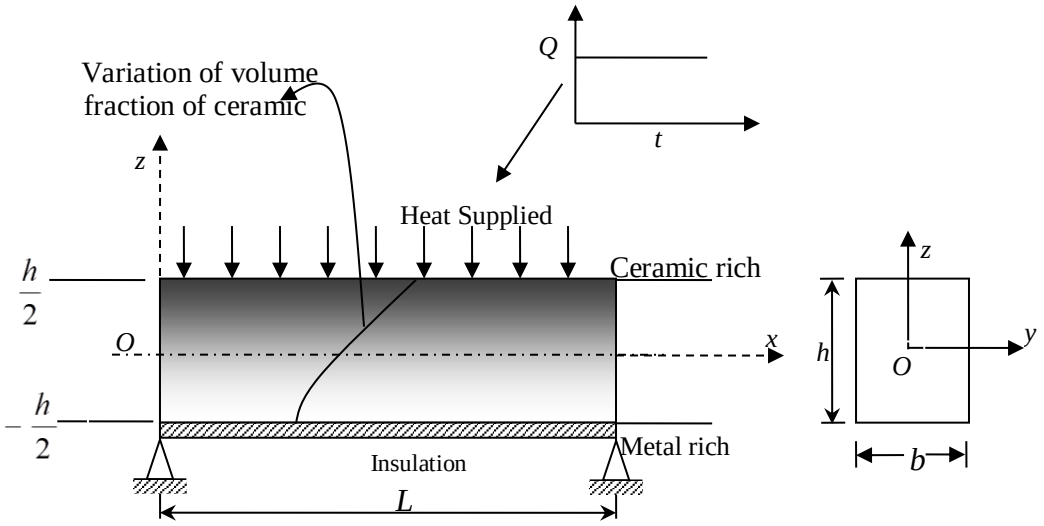

Fig.3.1 Configuration of simply supported FGM beam subjected to step heating.

Consider a rectangular cross section beam as $b \times h$. Let L be the length of the beam, with b being the width and h being referred to as height or thickness. As shown in Fig.3.1, the *x*-coordinate is taken along the mid-plane of the beam, *z*-coordinate along the thickness of the beam, and the y-coordinate is taken along the width of the beam. The volume fraction of metal or ceramic is based on the power law distribution. The variation of material properties is considered in thickness direction i.e. along z axis. The ceramic volume fraction is determined based on simple rule of mixture. Accordingly, the top surface of the beam is pure metal whereas bottom or outer surface is pure ceramic and for different values of n, one can obtain different volume fraction of metal. n is the power law index that takes on values greater than or equal to zero.

In a FGM beam with the volume fraction of metal or ceramic based on power law distribution, the following expressions hold for the evaluation of effective material property P_{eff} of FGM, like Young's Modulus E_{eff}, Shear modulus G_{eff}, mass density ρ_{eff}, Poisson's ratio ν_{eff}, coefficient of thermal expansion α_{eff}, thermal conductivity k_{eff} and specific heat $c_{p_{eff}}$:

$$P_{eff}(z) = P_m V_m(z) + P_c V_c(z) \tag{3.1}$$

where, subscript *c* and *m* denote the properties at the top and bottom surfaces of the beam respectively corresponding to either pure ceramic or pure metal. Variation of material properties is considered in thickness direction i.e. along z axis. The metal volume fraction V_m is determined based on simple rule of mixture (ROM) i.e.

$$V_m = 1 - V_c. \tag{3.2a}$$

Volume fraction of ceramic V_c is given as follows:

$$V_c = \left(\frac{z}{h} + \frac{1}{2}\right)^n \tag{3.2b}$$

accordingly, the top surface, $z = h/2$, of the beam is pure ceramic whereas bottom surface is pure metal and for different values of n, one can obtain different volume fraction of ceramic. n is the power law index that takes on values greater than or equal to zero. h is the thickness of the beam. Eq.(3.1) is based on the fact that FGM structure is considered as a laminate of multiple perfectly bonded layers of isotropic material with each layer having a composition of V_c and V_m being different from the adjacent layers and so on. Fig.3.2 shows the variation of volume fraction of ceramic across the thickness of the beam for various power law index n for FGM beam.

To evaluate the temperature dependency of the material property, the individual constituent material properties, P_m or P_c ($E_m, \rho_m, k_m, \alpha_m, c_{p_m}, E_c, \rho_c, k_c, \alpha_c, c_{p_c}$) namely of the metal and ceramic used in FGM beam are expressed as the function of temperature T (measured in Kelvin). All the material properties are expressed in the form of $P_m(T)$ or $P_c(T)$ as follows

$$P_i(T) = P_0(P_{-1}T^{-1} + 1 + P_1T + P_2T^2 + P_3T^3) \tag{3.3}$$

in which P_0, P_{-1}, P_1, P_2 and P_3 are the temperature coefficients in the cubic fit unique to each property of the material constituent (Reddy and Chin, 1998).

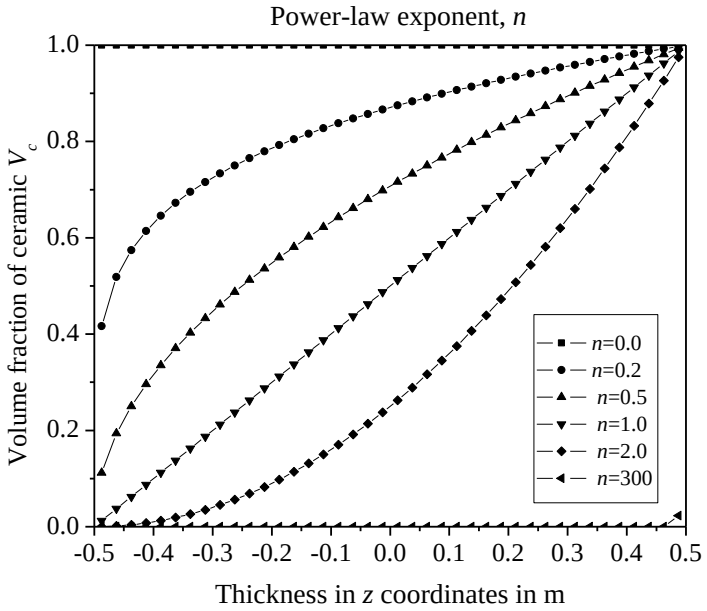

Fig.3.2 Variation of volume fraction of ceramic based on power law scheme.

3.3 FORMULATION OF HEAT TRANSFER PROBLEM

Consider a solid through which there is heat conduction due a heat generating source. The temperature T at the point $P(x,y,z)$ will be a continuous function of x,y,z and time t, (for details refer to Carslaw and Jaeger (1959)). The generalized work domain for heat transfer problem is shown in Fig.3.3.

The heat conduction equations, will be complete for any problem only if the appropriate boundary and initial conditions are stated. With the necessary boundary and initial conditions, a solution to the heat conduction equations is possible. Referring Fig.3.3, the general heat transfer problem domain can be described as follows:

1. Internal heat will be generated in material body because of supply of electric current and is time dependent.
2. Heat transfer will occur from one surface to other by conduction, Ω.
3. Convective heat loss from surface, Γ1.
4. Heat loss by convection from the end surface, Γ2.
5. Heat influx or efflux, Γ3.

Following are the assumptions:-

1. There is no temperature variation around the body of solid, T_∞ .

2. Radiation heat transfer is neglected.
3. The thermal conductivity and specific heat vary with respect to temperature i.e. temperature dependent material properties are considered.

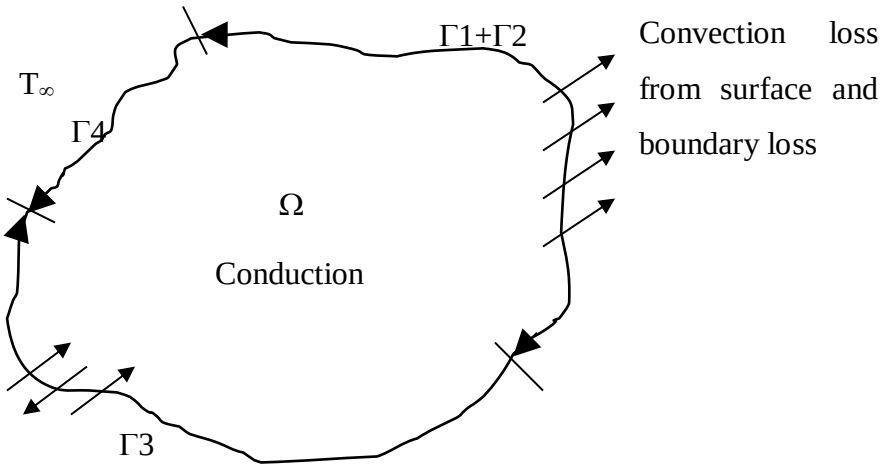

Fig.3.3 Generalised work domain for heat transfer problem.

3.3.1 Formulation of the heat conduction equation with convection

The generalized energy equation for the system is written as,

Energy into the element + Energy generated within the element = Change in internal energy + Energy out of element

For a functionally graded material solid whose thermal conductivity k_{eff} is dependent on temperature, the equation of conduction of heat in three dimensional co-ordinates is given by,

$$-k_{eff}\left(\frac{\partial^2 T}{\partial x^2}+\frac{\partial^2 T}{\partial y^2}+\frac{\partial^2 T}{\partial z^2}\right)+\dot{q}_{vol}=\rho_{eff}\,c_{p_{eff}}\frac{\partial T}{\partial t} \qquad (3.4)$$

where, ρ_{eff} is the effective mass density, $c_{p_{eff}}$ is the effective specific heat, and $\dot{q}_{vol}$ is the internal heat generation rate per unit volume. The time dependent one dimensional heat conduction equation for functionally graded material with temperature dependent material properties can be deduced from above equation to give

$$-k_{eff}\left(\frac{\partial^2 T}{\partial x^2}\right)+\dot{q}_{vol}=\rho_{eff}\,c_{p_{eff}}\,\frac{\partial T}{\partial t} \tag{3.5}$$

The thermal conduction equation, Eq.(3.5), must be solved for prescribed boundary and initial conditions. The initial condition specifies the temperature distribution at time zero, i.e. $T(x,0)=T_\infty$, where, T_∞ is the free air stream temperature. The presence of convective heat transfer on the bottom surface of the beam at $z=-h/2$ is represented by a boundary condition given as

$$-k_{eff}\,\frac{\partial T}{\partial x}=h_c(T-T_\infty) \tag{3.6}$$

where, h_c is convective heat transfer coefficient in W/m^{2}K.

The governing equation takes the form

$$-k_{eff}\left(\frac{\partial^2 T}{\partial x^2}\right)+\dot{q}_{vol}=\rho_{eff}\,c_{p_{eff}}\,\frac{\partial T}{\partial t}+q_h S \tag{3.7a}$$

where,

$$q_h=h_c(T-T_\infty) \tag{3.7b}$$

q_h is the heat loss by convection while S is the area of surface which is subjected to convective heat loss. The close form solution for temperature distribution T in one dimension, across the thickness of the isotropic beam, as given by Carslaw and Jaeger (1959) when a step heat flux Q in W/m^2, constant along *x* coordinate, is assumed to be applied over the surface $z=h/2$, while the surface at $z=-h/2$ is insulated is

$$T=\left(\frac{hQ}{k}\right)\left[\tau+\frac{1}{2}\left(\frac{z}{h}+\frac{1}{2}\right)^2-\frac{1}{6}-\frac{2}{\pi^2}\sum_{j=1}^{\infty}\frac{(-1)^j\,e^{-j^2\pi^2\tau}}{j^2}\cos j\pi\left(\frac{z}{h}+\frac{1}{2}\right)\right] \tag{3.8}$$

provided that the beam is initially at $T=0$. Here k is the thermal conductivity, τ is non-dimensional time parameter defined by

$$\tau=\frac{\kappa t}{h^2} \tag{3.9a}$$

where, κ is the thermal diffusivity given as

$$\kappa = k \Big/ \rho c_p \tag{3.9b}$$

Similarly, the equations governing the conduction of heat in two dimension for functionally graded material with temperature dependent material properties is given by,

$$k_{eff}\left(\frac{\partial^2 T}{\partial x^2}+\frac{\partial^2 T}{\partial z^2}\right)+\dot{q}_{vol}=\rho_{eff}\, c_{p_{eff}}\frac{\partial T}{\partial t} \tag{3.10}$$

The thermal conduction equation, Eq.(3.10), must be solved for prescribed boundary and initial conditions. The initial condition specifies the temperature distribution at time zero, i.e. $T(z,0)=T_\infty$. The presence of convective heat transfer on the bottom surface of the beam at $z=-h/2$ is represented by a boundary condition given by Eq.(3.6). The governing equation Eq.(3.10) takes the form

$$k_{eff}\left(\frac{\partial^2 T}{\partial x^2}+\frac{\partial^2 T}{\partial z^2}\right)+\dot{q}_{vol}=\rho_{eff}\, c_{p_{eff}}\frac{\partial T}{\partial t}+q_h S \tag{3.11}$$

3.4 FINITE ELEMENT DISCRETIZATION IN ONE DIMENSION FOR HEAT TRANSFER PROBLEM

An analytical solution allows for the temperature determination at any point in the domain while a numerical solution enables the determination of temperature only at discrete points. Here, the evaluation of the temperature distribution across the section of the beam is found by using the finite element idealization as illustrated in Fig.3.4.

The theoretical model based on finite element considers the beam as one-dimensional problem. Here it is assumed that the top surface is subjected to heat and all the other sides are insulated. It is assumed that heat conducts only in the thickness direction. Applying the Galerkin's approach i.e. multiply Eq.(3.5) by the linear test or shape function N_L^T, then integrating over the entire domain Ω and equating to zero, (Lewis et al. (2004)),

$$-\int_\Omega N_L^T\left[k_{eff}A\frac{\partial^2 T}{\partial x^2}-\rho_{eff}c_{p_{eff}}A\frac{\partial T}{\partial t}+\dot{q}_{vol}A\right]\delta x=0 \tag{3.12}$$

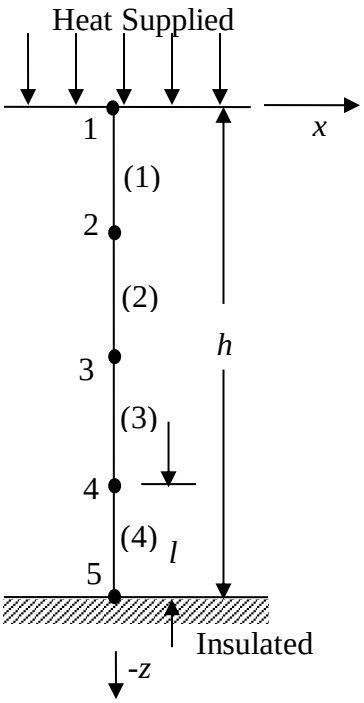

Fig.3.4 Finite element idealization of beam for one dimensional thermal analysis.

The weak form of the heat transfer governing equation for the beam with heat conduction, exposed to sudden heating on one side and insulated on other side is as follows:

$$-N_L^T k_{eff} A \frac{\partial T}{\partial x}\bigg|_o^l + \int k_{eff} A \frac{\partial T}{\partial x}\frac{\partial N_L^T}{\partial x} dx + \int N_L^T \rho_{eff} c_{p_{eff}} A \frac{dT}{dt} dx - \int N_L^T \dot{q}_{vol} A dx = 0 \tag{3.13}$$

The first term in the above equation evaluates to zero since the heat flux is not specified either at $x = 0$ and $x = l$. The boundary conditions being, temperature specified at time $t = 0$. Linear shape functions

$$N_i = 1 - \frac{x}{l} \qquad \text{and} \qquad N_j = \frac{x}{l} \tag{3.14}$$

are used to develop the various finite element matrices. l is the length of the element as shown in Fig.3.4. The finite element equation for temperature evaluation across beam thickness when the beam is exposed to sudden heating on one surface and insulated on other surface is as follows:

$$\frac{k_{eff}A}{l}\begin{bmatrix}1 & -1\\ -1 & 1\end{bmatrix}\begin{Bmatrix}T_1\\ T_2\end{Bmatrix}+\frac{\rho_{eff}c_{p_{eff}}Al}{6}\begin{bmatrix}2 & 1\\ 1 & 2\end{bmatrix}\begin{Bmatrix}\dot{T}_1\\ \dot{T}_2\end{Bmatrix}=\dot{q}_{vol}A\begin{Bmatrix}1\\ 1\end{Bmatrix} \qquad (3.15)$$

The finite element equation for temperature evaluation across beam thickness when the beam is exposed to sudden heating on one surface and uniform convection on the other surface of the beam as boundary condition can be obtained from governing equation Eq.(3.7a) as follows:

$$\left\{\frac{k_{eff}A}{l}\begin{bmatrix}1 & -1\\ -1 & 1\end{bmatrix}+\begin{bmatrix}0 & 0\\ 0 & h_cA\end{bmatrix}\right\}\begin{Bmatrix}T_1\\ T_2\end{Bmatrix}+\frac{\rho_{eff}c_{p_{eff}}Al}{6}\begin{bmatrix}2 & 1\\ 1 & 2\end{bmatrix}\begin{Bmatrix}\dot{T}_1\\ \dot{T}_2\end{Bmatrix}=\dot{q}_{vol}A\begin{Bmatrix}1\\ 1\end{Bmatrix}+h_cAT_\infty\begin{Bmatrix}0\\ 1\end{Bmatrix} \qquad (3.16)$$

In Eq(3.16) the second matrix on LHS and second vector on RHS are contribution from convection and will be taken into consideration only for last element. T_1 and T_2 are the nodal temperatures and T_∞ is the ambient temperature.

3.5 FINITE ELEMENT DISCRETIZATION IN TWO DIMENSION FOR HEAT TRANSFER PROBLEM

Consider a beam to undergo a sudden temperature rise due to step heat flux, moving line heat source, concentrated line heat source at center and shock load. In case of step heating or shock load, since the constant heat is applied on entire surface of the beam, the temperature variation is only across the thickness of the beam and can be solved with one dimensional heat transfer problem. In case of moving line heat source or concentrated line heat source at center, in addition to temperature variation across the thickness there is also temperature variation along the length of the beam and we need to solve a two dimensional heat transfer problem. This type of heat sources have relevance to laser cutting, heating of billet in furnace, surface hardening, flame hardening, plasma spraying, high velocity oxy-fuel spray, etc. In such a case, the equations governing the conduction of heat in two dimensional co-ordinate is given by Eq.(3.10). The thermal conduction equation, Eq.(3.10), must be solved for prescribed boundary and initial conditions. The boundary conditions are, the bottom surface of the beam experience heat flux, the top, rear, front, left and right surface of the beam are insulated.

The initial condition is

$$T(x,z,t=0)=T_{\infty}, \qquad (3.17)$$

where, T_{∞} is the free air stream temperature and that of the beam. It is assumed that the temperature along the width of the beam does not vary. To solve the Eq.(3.10) for specified boundary and initial conditions, the two dimensional FEM is used.

To discretize the two dimensional domain, consider a beam subjected to moving heat source as shown in Fig.3.5. Let the heat source be assumed as though emanating from a rectangular slit. Thus it will appear as line of finite width equal to the width of beam and infinitesimal thickness, see Fig.3.5. The temperature of the beam across the width is negligible (i.e. along the *y*-axis). The temperature varies in the *x*-*z* plane only, see Fig.3.6. The section of the beam is taken across *x*-*z* plane to discretize the problem as 2 dimensional as shown in Fig.3.6.

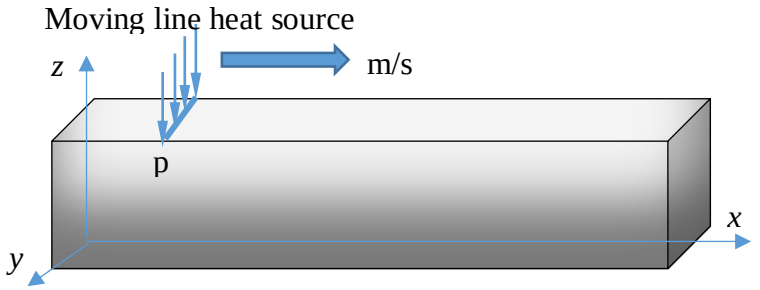

Fig.3.5 FGM beam subjected to moving line heat source

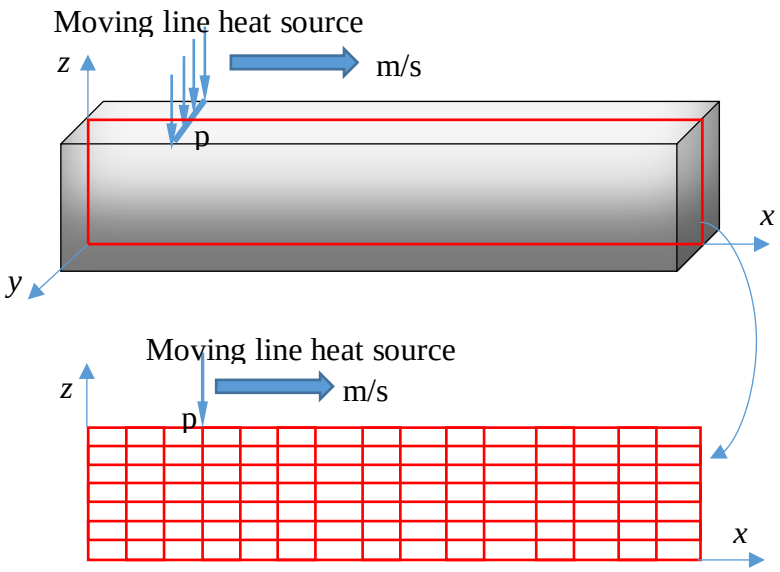

Fig.3.6 Finite element idealization of beam for two dimensional thermal analysis.

Let us assume that the lateral plane of the beam is divided into number of elements as shown in Fig.3.6. Consider one element of the domain. Using the Galerkin method to solve Eq.(3.10), the finite element equation for 2D heat conduction corresponding to Eq.(3.10) is obtained as follows,

$$\int_{A_e} N^T \left(k_{eff} \left(\frac{\partial^2 T}{\partial x^2} + \frac{\partial^2 T}{\partial z^2} \right) - \rho_{eff}\, c_{p_{eff}} \frac{\partial T}{\partial t} + \dot{q}_{vol} \right) dA = 0 \tag{3.18}$$

Using the integration by parts to solve this equation we obtain,

$$\int_{A_e} k_{eff} \left(\frac{\partial N^T}{\partial x} \frac{\partial T}{\partial x} + \frac{\partial N^T}{\partial z} \frac{\partial T}{\partial z} \right) dA + \int_{A_e} \rho_{eff}\, c_{p_{eff}} N^T \frac{\partial T}{\partial t} dA = \int_{A_e} \dot{q}_{vol} N^T dA \tag{3.19}$$

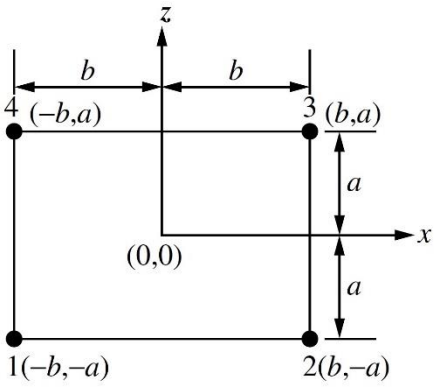

Fig.3.7 A simple rectangular element.

A four noded Lagrange rectangular element is used to discretise the domain. The quadrilateral element has four nodes located at the vertices as shown in Fig.3.7. The temperature within a quadrilateral is represented by

$$T = N_1 T_1 + N_2 T_2 + N_3 T_3 + N_4 T_4 \tag{3.20}$$

For a rectangular element, the shape functions can be obtained using Lagrange interpolation functions as

$$N_1 = \frac{(x-b)(z-a)}{(-b-b)(-a-a)} = \frac{1}{4ab}(b-x)(a-z) \tag{3.21a}$$

$$N_2 = \frac{(x-(-b))(z-a)}{(b-(-b))(-a-a)} = \frac{1}{4ab}(b+x)(a-z) \tag{3.21b}$$

$$N_3 = \frac{(x-(-b))(z-(-a))}{(b-(-b))(-a-a)} = \frac{1}{4ab}(b+x)(a+z) \tag{3.21c}$$

$$N_4 = \frac{(x-b)(z-(-a))}{(-b-b)(a-(-a))} = \frac{1}{4ab}(b-x)(a+z) \tag{3.21d}$$

Since the shape functions are linear in the x and z directions, they are referred to as a bilinear configuration. The derivatives can be expressed as follows:

$$\begin{aligned}\frac{\partial T}{\partial x} &= \frac{\partial N_1}{\partial x}T_1 + \frac{\partial N_2}{\partial x}T_2 + \frac{\partial N_3}{\partial x}T_3 + \frac{\partial N_4}{\partial x}T_4 \\ &= \frac{1}{4ab}\left[-(a-z)T_1 + (a-z)T_2 + (a+z)T_3 - (a+z)T_4\right]\end{aligned} \tag{3.22a}$$

Similarly,

$$\frac{\partial T}{\partial z} = \frac{1}{4ab}\left[-(b-x)T_1 - (b+x)T_2 + (b+x)T_3 + (b-x)T_4\right] \tag{3.22b}$$

The gradient matrix can be written as

$$\{g\} = \begin{Bmatrix}\frac{\partial T}{\partial x} \\ \frac{\partial T}{\partial z}\end{Bmatrix} = \frac{1}{4ab}\begin{bmatrix}-(a-z) & (a-z) & (a+z) & -(a+z) \\ -(b-x) & -(b+x) & (b+x) & (b-x)\end{bmatrix}\begin{Bmatrix}T_1 \\ T_2 \\ T_3 \\ T_4\end{Bmatrix} \tag{3.23a}$$

$$\{g\} = [\mathbf{B}]\{\mathbf{T}\} \tag{3.23b}$$

The $[\mathbf{B}]$ matrix is written as

$$[\mathbf{B}] = \frac{1}{4ab}\begin{bmatrix}-(a-z) & (a-z) & (a+z) & -(a+z) \\ -(b-x) & -(b+x) & (b+x) & (b-x)\end{bmatrix} \tag{3.23c}$$

The finite element equations for evaluation of temperature in 2- dimension domain are obtained as follows:

The stiffness matrix is evaluated as

$$\left[k_{ij}^e\right] = \int_{A^e}[\mathbf{B}]^{\mathrm{T}}[\mathbf{D}][\mathbf{B}]dA^e \tag{3.24}$$

where, $[\mathbf{D}] = \begin{bmatrix}k_{x,eff} & 0 \\ 0 & k_{z,eff}\end{bmatrix}$

Substituting, the **[B]** and **[D]** matrices in the Eq.3.24, results in a 4×4 matrix. A typical term in the matrix is

$$\int_{-b}^{b}\int_{-a}^{a}\frac{k_{x,eff}}{16a^2b^2}(a-z)^2\,dzdx+\int_{-a}^{a}\int_{-b}^{b}\frac{k_{z,eff}}{16a^2b^2}(b-x)^2\,dxdz \tag{3.25}$$

After solving for all the terms, the stiffness matrix is evaluated as follows,

$$\left[k_{ij}^{e}\right]=\frac{D_x a}{6b}\begin{bmatrix}2&-2&-1&1\\-2&2&1&-1\\-1&1&2&-2\\1&-1&-2&2\end{bmatrix}+\frac{D_z b}{6a}\begin{bmatrix}2&1&-1&-2\\1&2&-2&-1\\-1&-2&2&1\\-2&-1&1&2\end{bmatrix} \tag{3.26}$$

The capacitance matrix can be evaluated as

$$\left[C_{ij}^{e}\right]=\int_{A^e}\rho_{eff}c_{p_{eff}}\left[\mathbf{N}\right]^{\mathrm{T}}\left[\mathbf{N}\right]dA^e$$

$$=ab\rho_{eff}c_{p_{eff}}\int_{A_e}\begin{bmatrix}N_1^2&N_1N_2&N_1N_3&N_1N_4\\N_1N_2&N_2^2&N_2N_3&N_2N_4\\N_1N_3&N_2N_3&N_3^2&N_3N_4\\N_1N_4&N_2N_4&N_3N_4&N_4^2\end{bmatrix}dxdz \tag{3.27}$$

which results in

$$\left[C_{ij}^{e}\right]=\frac{t\rho_{eff}c_{p_{eff}}2A}{36}\begin{bmatrix}4&2&1&2\\2&4&2&1\\1&2&4&2\\2&1&2&4\end{bmatrix} \tag{3.28}$$

The element force vector involves the integration of the shape functions. With substitution of the shape functions, it can be obtained as

$$\left[F_i^e\right]=\int_{A^e}\dot{q}_{vol}\left[N\right]^T dA^e=\dot{q}_{vol}\int_{A^e}\begin{Bmatrix}N_1\\N_2\\N_3\\N_4\end{Bmatrix}dA^e=\frac{\dot{q}_{vol}A}{4}\begin{Bmatrix}1\\1\\1\\1\end{Bmatrix} \tag{3.29}$$

Note that in the above equation, $\dot{q}_{vol}$ is assumed to be constant within the element. The value of $\dot{q}_{vol}A$ is equally shared by the four nodes of the rectangular element.

When one surface is exposed to heat and other surface is subjected to convective heat transfer, the stiffness matrix considering heat loss due to convective heat transfer is evaluated as

$$\left[k_{ij}^{e}\right]=\int_{A^e}\left[\mathbf{B}\right]^{\mathrm{T}}\left[\mathbf{D}\right]\left[\mathbf{B}\right]dA^{e}+\int_{\Gamma}h_c\left[\mathbf{N}\right]^{\mathrm{T}}\left[\mathbf{N}\right]d\Gamma \tag{3.30a}$$

$$\left[k_{ij}^{e}\right]=\frac{D_x a}{6b}\begin{bmatrix}2&-2&-1&1\\-2&2&1&-1\\-1&1&2&-2\\1&-1&-2&2\end{bmatrix}+\frac{D_z b}{6a}\begin{bmatrix}2&1&-1&-2\\1&2&-2&-1\\-1&-2&2&1\\-2&-1&1&2\end{bmatrix}+\frac{h_c b}{6}\begin{bmatrix}0&0&0&0\\0&0&0&0\\0&0&2&1\\0&0&1&2\end{bmatrix} \tag{3.30b}$$

while the force vector is evaluated as

$$\left[F_i^{e}\right]=\frac{\dot{q}_{vol}A}{4}\begin{Bmatrix}1\\1\\1\\1\end{Bmatrix}+\frac{h_c bT_{\infty}}{2}\begin{Bmatrix}0\\0\\1\\1\end{Bmatrix} \tag{3.31}$$

The global finite element equation for time dependent temperature distribution has the following form:

$$\mathbf{K}_{\mathrm{comb}}^{e}\mathbf{T}+\mathbf{K}_{\mathrm{cap}}^{e}\dot{\mathbf{T}}=\bar{\mathbf{F}}_{Q}^{e} \tag{3.32}$$

$\mathbf{K}_{\mathrm{comb}}^{\mathrm{e}}$=elemental conduction and or convection matrix, $\mathbf{K}_{\mathrm{cap}}^{e}$=elemental capacitance matrix and $\bar{\mathbf{F}}_{Q}^{e}$=force vector due to internal heat generation, external heat flux like step heat load, shock heat load, moving and concentrated line heat source. Eq.(3.32) must be solved for the variation of temperature in space and time domain to obtain the temperature distribution across the thickness of the beam. The solution method will be discussed in the next section.

3.6 FINITE DIFFERENCE SOLUTION OF HEAT TRANSFER PROBLEM IN TIME

The finite element solution of time dependent field problems produces a system of linear first order differential equations in time domain, Eq.(3.32). These equations must

be solved for the variation of *T* in space and time. The details of the solution procedure may be referred to Segerlind (2004).

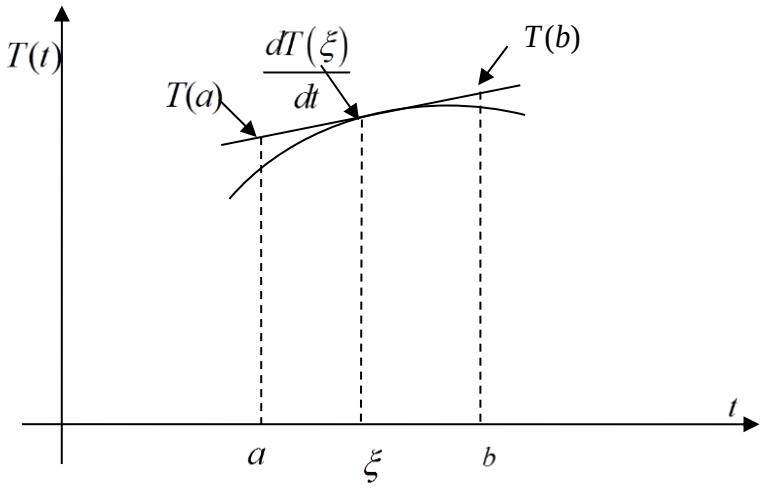

Fig.3.8 An approximation for $T(a)$ given $\partial T/\partial t$.

Given a function $T(t)$ and time interval [*a*, *b*]. The mean value theorem states that there is a value of *t*, call it ξ, such that

$$T(b) - T(a) = (b - a)\frac{dT}{dt}(\xi) \tag{3.33}$$

Rearranging gives

$$\frac{dT}{dt}(\xi) = \frac{T(b) - T(a)}{\Delta t} \tag{3.34}$$

where, $\Delta t = (b - a)$ is the length of the interval. The location of ξ in Eq.(3.33) and Eq.(3.34) is not known.

The value of *T* at *t*=*a*, *T*(*a*), can be approximated as shown in Fig 3.8.

$$T(a) = T(\xi) - (\xi - a)\frac{dT}{dt}(\xi) \tag{3.35}$$

Rearranging gives,

$$T(\xi) = T(a) + (\xi - a)\frac{dT}{dt}(\xi) \tag{3.36}$$

After substituting Eq.(3.34) in Eq.(3.36),

$$T(\xi) = T(a) + (\xi - a)\frac{T(b) - T(a)}{\Delta t} \tag{3.37}$$

$$T(\xi) = (1-\theta)T(a) + \theta T(b) \tag{3.38}$$

where, $\theta = \dfrac{(\xi - a)}{\Delta t}$ (3.39)

Eq.(3.34) and Eq.(3.38) can be generalized to a set of nodal values by replacing $T(a)$ and $T(b)$ by column vectors containing the nodal values, $\{T\}_a$ and $\{T\}_b$ at time a and b as follows

$$\frac{d\{T\}}{dt} = \frac{\{T\}_b - \{T\}_a}{\Delta t} \tag{3.40}$$

$$\{T\} = (1-\theta)\{T\}_a + \theta\{T\}_b \tag{3.41}$$

at the point, $t = \xi$.

Using the procedure outlined above with regards to Eq.(3.41), the force vector $\{\mathrm{F}\}$ due to temperature specified boundary condition or heat flux at $t = \xi$ can be derived as follows

$$\{\mathrm{F}\} = (1-\theta)\{\mathrm{F}\}_a + \theta\{\mathrm{F}\}_b \tag{3.42}$$

Eq.(3.32) can now be written in terms of $\{T\}_a$, $\{T\}_b$, $\{\mathrm{F}\}_a$ and $\{\mathrm{F}\}_b$ by substituting Eq.(3.40), Eq.(3.41) and Eq.(3.42). The result is

$$\begin{aligned}\left(\left[\mathrm{K}_{cap}\right] + \theta\Delta t\left[\mathrm{K}_{comb}\right]\right)\{T\}_b = \left(\left[\mathrm{K}_{cap}\right] - (1-\theta)\Delta t\left[\mathrm{K}_{comb}\right]\right)\{T\}_a \\ + \Delta t\left((1-\theta)\{\mathrm{F}\}_a + \theta\{\mathrm{F}\}_b\right)\end{aligned} \tag{3.43}$$

Eq.(3.43) gives the nodal values, $\{T\}_b$, in terms of a set of known values, $\{T\}_a$, the force vector at times *a* and *b* and the ratio θ. The force vectors, $\{\mathrm{F}\}_a$ and $\{\mathrm{F}\}_b$, must be known. The value of θ must also be specified. This is equivalent to specifying the location of ξ at which the mean value theorem is applied.

For the current problem, the value of θ *is chosen as ½.* Regardless of which value is specified for θ, the final system of equations has the general form

$$[A]\{T\}_b = [B]\{T\}_a + \{F^*\} \tag{3.44}$$

where, $[A] = \left([\mathrm{K}_{cap}] + \theta\Delta t[\mathrm{K}_{comb}]\right)$

$$[B] = \left([\mathrm{K}_{cap}] - (1-\theta)\Delta t[\mathrm{K}_{comb}]\right)$$

$$\{F^*\} = \Delta t\left((1-\theta)\{\mathrm{F}\}_a + \theta\{\mathrm{F}\}_b\right)$$

It is seen that $[A]$ and $[B]$ are combinations of $[\mathrm{K}_{cap}]$ and $[\mathrm{K}_{comb}]$, and are dependent on the time step Δt. If Δt and material properties are independent of time or $\{T\}$, then $[A]$ is same for all times. If either Δt or material parameters change during the solution process, $[A]$ and $[B]$ are re-evaluated for the new time step. Each solution in time is equivalent to solving a single steady state problem when $[A]$ and $[B]$ are evaluated for each time step. The vector, $\{F^*\}$, in Eq.(3.42) is a combination of $\{\mathrm{F}\}_a$ and $\{\mathrm{F}\}_b$.

3.7 GOVERNING EQUATIONS FOR NON-LINEAR THERMO-ELASTIC VIBRATION ANALYSIS OF FGM BEAMS

The governing equation of motion for Euler–Bernoulli beam are based on von-Kármán nonlinear strain for functionally graded beam. Let (u, v, w) be the displacements along the coordinates (x, y, z). For beams, the displacements are only functions of the x and z coordinates. The x and z axes are the coordinate for length and height of the beam respectively. The x axis is taken along the centre of the beam. Here, it is further assumed that the displacement v is identically zero.

3.7.1 Displacement field and nonlinear strains for Euler Bernoulli beam

The Euler-Bernoulli hypothesis requires that plane sections perpendicular to the axis of the beam before deformation remain (a) plane, (b) rigid (not deform), and (c) rotate

such that they remain perpendicular to the axis after deformation. The assumptions amount to neglecting the Poisson effect and transverse strains.

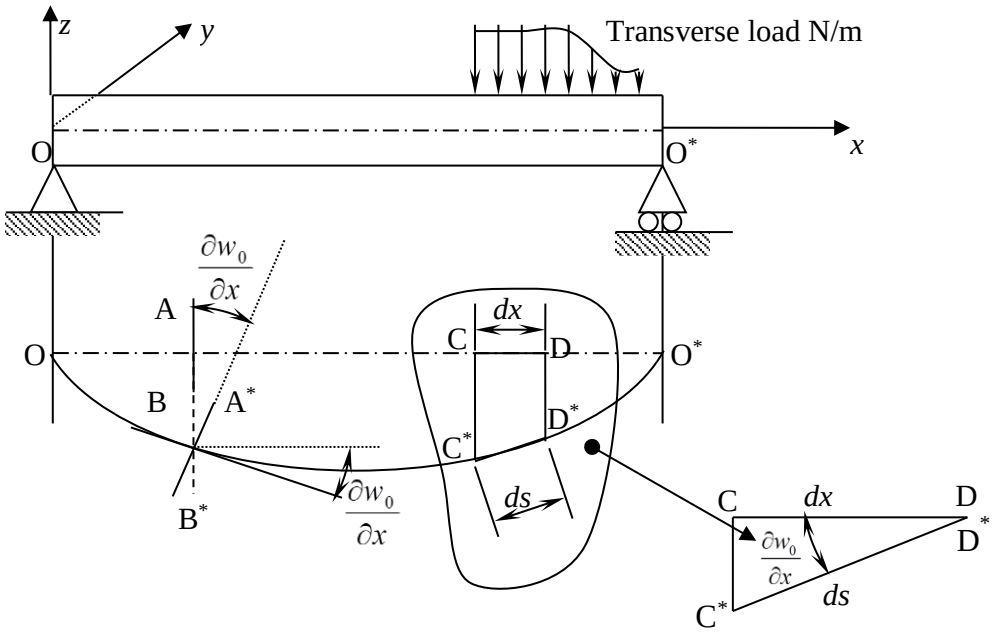

Fig.3.9 Kinematics due to transverse load on the simply supported Euler–Bernoulli beam.

The Fig.3.9 shows the beam with simply supported boundary condition, with uniform distributed transverse load acting over a length L. Let us assume that the beam is restrained from extension along *x*-direction. The transverse deflection is said to occur due to transverse load. Neglecting transverse shear, the natural consequence is that plane sections normal to neutral surface would remain straight and normal to beam neutral plane before deformation AB and after deformation as A^*B^*.

The Fig.3.9 also illustrates the extension of an elemental length CD = *dx* to C^*D^* = *ds*. Thus we have transverse deformation superimposed with the axial deformation, also referred to as membrane strain (Timoshenko and Woinowsky-Krieger 1959). The total displacements (u, w) along the coordinate directions (x, z) for thin beam undergoing transverse deflection and longitudinal elongation as implied by the Euler–Bernoulli hypothesis are given by (Bathe 1996; Reddy 2004):

$$u(x,z,t) = u_0(x,t) + z\theta_x(x,t) \tag{3.45}$$

where, $\theta_x \equiv -\dfrac{\partial w_0}{\partial x}$

$$w(x,z,t) = w_0(x,t) \tag{3.46}$$

where, w_0 and u_0 denotes the transverse and axial displacement of a point on the mid-plane of the beam respectively at time t.

The nonlinear strain is deduced as follows:

Referring to Fig.3.9, consider the right angled triangle due to CD, CC* and C*D*, the included angle between CD and C*D* is $\dfrac{\partial w_0}{\partial x}$. Now CC* from Pythagoras theorem is,

$ds^2 = \left(dx \tan \dfrac{dw_0}{dx} \right)^2 + dx^2$ for small angle or small deformation

$$ds^2 = \left(dx \frac{dw_0}{dx} \right)^2 + dx^2 \Rightarrow ds = \sqrt{\left(dx \frac{dw_0}{dx} \right)^2 + dx^2} \Rightarrow ds = dx \sqrt{\left(\frac{dw_0}{dx} \right)^2 + 1}$$

$$\Rightarrow \frac{ds}{dx} = \sqrt{\left(\frac{dw_0}{dx} \right)^2 + 1}$$

Applying Binomial expansion for the term on RHS and neglecting higher order terms

$$\frac{ds}{dx} = 1 + \frac{1}{2}\left(\frac{dw_0}{dx} \right)^2 \Rightarrow \frac{ds}{dx} - 1 = \frac{1}{2}\left(\frac{dw_0}{dx} \right)^2 \Rightarrow \frac{ds - dx}{dx} = \frac{1}{2}\left(\frac{dw_0}{dx} \right)^2$$

The term, $\dfrac{1}{2}\left(\dfrac{dw_0}{dx} \right)^2$ is the nonlinear strain.

Hence, the nonlinear strain-displacement relation will be as follows,

$$\varepsilon_{xx}(x,z,t) \equiv \varepsilon_{xx}^0 + z\varepsilon_{xx}^1 = \frac{\partial u_0}{\partial x} + \frac{1}{2}\left(\frac{\partial w_0}{\partial x} \right)^2 + z\left(-\frac{\partial^2 w_0}{\partial x^2} \right) \tag{3.47}$$

where,

$$\varepsilon_{xx}^0 = \frac{\partial u_0}{\partial x} + \frac{1}{2}\left(\frac{\partial w_0}{\partial x} \right)^2, \quad \varepsilon_{xx}^1 = -\frac{\partial^2 w_0}{\partial x^2} \tag{3.48}$$

Strains in other direction and transverse shear stresses are absent.

$$\sigma_{yy} = 0;\ \sigma_{zz} = 0;\ \varepsilon_{yy} = 0;\ \varepsilon_{zz} = 0;\ \gamma_{xy} = 0;\ \gamma_{xz} = 0;\ \gamma_{yz} = 0 \tag{3.49}$$

3.7.2 Virtual work statement

The weak form for the structural problems can be directly derived using the principle of virtual displacements. The principle states that if a body is in equilibrium, the total virtual work done by actual internal as well as external forces in moving through their respective virtual displacements is zero. The virtual displacements are arbitrary except that they are zero where displacements are prescribed. The dynamic version of the principle of virtual displacements (i.e. Hamilton's principle for deformable bodies) is given by

$$\int_0^T [\delta\Pi - \delta K]dt = 0 \tag{3.50a}$$

$$\delta\Pi = \delta U - \delta V \tag{3.50b}$$

where δU is the virtual work due to internal forces or virtual strain energy, δV the virtual work due to external forces, and δK is the virtual kinetic energy in the beam. Virtual strain energy is

$$\delta U = \int_0^L \int_A \sigma_{xx}\delta\varepsilon_{xx} dA dx = \int_0^L \int_A \sigma_{xx}\left(\delta\varepsilon_{xx}^{(0)} + z\delta\varepsilon_{xx}^{(1)}\right)dA dx \tag{3.51a}$$

$$= \int_0^L \left(N_{xx}\left(\frac{\partial\delta u_0}{\partial x} + \frac{\partial w_0}{\partial x}\frac{\partial\delta w_0}{\partial x}\right) + M_{xx}\frac{\partial\delta\theta_x}{\partial x}\right)dx$$

$$\delta V = -\int_0^L \left(f\delta u_0 + q\delta w_0\right)dx$$
$$-\left[Q_1\delta u_0(0,t) + Q_2\delta w_0(0,t) + Q_3\delta\theta_x(0,t) + Q_4\delta u_0(L,t) + Q_5\delta w_0(L,t) + Q_6\delta\theta_x(L,t)\right] \tag{3.51b}$$

$$\delta K = \int_0^L \int_A \rho_{eff}\left[\left(\dot{u}_0 - z\frac{\partial\dot{w}_0}{\partial x}\right)\left(\delta\dot{u}_0 - z\frac{\partial\delta\dot{w}_0}{\partial x}\right) + \dot{w}_0\delta\dot{w}_0\right]dA dx$$
$$= \int_0^L \left[I'\left(\frac{\partial\delta u_0}{\partial t}\frac{\partial u_0}{\partial t} + \frac{\partial\delta w_0}{\partial t}\frac{\partial w_0}{\partial t}\right) + \tilde{I}\left(\frac{\partial\delta u_0}{\partial t}\frac{\partial\theta_x}{\partial t} + \frac{\partial\delta\theta_x}{\partial t}\frac{\partial u_0}{\partial t}\right) + \hat{I}\frac{\partial\delta\theta_x}{\partial t}\frac{\partial\theta_x}{\partial t}\right]dx \tag{3.51c}$$

where, $f(x)$ and $q(x)$ are the distributed axial and transverse loads per unit length along the x axis and Q_i are the specified generalized forces at the ends of the beam as shown in Fig.3.10. ρ_{eff} is the effective mass density of the beam material; A is the cross-sectional areas of the beam material.

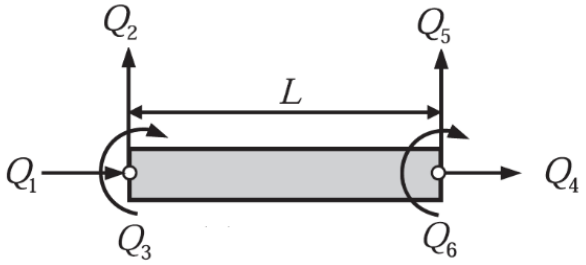

Fig.3.10 The external forces applied on the two ends of a beam.

3.7.3 Euler-Lagrange equations

Using the beam kinematics, strain-displacement and stress and strain relation, the Hamiltonian for deformable bodies over a typical element $\Omega_e = (x_a, x_b)$ can be derived. Substituting the expressions from Eq.(3.51) for δU, δV and δK in Eq.(3.50a) and integrating-by-parts with respect to t and x we arrive at following expression:

$$
\begin{aligned}
0 = \int_0^T \Bigg\{ \int_0^L \Bigg[& -\left(I' \frac{\partial^2 u_0}{\partial t^2} - \tilde{I} \frac{\partial^3 w_0}{\partial t^2 \partial x} \right) \delta u_0 - \left(I' \frac{\partial^2 w_0}{\partial t^2} + \tilde{I} \frac{\partial^3 u_0}{\partial t^2 \partial x} - \hat{I} \frac{\partial^4 w_0}{\partial t^2 \partial x^2} \right) \delta w_0 + \frac{\partial N_{xx}}{\partial x} \delta u_0 \\
& + \frac{\partial}{\partial x} \left(N_{xx} \frac{\partial w_0}{\partial x} \right) \delta w_0 + \frac{\partial^2 M_{xx}}{\partial x^2} \delta w_0 + f \delta u_0 + q \delta w_0 \Bigg] dx \\
& + \Big[Q_1 \delta u_0(0,t) + Q_2 \delta w_0(0,t) + Q_3 \delta \theta_x(0,t) + Q_4 \delta u_0(L,t) + Q_5 \delta w_0(L,t) + Q_6 \delta \theta_x(L,t) \Big] \Bigg\} dt \\
& + \int_0^L \left[\left(I' \frac{\partial u_0}{\partial t} + \tilde{I} \frac{\partial \theta_x}{\partial t} \right) \delta u_0 + I' \frac{\partial w_0}{\partial t} \delta w_0 + \left(\tilde{I} \frac{\partial u_0}{\partial t} + \hat{I} \frac{\partial \theta_x}{\partial t} \right) \delta \theta_x \right]_0^T dx \\
& + \int_0^T \left\{ -N_{xx} \delta u_0 - \left[N_{xx} \frac{\partial w}{\partial x} + \frac{\partial M_{xx}}{\partial x} + \tilde{I} \frac{\partial^2 u_0}{\partial t^2} - \hat{I} \frac{\partial^3 w_0}{\partial t^2 \partial x} \right] \delta w_0 - (M_{xx}) \delta \theta_x \right\}_0^L dt
\end{aligned}
\tag{3.52}
$$

wherein all the terms involving derivative w.r.t. time, $[.]_0^T$ vanish on account of the assumption that all variations and their derivatives are zero at $t = 0$ and $t = T$. The generalized forces, Q_i are defined as

$$
Q_1 = \left[-N_{xx} \right]_{x_a} \qquad Q_4 = \left[N_{xx} \right]_{x_b}
$$

$$
Q_2 = \left[-\frac{\partial M_{xx}}{\partial x} - N_{xx} \frac{\partial w_0}{\partial x} - \tilde{I} \frac{\partial^2 u_0}{\partial t^2} + \hat{I} \frac{\partial^3 w_0}{\partial t^2 \partial x} \right]_{x_a} \qquad Q_5 = \left[\frac{\partial M_{xx}}{\partial x} + N_{xx} \frac{\partial w_0}{\partial x} + \tilde{I} \frac{\partial^2 u_0}{\partial t^2} - \hat{I} \frac{\partial^3 w_0}{\partial t^2 \partial x} \right]_{x_b}
$$

$$Q_3 = \left[-M_{xx}\right]_{x_a} \qquad Q_6 = \left[M_{xx}\right]_{x_b} \tag{3.53}$$

which are all zero due to assumed boundary condition and loading.

Thus, the Euler-Lagrange equations of motion are

$$\delta u_0: \quad -\frac{\partial N_{xx}}{\partial x} + m\frac{\partial^2 u_0}{\partial t^2} - \tilde{I}\frac{\partial^3 w_0}{\partial t^2 \partial x} - f = 0 \tag{3.54}$$

$$\delta w_0: \quad -\frac{\partial^2 M_{xx}}{\partial x^2} - \frac{\partial}{\partial x}\left(N_{xx}\frac{\partial w_0}{\partial x}\right) + m\frac{\partial^2 w_0}{\partial t^2} + \tilde{I}\frac{\partial^3 u_0}{\partial t^2 \partial x} - \hat{I}\frac{\partial^4 w_0}{\partial x^2 \partial t^2} - q = 0 \tag{3.55}$$

Equations (4.10) and (4.11) represent coupled nonlinear equations among (u_0, w_0). The variables introduced in arriving at the above expression are defined as follows:

$$\begin{Bmatrix} N_{xx} \\ M_{xx} \end{Bmatrix} = \int_A \begin{Bmatrix} 1 \\ z \end{Bmatrix} \sigma_{xx} dA \tag{3.56a}$$

$$m = I' = \int_A \rho dA, \qquad \tilde{I} = \int_A \rho z dA \quad \text{and} \quad \hat{I} = \int_A \rho z^2 dA \tag{3.56b}$$

For functionally graded material subjected to thermal load, the uniaxial stress-strain relation is used to evaluate stress as follows

$$\sigma_{xx} = \bar{Q}_{11}\left[\varepsilon_{xx} - \alpha_{eff}\Delta T\right], \qquad \Delta T = T - T_0 \tag{3.57}$$

where, A is the cross-sectional area of the beam; $m = \rho A$ is the mass density of the beam per unit length, α_{eff} is effective coefficient of thermal expansion for FGM beam, ΔT is the temperature increment from room temperature, T_0 and; $f(x,t)$ and $q(x,t)$ are axial and transverse distributed loads on the beam. The temperature T is assumed to vary through the thickness for one dimensional problem and through the thickness and along the length for two dimensional problem. $\bar{Q}_{11}$ is the stiffness coefficient for the FGM layer given as

$$\bar{Q}_{11} = \frac{E_{eff}(z)}{1 - \nu_{eff}^2(z)} \tag{3.58}$$

E_{eff} = Temperature dependent effective Young's modulus and ν_{eff} = temperature dependent effective Poisson's ratio for FGM beam.

The stress resultants N_{xx} and moment resultant M_{xx} on the beam element with thermal load are related to the displacements (u_0, w_0) and are derived as follows:

$$N_{xx} = \int_A \sigma_{xx} dA = \int_A \bar{Q}_{11} \left[\varepsilon_{xx} - \alpha_{eff} \Delta T \right] dA$$

$$= \int_A \bar{Q}_{11} \left[\left[\frac{\partial u_0}{\partial x} + \frac{1}{2} \left(\frac{\partial w_0}{\partial x} \right)^2 + z \left(-\frac{\partial^2 w_0}{\partial x^2} \right) \right] - \alpha_{eff} \Delta T \right] dA$$

$$N_{xx} = A_{xx} \left[\frac{\partial u_0}{\partial x} + \frac{1}{2} \left(\frac{\partial w_0}{\partial x} \right)^2 \right] - B_{xx} \frac{\partial^2 w_0}{\partial x^2} - N_{xx}^T \tag{3.59}$$

$$M_{xx} = \int_A \sigma_{xx} z dA = \int_A \bar{Q}_{11} \left[\varepsilon_{xx} - \alpha_{eff} \Delta T \right] z dA$$

$$= \int_A \bar{Q}_{11} \left[\left[\frac{\partial u_0}{\partial x} + \frac{1}{2} \left(\frac{\partial w_0}{\partial x} \right)^2 + z \left(-\frac{\partial^2 w_0}{\partial x^2} \right) \right] - \alpha_{eff} \Delta T \right] z dA$$

$$M_{xx} = B_{xx} \left[\frac{\partial u_0}{\partial x} + \frac{1}{2} \left(\frac{\partial w_0}{\partial x} \right)^2 \right] - D_{xx} \frac{\partial^2 w_0}{\partial x^2} - M_{xx}^T \tag{3.60}$$

A_{xx} , B_{xx} and D_{xx} are the extensional, extensional-bending, and bending stiffness coefficients of the beam element defined as

$$\left(A_{xx}, B_{xx}, D_{xx} \right) = \int_z \bar{Q}_{11} \left(1, z, z^2 \right) b dz \tag{3.61}$$

For beams made of an isotropic material i.e. either pure metal or pure ceramic, the extensional-bending stiffness B_{xx} is zero when the x-axis is taken along the geometric centroidal axis as in present case.

N_{xx}^T and M_{xx}^T are the thermal stress resultants and moment resultants which are due to temperature gradient across the thickness or length of the beam. For the beam subjected to heat flux on one side and insulated on the other side the thermal moment acts as a forcing function, the corresponding stress resultants and moment resultants due to thermal load are given as

$$N_{xx}^T = \int_A \bar{Q}_{11} . \alpha_{eff} . \Delta T . dA = A_{xx} . \alpha_{eff} . \Delta T \tag{3.62}$$

$$M_{xx}^T = \int_A \bar{Q}_{11} . \alpha_{eff} . \Delta T . z . dA = B_{xx} . \alpha_{eff} . \Delta T \tag{3.63}$$

The thermal moment is calculated at uniform intervals across the thickness from the top to bottom surfaces of the beam and it is summed up in order to obtain the total thermal moment across the section.

3.7.4 Beam Finite element model

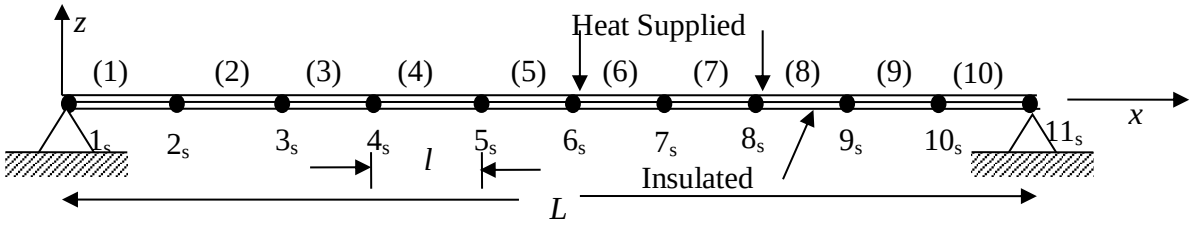

Fig.3.11 Finite element idealization of beam for structural analysis.

Fig.3.11 shows the finite element idealization of beam for structural analysis using simple one dimensional beam element of length *l* along *x* axis wherein numbers with suffix 's' denote node numbers and numbers in brackets denote element numbers. Fig.3.12 shows the simple one dimensional beam element.

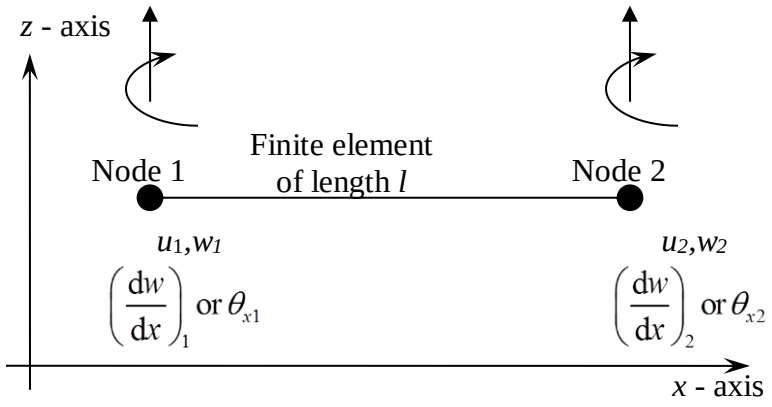

Fig.3.12 One-dimension beam bending element and nodal degrees of freedom

The weak form for the finite element model of the Lagrange equations of motion Eq.(3.54) and Eq.(3.55) is obtained as follows.

Let $(\delta u_0, \delta w_0)$ be the virtual variations of (u, w). Then, the virtual work statement over a typical element (x_a, x_b) yields the following two weak statements:

$$0 = \int_{x_a}^{x_b} \left[I' \delta u_0 \frac{\partial^2 u_0}{\partial t^2} - \tilde{I} \delta u_0 \frac{\partial^3 w_0}{\partial t^2 \partial x} + \frac{\partial \delta u_0}{\partial x} N_{xx} - f \delta u_0 \right] dx \qquad (3.64)$$

$$0=\int_{x_a}^{x_b}\left[I'\delta w_0\frac{\partial^2 w_0}{\partial t^2}-\tilde{I}\frac{\partial\delta w_0}{\partial x}\frac{\partial^2 u_0}{\partial t^2}+\hat{I}\frac{\partial\delta w_0}{\partial x}\frac{\partial^3 w_0}{\partial x\partial t^2}-\frac{d^2\delta w_0}{dx^2}M_{xx}+\frac{\partial\delta w_0}{\partial x}N_{xx}\frac{\partial w_0}{\partial x}-q\delta w_0\right]dx \tag{3.65}$$

Substituting the stress resultants N_{xx} and moment resultants M_{xx}, Eq.(3.59) and Eq.(3.60) respectively into the above equations, Eq.(3.64) and Eq.(3.65), provides an alternate form of the weak statement:

$$\begin{aligned}0=\int_{x_a}^{x_b}\Bigg[& I'\delta u_0\frac{\partial^2 u_0}{\partial t^2}-\tilde{I}\delta u_0\frac{\partial^3 w_0}{\partial t^2\partial x}+A_{xx}\frac{\partial\delta u_0}{\partial x}\left\{\frac{\partial u_0}{\partial x}+\frac{1}{2}\left(\frac{\partial w_0}{\partial x}\right)^2\right\}\\ & -B_{xx}\frac{\partial\delta u_0}{\partial x}\frac{\partial^2 w_0}{\partial x^2}-N_{xx}^T\frac{\partial\delta u_0}{\partial x}-f\delta u_0\Bigg]dx\end{aligned} \tag{3.66}$$

$$\begin{aligned}0=\int_{x_a}^{x_b}\Bigg[& I'\delta w_0\frac{\partial^2 w_0}{\partial t^2}-\tilde{I}\frac{\partial\delta w_0}{\partial x}\frac{\partial^2 u_0}{\partial t^2}+\hat{I}\frac{\partial\delta w_0}{\partial x}\frac{\partial^3 w_0}{\partial x\partial t^2}+D_{xx}\frac{d^2\delta w_0}{dx^2}\frac{\partial^2 w_0}{\partial x^2}+M_{xx}^T\frac{d^2\delta w_0}{dx^2}\\ & -B_{xx}\frac{d^2\delta w_0}{dx^2}\left\{\frac{\partial u_0}{\partial x}+\frac{1}{2}\left(\frac{\partial w_0}{\partial x}\right)^2\right\}+A_{xx}\frac{\partial\delta w_0}{\partial x}\frac{\partial w_0}{\partial x}\left\{\frac{\partial u_0}{\partial x}+\frac{1}{2}\left(\frac{\partial w_0}{\partial x}\right)^2\right\}\\ & -B_{xx}\frac{\partial\delta w_0}{\partial x}\frac{\partial w_0}{\partial x}\frac{\partial^2 w_0}{\partial x^2}-\frac{\partial\delta w_0}{\partial x}\frac{\partial w_0}{\partial x}N_{xx}^T-q\delta w_0\Bigg]dx\end{aligned} \tag{3.67}$$

Eq.(3.66) represents the weak form of the axial motion of beam. Axial displacement is coupled with gradient of the transverse deflection (nonlinear strain). Similarly, Eq.(3.67) is the weak form of the transverse deflection containing coupling with axial deflection as well as gradient of the transverse deflection. Assuming finite element approximations of the form

$$u_0(x,t)=\sum_{j=1}^{2}U_j(t)\mathrm{N}_j^L(x),\qquad w_0(x,t)=\sum_{J=1}^{4}W_J(t)\mathrm{N}_J^H(x) \tag{3.68}$$

where, $\mathrm{N}_j^L(x)$ are the linear Lagrange interpolation functions (i,j=1,2), and $\mathrm{N}_J^H(x)$ are the Hermite cubic interpolation functions (I,J=1,2,3,4). (U_1,U_2) are the nodal values of u_0 at x_a and x_b, respectively, and W_J are the nodal values associated with w_0, i.e.

$$W_1(t)\equiv w_0(x_a,t),\quad W_2(t)\equiv-\theta(x_a,t),\quad W_3(t)\equiv w_0(x_b,t),\quad W_4(t)\equiv-\theta(x_b,t) \tag{3.69}$$

Substituting Eq.(3.68) and Eq.(3.69) for $u_0(x,t)$ and $w_0(x,t)$, and $\delta u_0(x) = \mathrm{N}_j^L(x)$ and $\delta w_0(x) = \mathrm{N}_J^H(x)$ into the weak forms, Eq.(3.66) and Eq.(3.67), we obtain

$$\begin{bmatrix} \mathbf{M}^{11} \mathbf{M}^{12} \\ \mathbf{M}^{21} \mathbf{M}^{22} \end{bmatrix} \begin{Bmatrix} \ddot{\mathbf{U}} \\ \ddot{\mathbf{W}} \end{Bmatrix} + \begin{bmatrix} \mathbf{K}^{11} \mathbf{K}^{12} \\ \mathbf{K}^{21} \mathbf{K}^{22} \end{bmatrix} \begin{Bmatrix} \mathbf{U} \\ \mathbf{W} \end{Bmatrix} = \begin{Bmatrix} \mathbf{F}^1 \\ \mathbf{F}^2 \end{Bmatrix} \tag{3.70}$$

The coefficient matrices $\mathbf{K}^{12}$, $\mathbf{K}^{21}$ and $\mathbf{K}^{22}$ are functions of the unknown $w_0(x,t)$ and its coefficients for FGM beam are directly influenced by coupling stiffness B_{xx}. Higher the value of power law index n, more is the coupling. Also, $\mathbf{K}^{12^{\mathrm{T}}} \neq \mathbf{K}^{21}$; hence, the overall element stiffness matrix is unsymmetric. $\mathbf{F}^1$ is the force vector due to mechanical or thermal axial load. $\mathbf{F}^2$ is the force vector due to thermal moments or mechanical transverse load.

The equation of motion Eq.(3.70) can be expressed in the standard form as

$$\mathbf{M}\ddot{\mathbf{d}} + \mathbf{K}\mathbf{d} = \mathbf{F} \tag{3.71}$$

where, $\ddot{\mathbf{d}} = \begin{Bmatrix} \ddot{\mathbf{U}} \\ \ddot{\mathbf{W}} \end{Bmatrix}$ and $\mathbf{d} = \begin{Bmatrix} \mathbf{U} \\ \mathbf{W} \end{Bmatrix}$

The individual stiffness matrices used in getting the overall stiffness matrix $\mathbf{K}$ for the nonlinear Euler Bernoulli beam are as follows:

$$\mathbf{K} = \begin{bmatrix} \mathbf{K}^{11} \mathbf{K}^{12} \\ \mathbf{K}^{21} \mathbf{K}^{22} \end{bmatrix}$$

$$K_{ij}^{11} = \int_{x_a}^{x_b} A_{xx} \frac{dN_i^L}{dx} \frac{dN_j^L}{dx} dx \tag{3.72a}$$

$$K_{iJ}^{12} = -\int_{x_a}^{x_b} B_{xx} \frac{dN_i^L}{dx} \frac{d^2N_J^H}{dx^2} dx + \frac{1}{2} \int_{x_a}^{x_b} A_{xx} \left(\frac{\partial w_0}{\partial x} \right) \frac{dN_i^L}{dx} \frac{dN_J^H}{dx} dx ; \tag{3.72b}$$

$$K_{Ij}^{21} = -\int_{x_a}^{x_b} B_{xx} \frac{d^2N_I^H}{dx^2} \frac{dN_j^L}{dx} dx + \int_{x_a}^{x_b} A_{xx} \left(\frac{\partial w_0}{\partial x} \right) \frac{dN_I^H}{dx} \frac{dN_j^L}{dx} dx ; \tag{3.72c}$$

$$K_{IJ}^{22}=\int_{x_a}^{x_b}\left[\frac{1}{2}A_{xx}\left(\frac{\partial w_0}{\partial x}\right)^2\frac{dN_I^H}{dx}\frac{dN_J^H}{dx}-B_{xx}\left(\frac{\partial w_0}{\partial x}\right)\left(\frac{1}{2}\frac{d^2N_I^H}{dx^2}\frac{dN_J^H}{dx}+\frac{dN_I^H}{dx}\frac{d^2N_J^H}{dx^2}\right)\right]dx$$
$$+\int_{x_a}^{x_b}D_{xx}\frac{d^2N_I^H}{dx^2}\frac{d^2N_J^H}{dx^2}dx \tag{3.72d}$$

The mass matrix $\mathbf{M}$ is given as

$$\mathbf{M}=\begin{bmatrix}\mathbf{M}^{11}\,\mathbf{M}^{12}\\ \mathbf{M}^{21}\,\mathbf{M}^{22}\end{bmatrix}$$

$$M_{ij}^{11}=\int_{x_a}^{x_b}I'N_i^LN_j^Ldx \tag{3.73a}$$

$$M_{iJ}^{12}=-\int_{x_a}^{x_b}\tilde{I}N_i^L\frac{\partial N_J^H}{\partial x}dx \tag{3.73b}$$

$$M_{Ij}^{21}=-\int_{x_a}^{x_b}\tilde{I}\frac{\partial N_I^H}{\partial x}N_j^Ldx \tag{3.73c}$$

$$M_{IJ}^{22}=\int_{x_a}^{x_b}\left(I'N_I^HN_J^H+\hat{I}\frac{\partial N_I^H}{\partial x}\frac{\partial N_J^H}{\partial x}\right)dx \tag{3.73d}$$

The force vector $\mathbf{F}$ is given as

$$\mathbf{F}=\begin{Bmatrix}\mathbf{F}^1\\ \mathbf{F}^2\end{Bmatrix}$$

$$F_i^1=\int_{x_a}^{x_b}\left(\frac{dN_i^L}{dx}N_{xx}^T+N_i^Lf\right)dx \tag{3.74a}$$

$$F_I^2=\int_{x_a}^{x_b}\left(-\frac{d^2N_I^H}{dx^2}M_{xx}^T+\frac{dN_I^H}{dx}\frac{dw}{dx}N_{xx}^T+N_I^Hq\right)dx \tag{3.74b}$$

To evaluate linear stiffness matrix for functionally graded material beam, we need to omit the nonlinear term $\frac{1}{2}\left(\frac{dw_0}{dx}\right)^2$ from Eq.(3.47) so that linear strain-displacement relations will be as follows,

$$\varepsilon_{xx}(x,z,t)=\frac{\partial u_0}{\partial x}+z\left(-\frac{\partial^2w_0}{\partial x^2}\right) \tag{3.75}$$

This will result in omission of all the nonlinear terms in the nonlinear stiffness matrix coefficient Eq.(3.72) and the coefficients of linear stiffness matrix will be as follows

$$K_{ij}^{11} = \int_{x_a}^{x_b} A_{xx} \frac{dN_i^L}{dx} \frac{dN_j^L}{dx} dx ; \tag{3.76a}$$

$$K_{iJ}^{12} = -\int_{x_a}^{x_b} B_{xx} \frac{dN_i^L}{dx} \frac{d^2N_J^H}{dx^2} dx ; \tag{3.76b}$$

$$K_{Ij}^{21} = -\int_{x_a}^{x_b} B_{xx} \frac{d^2N_I^H}{dx^2} \frac{dN_j^L}{dx} dx ; \tag{3.76c}$$

$$K_{IJ}^{22} = \int_{x_a}^{x_b} D_{xx} \frac{d^2N_I^H}{dx^2} \frac{d^2N_J^H}{dx^2} dx \tag{3.76d}$$

For the linear case, the axial displacement u_0 and bending deflection w_0 are uncoupled, and can be determined independently from the finite element models. However, for nonlinear case, the coupling between u_0 and w_0 will cause the beam to undergo axial displacement even when there are no axial forces. The solution (u_0, w_0) will be different for the two cases. If we consider the hinged-hinged beam, it does not have any end constraints and hence, the beam does not experience any axial strain. On the other hand, the pinned-pinned beam is constrained from axial movement at both the ends. As a result, it will develop axial strain to accommodate the transverse deflection. The hinge-hinge beam will have larger transverse deflection as compared to the pinned-pinned beam, as the pinned-pinned beam offers axial stiffness to stretching, and the axial stiffness increases with the load.

For a hinged-hinged beam, if the element should not experience any stretching, then,

$$\varepsilon_{xx}^0 = \frac{du_0}{dx} + \frac{1}{2}\left(\frac{dw_0}{dx}\right)^2 = 0 \text{ (membrane strain)} \tag{3.77a}$$

In order to satisfy this constraint in Eq.3.77(a), we must have,

$$\frac{du_0}{dx} \sim \left(\frac{dw_0}{dx}\right)^2 \tag{3.77b}$$

The similarity is in the sense of having the same degree of polynomial variation of du_0/dx and $\left(dw_0/dx\right)^2$. For example, when u_0 is interpolated using linear functions

and w_0 with cubic, the constraint in Eq.4.33(b) is clearly not met and the resulting element stiffness matrix is excessively stiff (hence, results in zero displacement field), and the element is said to lock. This phenomenon is known as the membrane locking. A practical way is to use the minimum interpolation of u_0 and w_0 (i.e. linear interpolation of u_0 and Hermite cubic interpolation of w_0). Thus, all nonlinear stiffness coefficients should be evaluated using one-point Gauss quadrature, that is, use the reduced integration and linear terms may be evaluated exactly using two-point quadrature. The nonlinear equations after assembly must be solved by imposing boundary conditions, using suitable iterative method. Non-linear coupled equations of motion are solved via the iterative Newton–Raphson method accompanied with the β-Newmark time approximation technique for vibration analysis. The iteration process is continued until the difference between the two solutions reduces to a preselected error tolerance. The global error criterion is of the form

$$\sqrt{\frac{\sum_{I=1}^{N}\left|\vartheta_I^{r+1}-\vartheta_I^{r}\right|^2}{\sum_{I=1}^{N}\left|\vartheta_I^{r+1}\right|^2}}<\in \tag{3.78}$$

where, $\left\{\vartheta^e\right\}^r$ and $\left\{\vartheta^e\right\}^{r+1}$ are solutions at r and $r+1$ iteration, N is the total number of nodal generalised displacements in the finite element mesh and $\in$ is the error tolerance.

3.7.5 Solutions of nonlinear equations

The solution of nonlinear equations (4.26) using Newton's iterative method involves the computation of the coefficients of the element tangent stiffness matrix (refer Reddy, 2004).

$$\hat{\mathbf{T}}^e=\begin{bmatrix}\hat{\mathbf{T}}^{11}\hat{\mathbf{T}}^{12}\\ \hat{\mathbf{T}}^{21}\hat{\mathbf{T}}^{22}\end{bmatrix}^r\begin{Bmatrix}\delta\mathbf{U}\\ \delta\mathbf{W}\end{Bmatrix}^{r+1}=-\begin{Bmatrix}\mathbf{R}^1\\ \mathbf{R}^2\end{Bmatrix}^r \tag{3.79}$$

where symbol δ denotes the increment of the displacements from the r^{th} iteration to the $(r+1)^{\text{th}}$ iteration. The components of the tangent stiffness matrix are evaluated at the r^{th} iteration as follows

$$\hat{T}_{ij}^{\alpha\beta} = \frac{\partial R_i^{\alpha}}{\partial d_j^{\beta}} \qquad \alpha, \beta = 1,2 \tag{3.80a}$$

where, d_j^{β} are the components of the displacement vector and R_i^{α} are the components of the residual vector $\mathbf{R}$ which can be expressed as

$$R_i^{\alpha} = \sum_{\gamma=1}^{2}\sum_{p=1}^{N_\gamma} \hat{K}_{ip}^{\alpha\gamma} d_p^{\gamma} - \hat{F}_i^{\alpha} = \sum_{p=1}^{2} \hat{K}_{ip}^{\alpha 1} d_p^{1} + \sum_{p=1}^{4} \hat{K}_{iP}^{\alpha 2} d_p^{2} - \hat{F}_i^{\alpha}$$

$$= \sum_{p=1}^{2} \hat{K}_{ip}^{\alpha 1} U_p + \sum_{p=1}^{4} \hat{K}_{iP}^{\alpha 2} W_p - \hat{F}_i^{\alpha} \tag{3.80b}$$

where N_γ ($\gamma = 1,2$) denotes the number of element degrees of freedom [N_1 = 2 and N_2 = 4]. We have

$$\hat{T}_{ij}^{\alpha\beta} = \frac{\partial R_i^{\alpha}}{\partial d_j^{\beta}} = \frac{\partial}{\partial d_j^{\beta}} \left(\sum_{\gamma=1}^{2}\sum_{p=1}^{N_\gamma} \hat{K}_{ip}^{\alpha\gamma} d_p^{\gamma} - \hat{F}_i^{\alpha} \right)$$

$$= \sum_{\gamma=1}^{2}\sum_{p=1}^{n(\gamma)} \left(\hat{K}_{ip}^{\alpha\gamma} \frac{\partial d_p^{\gamma}}{\partial d_j^{\beta}} + \frac{\partial \hat{K}_{ip}^{\alpha\gamma}}{\partial d_j^{\beta}} d_p^{\gamma} \right) - \frac{\partial \hat{F}_i^{\alpha}}{\partial d_j^{\beta}}$$

$$= \hat{K}_{ij}^{\alpha\beta} + \sum_{p=1}^{2} \frac{\partial}{\partial d_j^{\beta}} \left(\hat{K}_{ip}^{\alpha 1} \right) U_p + \sum_{p=1}^{4} \frac{\partial}{\partial d_j^{\beta}} \left(\hat{K}_{iP}^{\alpha 2} \right) W_P - \frac{\partial \hat{F}_i^{\alpha}}{\partial d_j^{\beta}} \tag{3.80c}$$

Since $\hat{F}_i^{\alpha}$ and $\hat{K}_{ip}^{\alpha\gamma}$ depend at most only on w and not on u, we have

$$\hat{T}_{ij}^{\alpha 1} = K_{ij}^{\alpha 1} \qquad \text{for } \alpha = 1,2 \tag{3.81}$$

The coefficients of the tangent stiffness matrix that are different from their counterparts are as follows:

$$\hat{T}_{iJ}^{12} = K_{iJ}^{12} + \frac{1}{2}\int_{x_a}^{x_b} A_{xx} \left(\frac{\partial w_0}{\partial x} \right) \frac{dN_i^L}{dx} \frac{dN_J^H}{dx} dx = K_{Ij}^{21} \tag{3.82a}$$

$$\hat{T}_{iJ}^{22} = K_{IJ}^{22} + \int_{x_a}^{x_b} A_{xx} \frac{\partial u_0}{\partial x} \frac{dN_I^H}{dx} \frac{dN_J^H}{dx} dx + \int_{x_a}^{x_b} A_{xx} \left(\frac{\partial w_0}{\partial x} \right)^2 \frac{dN_I^H}{dx} \frac{dN_J^H}{dx} dx$$
$$- \int_{x_a}^{x_b} B_{xx} \left(\frac{1}{2} \frac{\partial w_0}{\partial x} \frac{d^2 N_I^H}{dx^2} \frac{dN_J^H}{dx} + \frac{\partial^2 w_0}{\partial x^2} \frac{dN_I^H}{dx} \frac{d^2 N_J^H}{dx^2} \right) dx - \int_{x_a}^{x_b} N_{xx}^T \frac{dN_I^H}{dx^2} \frac{dN_J^H}{dx^2} dx \tag{3.82b}$$

It is to be noted that the tangent stiffness matrix for functionally graded material Euler-Bernoulli beam element with the von Karman nonlinearity is symmetric.

3.8 DETERMINATION OF DYNAMIC STRESSES

Neglecting the thermal strains, the dynamic stress at a point can be found using the equation

$$\sigma_{xx} = \bar{Q}_{11}\varepsilon_{xx} = \bar{Q}_{11}\varepsilon^0_{xx} + z\bar{Q}_{11}\varepsilon^1_{xx} \tag{3.83}$$

where, ε^0_{xx} is the axial strain and ε^1_{xx} is the beam curvature. To evaluate the dynamic stress, the displacement vector $\{d\}$ is given by

$$\{d\} = \begin{Bmatrix} u_1 \\ w_1 \\ w_{x,1} \\ u_2 \\ w_2 \\ w_{x,2} \end{Bmatrix} \tag{3.84}$$

where,

$$w_{1,x} = \frac{\partial w_1}{\partial x} \quad \text{and} \quad w_{2,x} = \frac{\partial w_2}{\partial x} \tag{3.85}$$

are the slope of the beam.

Since there are four nodal values, we select a polynomial with four constants. Making use of the linear polynomial for axial displacement variation and cubic polynomial for transverse displacement variation, as,

$$u = a_1 + a_2 x \tag{3.86a}$$

$$w = c_1 + c_2 x + c_3 x^2 + c_4 x^3 \tag{3.86b}$$

Therefore, the strains are evaluated as follows,

The axial strain at a point along the length of beam in local coordinates is given as

$$\varepsilon_{xx}^{0}=\begin{bmatrix}0 & 0 & 0 & 1 & 0 & 0\end{bmatrix}\begin{bmatrix}1 & 0 & 0 & 0 & 0 & 0\\ 0 & 1 & 0 & 0 & 0 & 0\\ 0 & 0 & 1 & 0 & 0 & 0\\ 1 & 0 & 0 & l & 0 & 0\\ 0 & 1 & l & 0 & l^2 & l^3\\ 0 & 0 & 1 & 0 & 2l & 3l^2\end{bmatrix}^{-1}\begin{Bmatrix}u_1\\ w_1\\ w_{x,1}\\ u_2\\ w_2\\ w_{x,2}\end{Bmatrix}+\frac{1}{2}\left(w_{x,2}\right)^2 \qquad (3.87)$$

and the bending strain at a point along the length of beam in local coordinates is given as

$$\varepsilon_{xx}^{1}=\begin{bmatrix}0 & 0 & 0 & 0 & 2 & 6x\end{bmatrix}\begin{bmatrix}1 & 0 & 0 & 0 & 0 & 0\\ 0 & 1 & 0 & 0 & 0 & 0\\ 0 & 0 & 1 & 0 & 0 & 0\\ 1 & 0 & 0 & l & 0 & 0\\ 0 & 1 & l & 0 & l^2 & l^3\\ 0 & 0 & 1 & 0 & 2l & 3l^2\end{bmatrix}^{-1}\begin{Bmatrix}u_1\\ w_1\\ w_{x,1}\\ u_2\\ w_2\\ w_{x,2}\end{Bmatrix} \qquad (3.88)$$

The dynamic stress can be calculated by substituting value of axial strain and bending strain in the equation for stress given by Eq.(3.83). To evaluate thermal stresses, substitute the value of axial strain, Eq.(3.87), and bending strain, Eq.(3.88) in Eq.(3.57) which accounts for thermal strain.

3.9 SOLUTION OF THE FGM EQUATION OF MOTION FOR THERMAL LOAD

Consider the finite element equation of motion, Eq.(3.71), in absence of damping and acted upon by a time dependent force. Newmark's method is used to solve this form of second order equation. It enables the determination of nodal displacements at different time increments for a given dynamic system. The details of the Newmark's method for the solution of Eq.(3.71) is outlined in Logan (2002).

3.10 SUMMARY

In the first part, the basic equation for material gradation through thickness of functionally graded beam considering temperature dependent material properties is presented. In the second part, the formulation of the heat conduction problem in one and two dimension with convection and discretization of this problem using finite

element method is detailed. Later, the finite difference solution of heat transfer problem in time is presented. In the last part, the nonlinear strain displacement relation are derived for the Euler-Bernoulli beam followed by the equation of the motion to develop the weak forms using the principle of virtual displacements and the associated finite element model. The nonlinear theoretical analysis is presented to predict the thermo-elastic response of layered FGM beams subjected to thermal load under various structural boundary conditions. The detailed derivation is presented for evaluation of the dynamic stresses for the FGM beam. The solution procedure using Newton's iteration method and Newmark's method for the problem is also discussed at the end of the chapter.

CHAPTER - 4

FABRICATION OF FUNCTIONALLY GRADED BEAMS USING PLASMA SPRAY AND POWDER METALLURGY PROCESS

4.1 INTRODUCTION

Functionally graded material beam samples with multiple layers of metal-ceramic combination with their volume fractions varying from layer to layer were prepared for the experimental investigation. SUS316-Al_2O_3 FGM samples were prepared by thermal spray technique and Al-Al_2O_3 FGM samples were made by powder metallurgy route. The different steps involved in the sample fabrication by thermal spray is explained. Powder metallurgy is another suitable method for manufacturing of functionally graded material components. In this regards, various steps involved like powder mixing, powder filling, uniaxial die compaction and sintering of the sample are discussed in detail in this chapter. The various parameters used while preparing the FGM and pure aluminium beam samples are listed in the chapter. Microstructure studies of FGM powder mixtures and beam samples by using scanning electron microscope (SEM) are also discussed in this chapter.

4.2 THE FGM BEAM

Consider a rectangular cross section beam of length L. The x-coordinate is taken along the neutral plane of the beam, z-coordinate along the thickness (the height) of the beam, and the y-coordinate is taken along the width of the beam, as shown in Fig.4.1.

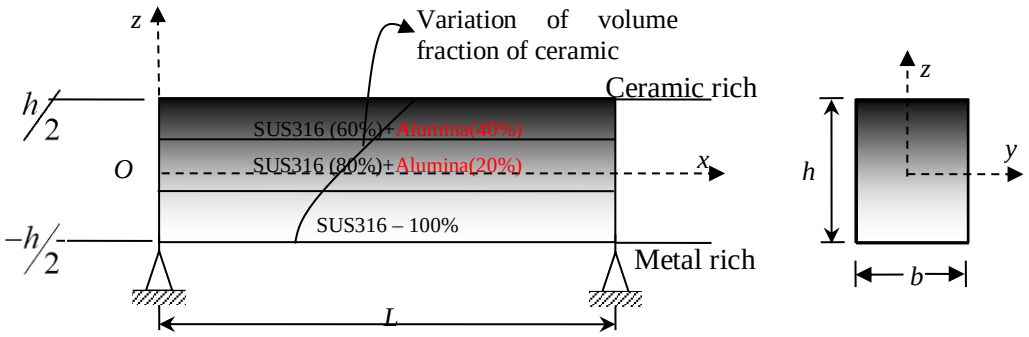

Fig.4.1 Geometry of typical 3 layer FGM made of SUS316 and Al_2O_3.

FGM beam samples of SUS316-Al_2O_3 metal and ceramic combination with their volume fractions varying for each layer are prepared for the experimental studies by thermal spray technique. One of the popular coating process having the greatest range of coating materials, coating thicknesses and possible coating characteristics is thermal spray. 100% pure SUS316 powder of 63 micron size and 99.9% pure Al_2O_3 of 15/45 micron size are used as the raw materials (ref Fig.4.2). Using thermal spray system, three-layered samples are made with the thickness of each FGM layer being approximately 0.1 to 0.2 mm as shown in Fig.4.1. The thickness depends on the number of passes of the plasma spray gun over the base material. Each pass provides the thickness approximately equal to 0.1 mm.

Fig.4.2 Powders used for FGM fabrication (a) Aluminium powder–200 mesh (Al) (b) Al_2O_3 powder – 15/45 micron (c) SUS316 powder – 63micron size.

The volume fraction, length, height and width of FGM beam samples are as listed in Table 4.1. The thickness indicted in the Table 4.1 is average thickness of the beam over the length. The ceramic content in the layers of the FGM samples was linearly varied from 0% to 40% considering power law index of $n = 1$ as shown in Fig.4.1 with the

bottom layer being of pure metal and the top layer having 40% ceramic content. Sample 9 is a beam made of commercially available SUS316 cold rolled sheet.

Table 4.1: Details of the thermally sprayed SUS316-Al_2O_3 functionally graded beam samples.

Sample No.	No. of Layers	Volume fraction of metal and ceramic (SUS316:Al_2O_3)			Length "L"	Thickness "h"	Width "b"
		1	2	3			
1	3	100:0	80:20	60:40	150	0.925	30
2	3	100:0	80:20	60:40	180	0.75	17.5
3	3	100:0	80:20	60:40	180	0.78	30
4	2	100:0	0:100	-	150	0.70	30
9	1	100:0	-	-	150	0.6	30

A 5 layer FGM beam samples of Al-Al_2O_3 were prepared by the powder metallurgy process. 99.5% pure aluminium atomized powder of 200 mesh size and 99.9% pure Al_2O_3 of 15/45 micron size are used as the raw materials. For this system, five-layer samples are made with the thickness of each layer being approximately 0.45 to 0.5 mm. The thickness depends on the weight of the powder used for each layer, compaction pressure and sintering. The average weight of the powder for pure aluminium layer is 4.05 gm and for FGM layer is 4.4 to 4.57 gm to achieve layer thickness of around 0.5 mm. The ceramic content in the layers of the FGM samples was linearly varied from 0% to 50% considering power law index of $n = 1$ as shown in Fig.3.2 with the bottom layer being of pure metal and the top layer having 10 to 50% ceramic content.

The following dimensions are considered for preparing 5 layer Al-Al_2O_3 FGM beam sample using powder metallurgy process as shown in Fig.4.3,

Length, L =150 mm, width, b =20 mm and thickness, h =2.54 mm

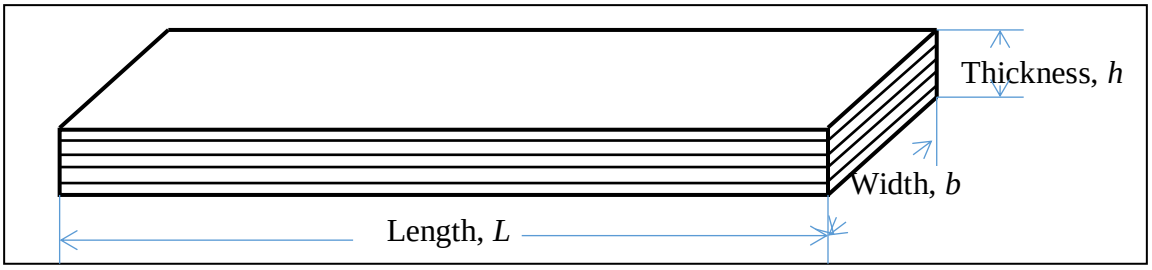

Fig.4.3 Schematic representation of 5 layer functionally graded beam.

4.3 FABRICATION OF FGM BEAM SAMPLES BY PLASMA SPRAY PROCESS

4.3.1 Powder preparation

Two stocks of SUS316-Al_2O_3 with ceramic volume fraction of 20% and 40% were made available and mechanical alloying was done in a high energy rate planetary ball mill RETSCH PM-100. A photograph of the machine is as shown in Fig.4.4. The container used for milling was of stainless steel with tungsten carbide balls. The number of balls used depends on the total weight of the powder to be milled. The total weight of the balls used in present study was equal to weight of the powder. The rotation speed and the milling time were maintained at 200 rpm and 2 h, respectively. The size of the FGM powder after proper mixing in ball mill was expected to be in the range of 5–50 micron.

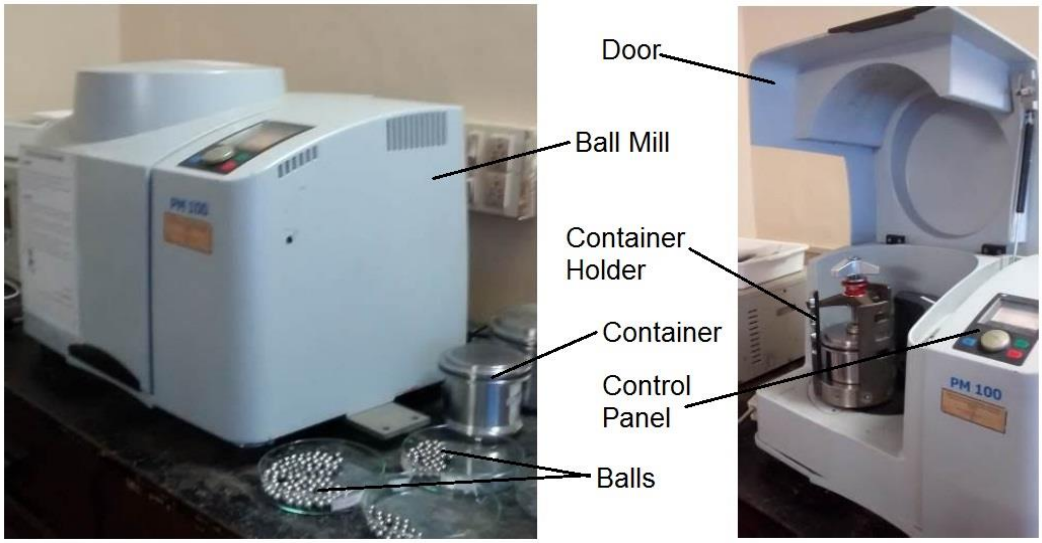

Fig.4.4 Planetary Ball Mill (PM-100) for mixing powders (Metallurgical and Materials Engineering Department, NITK, Surathkal).

4.3.2 Substrate preparation

100% pure SUS316 plate with a thickness of 0.6 mm was used as the substrate onto which subsequent layers of the molten material in powder form were sprayed. The substrate was cut to required beam size as listed in Table 4.1. The thickness of the substrate is very small, hence to avoid distortions like warping of the substrate during

plasma spraying, the substrate was held on a steel backing plate by means of brazing. The details are illustrated in Fig.4.5.

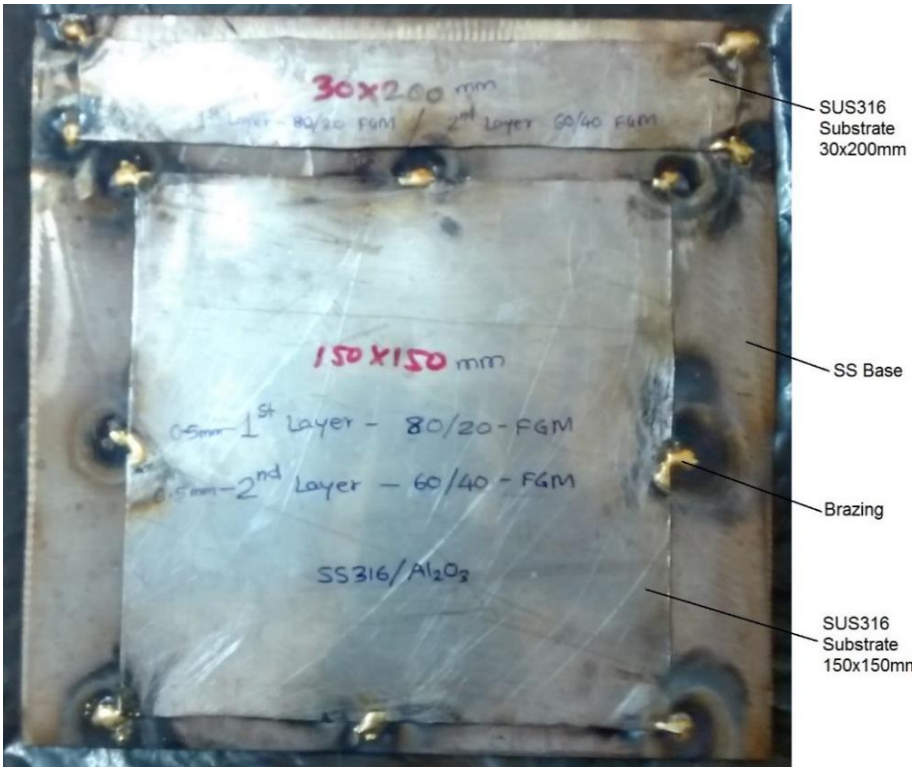

Fig.4.5 SUS316 substrate preparation for plasma spraying.

4.3.3 Plasma spraying process

In the present study, the samples of SUS316-Al_2O_3 were prepared by the plasma spray process known as the flame or thermal spray process. The limitation of this process is that, the materials used for spraying should have melting temperature lesser than flame temperature. The temperature within the plume can reach as high as 16000 K. The spray material is injected as a powder outside of the gun nozzle into the plasma plume, where it is melted, and hurled by the gas onto the substrate surface. The principle of plasma spraying is shown schematically in Fig.4.6(a) while Fig.4.6(b) shows the typical plasma spraying machine setup.

The plasma gun utilizes a chamber with one or more electrodes called cathode and the nozzle being anode. A high frequency arc is ignited between an anode and a tungsten cathode. With process gases flowing through the chamber, direct current power is

applied to the cathode, which arcs to the anode. The powerful arc strips the gas molecules of their electrons to form a plasma plume. As the unstable plasma ions recombine back to the gaseous state, a tremendous level of thermal energy is released.

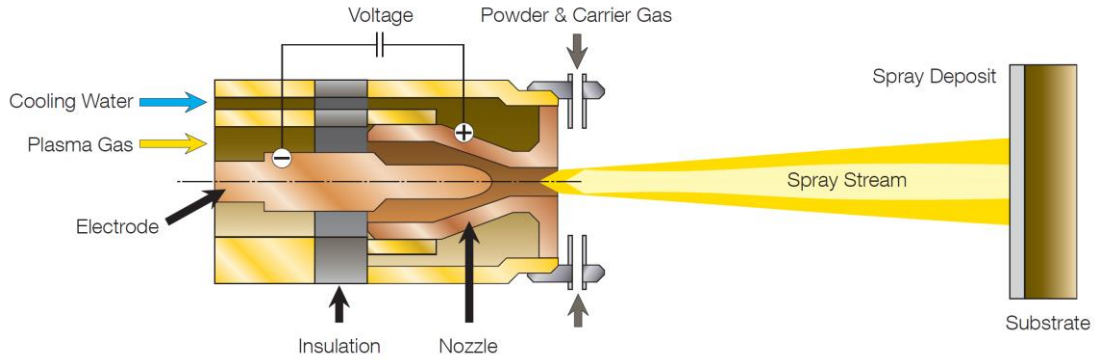

(a) Schematic diagram of a typical plasma spray gun (www.oerlikon.com/metco).

(b) A typical Plasma spraying machine setup (www.oerlikon.com/metco).

Fig.4.6 The plasma spray process.

The gas flowing between the electrodes is ionized such that a plasma plume several centimetres in length develops. The feedstock material is injected into the hot gas plume, where it is melted and propelled towards the target substrate to form the coating. The process gases typically used are argon, hydrogen, nitrogen and helium, either individually or in mixtures of two, or even three of these gases. The gases used in combination with the current applied to the electrode controls the amount of energy produced. Since gas flows and the applied current can be accurately regulated, repeatable and predictable coating results can be obtained. In addition, the shape and bore size of the nozzle, the point and angle that the material is injected into the plume, as well as the distance of the gun to the target surface are also controlled. This provides a high degree of flexibility to develop reproducible parameters for materials with

melting temperatures across a very large range. The gas-stabilized plasma (GSP) gun PTF4 (SULZER METCO, Switzerland) with 3MB spraying gun of 40 kW power capability was used for simultaneous spraying of mixture of SUS316 and Al_2O_3. The cylindrical nozzle is made of copper and functions as anode. While the cathode is made of thoriated tungsten (2 wt.% of Thoria) (see Fig.4.6(a)). Prior to spraying, the SUS316 substrate surface was grit blasted using SiC grits to remove any rust followed by cleaning in acetone. The FGM material in powder form was melted in an oxy-acetylene flame to form a fine spray. The dry acetylene pressure was maintained at 1 kgf/cm^2 and oxygen pressure was set to 1.75 kgf/cm^2. In order to avoid any metallurgical changes, damage or distortion to the substrate, the substrate was kept at low temperature during the spray process so as to allow the fine molten droplets solidify rapidly to form a coating. The samples were cooled during plasma spraying by compressed air to avoid the substrate heating by the plasma plume. The material was sprayed carefully all over the surface of the substrate to obtain uniformity of thickness. Basic setup parameters used for spray procedures are summarized in Table 4.2. Three beam samples with three-layers were prepared in the same manner to examine the repeatability of experimental results. For the fourth sample, 100% Al_2O_3 was sprayed on SUS316 substrate to study the difference between FGM material and pure ceramic coating on metal substrate. Fig.4.7 shows 4 different samples prepared with plasma spray process.

Table 4.2: Plasma spraying setup parameters for sample manufacturing.

Parameters	**GSP**
Gas flow rate Ar/H2	45/15 NL/min
Spray rate	2 – 10 kg/h
Particle velocity	$\leq$ 450 m/s
Gas temperature	12000 – 16000 ^{0}C
Stand-off distance	100 mm
Substrate preheating temperature	200 °C

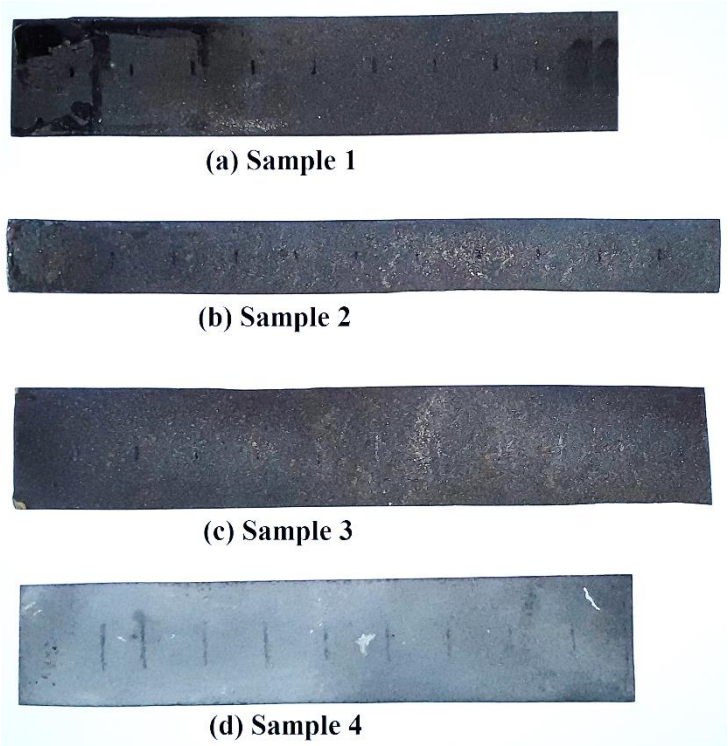

Fig.4.7 FGM samples prepared using plasma spray process.

4.4 FABRICATION OF FGM BEAM SAMPLES BY POWDER METALLURGY PROCESS

4.4.1 Die fabrication

i. Die design

Die is used to compact the powders in a press to produce the green compact in powder metallurgy process. The die used is made up of three parts, (a) top die, (b) middle die and (c) bottom die. Schematic 2D drawing of die assembly is shown in the APPENDIX-I, Fig.I.1. Two pins are used to align the top die, middle die and bottom die of the die assembly. Two bolts are used which functions as ejector pins.

ii. Material selection for die

For soft powders like aluminum and copper, abrasion resistant steel such as air hardened steels, die steels are used for making die (powder metallurgy, www.nptel.ac.in). Different die materials, their chemical composition and applications are given in the APPENDIX-I, Table I.1. AISI A2 is air-hardening tool steel which has properties such as safer hardening, less distortion and increased wear resistance.

AISI D2 is an air-hardening, high carbon, high chromium tool steel with extremely high wear resisting properties. It is a very deep hardening steel and will be practically free from size change after proper treatment. The presence of high percentage of chromium imparts mild corrosion-resisting properties in the hardened condition (material datasheet, Alro steels). Based on the availability of material, AISI D2 is chosen as the material for the die fabrication.

iii. Die machining

Machining of raw materials into die was carried out by professionals working in Government Tool Room and Training Center (GTTC) at Baikampady industrial area, near Mangaluru. Draft angle of 2^0 is provided on inside walls of the middle die for easy removal of the sample. Final machined die assembly is shown in the Fig.4.8.

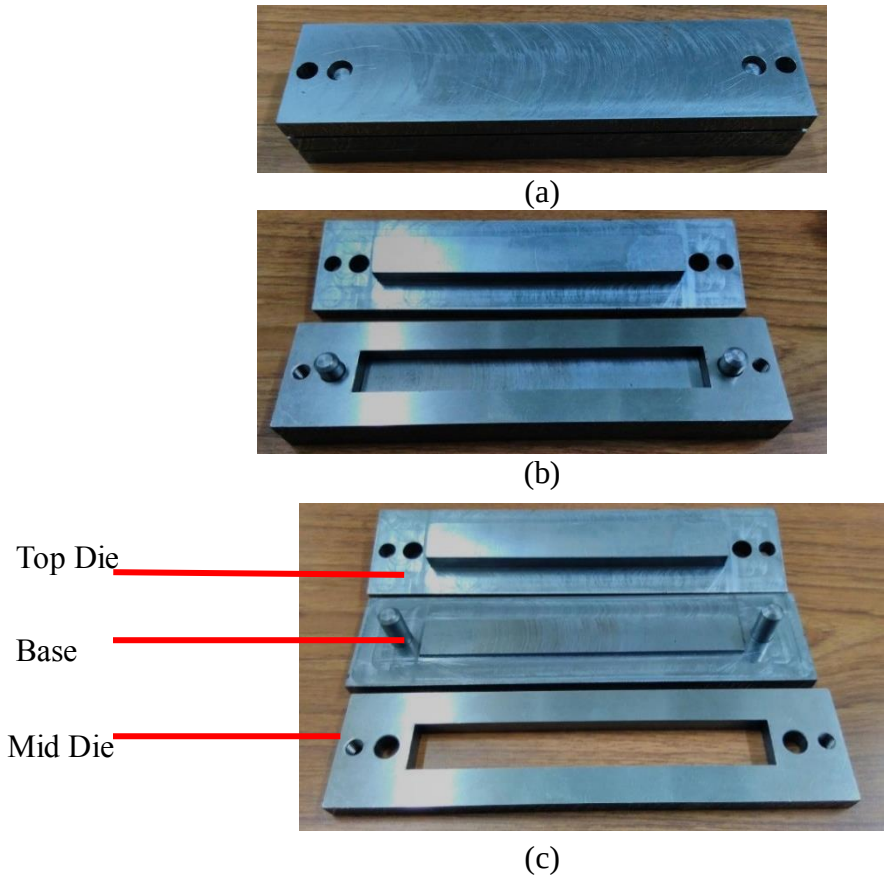

Fig.4.8 (a) Final assembly of machined die, (b) Assembly of base and middle die and (c) top die, base and middle die in FGM die assembly.

4.4.2 Powder mixing

Commercially available aluminium powder of particle size 200 mesh and alumina powders of particle size 15/45 micron are mixed in different proportion based on the volume fraction. Volume fraction of alumina is assumed to vary according to power law distribution. Schematic representation of variation of volume fraction of alumina in a five layered FGM beam based on power law distribution along the thickness direction is shown in Fig.4.9. A graph of V_c v/s z is plotted which indicates the variation of volume fraction of alumina along the thickness direction as shown in the Fig.4.9. Aluminium and alumina powders as per required proportions are mixed and blended for 1 hour in ball milling machine (RETSCH PM 100 high energy rate planetary ball mill) with rotation speed of 200 rpm for proper mechanical alloying. The number of balls used for milling were 50. Pure aluminium, pure alumina and Al-Al_2O_3 powder mixtures with different composition are shown in the Fig.4.2. and Fig.4.10 respectively.

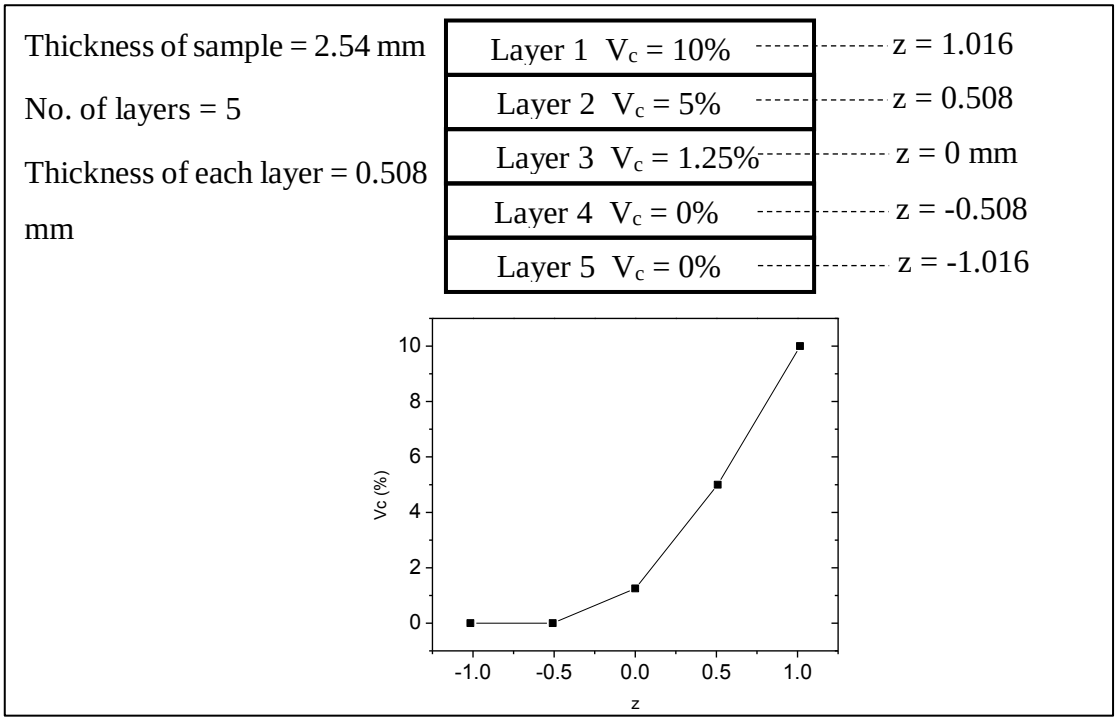

Fig.4.9 Variation of volume fraction of alumina, V_c with respect to thickness coordinate, z.

4.4.3 Powder compaction

Powder stocks with different volume fraction of alumina are taken. Zinc stearate was used as a die wall lubricant. The same is applied each time before using die assembly for powder pressing. Ethanol is used as a binding agent which is mixed with the powders. Layers of different stocks were put in the die successfully, ensuring uniform thickness and distribution of powders in each layer. The specimen is then subjected to unidirectional compaction to a maximum force of 40 to 60 tons along thickness direction. The compaction is carried out in a universal testing machine (UTM). Few details of the universal testing machine are described in the photograph of the machine in the Fig.4.11.

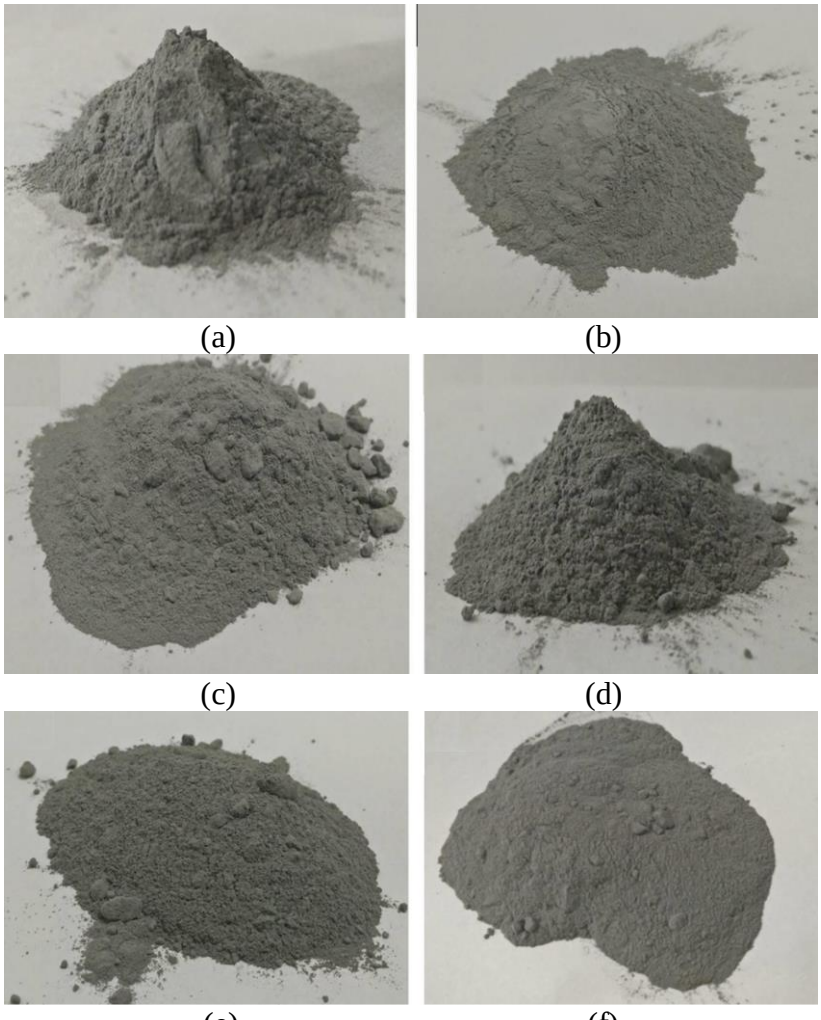

Fig.4.10 Powder mixtures with different composition (a) 98.75%Al - 1.25% Al_2O_3 (b) 97.5%Al - 2.5% Al_2O_3 (c) 95%Al - 5% Al_2O_3 (d) 90%Al - 10%Al_2O_3 (e) 80%Al - 20%Al_2O_3 and (f) 50%Al - 50% Al_2O_3.

4.4.4 Sintering process

Sintering is a process of consolidating a green compact of the desired composition under controlled conditions of temperature and time to obtain the final product. Sintering of the sample is done at a temperature near to the melting point of aluminium. It results in fusing of aluminium and alumina particles together and thereby increasing the strength of the compacted sample. Sintering of green compact is carried out in a furnace at 550^0C to 650^0C for duration of 3.5 to 7 hours. The sintering furnace is shown in the Fig.4.12.

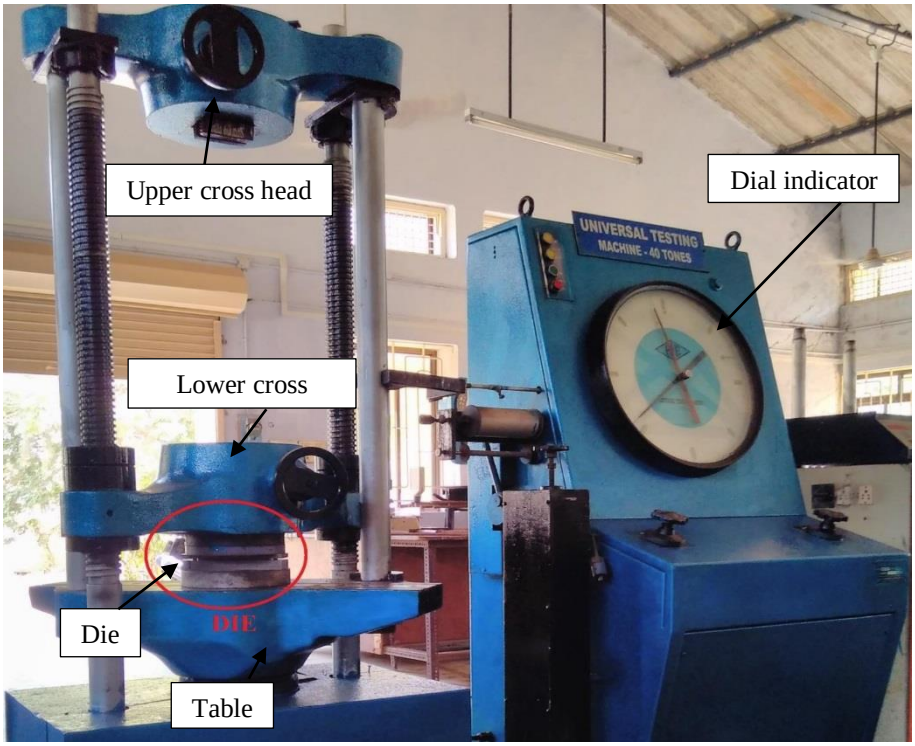

Fig.4.11 Unidirectional compacting of die filled with layer wise powder mixture in Universal Testing Machine (Strength of materials laboratory, NITK Surathkal).

During the early stages of sample preparation, the sintering temperature was set at 550^0C for a duration of 3.5 hours. It was found that the sample thus prepared was defective, see Table I.2 (APPENDIX-I). As a result of this, the process parameters like sintering temperature, sintering duration, green compaction load was changed from 550^0C to 650^0C, 3.5 to 7 hours and 40 tons to 60 tons respectively. Few of the defects observed while preparing functionally graded beam samples using powder metallurgy

process were as follows: (i) breakage, (ii) cracks, (iii) surface peeling, (iv) erosion of powder at the edges, (v) overall bending after sintering. Each one of the above defect was eliminated one after other based on manipulating the process parameters.

Fig.4.12 Sintering furnace with sintering temperature set at 650^0C (Heat treatment laboratory, NITK Surathkal).

4.4.5 Steps in powder metallurgy sample preparation

Zinc stearate powder is mixed with acetone to form a semi liquid solution. When this semi liquid solution is applied on the walls of the die, acetone evaporates leaving behind thin layer of zinc stearate. Since base material is aluminium, the idea of using ethanol as a binding agent is incorporated while preparing the sample. With the addition of ethanol green compact shows significant improvement in strength. Layers of different stocks were put in the die successfully, ensuring uniform thickness and distribution of powders in each layer. The specimen is then subjected to unidirectional compaction to a maximum force of 40 to 60 tons along thickness direction. Universal testing machine (UTM) which is used to compact the powders. The compacted sample is removed from the die using the UTM by applying load slowly. After removing the sample from the die, the sample is compacted again at room temperature, green compaction, by pressing the sample between top die and bottom die. The load applied during green compacting is from 5 tons to 10 tons with an understanding that better sample may result. Liu (2009) has studied the effect of variation of sintering temperature from 600^0C to 650^0C on relative density of aluminium during sintering of aluminum powder. Liu had

concluded that sintering temperature of 650^0C provides better relative density. Based on the findings of Liu (2009), in the present work the sintering temperature was increased to 650^0C from 600^0C. Increasing sintering temperature to 650^0C resulted in better samples which did not undergo breakage when slight manual flexure load was applied. The detail parameters for all the Al-Al_2O_3 FGM and aluminium samples prepared by powder metallurgy process are given in Table 4.3 and Table 4.4 respectively. Step-wise increase of temperature was employed during sintering. Instead of keeping the sample for sintering directly at 650^0C. The temperature was increased in steps of 10^0C per minute by manually adjusting the control knob, till it reaches 650^0C. Since, pure aluminium and Al_2O_3 has different thermal expansion coefficient, the sudden temperature rise causes bending of the samples. The step wise increase of sintering temperature is believed to sinter the sample more thoroughly. The sample prepared did not under go any bending and was free from crack. By adopting step-wise increase of temperature, the problem of bending faced during sintering of earlier samples (FG#1–7) was thus eliminated. Volume fraction of alumina, for five layer FGM is shown in the Table I.2 (APPENDIX I). This table also shows the corresponding wall thickness of the FGM sample and photograph of the sample. Various defects encountered during sample preparation are also marked on the sample photos.

Following are the parameters finalized for preparing the Al-Al_2O_3 FGM beam samples using powder metallurgy process

1. Die wall lubricant: Zinc stearate.
2. Binding agent: Ethanol.
3. In mould compaction load: 60 tons for 5 min.
4. Compacting load out of mould: 10 tons for 1 min.
5. Sintering temperature: 650^0C.
6. Stepwise increase of temperature: 10^0C per min.
7. Sintering duration: 5 hours.
8. Cooling: Furnace cooling.

Table 4.3: History of the process parameters of powder metallurgy process during preparation of Al-Al_2O_3 FGM beam samples.

Sample #	Die wall lubricant	Binding agent	Die compacting load	Loading duration	Open compacting load	Sintering temp (^{0}C)	Stepwise increase of temp	Sintering duration (hours)	Cooling
FG#1	Graphite powder	-	294.2 kN (30 tons)	-	-	550	-	3.5	Furnace cooling
FG#2	Zinc stearate	-	392.27 kN (40 tons)	-	-	600	-	5	Furnace cooling
FG#3	Zinc stearate	-	392.27 kN (40 tons)	-	-	600	-	5	Furnace cooling
FG#4	Zinc stearate	-	392.27 kN (40 tons)	-	-	600	-	5	Furnace cooling
FG#5	Zinc stearate	Ethanol	392.27 kN (40 tons)	-	-	600	-	6	Furnace cooling
FG#6	Zinc stearate	Ethanol	392.27 kN (40 tons)	-	-	600	-	7	Furnace cooling
FG#7	Zinc stearate	Ethanol	392.27 kN (40 tons)	-	-	600 (Vacuum)	-	5	Furnace cooling
FG#8	Zinc stearate	Ethanol	392.27 kN (40 tons)	-	-	600	10^0C per min	5	Furnace cooling
FG#9	Zinc stearate	Ethanol	392.27 kN (40 tons)	5 min	-	600	10^0C per min	5	Furnace cooling
FG#10	Zinc stearate	Ethanol	392.27 kN (40 tons)	5 min	-	600	10^0C per min	5	Furnace cooling
FG#11	Zinc stearate	Ethanol	392.27 kN (40 tons)	5 min	49.03 kN (5 tons)	600	10^0C per min	5	Furnace cooling
FG#12	Zinc stearate	Ethanol	392.27 kN (40 tons)	5 min	49.03 kN (5 tons)	600	10^0C per min	5	Furnace cooling
FG#13	Zinc stearate	Ethanol	392.27 kN (40 tons)	5 min	49.03 kN (5 tons)	600	10^0C per min	5	Furnace cooling
FG#14	Zinc stearate	Ethanol	392.27 kN (40 tons)	5 min	49.03 kN (5 tons)	600	10^0C per min	5	Furnace cooling
FG#15	Zinc stearate	Ethanol	392.27 kN (40 tons)	5 min	98.07 kN (10 tons)	650	10^0C per min	5	Furnace cooling
FG#16	Zinc stearate	Ethanol	392.27 kN (40 tons)	5 min	98.07 kN (10 tons)	650	10^0C per min	5	Furnace cooling
FG#17	Zinc stearate	Ethanol	392.27 kN (40 tons)	5 min	98.07 kN (10 tons)	650	10^0C per min	5	Furnace cooling
FG#18	Zinc stearate	Ethanol	392.27 kN (40 tons)	5 min	98.07 kN (10 tons)	650	10^0C per min	5	Furnace cooling
FG#19	Zinc stearate	Ethanol	392.27 kN (40 tons)	5 min	98.07 kN (10 tons)	650	10^0C per min	5	Furnace cooling
FG#20	Zinc stearate	Ethanol	588.40 kN (60 tons)	5 min	98.07 kN (10 tons)	650	10^0C per min	5	Furnace cooling

Table 4.4: History of the process parameters of powder metallurgy process during preparation of pure aluminium beam samples.

Sample #	Die wall lubricant	Binding agent	Die compacting load	Loading duration	Open compacting load	Sintering temp (^{0}C)	Stepwise increase of temp	Sintering duration (hours)	Cooling
Al#1	Zinc stearate	Ethanol	392.27 kN (40 tons)	5 min	98.07 kN (10 tons)	650	10^0C per min	5	Furnace cooling
Al#2	Zinc stearate	Ethanol	392.27 kN (40 tons)	5 min	98.07 kN (10 tons)	650	10^0C per min	5	Furnace cooling
Al#3	Zinc stearate	Ethanol	392.27 kN (40 tons)	5 min	98.07 kN (10 tons)	650	10^0C per min	5	Furnace cooling
Al#4	Zinc stearate	Ethanol	588.40 kN (60 tons)	5 min	98.07 kN (10 tons)	650	10^0C per min	5	Furnace cooling

4.5 MICROSTRUCTURAL STUDIES OF POWDER MIXTURES AND FGM BEAMS

The microstructure studies of SUS316, Al and Al_2O_3 powder and their mixtures of different composition and metallographically polished FGM beams were carried out using a JEOL JSM 6380LA scanning electron microscope (SEM). This is a high performance scanning electron microscope with a high resolution of 3 nm (Instrument database, EVISA).

4.5.1 Principle of Scanning Electron Microscope (SEM)

The scanning electron microscope (SEM) is used for analyzing the surface of the sample. This is done by irradiating the sample surface with a fine electron beam. These electrons interact with atoms in the sample, producing various signals which contain the information of surface topography of the sample (SEM A to Z, JEOL). The most common mode in SEM is detection of secondary electrons (SE) emitted by the atoms in the sample excited by the electron beam. The other different modes found in the SEM are back – scattered electrons (BEC), photons of characteristic X – ray and transmitted electrons. However secondary electrons imaging (SEI) is the most common detection mode used in the SEM in which secondary electrons are emitted from very close to the surface, hence high resolution images of the sample surface can be obtained. Whereas back – scattered electrons (BEC) are the beam electrons which are reflected from the surface of the sample. Generally the resolution of BEC images is poorer compared to SE images. BEC images are used to get the information about

distribution of various elements in the sample (Scanning electron microscope, Wikipedia).

4.5.2 Procedure for SEM analysis of powder mixtures

1. Powder mixtures of different composition of SUS316-Al_2O_3 and Al-Al_2O_3 are prepared by ball milling. A small quantity of each pure powder and powder mixtures is taken for SEM analysis.
2. A pinch of the powder is sprinkled gently with a spatula on the carbon tape stick to the stub or sample holder. Then the stub is tapped to remove the loosely held powder particles.
3. A drier is used to remove the moisture content if any and further remove any loose particles if present.
4. The stub is then kept inside the chamber for SEM analysis of the powder mixtures.

4.5.3 Procedure for SEM analysis of FGM beam samples

1) A small portion of the FGM beam sample is cut using hacksaw.
2) The sample to be polished is held in the sample holder with acrylic repair material used in dentistry.
3) The surface of the cut portion which is to be analyzed is then polished first using the grade 80 emery paper and then using the grade 1/0 emery paper for 60 min.
4) Finally after polishing the surface with emery paper, the sample is further polished in a polishing machine with an abrasive cloth with diamond polishing paste for 60 min to obtain a metallographic sample with mirror like finishing. Scratches should not be present on the surface to be analyzed.
5) The FGM beam metallographic sample is mounted on the sample holder and kept in the chamber for SEM analysis.

4.5.4 Discussion on SEM analysis of powders

The SEM micrographs of SUS316-Al_2O_3 and Al-Al_2O_3 FGM powder mixtures and FGM beam samples are discussed in the following sections separately.

4.5.4.1 SEM analysis of powders

Fig.4.13(a) shows the SEM micrograph of pure aluminium powder. From the image it can be seen that the aluminium particles are irregularly shaped with varying sizes from 6.62µm to 32.5µm. Fig.4.13(b) shows the SEM micrograph of aluminium oxide powder. This shows the flake like structure of aluminium oxide with particle size of 13.9µm to 72µm. Both the micrographs are taken at a magnification of ×750 in secondary electrons imaging (SEI) mode. Fig.4.13(c) shows the SEM micrograph of pure SUS316 powder. From the image it can be seen that the SUS316 particles are spherical in shape with varying size of powder molecules from 4.95µm to 36.6µm.

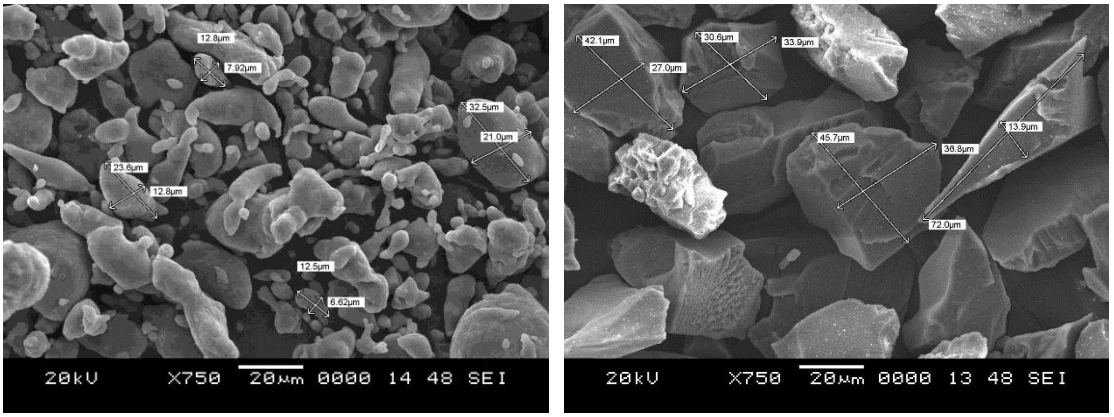

(a) (b)

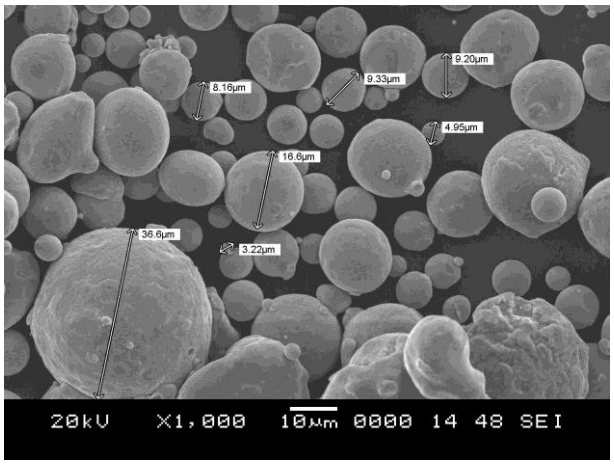

(c)

Fig.4.13 SEM micrographs of (a) aluminium powder (b) aluminium oxide (Al_2O_3) powder and (c) SUS316 powder.

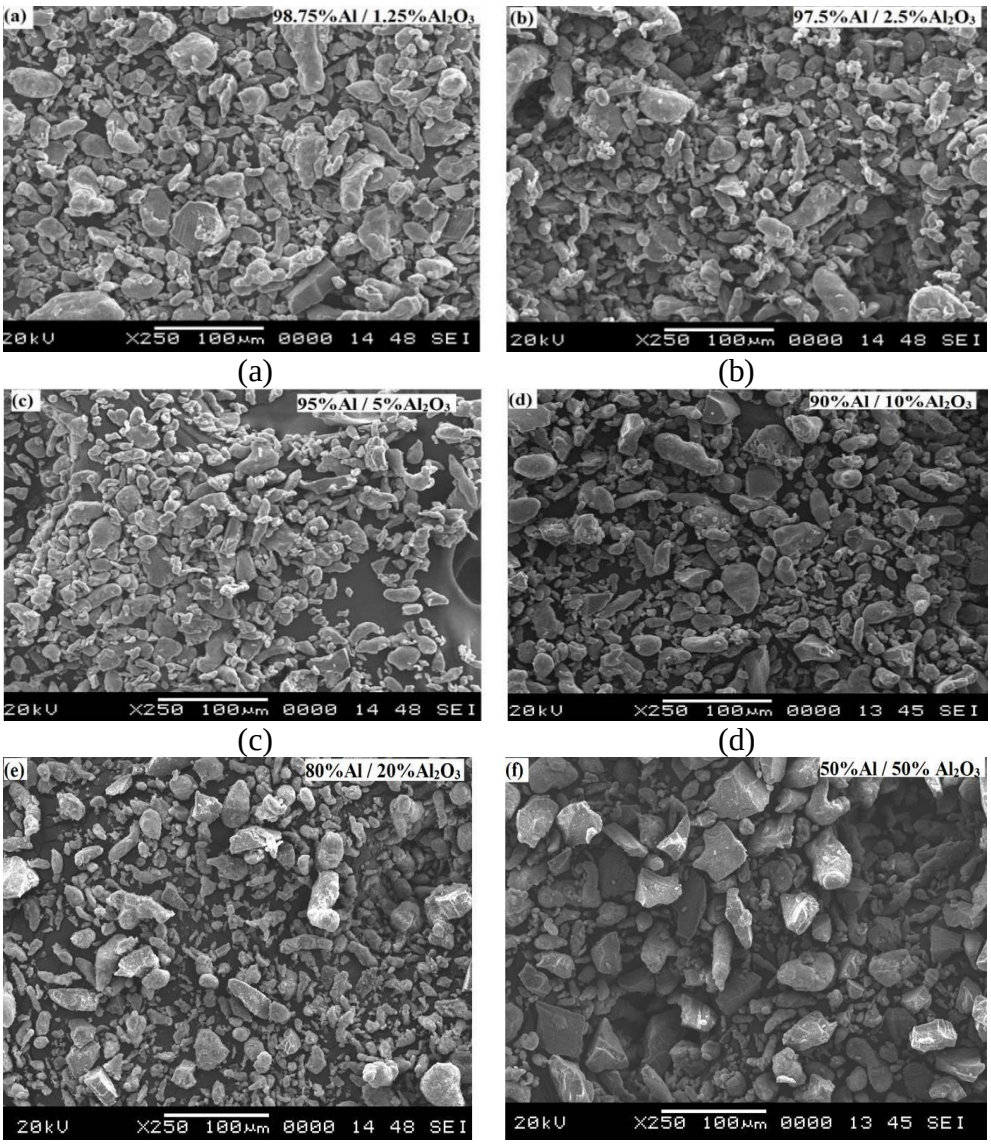

Fig.4.14 SEM micrographs of powder mixtures of different compositions (a) 98.75%Al-1.25%Al_2O_3 (b) 97.5%Al-2.5%Al_2O_3 (c) 95%Al-5%Al_2O_3 (d) 90%Al-10%Al_2O_3 (e) 80%Al-20%Al_2O_3 and (f) 50%Al-50%Al_2O_3.

Fig.4.14 shows the SEM micrographs of powder mixtures after ball milling with different composition of aluminium and aluminium oxide. The different composition of powder mixture prepared by ball milling are (a) 98.75%Al-1.25%Al_2O_3 (b) 97.5%Al-2.5%Al_2O_3 (c) 95%Al-5%Al_2O_3 (d) 90%Al-10%Al_2O_3 (e) 80%Al-20%Al_2O_3 and (f) 50%Al-50%Al_2O_3. Fig.4.15 show the SEM micrographs of SUS316-Al_2O_3 powder mixtures with composition of SUS316 and Al_2O_3 as 60:40 and 80:20. All the SEM micrographs are taken at a magnification of ×250 in secondary electrons

imaging (SEI) mode for Al-Al_2O_3 powders while x500 for SUS316-Al_2O_3 powders. SEM micrographs observation shows that as the volume fraction of the aluminium oxide is increased, more and more flake like structure appears which confirms the increase in volume fraction of aluminium oxide. Also the SEM micrographs show the uniform distribution of aluminium oxide in aluminium and SUS316 powders.

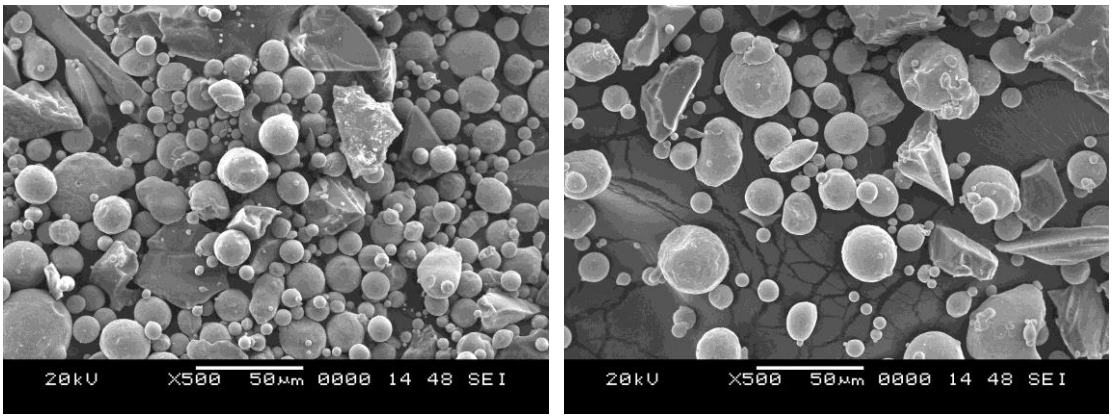

(a) 60%SUS316-40%Alumina (b)80%SUS316-20%Alumina

Fig.4.15 SEM micrographs of SUS316-Al_2O_3 powders.

4.5.4.2 SEM analysis of FGM beam samples

Fig.4.16(a) shows SEM micrograph of Al-Al_2O_3 FGM beam sample 3 along the thickness. It can be observed that the composition varies along the thickness direction. The dark spots in the micrograph correspond to aluminium oxide particles and plane area corresponds to aluminium. The micrograph is taken at a magnification of ×25 in BEC mode. The back – scattered electrons (BEC) mode is used to view the distribution of Al_2O_3 particles in powder mixture. The FGM beam sample 3 is prepared by keeping bottom layer as 100% aluminium and top layer as 50% aluminium and 50% aluminum oxide. The variation of volume fraction of aluminium oxide (ceramic) follows power law distribution with $n = 6.5$ along thickness direction. The composition of FGM beam is, bottom two layers is 100% Al, 3rd layers is 98.75% Al-1.25% Al_2O_3, 4th layer is 90%Al-10% Al_2O_3 and top layer is 50%Al-50% Al_2O_3. Fig.4.16(b) shows the interface between the 50%Al-50% Al_2O_3 and 90%Al-10% Al_2O_3 layers. The micrograph is taken at a magnification of ×250 in BEC mode. Fig.4.16(c) shows the

interface between the 90%Al-10% Al_2O_3 and 98.75%Al-1.25% Al_2O_3 layers. This micrograph is taken at a magnification of ×100 in BEC mode.

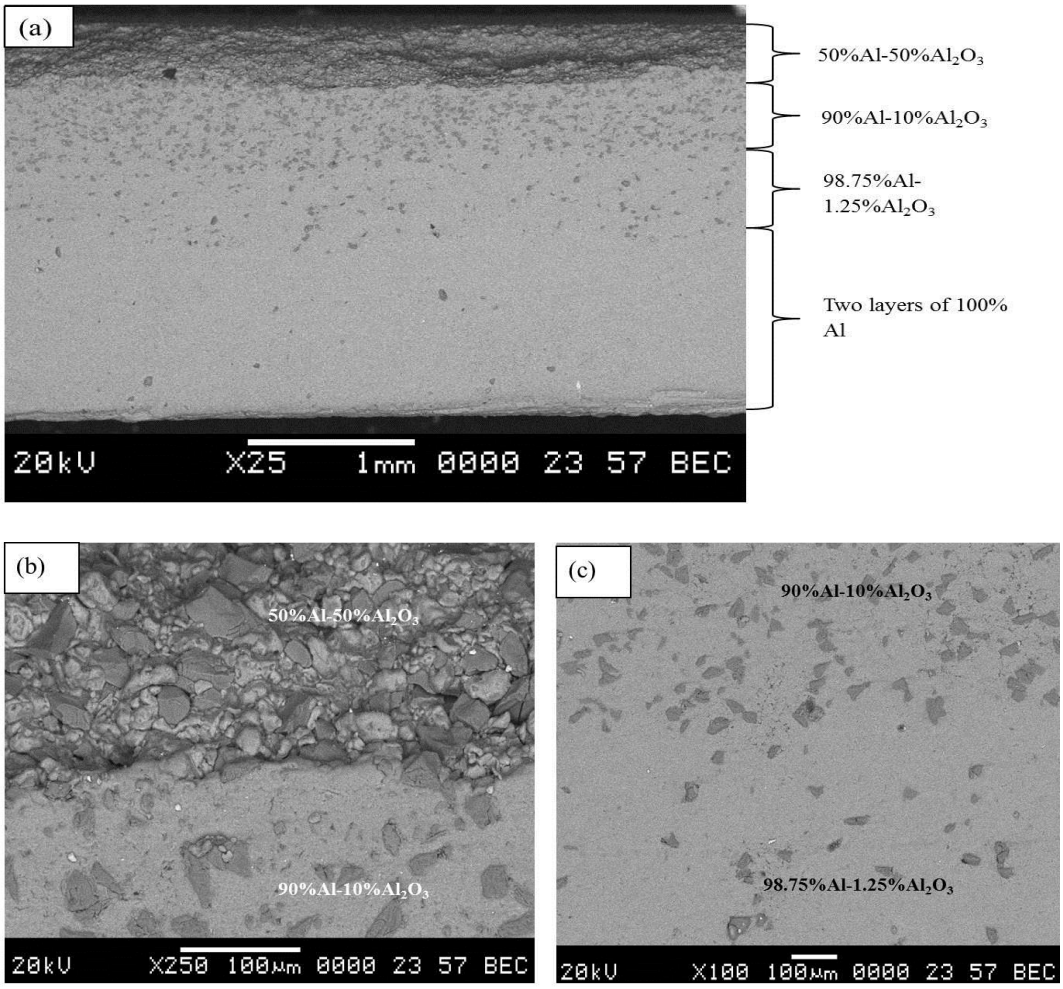

Fig.4.16 SEM micrographs of FGM beam sample no. 3 showing (a) variation of composition of Al – Al_2O_3 along thickness (b) interface of 50%Al-50%Al_2O_3 and 90%Al-10%Al_2O_3 and (c) interface of 90%Al-10%Al_2O_3 and 98.75%Al-1.25%Al_2O_3.

Fig.4.17(a) shows the SEM micrograph of FGM beam sample 10 along the thickness taken at a magnification of ×25 in BEC mode. From the micrograph it can be inferred that the composition of aluminium and aluminium oxide varies along the thickness. The dark spots in the micrograph correspond to aluminium oxide particles and plane area corresponds to aluminium. The back – scattered electrons (BEC) mode is used to view the distribution of Al_2O_3 particles in powder mixture. The FGM beam sample 10 is prepared by keeping bottom layer as 100% aluminium and top layer as 90% aluminium

and 10% aluminum oxide. The discontinuous variation of volume fraction of aluminium oxide (ceramic) is considered here.

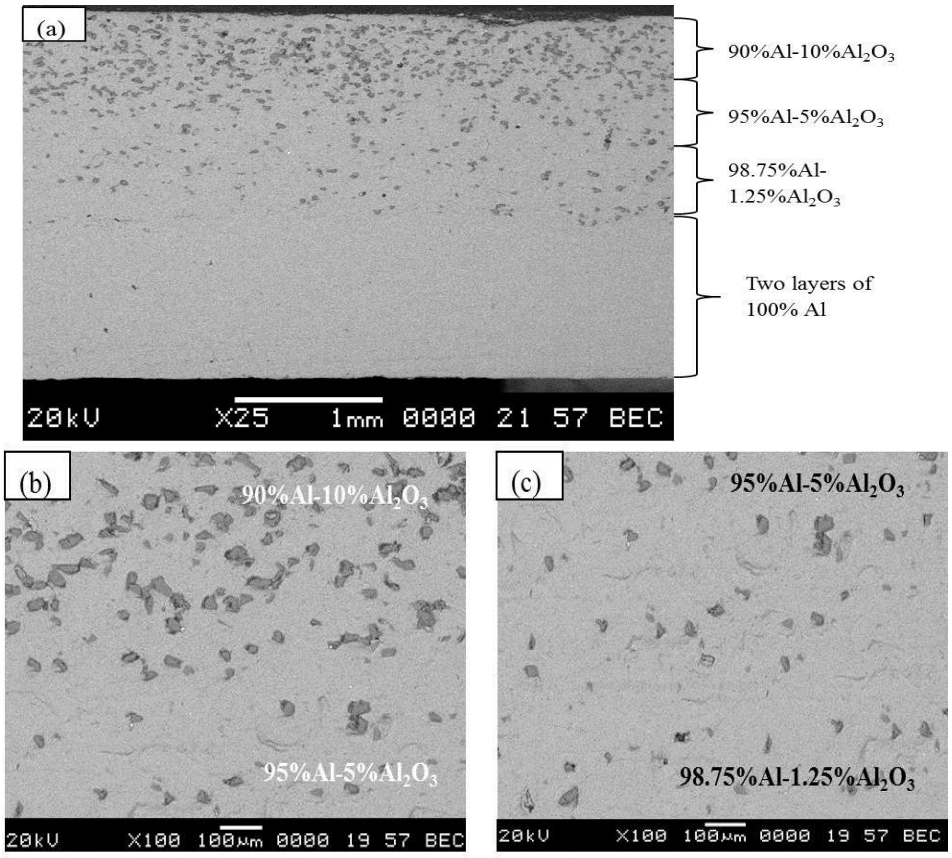

Fig.4.17 SEM micrographs of FGM beam sample no. 10 showing (a) variation of composition of Al – Al_2O_3 along thickness (b) interface of 90%Al-10%Al_2O_3 and 95%Al-5%Al_2O_3 and (c) interface of 95%Al-5%Al_2O_3 and 98.75%Al-1.25%Al_2O_3.

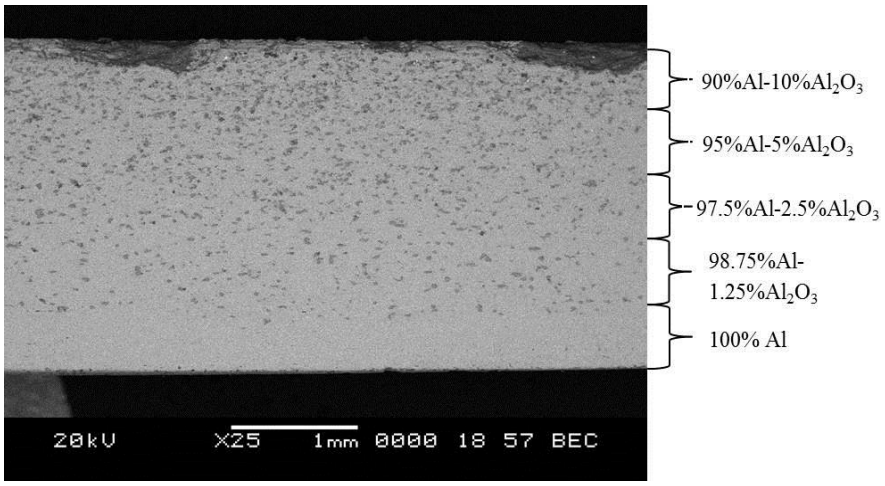

Fig.4.18 SEM micrographs of FGM beam sample no. 12 showing variation of composition of Al –Al_2O_3 along thickness.

Fig.4.17(b) shows the interface between 90%Al-10% Al_2O_3 and 95%Al-5% Al_2O_3 layers. Fig.4.17(c) shows the interface between 95%Al-5% Al_2O_3 and 98.75%Al-1.25% Al_2O_3 layers. Both the micrographs are taken at a magnification of ×100 in BEC mode. Fig.4.18 shows the SEM micrograph of FGM beam sample 12 along the thickness taken at a magnification of ×25 in BEC mode. From the micrograph it can be inferred that the composition of aluminium and aluminium oxide varies along the thickness. The dark spots in the micrograph correspond to aluminium oxide particles and plane area corresponds to aluminium. The back – scattered electrons (BEC) mode is used to view the distribution of Al_2O_3 particles in powder mixture. The FGM beam sample 12 is prepared by keeping bottom layer as 100% aluminium and top layer as 90% aluminium and 10% aluminum oxide. The discontinuous variation of volume fraction of aluminium oxide (ceramic) is considered here. From the Fig.4.18 it can be observed that, it is difficult to differentiate the interface between different layers as the composition of Al_2O_3 considered is very close to each other. However we can differentiate bottom (100%Al) and top (90%Al and 10%Al_2O_3) layers easily.

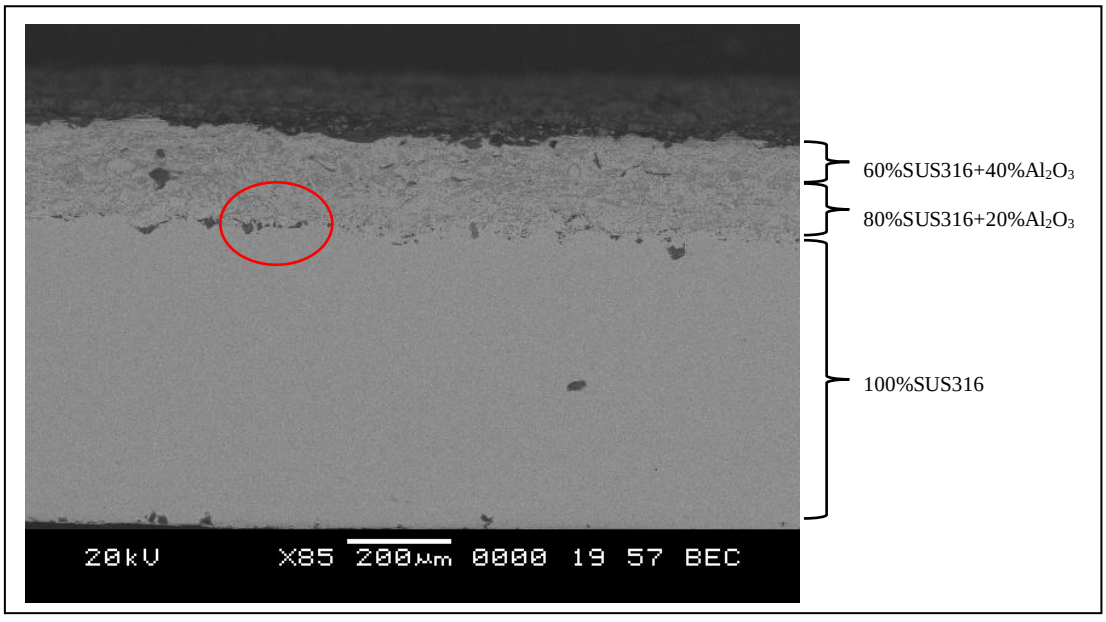

Fig.4.19 SEM micrographs of FGM beam sample no. 2 showing variation of composition of SUS316-Al_2O_3 along thickness.

Fig.4.19 shows the SEM micrographs for SUS316-Al_2O_3 FGM beam sample no.2 along the thickness taken at a magnification of ×85 in BEC mode. From the micrograph it can be inferred that the composition of stainless steel and aluminium oxide varies along the thickness. There is a good interface bonding of the FGM mixture with the SUS316 substrate with minor porosity as seen from Fig.4.20 which is the magnified view of the SEM micrograph of Fig.4.20 in the circled area. The dark spots in the micrograph correspond to aluminium oxide particles and plane area corresponds to SUS316.

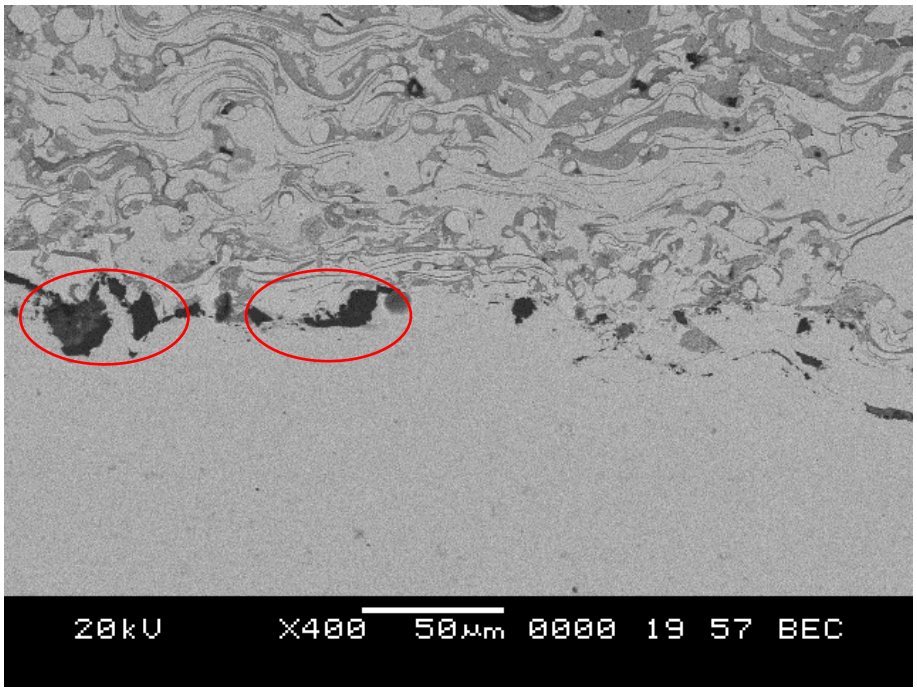

Fig.4.20 SEM micrographs of FGM beam sample no. 2 showing interface and defects of SUS316-Al_2O_3 FGM along thickness.

Fig.4.21 shows the SEM micrographs for SUS316-Al2O3 FGM beam sample no.3 along the thickness taken at a magnification of ×200 in SEI mode. From the micrograph it can be inferred that there is no good interface bonding of the FGM mixture with the SUS316 substrate with minor porosity as seen from Fig.4.22 which is the magnified view of the SEM micrograph of Fig.4.21 in the circled area.

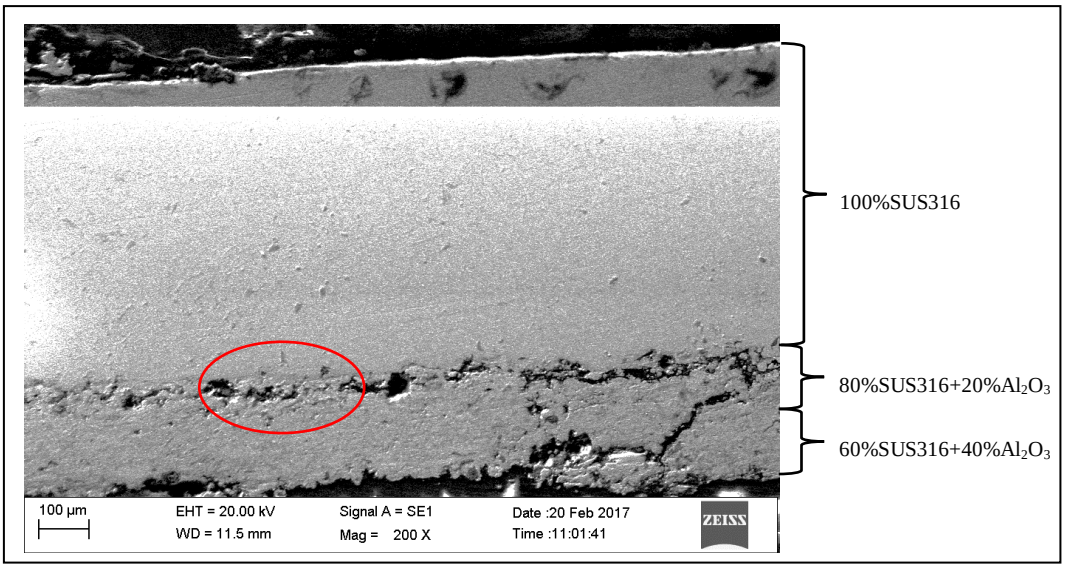

Fig.4.21 SEM micrographs of FGM beam sample no. 3 showing variation of composition SUS316-Al_2O_3 FGM along thickness.

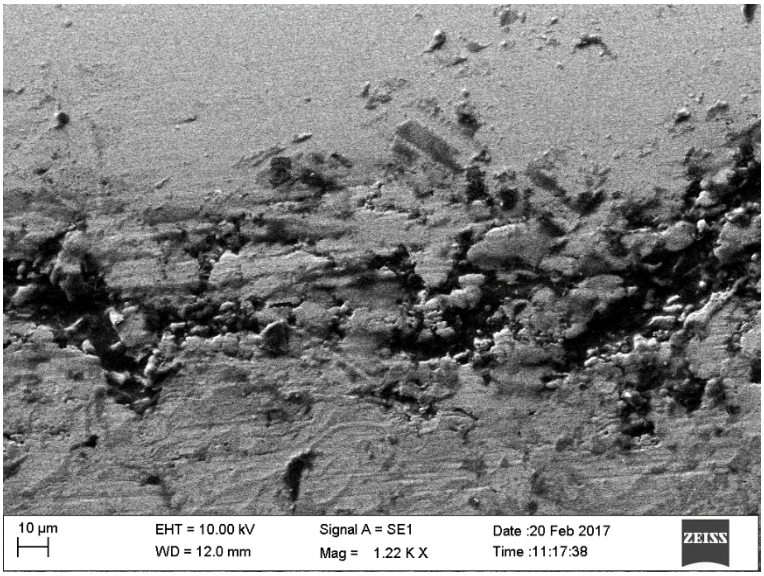

Fig.4.22 SEM micrographs of FGM beam sample no. 3 showing interface of SUS316-Al_2O_3 along thickness.

4.6 ENERGY DISPERSIVE X-RAY SPECTROMETRY (EDS) ANALYSIS

EDS makes use of the X-ray spectrum emitted by a solid sample bombarded with a focused beam of electrons to obtain a localized chemical analysis. All elements from atomic number 4 (Be) to 92 (U) can be detected in principle, though not all instruments are equipped for 'light' elements (Z < 10). Qualitative analysis involves the

identification of the lines in the spectrum and is fairly straightforward owing to the simplicity of X-ray spectra. Quantitative analysis (determination of the concentrations of the elements present) entails measuring line intensities for each element in the sample and for the same elements in calibration standards of known composition. Also, images produced by electrons collected from the sample reveal surface topography or mean atomic number differences according to the mode selected.

Fig.4.23 show the SEM-EDX with back scattered electron (BSE) image of Al-Al_2O_3 FGM beam Sample-20 and its corresponding atom profiles. As the FGM beam is made up of Al and Al_2O_3, the major contributing element is seen to be Al with 76.82% weight and next the O_2 with 13.25%. C and Fe is contributing to a total of 9.92% which are impurities in the test sample transferred during polishing of sample.

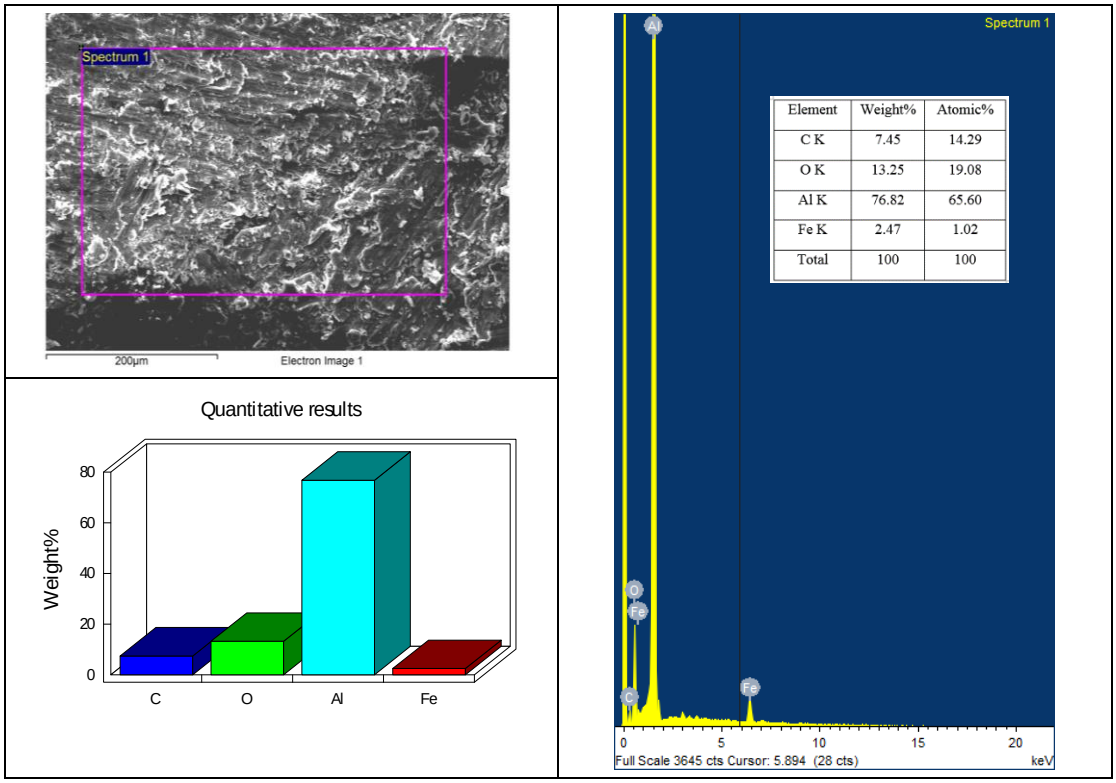

Fig.4.23 SEM-EDX of Al-Al_2O_3 FGM Sample - 20 and its corresponding atom profiles.

Fig.4.24 show the SEM-EDX image of pure Al beam Sample-4 and its corresponding atom profiles. As the beam is made up of Al, the major contributing element is seen to

be Al with 97.5% weight. Si is contributing to a total of 2.5% which is impurity in the test sample during sample polishing.

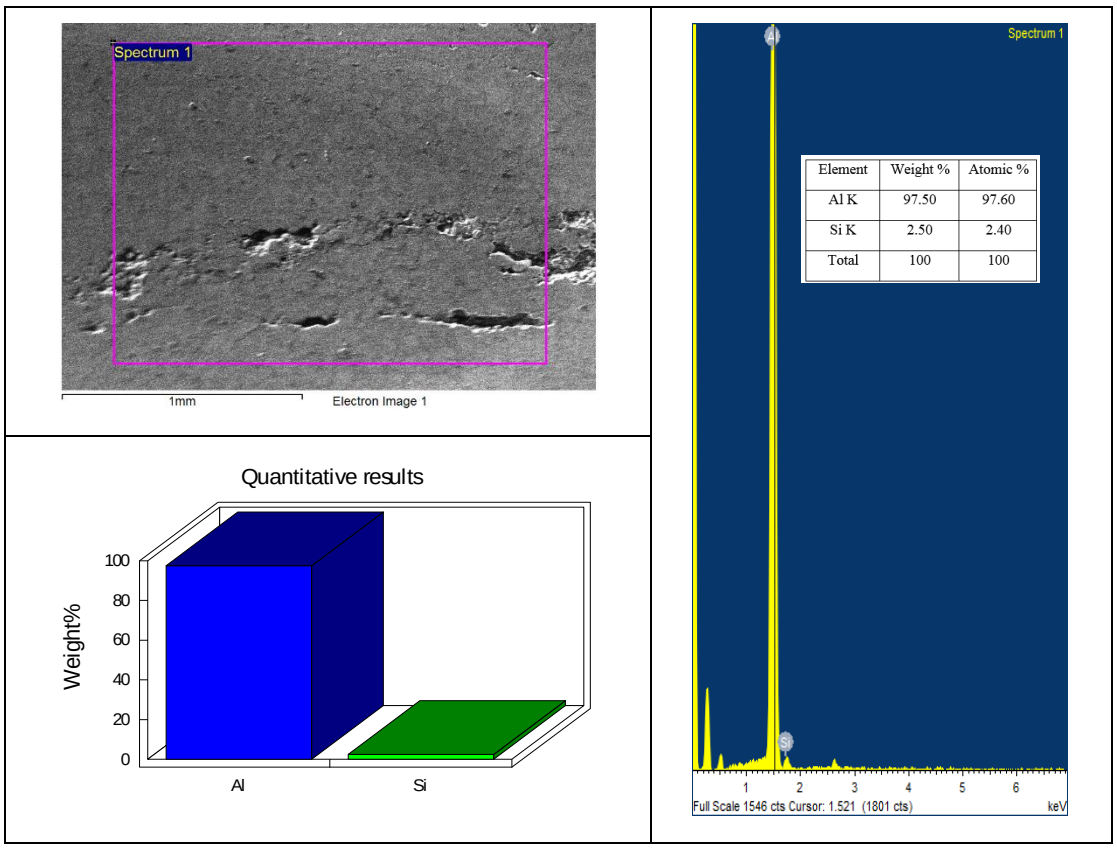

Fig.4.24 SEM-EDX of pure Al Sample - 4 and its corresponding atom profiles.

4.7 SUMMARY

Thermal spray and powder metallurgy technique was used to fabricate stainless steel-alumina and aluminium-alumina FGM beams respectively. The various steps involved in the fabrication of the FGM beam samples using thermal spray and powder metallurgy process are discussed. A brief explanation on, material selection and fabrication of die was discussed in the present chapter. The chapter described a series of attempt in producing the FGM beam sample using the powder metallurgy approach. It was found that an unconventional continuous distribution of volume fraction of alumina, deviating from power law approach was found to provide a better FGM sample. This is primarily because, as per $n = 6.5$ the volume fraction of alumina on one reference layer caused large difference in coefficient of thermal expansion, leading to failure of sample during

sintering. At the end of the chapter, microstructural studies of FGM powder mixtures and FGM beam samples were presented. SEM-EDX analysis is also presented for Al-Al_2O_3 FGM beam and pure aluminium beam sample.

CHAPTER - 5

EXPERIMENTAL VALIDATION OF STATIC DEFLECTION AND FREE VIBRATION ANALYSIS OF FUNCTIONALLY GRADED BEAMS

5.1 INTRODUCTION

From the literature review, it is understood that no results have been reported till date which concern nonlinear analysis of FGM beams accounting the vonKármán nonlinearity and its experimental validation for the static deflection and natural frequencies. This study aims to investigate the effects of the material grading index and the nonlinearity on the displacement fields under clamped-free and clamp-simple support boundary condition. A finite element FORTRAN computer code is developed to evaluate linear and nonlinear transverse deflection and natural frequency of FGM beams. The functionally graded beams synthesized in the present work, especially the one prepred by powder metallurgy process do not follow the traditional power law index. Hence they are modelled as discrete layers of varying volume fraction from 1.25% to 50%. The results are validated with the functionally graded material SUS316-Al_2O_3 coating beam with three layers fabricated using the plasma thermal spraying and Al-Al_2O_3 FGM beam manufactured using powder metallurgy process for the transverse deflection and natural frequencies under clamped-free and clamp-simple support boundary conditions. ANSYS 3D 20 noded structural solid element is used to study the role of shear deformation of the SUS316-Al_2O_3 FGM samples on displacements and natural frequencies.

5.2 EXPERIMENTAL SETUP

5.2.1 Static response measurements of FGM beam

The experimental set-up for the static load-deflection behaviour of the FGM beam samples for clamped-free boundary condition is shown schematically in Fig.5.1. The sample was loaded with a concentrated load at the free end. The deflection at the free end of the beam was measured using a laser optical displacement sensor (micro-epsilon make) with a resolution of 0.001 mm and sampling rate of 10 ms. The analog output from the sensor was communicated to the RS422 analog to digital USB converter, and was read into a computer using the NI software LABVIEW.

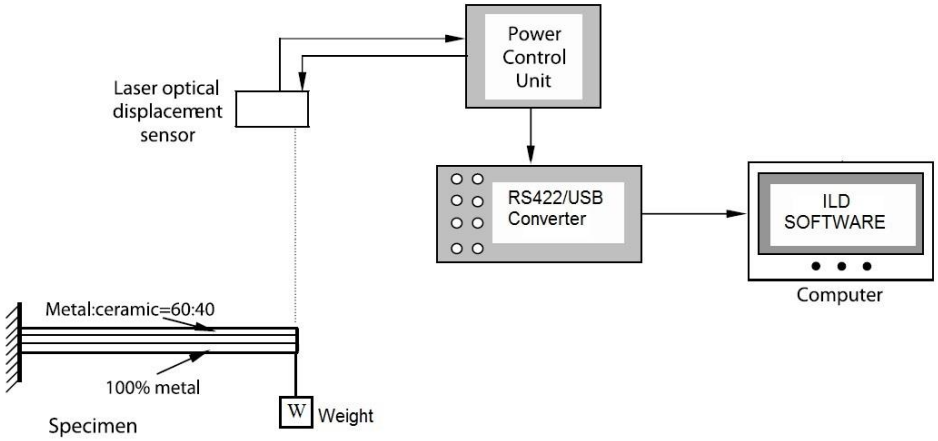

Fig.5.1 Schematic diagram of experimental set-up for static response measurement.

5.2.2 Dynamic response measurements of FGM beam

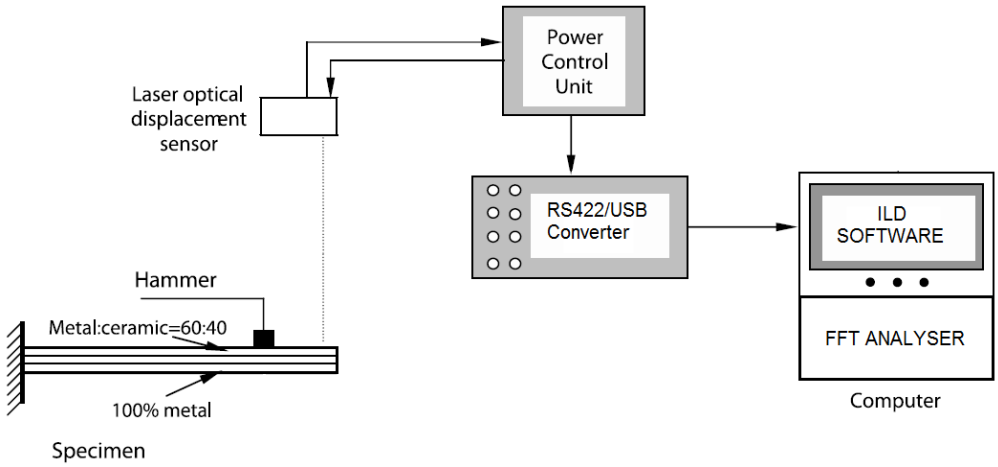

Fig.5.2 Schematic diagram of experimental set-up for natural frequency measurement.

The natural frequencies were measured for cantilever FG beam using the impact hammer testing method. The experimental setup is schematically shown in Fig.5.2. The impulse was provided with an impact hammer with steel tip. The response was measured with laser optical displacement sensor. The signal from the laser sensor was fed into a computer having LABVIEW software. The FFT of the time domain response was computed using the data processing software to obtain the frequency response. The peak locations give the natural frequencies at various modes. The detail procedure for conducting experiment and various accessories in the experimental setup is explained in detail in the APPENDIX II (refer section, II.1).

5.3 VERIFICATION OF CENTRAL DEFLECTION FOR EULER BERNOULLI BEAM

The numerical results obtained using the nonlinear finite element computer programme is verified with results presented by Arbind and Reddy (2013). The numerical exercise is for a homogeneous and functionally graded material beam of following geometric and material parameters:

E = 1.44 GPa; ν = 0:38; $h = 17.6\times10^{-6}$ m; $b = 2h$; $L = 20h$

for homogeneous beam and

E_1 = 14.4 GPa; E_2 = 1.44 GPa for functionally graded material beam.

The boundary condition considered is pinned-pinned for Euler Bernoulli (EB) beam. Sixty beam elements were used along the length and 64 layers were considered across the thickness of beam. The analytical solution, linear and the non-linear finite element solution for the maximum vertical deflection as obtained from present method and those available in Arbind and Reddy (2013) are compared in Table.6.1. The non-dimensional centre deflection values have been magnified by 1000 times ($\bar{w}\times1000$) the original values for presentation. The analytical solution for displacement of pinned-pinned beam is given as $w = 5q_0L^4/384EI$ whereas the non-dimensional deflection obtained using linear and non-linear finite element analysis for Euler Bernoulli beam is given as: $\bar{w} = wEI/q_0L^4$.

Table 5.1: Comparison of analytical and FEM solution for non-dimensional centre deflection of simply supported homogeneous beam under uniform load for EBT.

Method	EBT (Present work)	EBT (Arbind and Reddy (2013))
Analytical	1.3021	1.3021
FEM (linear)	1.3019	1.3021
FEM (Non-linear)	1.2920	1.2900

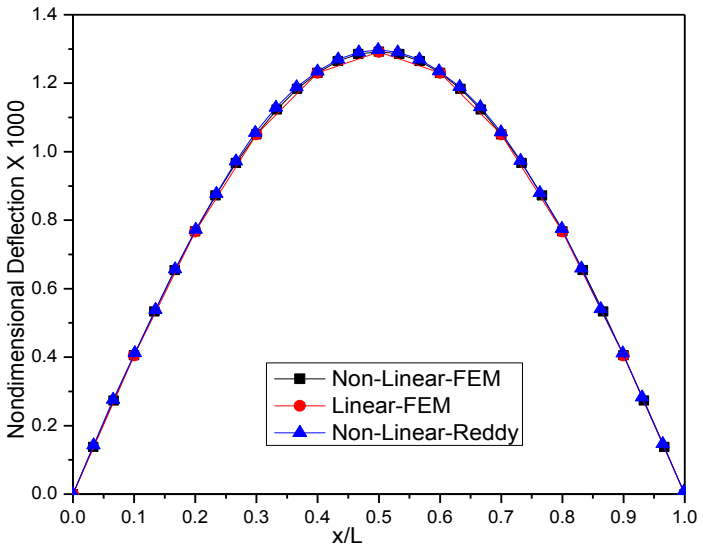

(a)

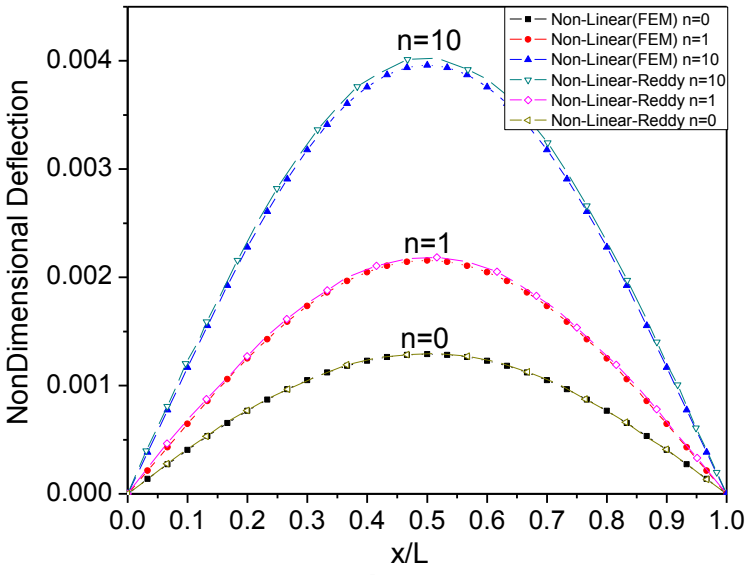

(b)

Fig.5.3 Transverse deflection versus distance along the length of a pinned–pinned Euler Bernoulli beam (a) Homogeneous (b) Functionally graded material.

The uniformly distributed load considered in the analysis is q_0=1 N/m for both linear and nonlinear analysis. It is clear from Table 5.1 and Fig.5.3(a), that the FORTRAN code developed for nonlinear formulation of Euler Bernoulli beam gives results which are in good agreement with the one given by Arbind and Reddy (2013). The non-dimensional transverse deflection obtained using non-linear Euler Bernoulli theory for functionally graded beam having power-law index of $n = 0$, $n = 1$ and $n = 10$, under uniformly distributed load, are shown in Fig.5.3(b). It has been observed that the results obtained from the computer code are in good agreement with the data given by Arbind and Reddy (2013) for various values of power law index n. For the homogenous beam, the coefficients of bending coupling matrix, B_{xx}, is negligible or zero, hence, the results from linear FEM and nonlinear FEM are identical. The same is not true for FGM beams. As the material power law index n increases beyond 1, the coefficients of nonlinear bending coupling matrix B_{xx} are considerable and effects the transverse bending of beam. Referring to Fig.5.4, there is a substantial difference between linear and non-linear transverse bending of the beam for $n = 0$, 1 and 10.

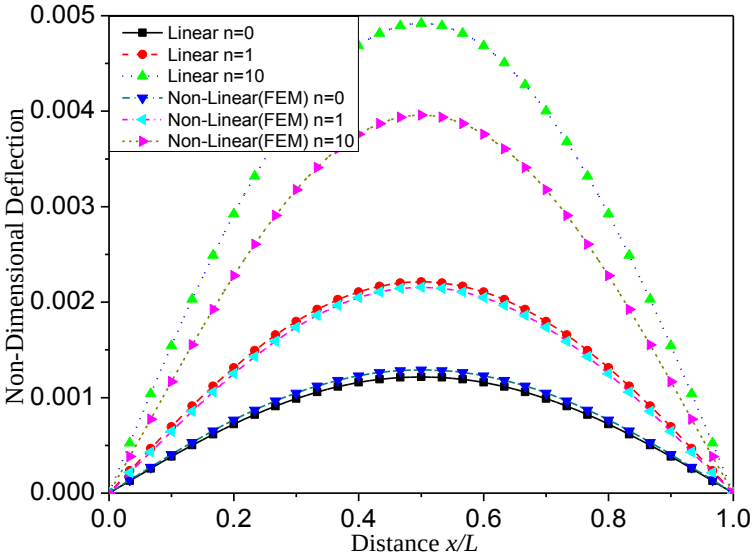

Fig.5.4 Transverse deflection versus distance along the length of a pinned–pinned Euler Bernoulli functionally graded material beam (linear and nonlinear – present method).

5.4 VALIDATION OF NON-LINEAR ANALYSIS USING EXPERIMENTAL STUDIES ON SUS316-AL_2O_3 FGM BEAM

The static deflection and free vibration response is obtained by solving linear and non-linear finite element equations and are compared with the experimental results. SUS316-Al_2O_3 functionally graded material beam with clamped free and clamp-simple support boundary condition is considered for the validation. SUS316 represent the metal and Al_2O_3 is the ceramic.

5.4.1 Calculation of density of SUS316-Al_2O_3 FGM beam sample

The material properties of the basic constituents SUS316 and Al_2O_3 of the FGM systems, considered for computing the effective properties of the layers, are referred from Mahi et al. (2010). The samples were weighed using precision balance machine of accuracy 1 mg. Volume was calculated considering average thickness of the sample and hence the densitiy, "measured density", of the samples were computed. The theoretical density of FGM beam samples is calculated using the following formulae.

$$\text{Density of FGM sample} = \frac{\text{Sum of densities of each layer}}{\text{Number of layers}} \tag{5.1}$$

Density of each layer in the SUS316-Al_2O_3 FGM beam sample is calculated using simple rule of mixture. The density of each layer of the FGM system is given by

$$\text{Density of each layer} = \rho_m V_m + \rho_c V_c \tag{5.2}$$

where ρ_m and ρ_c represents the density of metal and ceramic respectively, and V_m and V_c represents volume fraction of metal and ceramic respectively.

Table 5.2: Measured and rule of mixture theoretical densities of SUS316-Al_2O_3 FGM samples.

Sample No.	Density kg/m^3		% error
	Measured (Mass/Volume)	Theoretical (Eq.5.1)	
1	7285	7725	5.69
2	7315	7725	5.31
3	7250	7725	6.15
4	7111	7535	5.96

The average densities of the samples computed using the rule of mixture and their corresponding measured densities are listed in Table 5.2. It is observed that the measured densities differ from the theoretical densities by a maximum of 6.15% for sample 3. This difference in the densities may be due to porosity in the samples or non-uniform spraying of FG material which will be discussed in detail in section 6.5.1.

5.4.2 Transverse bending of SUS316-Al_2O_3 FGM beam

The static bending response of the cantilever FGM beam samples under a concentrated load W at the tip, is predicted using the linear and non-linear finite element formulation. Fig.5.5 shows the experimental setup for measuring the transverse bending of cantilever beam. The full length of the beam was discretized using 60 elements of equal length.

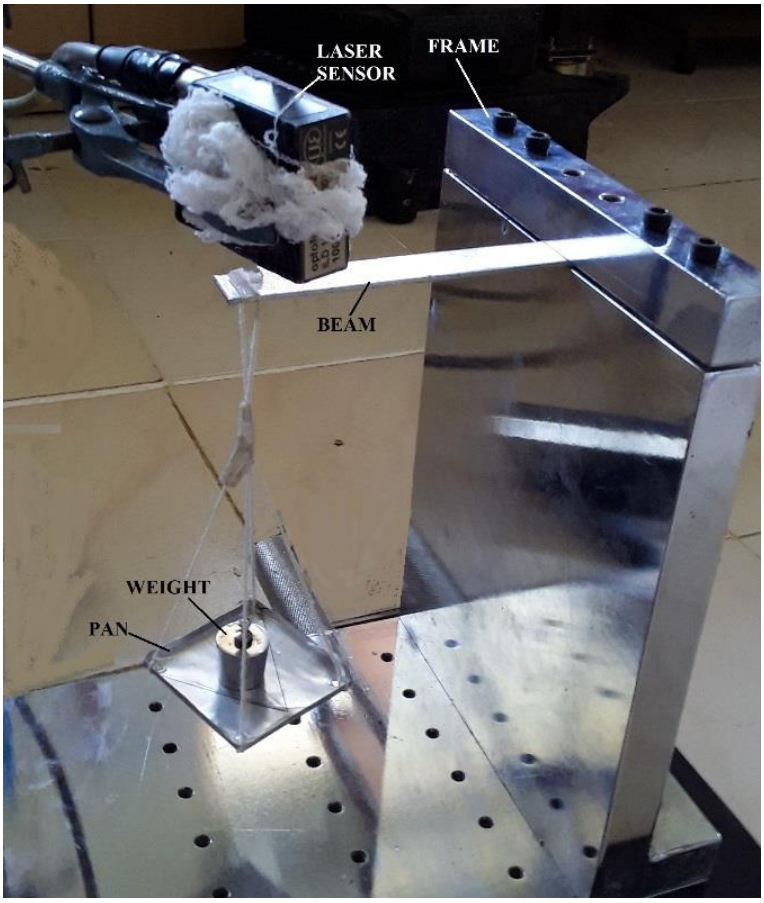

Fig.5.5 Experimental setup for transverse bending analysis of cantilever beam.

Theoretically predicted maximum deflection for pure SUS316 beam sample using linear and nonlinear finite element program are presented in Table 5.3. Three FGM

samples of the three-layer SUS316-Al_2O_3 beam and one SUS316 beam coated with 100% Al_2O_3 are considered in the study. Table.6.3 also makes a comparison of numerical results with the experimental results.

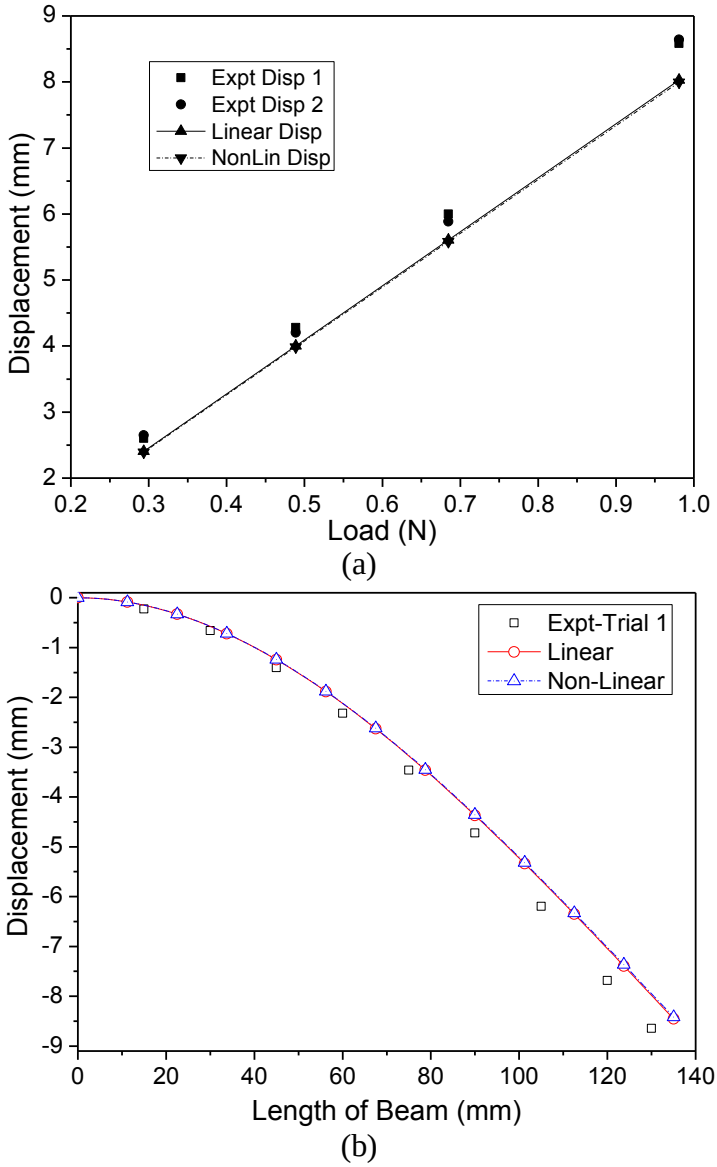

Fig.5.6 Theoretical and experimental (a) deflection v/s load plot and (b) static deflection profile for 0.981 N tip load on pure SUS316 beam (sample-9) under clamp free boundary condition.

The comparison of theoretical and experimental deflection is shown in Fig.5.6 to Fig.5.10 for commercially available SUS316 beam (sample 9) and all the four FGM beam samples. Considering the samples synthesized, it is noted that the linear and nonlinear deflection results deviate more or less equally with respect to experimental

deflections for the FGM beam samples 1, 3, 4 and pure SUS316 sample 9. Higher error of 10-13% is observed for FGM beam sample 2. The difference between the theoretical and the experimental results may be due to porosity which may exist due to the uneven spraying of powder on the samples, imperfect bonding between the adjacent layers (refer Fig.4.19 and Fig.4.21), and the error in maintaining constant thickness for all layers. It is also observed that the percentage error decreases with increase in the load at the tip of the beam. The FGM beams used in the analysis is fabricated with three discrete layers. The error can be further reduced if the numbers of layers are increased to reduce material discontinuity and achieve smooth gradation in FGM beam.

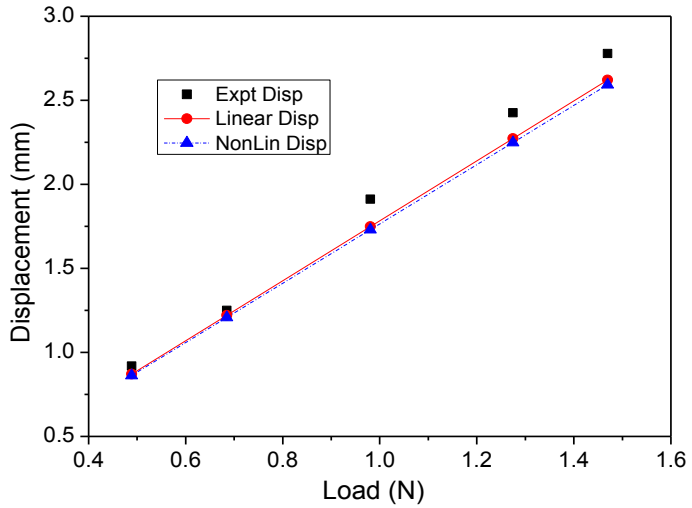

(a)

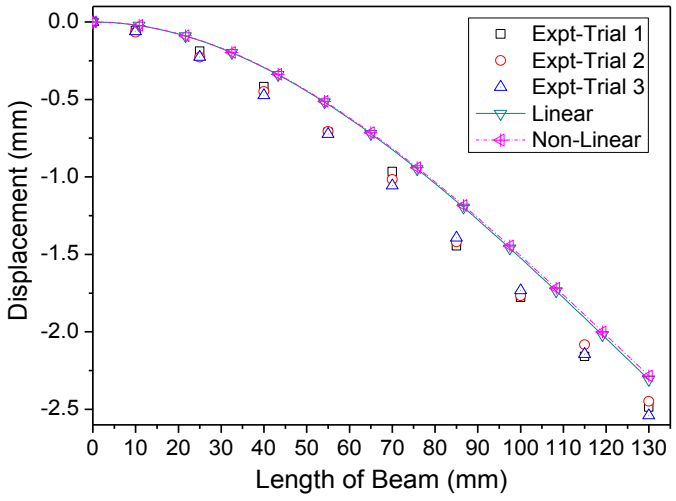

(b)

Fig.5.7 Theoretical and experimental deflection v/s load plot (a) and static deflection profile at 1.275 N tip load (b) for SUS316-Al_2O_3 FGM beam (sample-1) under clamp free boundary condition.

Table 5.3: Theoretical and experimental tip deflection for clamped-free SUS316-Al_2O_3 FGM and pure SUS316 beam samples.

Sample No.	Load "W" (N)	Theoretical deflection at tip (mm)		Experimental deflection at Tip (mm)	% Error in the results	
		Nonlinear EBT	Linear EBT		Nonlinear	Linear
1	1.280	2.2485	2.2726	2.425	7.30	6.31
1	1.469	2.5923	2.6202	2.778	6.68	5.68
2	0.549	2.6078	2.6095	2.891	9.79	9.73
2	0.981	8.7082	8.7141	9.998	12.91	12.85
3	0.981	5.4696	5.4681	5.700	4.05	4.07
3	1.469	8.1947	8.1923	8.5725	4.41	4.44
4	0.981	3.7089	3.6627	3.8978	4.85	6.03
4	1.469	5.5567	5.4875	5.8147	4.44	5.63
9	0.488	3.9842	4.0006	4.2822	6.96	6.57
9	0.981	7.9969	8.0299	8.5843	6.84	6.46

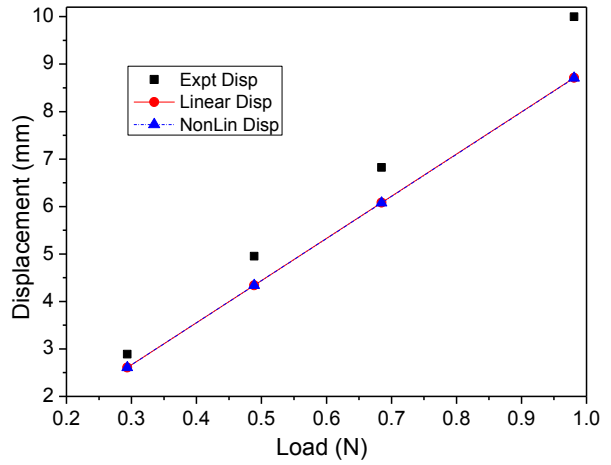

(a)

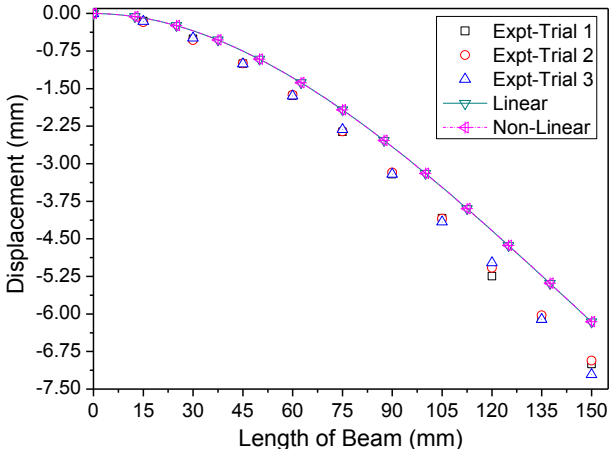

(b)

Fig.5.8 Theoretical and experimental deflection v/s load plot (a) and static deflection profile at 0.685 N tip load (b) for SUS316-Al_2O_3 FGM beam (sample-2) under clamp free boundary condition.

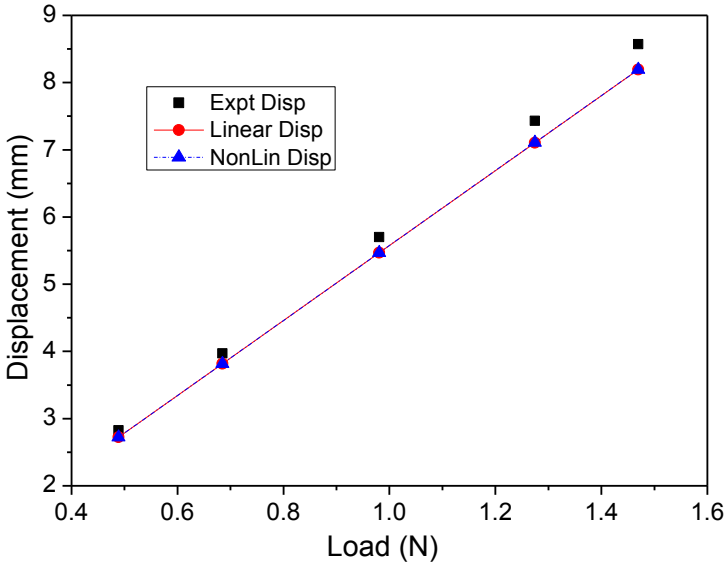

(a)

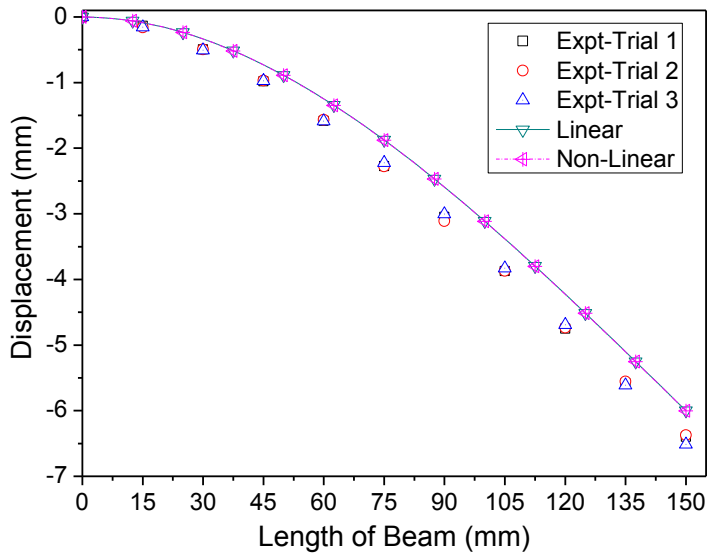

(b)

Fig.5.9 Theoretical and experimental deflection v/s load plot (a) and static deflection profile at 1.275 N tip load (b) for SUS316-Al_2O_3 FGM beam (sample-3) under clamp free boundary condition.

Fig.5.11 shows the experimental setup for transverse bending analysis of clamp-simple support beam. Fig.5.12 and Fig.5.13 show the comparison of theoretical and experimental deflection for SUS316-Al_2O_3 FGM beam sample 1 and 3 respectively. As tabulated in Table 5.4, the error range is 13-18% for FGM sample-1 while the error is

less than 10% for FGM sample 3. The error is greater when compared to clamp free boundary condition.

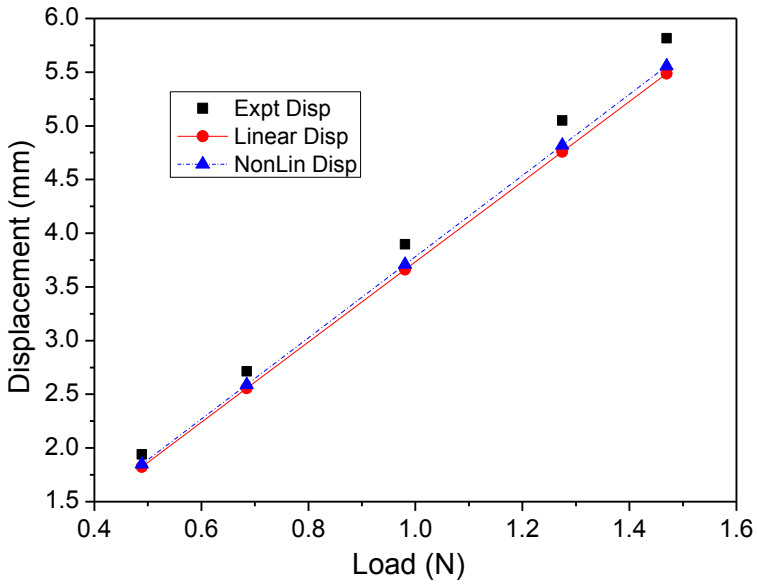

(a)

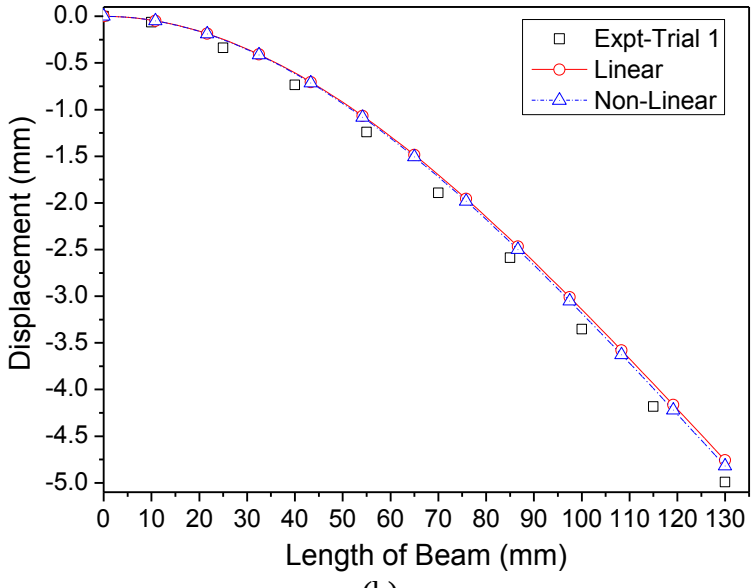

(b)

Fig.5.10 (a) Deflection v/s load plot and (b) static deflection profile for 0.981 N tip load on SUS316-Al_2O_3 FGM beam (sample-4) under clamp free boundary condition.

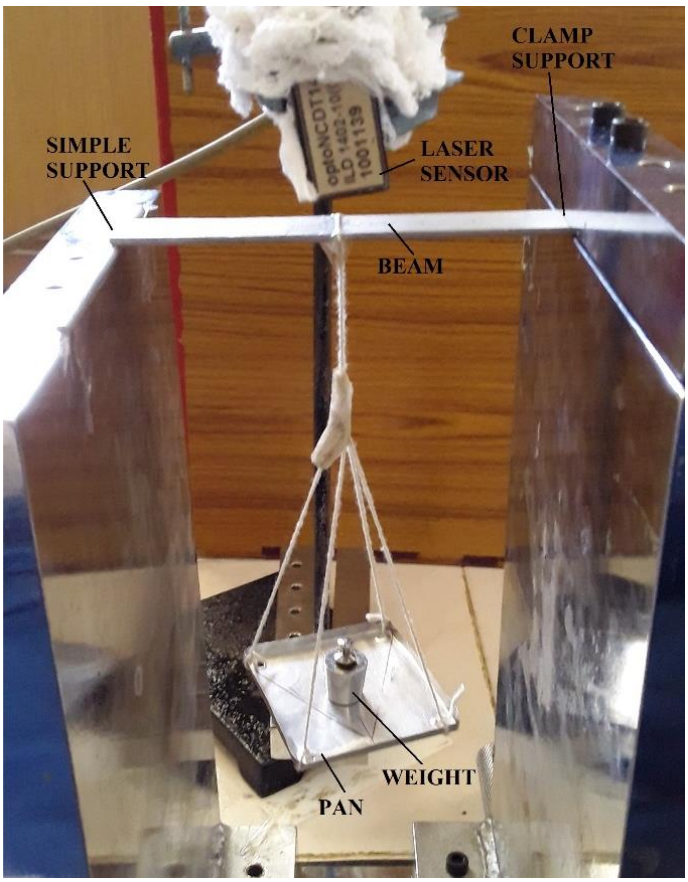

Fig.5.11 Experimental setup for transverse bending analysis of clamp-simple support beam.

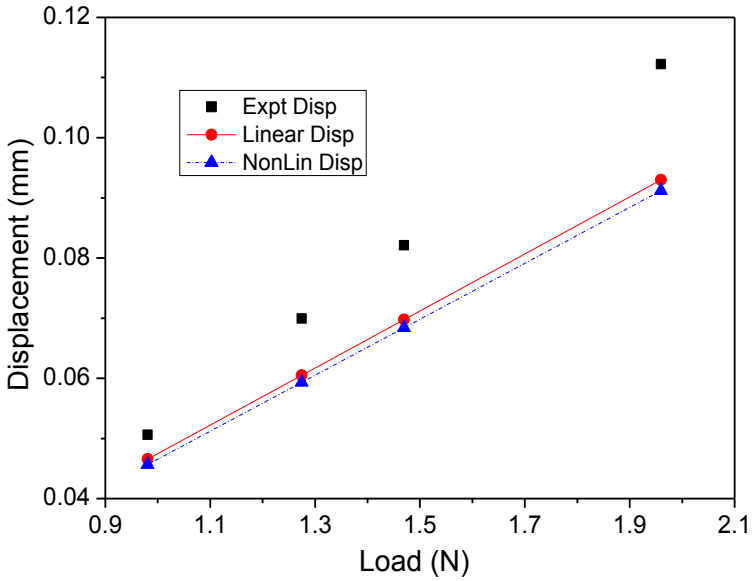

Fig.5.12 Deflection v/s load plot for SUS316-Al_2O_3 FGM beam (sample-1) under clamp-simple support boundary condition.

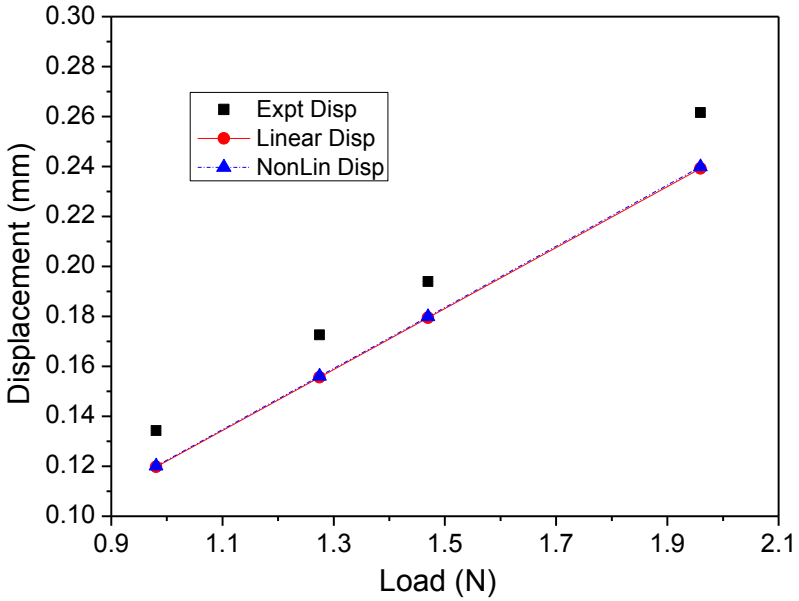

Fig.5.13 Deflection v/s load plot for SUS316-Al_2O_3 FGM beam (sample-3) under clamp-simple support boundary condition.

Table 5.4: Theoretical and experimental tip deflection for clamped-simple support SUS316-Al_2O_3 FGM beam samples.

Sample No.	Load "W" (N)	Theoretical deflection at tip (mm)		Experimental deflection at tip (mm)	% Error in the results	
		Nonlinear EBT	Linear EBT		Nonlinear	Linear
1	1.2746	0.05931	0.06049	0.06995	15.21	13.52
1	1.9594	0.09118	0.09299	0.11224	18.76	17.15
3	1.2746	0.15604	0.15561	0.17256	9.58	9.83
3	1.9594	0.23988	0.23922	0.26159	8.30	8.55

5.4.3 Free vibration response of SUS316-Al_2O_3 FGM beam

The cantilever beam is discretized with 60 equal-size elements to obtain converged finite element solution for natural frequencies. The test setup for free vibration response of clamp-free beam is shown in Fig.5.14. The predicted natural frequencies ω_n for first mode are compared with the experimental results for the three-layer SUS316-Al_2O_3 beams under cantilever boundary condition.

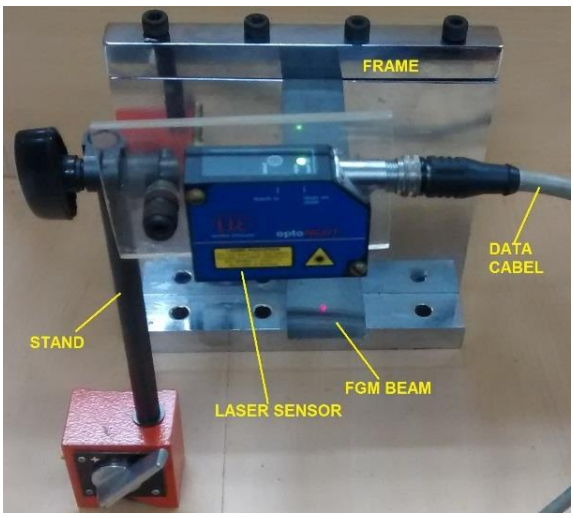

(a)

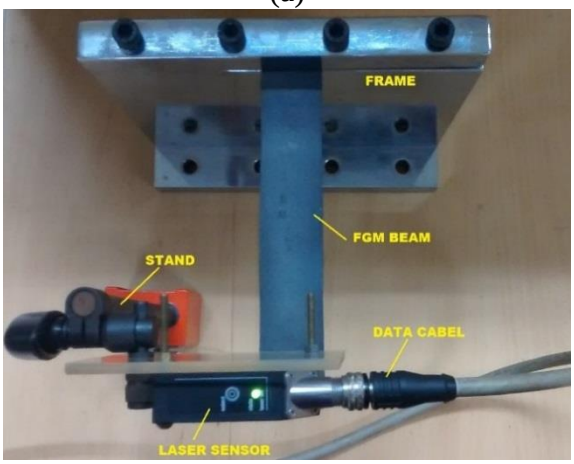

(b)

Fig.5.14 Experimental Setup for free vibration analysis (a) View at 30^0 to vertical (b) View from top.

The general solution provided in equation (Eq.3.70) is without considering damping which is not the practical case. When a beam is subjected to initial displacement, the beam will start vibrating and will come to rest after some time due to resistance offered by air and structural damping. If damping is considered, the finite element equation (Eq.3.70) can be expressed in the standard form as

$$\begin{bmatrix} \mathbf{M}^{11} & \mathbf{M}^{12} \\ \mathbf{M}^{21} & \mathbf{M}^{22} \end{bmatrix} \begin{Bmatrix} \ddot{\mathbf{U}} \\ \ddot{\mathbf{W}} \end{Bmatrix} + \begin{bmatrix} \mathbf{C}^{11} & 0 \\ 0 & \mathbf{C}^{22} \end{bmatrix} \begin{Bmatrix} \dot{\mathbf{U}} \\ \dot{\mathbf{W}} \end{Bmatrix} + \begin{bmatrix} \mathbf{K}^{11} & \mathbf{K}^{12} \\ \mathbf{K}^{21} & \mathbf{K}^{22} \end{bmatrix} \begin{Bmatrix} \mathbf{U}^{1} \\ \mathbf{W}^{2} \end{Bmatrix} = \begin{Bmatrix} \mathbf{F}^{1} \\ \mathbf{F}^{2} \end{Bmatrix} \tag{5.3a}$$

where, $\mathbf{C}$ is the damping matrix consisting of only diagonal elements ζ. The value of damping coefficient, ζ, is obtained from the experimental studies. The value of ζ

is calculated by taking the logarithmic decrement of free vibration response of the beam sample. The logarithmic decrement is given as

$$\frac{1}{n}\log_e \frac{x_0}{x_n} = \frac{2\pi\zeta}{\sqrt{1-\zeta^2}} \tag{5.3b}$$

where, x_0 and x_n refer to the amplitude of the vibration at time, $t = 0$ and $t = t_n$ respectively. The damping coefficient is calculated at 2 to 3 different location on the displacement history curve. The average value of the damping coefficient are 0.0055, 0.0035 and 0.0025 for sample 1, 2 and 3 respectively. These values of the damping coefficient ζ are used in the theoretical analysis to obtain the damped response. The free vibration response and the corresponding fast Fourier transform for sample 1 is presented in Fig.5.15 while the free vibration response and the corresponding fast Fourier transform for sample 2 and 3 are presented in APPENDIX-III, Fig.III.1 and Fig.III.2 respectively.

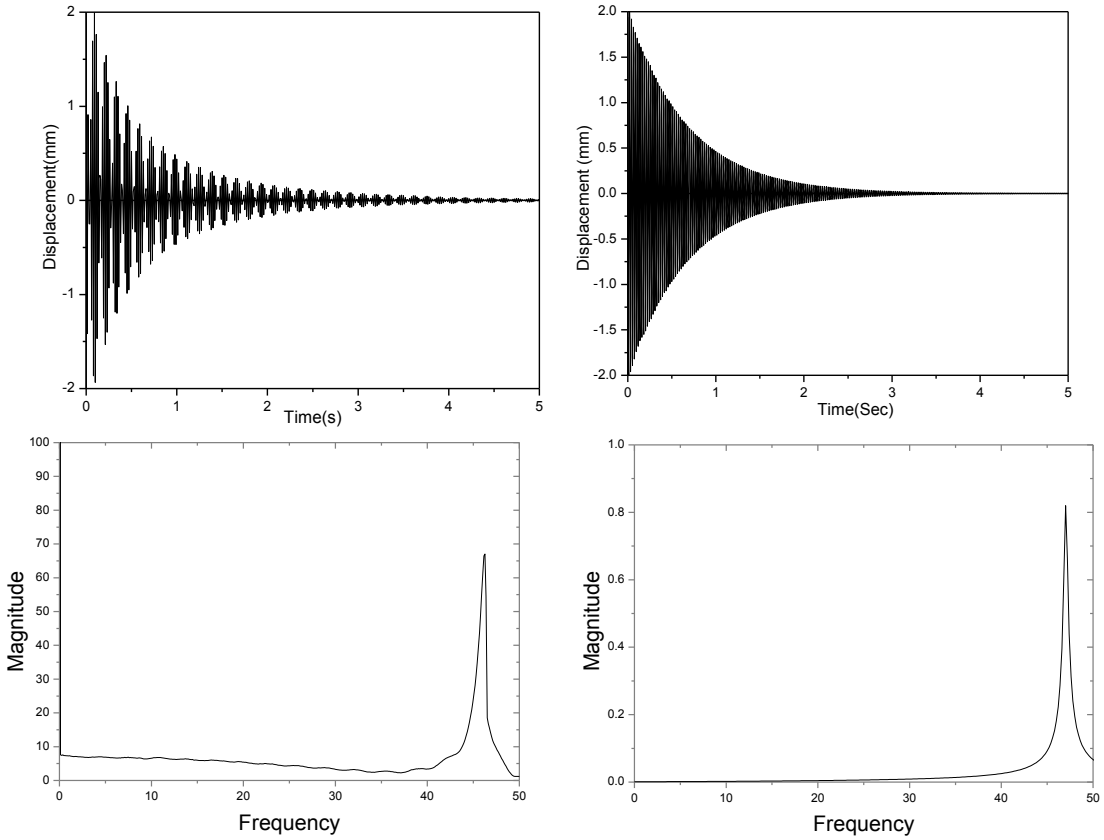

Experimental - 46.307 Hz (b) Theoretical - 47.27Hz

Fig.5.15 Natural frequencies of three-layer SUS316-Al_2O_3 FGM beams under cantilever boundary condition – Sample 1.

Theoretical and experimental damped natural frequencies for SUS316-Al_2O_3 FGM beam samples under clamped-free boundary condition are presented in Table 5.5. It can be seen from Table 5.5 that the present non-linear beam model in conjunction with the rule of mixture with the experimentally determined value of damping ratio ζ predicts the fundamental natural frequency of three-layer SUS316-Al_2O_3 beams reasonably well for the cantilever boundary condition. The higher value of error for sample 2 may be due to imperfect bonding between adjacent layers, distribution of material in the layers is largely different from the assumed uniform material distribution and thickness assumed in the analysis. Natural frequencies are also tabulated for sample 4 where in 100% Al_2O_3 is sprayed on base substrate of SUS316. The comparison of linear and nonlinear frequencies using EBT are also given in Table 5.5. It is observed that for the present volume fraction of the FGM (refer Table 4.1), the difference between linear and nonlinear frequencies is minimal. The free vibration response was also measured using 1.9 gm general purpose Kistler 8730A500 accelerometer (refer APPENDIX-II (II.1i) for more details) with sensitivity of 10 mV/g for sample-1. It was observed that there is reduction in the frequency from 46.46 Hz to 39.95 Hz due to added weight of the accelerometer and resistance offered by the accelerometer cable hanging from the tip of the beam. Table 5.6 gives the percentage deviation in displacement at chosen time between theoretical and experimental data for SUS316-Al_2O_3 FGM beam samples under clamped-free boundary condition. It can be inferred from Table 5.6 that the calculated average value of damping ratio, ζ, from experimental displacement history plot closely predicts the damped vibrations of the beam with maximum error of 9%.

To verify the effectiveness in using nonlinear Euler-Bernoulli beam theory, the frequency validation for the FGM samples were carried out using ANSYS R15. An APDL (ANSYS Parametric Design Language) code is developed for FGM material. 3D structural SOLID186 element was used for the analysis. 8-10 layers were considered across the thickness for discretising the depth of the beam. For sample 1 and 3 the number of layers considered were 10 and for sample 2 the number of layers were 8. The first 3 modes are evaluated. As tabulated in Table 5.5, it was observed that the fundamental frequency predicted by 3D solid element is very much close to the experimental frequency.

Table 5.5: Theoretical and experimental damped natural frequencies for a clamped free SUS316-Al_2O_3 FGM beam samples.

Sample No.	No. of layers	Theoretical frequency (Hz)		3D ANSYS frequency (Hz)	Experimental frequency (Hz)			Average % error (NL EBT v/s Expt.)
		Non-linear EBT	Linear EBT		Trial 1	Trial 2	Trial 3	
1	3	47.27	47.38	46.76	46.307	46.458	46.236	2.02
2	3	25.35	25.42	25.57	22.209	22.185	22.135	14.31
3	3	26.07	26.13	25.94	25.003	24.988	25.014	4.27
4	2	37.92	38.12	39.15	34.427	34.486	34.510	9.99

Table 5.6: Deviation in displacement as function of time for SUS316-Al_2O_3 FGM beam samples - Theoretical and experimental for clamped-free boundary condition.

Sample No.	Time (s)	Theoretical displacement (mm)	Experimental displacement (mm)	% error in displacement
1	1	0.4641	0.4390	5.71
	2	0.1062	0.1168	-9.13
2	2	1.3300	1.2224	8.80
	6	0.3074	0.2995	2.63
3	2	0.4859	0.4847	0.26
	6	0.1324	0.1288	2.71

The detail mode shapes are given in Fig.5.16, Fig.5.17 and Fig.5.18 for sample 1, 2 and 3 respectively. Table 5.7 presents the theoretical second mode damped frequencies for SUS316-Al_2O_3 FGM beam samples for clamped-free boundary condition. It is observed that the theoretically calculated frequencies using linear and nonlinear finite element code are close to the frequencies calculated with ANSYS using 3D solid element. As seen from Fig.5.16 and Fig.5.18, the third mode for sample 1 and 3 was observed to be a twisting mode. This suggests that shear effects need to be taken into account in the non-linear finite element formulation. For the three FGM samples, the mode shapes have been compared in Table 5.8.

Table 5.7: Theoretical damped frequencies (second mode) for SUS316-Al_2O_3 FGM beam samples for clamped-free boundary condition.

Sample No.	No. of layers	Theoretical frequency (Hz)		3D ANSYS Frequency (Hz)
		Non-linear EBT	Linear EBT	
1	3	296.37	296.86	292.67
2	3	159.13	159.30	160.19
3	3	163.53	163.73	162.45
4	2	237.77	238.87	245.11

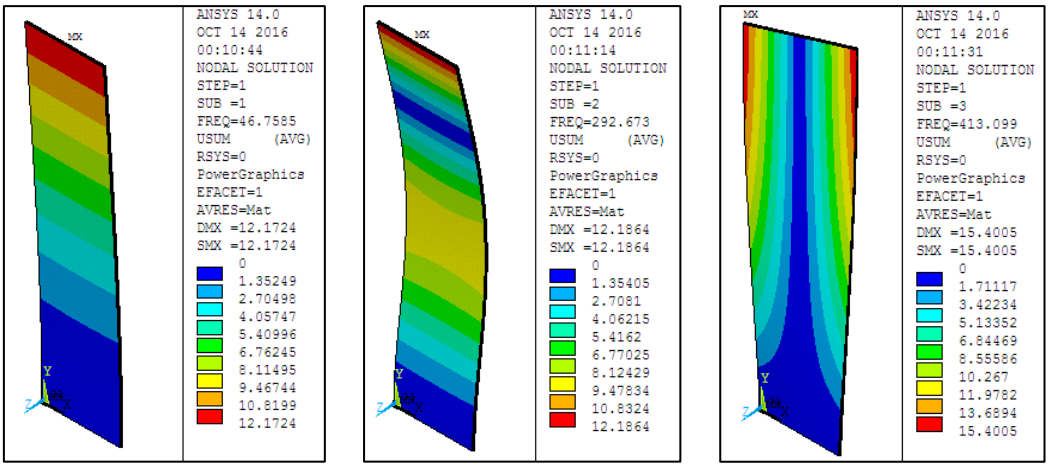

First mode- 46.7585Hz Second mode – 292.67Hz Third mode – 413.09Hz

Fig.5.16 Mode shapes for SUS316-Al_2O_3 FGM sample-1 in ANSYS.

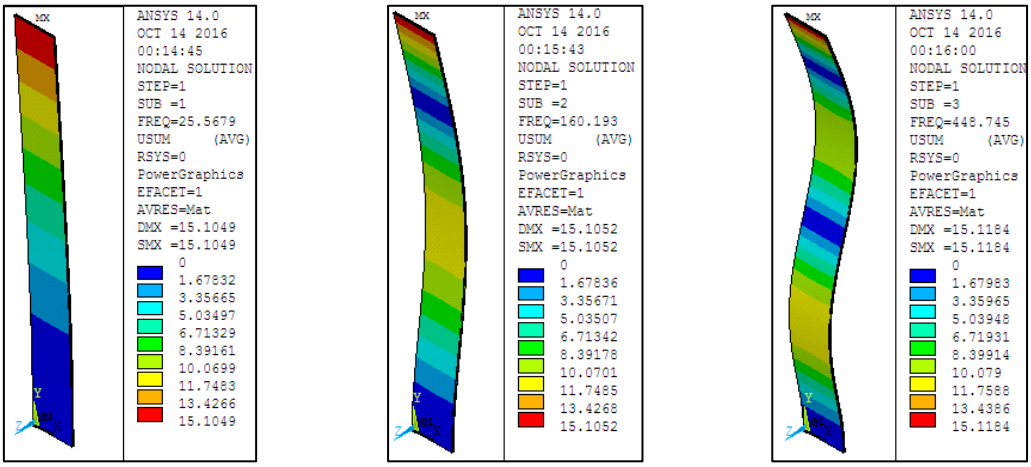

First mode- 25.57Hz Second mode -160.19Hz Third mode -448.74Hz

Fig.5.17 Mode shapes for SUS316-Al_2O_3 FGM sample-2 in ANSYS.

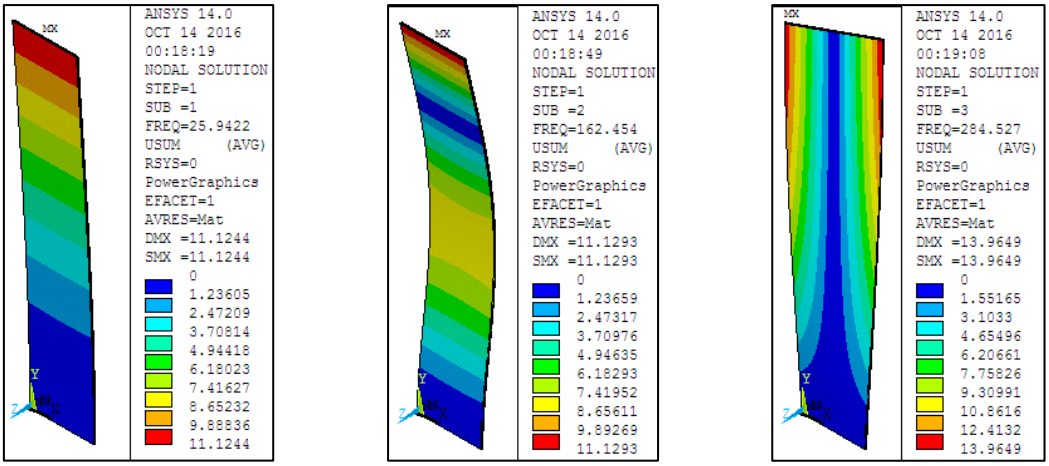

First mode- 25.94Hz Second mode -162.45Hz Third mode -284.52Hz

Fig.5.18 Mode shapes for SUS316-Al_2O_3 FGM sample-3 in ANSYS.

Table 5.8: Details of the mode shapes obtained from ANSYS.

Sample No.	"*b/h*" Ratio	Mode-1	Mode-2	Mode-3
1	32.8	Bending	Bending	Twisting
2	21.9	Bending	Bending	Bending
3	35.7	Bending	Bending	Twisting

5.5 STATIC DEFLECTION AND FREE VIBRATION ANALYSIS OF AL-AL_2O_3 FGM BEAM AND ALUMINIUM BEAM SAMPLES – THEORETICAL ANALYSIS AND EXPERIMENTAL VALIDATION

The details of the five layer FGM samples which are considered for free vibration experiment are detailed here. The material properties of the basic constituents Al and Al_2O_3 of the FGM system, considered for calculating effective properties of the layers, are listed in the Table 5.9.

Table 5.9: Material properties of the Al and Al_2O_3.

Properties	Unit	Aluminium (Al)	Alumina (Al2O3)
Young's modulus, E	GPa	69	320
Density, ρ	kg/m^3	2698	3750
Poisson's ratio, ν	-	0.33	0.26

The layer-wise material composition of Al-Al_2O_3 FGM samples selected for conducting free vibration experiment whose natural frequency is to be determined is given in the Table 5.10. The discontinuous variation of volume fraction of aluminium and alumina is considered for the FGM samples. The discrete layers have varying volume fraction of Al_2O_3 from 1.25% to 20%. The dimensions of pure aluminium and Al-Al_2O_3 FGM beam samples used in free vibration experimental setup for clamped free boundary condition are given in the Table 5.11. One end of the sample is clamped to the support stand. Now the length is measured from the clamped edge to the free end of the beam is referred to as effective length of the sample. Average thickness is the average of thickness of the beam sample measured at 5 different locations using vernier caliper.

Table 5.10: Layer-wise material composition of Al-Al_2O_3 FGM beam samples used in free vibration experimental setup for clamped free boundary condition.

Sl. No.	Description	Volume fraction of metal ans ceramic				
		Layer1	Layer2	Layer3	Layer4	Layer5
1	Sample 8	80-20	98.75-1.25	100-0	100-0	100-0
2	Sample 13	90-10	95-5	97.5-2.5	98.75-1.25	100-0
3	Sample 15	90-10	95-5	97.5-2.5	98.75-1.25	100-0
4	Sample 18	90-10	95-5	97.5-2.5	98.75-1.25	100-0
5	Sample 19	90-10	95-5	97.5-2.5	98.75-1.25	100-0
6	Sample 20	90-10	95-5	97.5-2.5	100-0	100-0

Table 5.11: Dimension of Al-Al_2O_3 FGM beam and pure aluminium beam samples used in free vibration experimental setup for clamped free boundary condition.

Sl. No.	Description	Effective length (mm)	Width (mm)	Average thickness (mm)
1	Sample 8	110	20	3.05
2	Sample 13	85	20	2.33
3	Sample 15	125	20	2.56
4	Sample 18	131	20	2.57
5	Sample 19	125	20	2.476
6	Sample 20	125	20	2.49
7	Pure Al 2	125	20	2.90
8	Pure Al 3	131	20	2.30
9	Pure Al 4	125	20	2.25
10	Pure Al (Ext)	125	20	2.05

The theoretical densities of each sample are calculated using Eq.5.1 and Eq.5.2. The FGM and aluminium beam samples are weighed using a precision balance machine with 1mg accuracy. Volume is calculated considering total length (150 mm), width (20 mm) and average thickness of the sample as listed in Table 5.11. The mass of the sample divided by its volume gives the actual density. The actual density of Al-Al_2O_3 FGM and pure aluminium beam samples are tabulated in the Table 5.12. For few samples, the densities were also calculated based on Archimedes principle on precision balance and its values are also tabulated in Table 5.12 for comparison. The percentage difference between the theoretical density and actual density gives the porosity value.

Table 5.12: Actual, Archimedes and theoretical density of Al-Al_2O_3 FGM and pure aluminium beam samples.

Sl. No.	Description	Mass (gm)	Volume ×10-6 (m^3)	Actual density (kg/m^3)	Theoretical density (Eq.5.1) (kg/m^3)	Archimedes density (kg/m^3)	% Error w.r.t. actual density
1	Sample 8	19.192	9.15	2097.48	2746.75	NA	23.64
2	Sample 13	14.595	6.99	2087.98	2737.45	NA	23.77
3	Sample 15	16.102	7.68	2096.61	2737.45	NA	23.46
4	Sample 18	16.475	7.71	2136.83	2737.45	NA	21.99
5	Sample 19	16.448	7.304	2251.85	2737.45	2572.4	17.74
6	Sample 20	17.737	7.47	2374.43	2737.45	2569.2	13.26
7	Pure Al 2	16.491	8.7	1895.52	2698	NA	29.74
8	Pure Al 3	16.239	7.32	2218.44	2698	2463.0	17.77
9	Pure Al 4	16.995	7.09	2396.62	2698	2527.0	11.17
10	Pure Al (Ext)	16.107	6.075	2651.35	2705	2659.4	1.73

The actual densities of FGM and aluminium beam samples calculated are compared with the theoretical densities as given in the Table 5.12. The percentage error is calculated between theoretical and actual density. The difference in the theoretical and actual densities of the beam samples may be due to multiple factors such as manual filling of powder mixtures in the die, porosity in the samples, compaction pressure and sintering temperature and time.

5.5.1 Static deflection studies of Aluminium and Al-Al_2O_3 FGM beam

The static bending response of the cantilever FGM beam samples under a concentrated load W at the tip, is predicted using the linear and non-linear finite element formulation. Theoretically predicted maximum deflection (linear and nonlinear) for the FGM samples of the five-layer Al-Al_2O_3 beam and pure aluminium beam are presented in Table 5.13 and is compared with the experimental results. The comparison of theoretical and experimental deflection is shown in Fig.5.19 to Fig.5.23 for two different aluminium and FGM beam samples. It is observed that, the results obtained using the finite element formulation computed using FORTRAN code is in good agreement with the experimental results for extruded aluminium sample (Al-Ext). For

all the other pure aluminium and FGM beam samples, the percentage error is approximately 45-54% and 71-77% respectively. The vast difference between the theoretical and the experimental results is due to porosity in the samples prepared using powder metallurgy process. The porosity is caused in the samples due to the uneven compaction of powder, the error in maintaining constant thickness for all layers and throughout the length of the beam and sintering temperature.

Table 5.13: Theoretical and experimental tip deflection for clamped-free Al-Al_2O_3 FGM beam samples without porosity effect.

Sample No.	Load "W" (N)	Free length of beam (mm)	Theoretical deflection at tip without porosity effect (mm)		Experimental deflection at tip (mm)	% Error in the results	
			Nonlinear EBT	Linear EBT		Non-linear	Linear
FGM-19	0.98086	120	0.28434	0.28049	1.231027	76.902	77.215
FGM-19	1.46953	120	0.42599	0.42024	1.846789	76.933	77.245
FGM-20	0.98086	120	0.27957	0.27579	0.971505	71.223	71.612
FGM-20	1.46953	120	0.41886	0.41318	1.491912	71.925	72.305
Al-3	0.98086	120	0.39149	0.39313	0.723672	45.902	45.676
Al-3	1.46953	120	0.58653	0.58898	1.105267	46.933	46.712
Al-4	0.98086	130	0.51203	0.51414	1.107491	53.767	53.576
Al-4	1.46953	130	0.76713	0.77029	1.65774	53.724	53.534
Al-Ext	0.98086	130	0.64173	0.63362	0.67381	4.762	5.965
Al-Ext	1.27459	130	0.83390	0.82336	0.87549	4.750	5.954

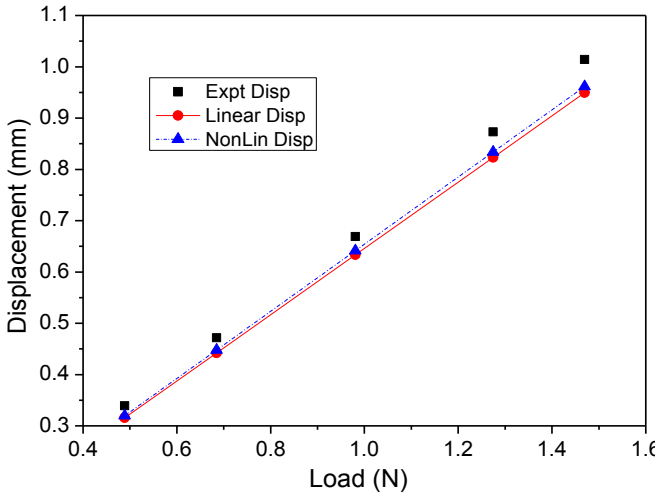

Fig.5.19 Deflection v/s load plot for pure extruded aluminium beam under clamp free boundary condition.

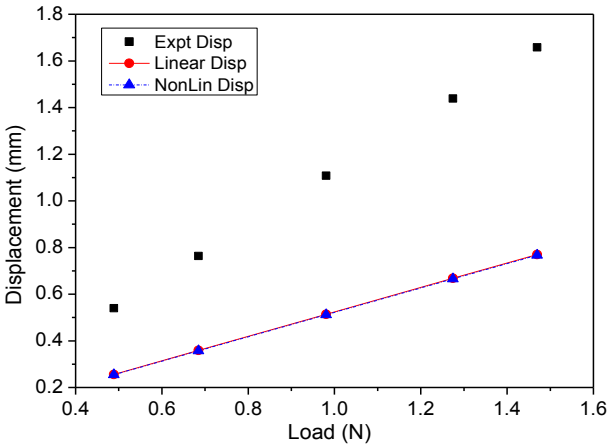

Fig.5.20 Deflection v/s load plot for pure sintered aluminium beam (sample-4) under clamp free boundary condition.

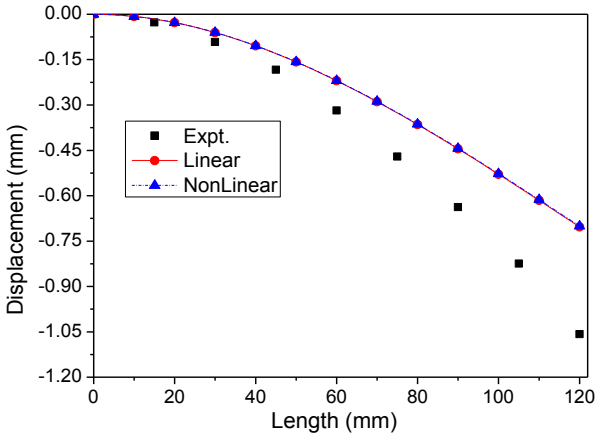

Fig.5.21 Static deflection profile for pure sintered aluminium beam (sample-4) under clamp free boundary condition at 1.275 N load.

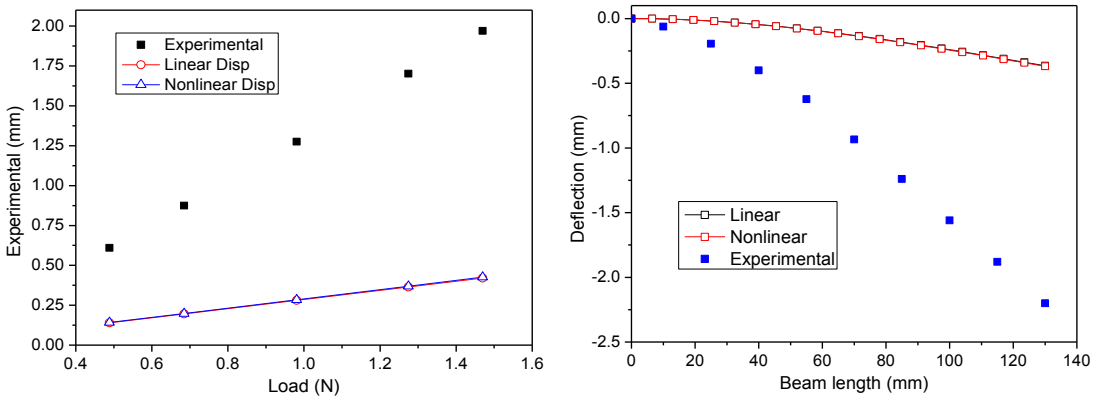

(a) (b)

Fig.5.22 (a) Deflection v/s load plot (L=120mm) and (b) static deflection profile at 1.275 N load (L=130mm) for Al-Al_2O_3 FGM beam (sample-19) under clamp free boundary condition.

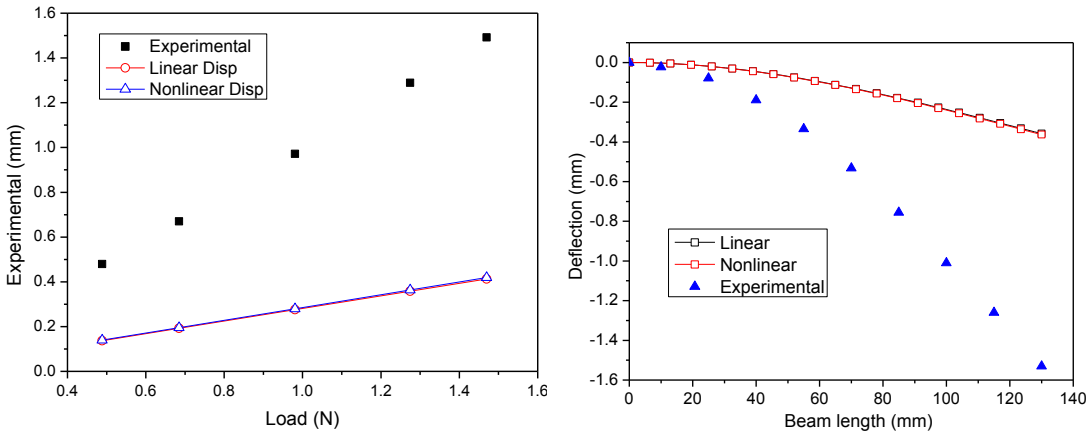

(a) (b)

Fig.5.23 (a) Deflection v/s load plot (L=120mm) and (b) static deflection profile at 1.275 N load (L=130mm) for Al-Al_2O_3 FGM beam (sample-20) under clamp free boundary condition.

Based on the experimental and numerical results presented in Fig.5.19 to Fig.5.23, it is observed that the error between theoretical and experimental results is more than 50%. It is likely that, porosity plays a major role in the theoretical analysis of the beam samples prepared using powder metallurgy process. The aforementioned analysis is carried out without considering the porosity effect. Literature on the features of the components manufactured using powder metallurgy process revealed that the sintered beam samples cannot have strength as good as commercially available extruded aluminium beam (Al-Ext). Apart, it was understood that the porosity plays an important role and governs the Young's modulus of the sintered material. Young's modulus is the important property of the material which directly effects the deflection and free vibration frequency results. Hence it becomes necessary to study the effect of porosity on the Young's modulus and density of the material under study. Limited literature is available on the effect of porosity on the Young's modulus of aluminium and alumina. Well known theoretical models for evaluating Young's modulus with porosity effect available in the literature are by Phani and Niyogi (1987), Boccaccini and Boccaccini (1997), Kovacik (1999) and Asmani et al. (2001). Phani and Niyogi (1987) were the first to propose theoretical model for evaluation of Young's modulus of alumina considering the porosity effected which was later followed and implemented by Kovacik (1999) for further studies on other ceramics and iron powder. The porosity

model proposed by Phani and Niyogi (1987) and further adopted by Kovacik (1999) is as follows,

$$E_p = E_0\left(1-\frac{p}{p_c}\right)^f \tag{5.4}$$

where E_p is the effective Young's modulus of porous material with porosity p; E_0 is Young's modulus of solid material, p_c is the porosity at which the effective Young's modulus becomes zero and f is the parameter dependent on the grain morphology and pore geometry of porous material.

Boccaccini and Boccaccini (1997) have proposed another model for evaluation of the Young's modulus of the porous material. It is also assumed that the Poisson's ratio of porous materials does not change significantly with porosity. Experimental data available in the literature on various sintered porous materials such as SiC, $A1_2O_3$, $YBa_2Cu_3O_{7-x}$, porcelain, sintered iron, Si_3N_4, and sintered tungsten, were used to verify the theoretical model. This model is said to predict results better than the model proposed by Phani and Niyogi (1987). The model proposed by Boccaccini and Boccaccini (1997) has been adopted by Asmani et al. (2001) for evaluation of the Young's modulus and Poisson's ratio of alumina ceramics as described below,

$$E(p) = E_0\left(1-p^{2/3}\right)^S \tag{5.5}$$

with

$$S = 1.21\left[\frac{z}{x}\right]^{\frac{1}{3}}\left[1+\left(\left(\frac{z}{x}\right)^{-2}-1\right)\cos^2\phi\right]^{\frac{1}{2}} \tag{5.6}$$

z/x is the mean axial ratio (shape factor) of the pores (for a spherical shape pore: z/x =1.0) and $\cos^2\phi$ is the factor of pore orientation (for isotropic medium $\cos^2\phi$ =0.33333).

For the comparison purpose, the results obtained from various theoretical models available in literature (Phani and Niyogi (1987), Boccaccini and Boccaccini (1997), Kovacik (1999) and Asmani et al. (2001)) are compared with the experimental results

and percentage error is calculated. The results are presented in Fig.5.24 for sample Al-4 considering the porosity effects proposed in all the theoretical models given in literature (Phani and Niyogi (1987), Boccaccini and Boccaccini (1997), Kovacik (1999) and Asmani et al. (2001)). For samples Al-3, FGM-19 and FGM-20, theoretical results are evaluated considering porosity effect model proposed by Boccaccini and Boccaccini (1997) and further adopted by Asmani et al. (2001) and the results are presented in Table 5.14. The model gives better results for pure aluminium powder metallurgy sample. The error reduces to less than 15% and 30% for aluminium sample 3 and 4 respectively when we consider the porosity effect in the theoretical model. The percentage error still remains on higher side for FGM sample 19 and 20. Further studies are required to understand the behavior of the powder mixture when 2 or more powders are mixed together to form FGM. Mechanical testing is required to evaluate the Young's modulus and correlation studies need to be carried out to arrive at new theoretical model for FGM beam prepared using powder metallurgy process.

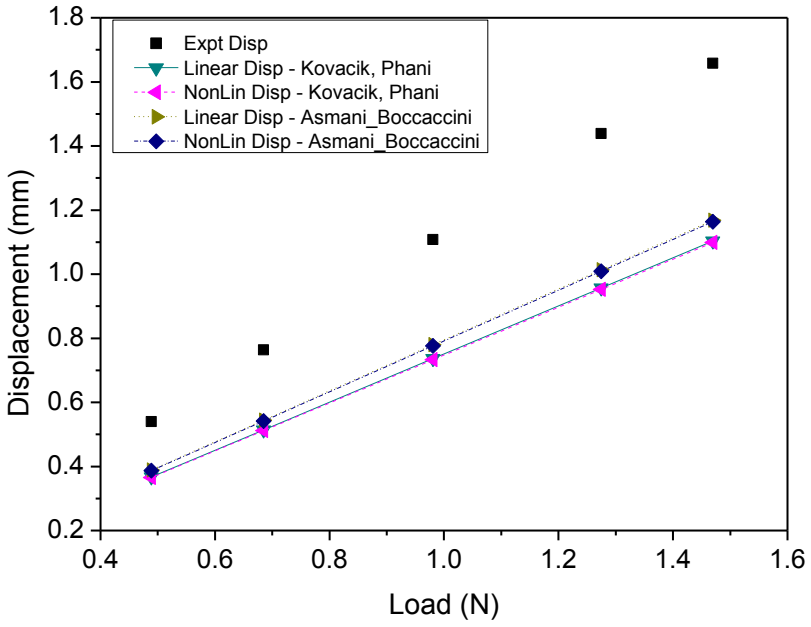

Fig.5.24 Deflection v/s load plot for pure sintered aluminium beam (sample-4) under clamp free boundary condition.

Table 5.14: Theoretical and experimental tip deflection for clamped-free Al-Al_2O_3 FGM beam samples considering porosity effect.

Sample No.	Load "W" (N)	Porosity %	Theoretical deflection (mm) at tip considering porosity effect – Asmani et al.(2001)		Experimental deflection (mm) at tip	% Error in the results	
			Nonlinear EBT	Linear EBT		Non-linear	Linear
FGM-19	0.98086	17.39	0.44998	0.44390	1.231027	63.447	63.941
FGM-19	1.46953	17.39	0.67416	0.66505	1.846789	63.496	63.989
FGM-20	0.98086	13.26	0.40250	0.39704	0.971505	58.569	59.131
FGM-20	1.46953	13.26	0.60302	0.59485	1.491912	59.581	60.128
Al-3	0.98086	17.79	0.62023	0.62282	0.723672	14.294	13.936
Al-3	1.46953	17.79	0.92923	0.93311	1.105267	15.927	15.576
Al-4	0.98086	15.71	0.77656	0.77975	1.107491	29.881	29.593
Al-4	1.46953	15.71	1.16340	0.77975	1.657740	29.820	29.531

5.5.2 Free vibration analysis of Aluminium and Al-Al_2O_3 FGM beam

Free vibration experiment is conducted on the Al-Al_2O_3 FGM and aluminium beam samples for clamped-free boundary condition. The displacement versus time data acquired from the laser displacement sensor using the ILD1402 DAQ software is plotted in Origin Pro 8. The data is taken for determining the natural frequency of the Al-Al_2O_3 FGM and aluminium beam samples using signal processing FFT toolbox of Origin Pro 8. Displacement versus time and magnitude versus frequency plots for different Al-Al_2O_3 FGM and aluminium beam samples are given in Figs.III.3-III.9, APPENDIX-III. The frequency value corresponding to the peak in the magnitude versus frequency plot gives the natural frequency for the particular beam sample. A FORTRAN computer code is developed to compute theoretical linear and nonlinear natural frequency of FGM and pure aluminium beam samples. The theoretical natural frequencies obtained from code are compared with the experimental natural frequencies for FGM and aluminium beam samples. The natural frequencies calculated are without considering the porosity effect and are presented in Table 5.15. Except for pure Al-3 beam, vast error is observed between the theoretical and experimental frequency which is due to non-consideration of the porosity effect in the theoretical model.

Table 5.15: Experimental and theoretical natural frequencies for Al-Al_2O_3 FGM and aluminium beam samples for clamped-free boundary condition without porosity effect.

Sl. No	Sample no.	*L/h*	*b/h*	Natural frequency (Hz)			Error (%)	
				Experimental	Theoretical		Linear	Non linear
					Linear	Non linear		
1	FGM-8	36.06	6.56	123.05	229.91	226.68	86.84	84.22
2	FGM-13	36.48	8.58	140.70	280.39	277.03	99.28	96.89
3	FGM-15	48.83	7.81	74.33	142.48	141.28	91.69	90.07
4	FGM-18	50.97	7.78	78.23	130.2	129.18	66.43	65.13
5	FGM-19	50.48	8.08	77.96	137.79	136.64	76.74	75.27
6	Pure Al-2	43.1	6.90	76.92	149.51	149.50	94.37	94.36
7	Pure Al-3	56.95	8.69	81.86	108.65	108.64	32.73	32.71

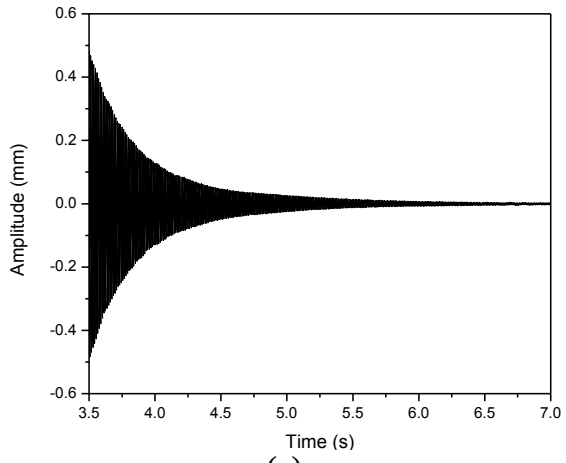

(a)

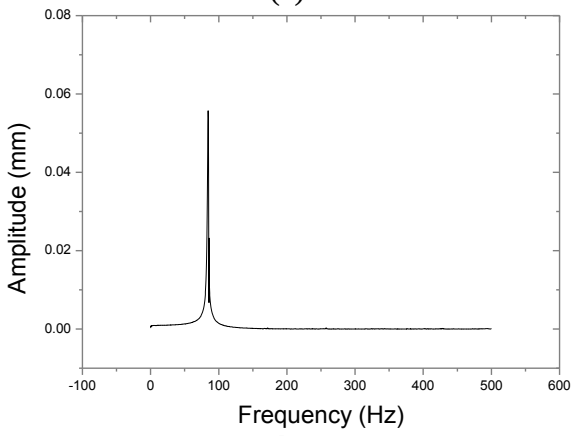

(b)

Fig.5.25 (a) Displacement versus time and (b) magnitude versus frequency plots for Al-Al_2O_3 FGM beam sample 20 in clamped-free boundary condition.

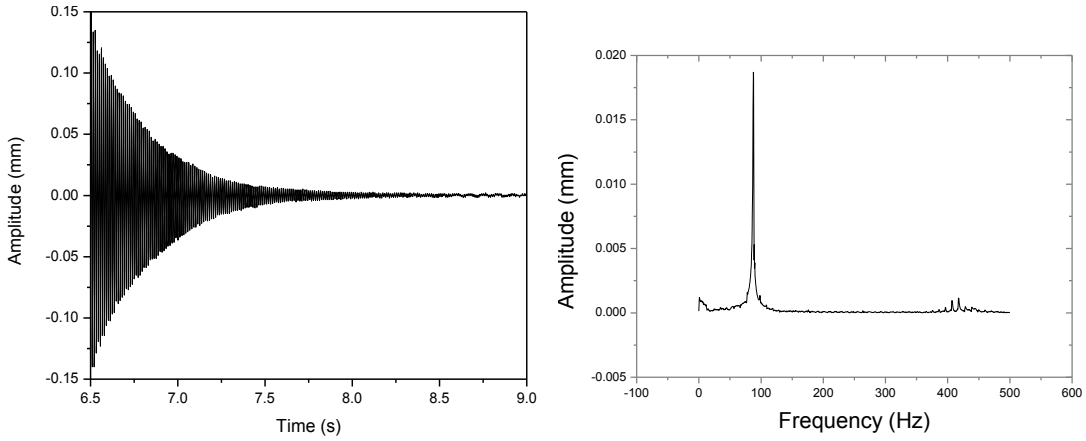

(a) (b)

Fig.5.26 (a) Displacement versus time and (b) magnitude versus frequency plots for pure Al beam sample 4 in clamped-free boundary condition.

Fig.5.25 to Fig.5.27 shows the (a) displacement versus time and (b) magnitude versus frequency plots for Al-Al_2O_3 FGM sample-20 and for aluminium beam samples 4 and Al-Ext. Table 5.16 show the detail analysis of the comparison of the natural frequency for the pure aluminium and FGM beam sample-20. The theoretical frequency is also evaluated considering the porosity factor of the powder metallurgy beam sample and it is observed that the there is considerable decrease in the error value between theoretical frequency and experimental natural frequency. Hence, it is concluded that the porosity effect need to be considered in order to theoretically model the beam sample prepared using powder metallurgy process.

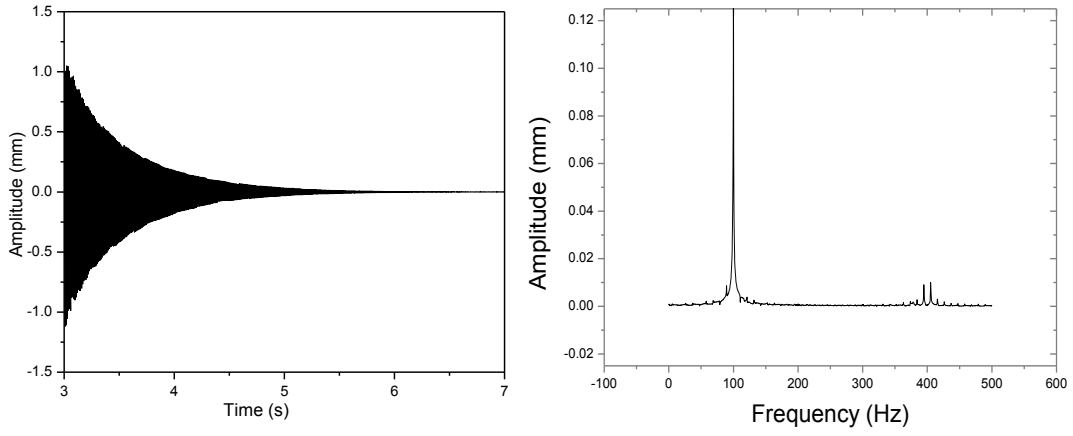

(a) (b)

Fig.5.27 (a) Displacement versus time and (b) magnitude versus frequency plots for pure Al (extruded) beam in clamped-free boundary condition.

Table 5.16: Free Vibration Analysis of Pure Aluminum and Al-Al_2O_3 FGM beam sample considering porosities.

		Pure Aluminium Extruded Sample	Pure Aluminium Powder Metallurgy Sample-4	Al-Al_2O_3 FGM beam sample-20
Effective Length (mm)		125	125	130
Length (mm)		150	150	150
Width (mm)		19.8	20	20
Thickness (mm)		2.05	2.25	2.49
Measured Weight (gm)		16.107	16.995	17.737
Calculated Density (mass/volume) (kg/m^3)		2645.48	2274	2374.43
Theoretical Density (Eq.5.1) (kg/m^3)		2705	2698	2737.45
Archimedes Principle Density (kg/m^3)		2659.4	2527.0	2569.2
Porosity w.r.t. Calculated Density (%)		NA	15.71	13.26
Experimental Frequency (Hz)	Trial 1	99.91	87.63	84.41
	Trial 2	99.83	86.77	84.33
	Trial 3	99.97	84.58	84.04
	Average	99.90	86.33	84.26
Linear Frequency (Hz)		106.181	116.69	150.31
Nonlinear Frequency (Hz)		106.176	116.68	149.05
Error in Frequency-Linear (%)		-6.28	-35.17	-78.39
Error in Frequency-Nonlinear (%)		-6.28	-35.16	-76.89
Linear Frequency- considering porosity - Asmani et al. (2001) (Hz)		NA	103.21	134.51
Nonlinear Frequency- considering porosity - Asmani et al. (2001) (Hz)		NA	103.20	133.38
Error in Frequency (considering porosity) – Linear (%)		NA	-19.56	-59.64
Error in Frequency (considering porosity) – Nonlinear (%)		NA	-19.55	-58.30

5.6 SUMMARY

The theoretical and actual densities of SUS316-Al_2O_3 and Al-Al_2O_3 FGM and pure aluminium beam samples are compared and it is found that the difference in theoretical and actual densities is highest for Al-Al_2O_3 as compared to SUS316-Al_2O_3 FGM beam.

The theoretical linear and nonlinear transverse deflection and natural frequencies are calculated for FGM, pure SUS316 and aluminium beams by using FEM code. The experimental transverse deflection and natural frequencies are compared with theoretical linear and nonlinear static deflection and natural frequency of beam samples. It is observed that the samples prepared using plasma spray process gives better correlation as compared to powder metallurgy beam samples. Porosity play an important role in theoretical modelling of beam samples prepared using powder metallurgy process. Mechanical testing is required to evaluate the Young's modulus value for pure aluminium and FGM beam samples prepared using powder metallurgy process.

CHAPTER - 6

RESULTS AND DISCUSSION - LINEAR FINITE ELEMENT ANALYSIS OF THIN FUNCTIONALLY GRADED MATERIAL BEAMS SUBJECTED TO STEP HEATING

6.1 INTRODUCTION

In this chapter, the detailed investigation on the thermal induced vibration of a functionally graded material beam when subjected to a step thermal load is presented. The elastic response of the FGM beam is discussed for two types of metal-ceramic combination. The study considers one surface of the beam subjected to heat load with opposite surface being thermally insulated or subjected to convective heat transfer. Considering the temperature dependency of material properties, 1-dimensional temperature distribution is obtained for various structural boundary conditions and corresponding results of the FGM beam in terms of time dependent deflection and thermal moment are analysed.

6.2 NUMERICAL RESULTS AND DISCUSSION ON LINEAR ANALYSIS OF FGM BEAM SUBJECTED TO STEP HEATING

A FORTRAN computer program is written based on the formulation outlined in Chapter 4 to study the thermo-elastic response of FGM beams. Numerical analyses are carried out for thin functionally graded beams with various structural boundary conditions such as simple support (SS), clamped-simple support (CS) and clamped-free (CF) to analyse the dynamic response and dynamic thermal moment. The beam is subjected to step heating with heat transfer boundary condition as insulation and

convective heat loss on the other surface. The slenderness ratios of the beam considered for the study is 165 and 100. Length of the beam is 0.254 m and has unit width. The evaluation of the temperature distribution across the depth of the beam has been verified with the close form solution given by Carslaw and Jaeger (1959), see also Boley (1956). The finite element analysis results of the dynamic response of aluminium-zirconia FGM beam with n=400 (beam is fully metallic) subjected to thermal boundary conditions has been verified with the non-dimensional results for aluminium beam reported by Boley (1956) and Manolis and Beskos (1981) for the simply supported beam. The fundamental non-dimensional free vibration frequencies of the beam are verified with the frequencies reported by Simsek and Kocaturk (2009) and Alshorbagy et al. (2011).

6.2.1 Verification of Simply supported FGM beam subjected to step heating

Studies are carried out for the simply supported FGM beam (Fig.3.1) subjected to heat source on top surface and insulated on the bottom surface. The thermo-physical data for the Aluminium-Zirconia FGM beam are as follows: k_m =201.87W/mK, α_m =22.0×10^{-6}/^{0}C, ρ_m =2700kg/m^3, c_{p_m} =869.38J/kg^{0}C, E_m =73.5×10^{9}Pa, G_m =26.0×10^{9}Pa for Aluminium and k_c =2.09W/mK, α_c =10.0×10^{-6}/^{0}C, ρ_c =3000kg/m^3, c_{p_c} =530J/kg^{0}C, E_c =151×10^{9}Pa for Zirconia. Geometric details of the beam are L =0.254 m, and by setting non dimensional parameter, $B=1$, as referred from Boley (1956), the thickness of the beam is h =0.001544 m, hence, L/h =165. The parameter B is the square root of the ratio of the characteristic time of heat transfer problem, to characteristic time of the vibration problem (i.e. proportional to the natural period of vibration), Boley (1956).

$$B=\frac{h}{L\sqrt{\kappa}\left(\rho A/EI\right)^{1/4}}=\left(\frac{h}{L}\frac{hc}{\kappa}\frac{1}{S}\right)^{1/2} \tag{6.1}$$

where, S is the slenderness ratio and

$$c=\sqrt{E/\rho} \tag{6.2}$$

is the velocity of propagation of longitudinal waves.

Dynamic response is obtained for time, t=0.04 s. When the power law index is set to n=400, FGM beam reduces to pure aluminium. Heat flux on the top surface is, Q =1.63×10^6 W/m^2. The properties are assumed to be independent of the temperature and results are evaluated considering ambient temperature of zero (0) degree Celsius.

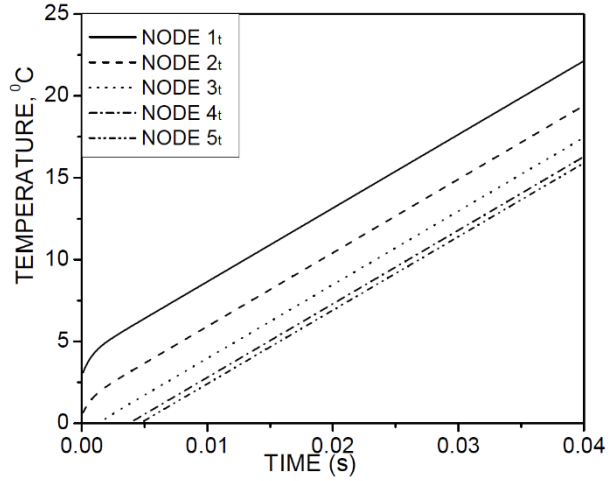

(a)

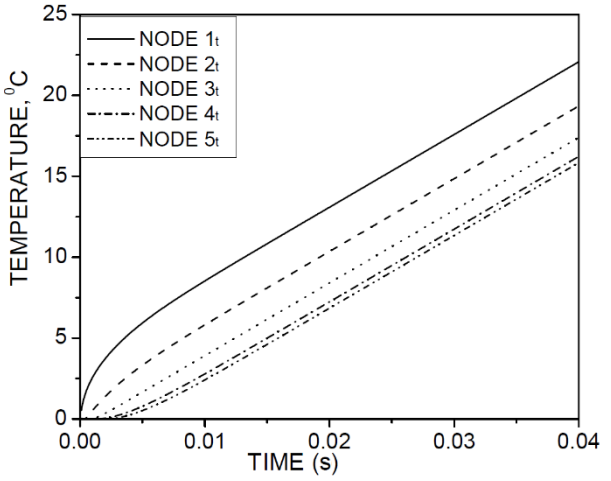

(b)

Fig.6.1 (a) Close form solution (Eq.3.8) and (b) Solution of temperature variation across the thickness of the beam as referred from Boley (1956) for B=1(present method).

Fig.6.1 shows the temperature distribution obtained across the thickness of the beam for B=1. Finite element mesh is defined across the thickness of the beam for thermal analysis problem. Node 1_t represents the node on the top surface of beam while Node 5_t represents the node on the bottom surface. Suffix 't' is used to differentiate the nodes

of thermal analysis problem with respect to structural problem. It was observed that the temperatures obtained using present method does tally with close form solution (Eq.3.8). During the initial time periods, from t=0 to t=0.005 s, temperatures do not tally due to numerical oscillations but for subsequent time periods the results are in close agreement with the close form solution. The non-dimensional plot of dynamic mid-span deflection (Fig.6.2) for a simply supported FGM beam with n=400 (Beam is fully metallic) subjected to step heat input are verified for $B=1$ as stated in Boley (1956) and Manolis and Beskos (1981). It is found that the trends of the results are in good agreement for simply supported beam subjected to rapid heating and maintain steady state deflection for further time interval.

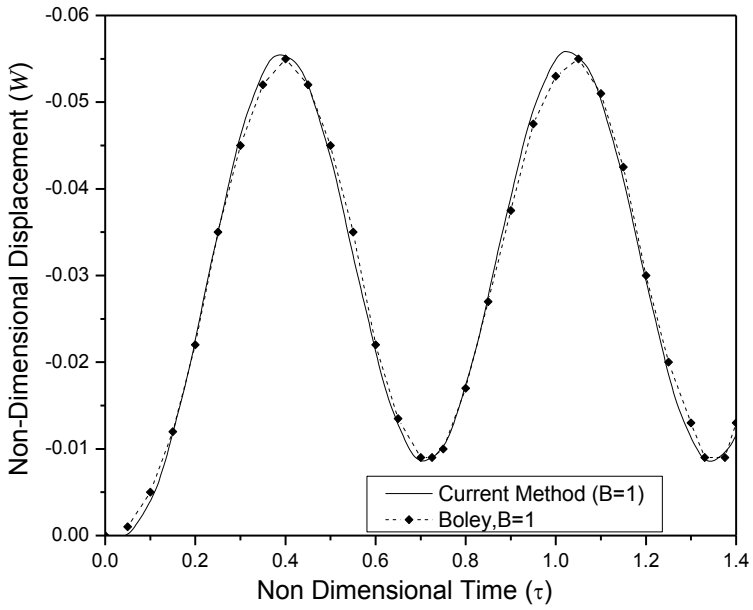

Fig.6.2 Non dimensional dynamic mid-span deflection of simply supported beam for B=1.

Fig.6.3 shows the study to understand how many layers are essential in a FGM beam so that the numerical solution for displacement is close to the analytical solution. The FGM beam was considered to comprise of varying number of laminae from 4 to 132 with n=400 (Beam is fully metallic). From Fig.6.3 it is clear that a FGM beam with 64 layers gives closer result to the analytical one. Hence the subsequent numerical result will use FGM beam with 64 layers. Convergence study was also carried out to understand the effect of the number of elements in the axial direction for 6, 10, 20 and

40 elements. It was observed that there is no much variation in the results for 10, 20 and 40 elements hence 10 elements were considered in the axial direction for subsequent numerical results (refer APPENDIX-IV for more details).

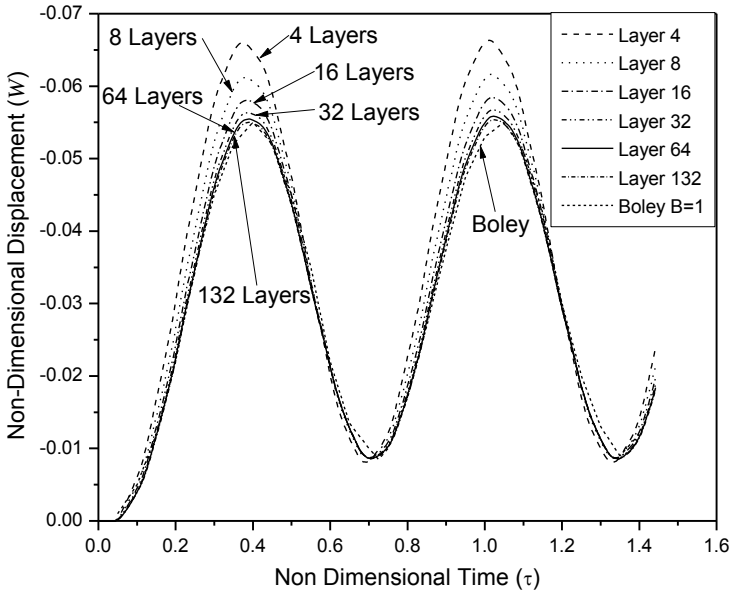

Fig.6.3 Convergence study for number of homogeneous layers for FGM beam.

6.2.2 Verification of free vibration characteristics of Simply Supported FGM Beam

The following non-dimensional quantities are introduced here as referred from Simsek and Kocaturk (2009), $E_{ratio} = \frac{E_U}{E_L}$, $\rho_{ratio} = \frac{\rho_U}{\rho_L}$, $\lambda^2 = \omega L^2 \sqrt{\frac{\rho_L A}{E_L I}}$ where, subscript "L" and "U" refers to lower and upper surface of the beam respectively. The bottom surface of the beam is pure steel, whereas the top surface of the beam is pure alumina. A set of linear homogeneous equations (frequency equation) can be expressed as

$$\mathbf{Kd} - \lambda^2 \mathbf{Md} = 0 \tag{6.3}$$

The non-dimensional frequencies (eigen values) λ are found from the condition that the determinant of the system of equations given by Eq.(6.3) must vanish. The parameters of the beam used for this study are: b = 0.4m, h = 1.0m and L = 20m.

Table 6.1 The first dimensionless frequency parameters λ for different material distribution.

E_{ratio}		n =0.0	n =0.1	n =0.2	n =0.5	n =1.0	n =2.0	n =5.0	n =10.0
0.25	Present Method	2.219	2.390	2.500	2.676	2.791	2.871	2.955	3.017
	Simsek, Kocaturk (2009)	2.2203	2.3739	2.4606	-	2.7035	2.8053	-	3.0084
	Alshorbagy et al. (2011)	2.2203	2.3746	2.4614	2.5979	2.7041	2.8057	2.9302	3.0085
0.50	Present Method	2.639	2.712	2.764	2.856	2.921	2.968	3.020	3.059
	Simsek, Kocaturk (2009)	2.6403	2.7104	2.7573	-	2.8944	2.9459	-	3.0562
	Alshorbagy et al. (2011)	2.6404	2.7107	2.7576	2.8363	2.8946	2.9461	3.0110	3.0563
1.00	Present Method	3.139	3.139	3.139	3.139	3.139	3.139	3.139	3.139
	Simsek, Kocaturk (2009)	3.1399	3.1399	3.1399	-	3.1399	3.1399	-	3.1399
	Alshorbagy et al. (2011)	3.1400	3.1400	3.1400	3.1400	3.1400	3.1400	3.1400	3.1400
2.00	Present Method	3.733	3.678	3.634	3.546	3.474	3.414	3.342	3.282
	Simsek, Kocaturk (2009)	3.7340	3.6775	3.6301	-	3.4421	3.3765	-	3.2725
	Alshorbagy et al. (2011)	3.7341	3.6773	3.6300	3.5296	3.4423	3.3768	3.3196	3.2726

In Table 6.1, the first non-dimensional frequencies of the FGM beam are given for different values of Young's modulus ratio, E_{ratio}, and the power-law exponent n for L/h=20. The material properties of steel are E=210 GPa and ρ=7800 kg/m^3 and for alumina, E=390 GPa and ρ=3960 kg/m^3. In these calculations, the mass ratio of the top and the bottom material is taken as constant (ρ_{ratio}=1). It is observed that, the natural frequencies increase with the increase in power exponent (when E_{ratio}<1), and decrease with an increase in power exponent (when E_{ratio}>1). It is seen from the table that E_{ratio} is more effective on the dimensionless frequencies for small values of n than for large values of n. As the values of n increase, the effect of increase of E_{ratio} on the natural frequencies decreases. For a constant power exponent, an increase in E_{ratio} causes the increase in fundamental frequencies. The comparison between the proposed model and the published work as presented in Table 6.1 concludes that the present results agree reasonably well with the published work [Simsek and Kocaturk (2009), Alshorbagy et al. (2011)].

6.2.3 Influence of temperature dependent and temperature independent material properties on thermal vibration of FGM Aluminium-Zirconia beam.

Studies are carried out for the simply supported FGM beam subjected to step heat source on top surface and insulated on the bottom surface. For temperature evaluation, the aluminium-zirconia FGM beam is discretised with 64 elements across its thickness. The value of power law index varies from n=0 to 400 with n=0 for fully ceramic beam and n=400 for fully metal beam. Non-dimensionalising is not carried out for the subsequent plots since effective material properties for FGM beam vary with each layer across the thickness. Fig.6.4 shows the dynamic mid span deflection for a simply supported FGM beam of L/h ratio of 165 which corresponds to B=1. It can be seen from Fig.6.4(a) that the dynamic displacement increases initially from time t=0.0 and as time progresses beam oscillates with constant amplitude about the static thermal deflection. The influence of the volume fraction of ceramic or metal is also being observed. The metal rich (i.e. n =1 to 400) beam undergoes smaller magnitude of static deflection and

the deflections become steady within 25 ms whereas beams with increasing ceramic percentage, (i.e. n =0.5, 0.1, 0.05 and 0.0) exhibits higher value of static deflection, increasing gradually with time and deflections are steady after 500 ms.

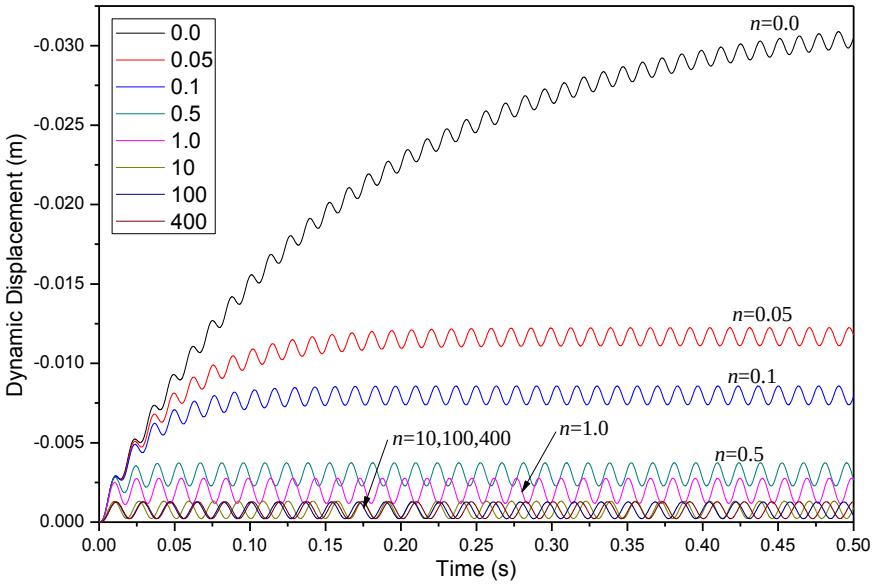

(a)

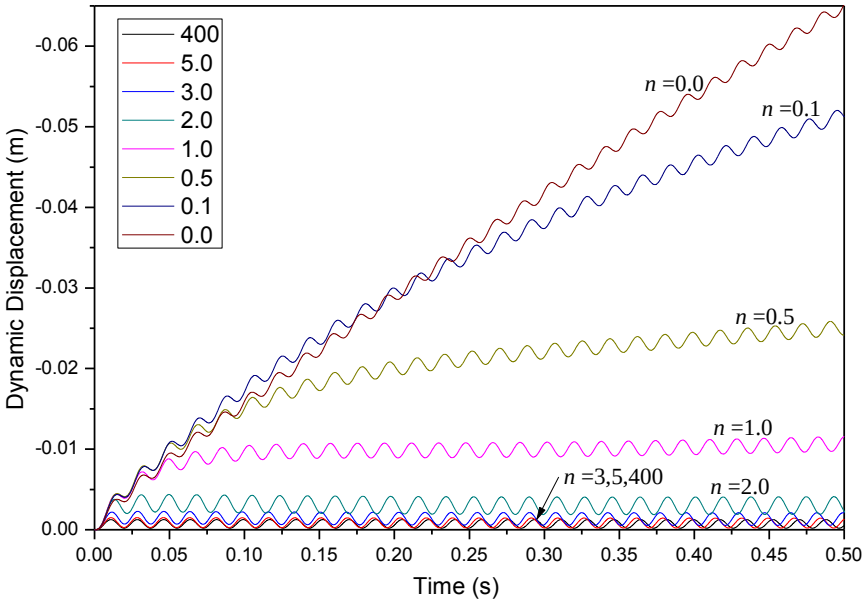

(b)

Fig.6.4 Dynamic mid-span deflection of simply supported Al-ZrO_2 FGM beam for $B = 1$ (a) temperature independent material properties (b) temperature dependent material properties.

Studies were also carried out for aluminium-zirconia beam with thermo-mechanical properties dependent on temperature since they are used in high temperature environments. The properties were expressed as functions of temperature as reported in the literature (Reddy and Chin, 1998). It is observed from Fig.6.4(b) that the metal rich beam exhibits thermal oscillations about the thermal static deflections. As in the case of temperature independent properties, the thermal deflections remain unchanged after 500 ms. The beams with increasing ceramic percentage exhibits higher value of thermal static deflection which increases gradually with time. Experimental investigations are required to be carried out to check the validity of the theoretical results of Al-ZrO_2 FGM beam with temperature dependent material properties.

6.2.4 Effect of thermo-physical properties of material and physical boundary conditions on thermally induced vibrations of beams subjected to step heating

The analysis considers FGM beam with L/h =100. The material considered for the study is gradation of Stainless Steel and Aluminium Oxide (SUS304-Al_2O_3). Thermo-physical properties for material are tabulated in Table 6.2 as referred from Reddy and Chin (1998) and are considered to be dependent on the temperature distribution across the thickness of the beam. The study has been carried out for a FGM beam with end supports such as SS, CS and CF. The beam is subjected to step heating on top surface and insulated on the bottom surface. The magnitude of the heat flux, Q, was maintained at 1.63×10^6 W/m^2.

Fig.6.5 shows the dynamic mid span deflection and Fig.6.6 shows dynamic mid span thermal moment for a simply supported SUS304-Al_2O_3 FGM beam for various volume fractions of ceramic. It is seen from Fig.6.5 that the dynamic displacement increases initially from time t=0 and as time progresses, the beam oscillates with constant amplitude about static displacement. The ceramic rich beam (n = 0.0, 0.05, 0.1 and 0.5) undergoes smaller magnitude of static deflections and deflections become steady within 100 ms whereas metal rich beams (n = 400.0, 100.0, and 10.0) exhibit higher value of static deflection, increasing gradually with time and deflection become steady after 300 ms. These results for simply supported SUS304-Al_2O_3 FGM beam of L/h =

100 when compared with results for Al-ZrO_2 FGM beam of L/h =165 (refer to Fig.6.4 (a)) shows the influence of the metal-ceramic combination on the mean thermal deflection.

Table 6.2 Temperature dependent coefficients for SUS316 and Al_2O_3.

Material	Property	P_0	P_{-1}	P_1	P_2	P_3
Aluminum Oxide	k (W/mK)	-14.087	-1123.6	-6.227×10^{-3}	0	0
	α (1/K)	6.8269×10^{-6}	0	1.838×10^{-4}	0	0
	E (N/m^2)	349.55×10^{9}	0	-3.853×10^{-4}	4.027×10^{-7}	-1.673×10^{-10}
	c_p (J/kg K)	1471.97	-138.87	-2.241×10^{-5}	0	0
	ν	0.2600	0	0	0	0
	ρ (kg/m^3)	3750.0	0	0	0	0
Stainless steel	k (W/mK)	15.379	0	-1.264×10^{-3}	2.092×10^{-6}	-7.223×10^{-10}
	α (1/K)	12.766×10^{-6}	0	8.086×10^{-4}	0	0
	E (N/m^2)	201.04×10^{9}	0	3.079×10^{-4}	-6.534×10^{-7}	0
	c_p (J/kg K)	496.56	0	-1.151×10^{-3}	1.636×10^{-6}	-5.863×10^{-10}
	ν	0.3262	0	-2.002×10^{-4}	3.797×10^{-7}	0
	ρ (kg/m^3)	8166	0	0	0	0

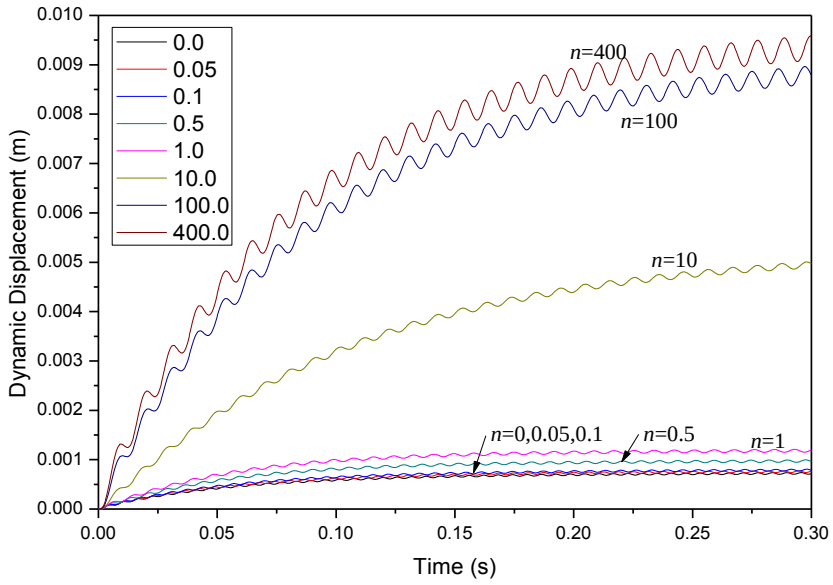

Fig.6.5 Dynamic mid-span deflection of simply supported SUS304-Al_2O_3 FGM beam for L/h=100.

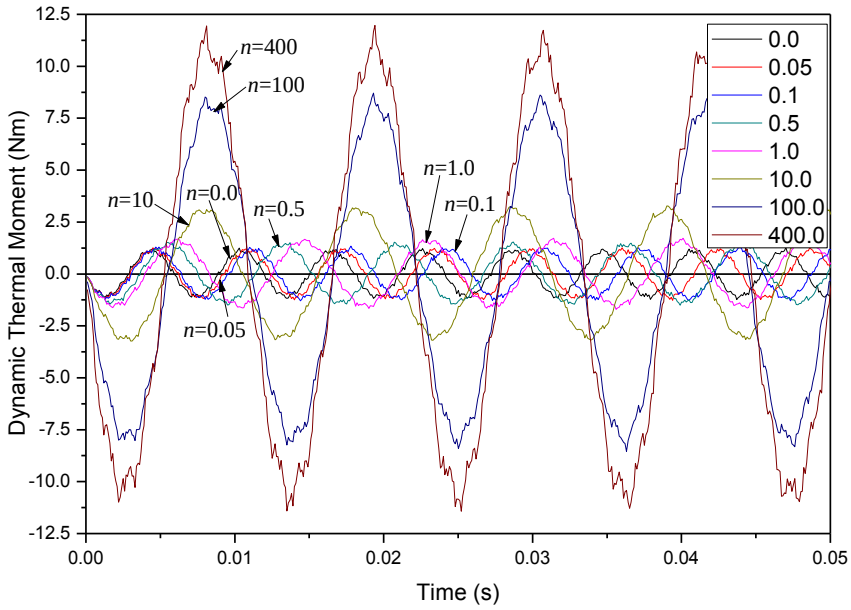

Fig.6.6 Dynamic mid-span thermal moment of simply supported SUS304-Al_2O_3 FGM beam for L/h=100.

The mean thermal deflection for metal rich beam for Al-ZrO_2 FGM beam is less as compared to SUS304-Al_2O_3 FGM beam and vice-versa for ceramic rich beam. The major influencing factors for such a behaviour of these FGM combinations is the modulus of elasticity, density and thermal conductivity of the material which influence the stiffness, mass and thermal moment causing vibrations. It is also observed from Fig.6.5 that the amplitude of the thermal oscillations for metal rich beam is more as compared to ceramic rich beam. Frequency of thermal oscillation about the mean static thermal deflection is less for ceramic rich beam and temperature induced oscillations occur about the static thermal deflection. The same phenomenon holds good for the cases of CS and CF beams as shown in Fig.6.7 and Fig.6.9 respectively. From Fig.6.5 and Fig.6.7 it is clearly seen that the displacements calculated at the mid-span for SS beam are four times that for CS beam. For SS beam, Fig.6.6, the dynamic thermal moment shows oscillatory trend about zero but for CS beam, Fig.6.8, the dynamic thermal moment first increases with time and shows the oscillatory trend about a mean thermal moment other than zero depending on the volume fraction of ceramic. This is because one end is fixed and the thermal moment at this end is zero but the thermal moment present at the simply supported end puts the beam into oscillatory state about a mean value.

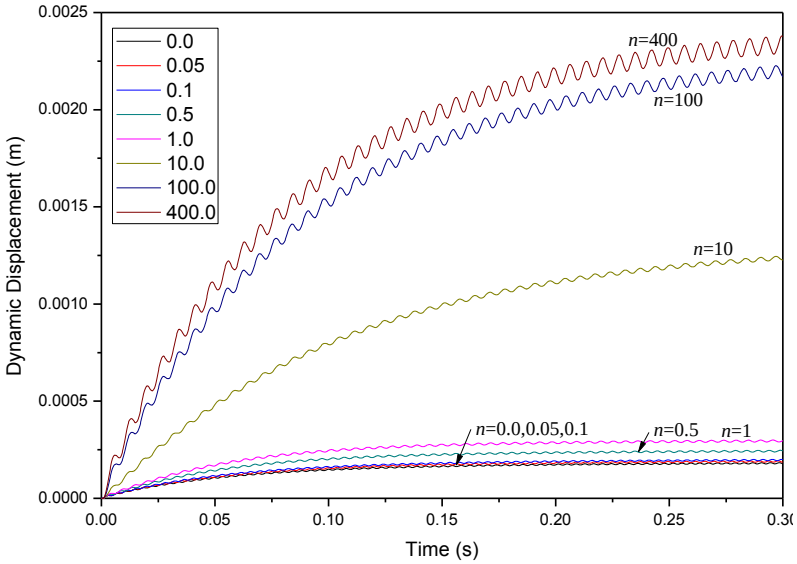

Fig.6.7 Dynamic mid-span deflection of clamped-simply supported SUS304-Al_2O_3 FGM beam for L/h=100.

The plots in Fig.6.9 for CF beam revealed that the mean displacements of the CF beam at the free end are four times that for SS beam and frequency of thermal vibration is less as compared to other two. Due to free expansion, as shown in Fig.6.10, the dynamic thermal moment for the CF beam at the free end is negligible as compared to the dynamic thermal moment in case of SS and CS as shown in Fig.6.6 and Fig.6.8 respectively.

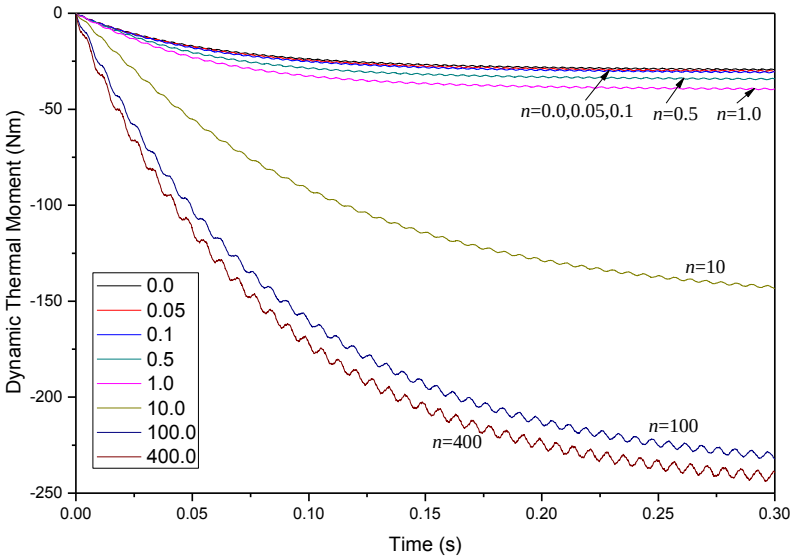

Fig.6.8 Dynamic mid-span thermal moment of clamped-simply supported SUS304-Al_2O_3 FGM beam for L/h=100.

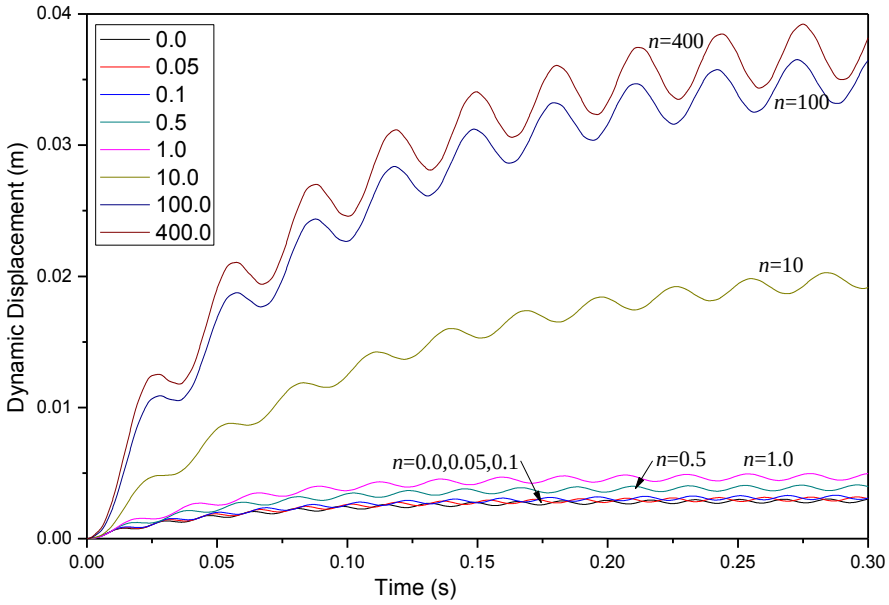

Fig.6.9 Dynamic mid-span deflection of clamped-free SUS304-Al_2O_3 FGM beam for *L/h*=100.

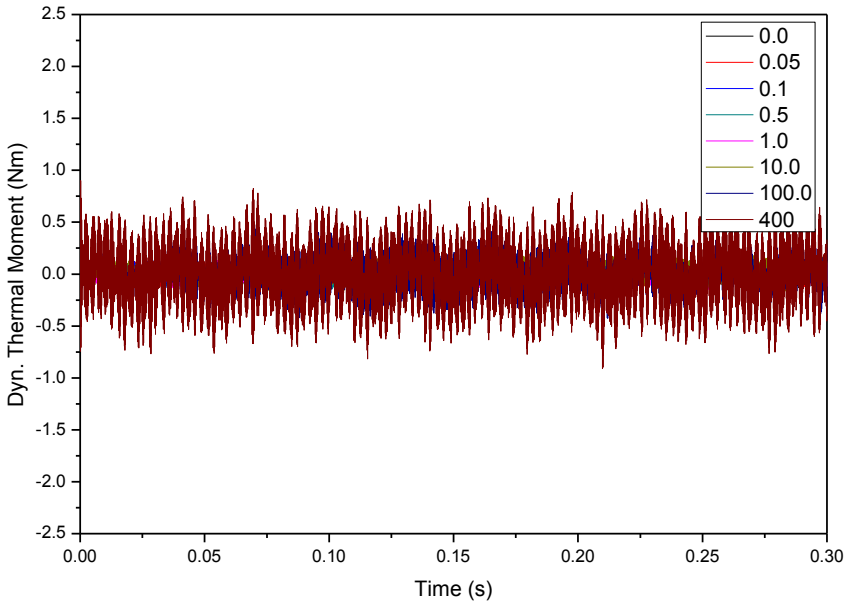

Fig.6.10 Dynamic mid-span thermal moment of clamp-free SUS304-Al_2O_3 FGM beam for *L/h*=100.

6.2.5 Effect of natural convection on thermally induced vibrations of FGM beam subjected to surface heating

Studies are also carried out on the simply supported SUS304-Al_2O_3 FGM beam of *L/h*=100 subjected to sudden heating on top surface and bottom surface subjected to natural convection as shown in Fig.6.11.

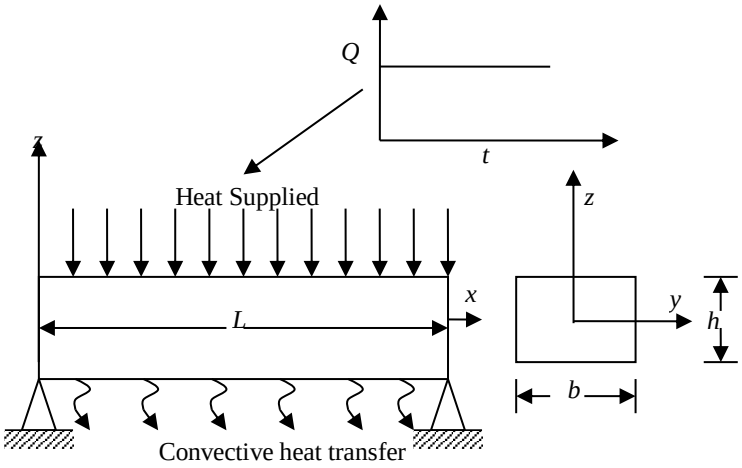

Fig.6.11 Simply supported beam subjected to step heating on one side and convection on other side.

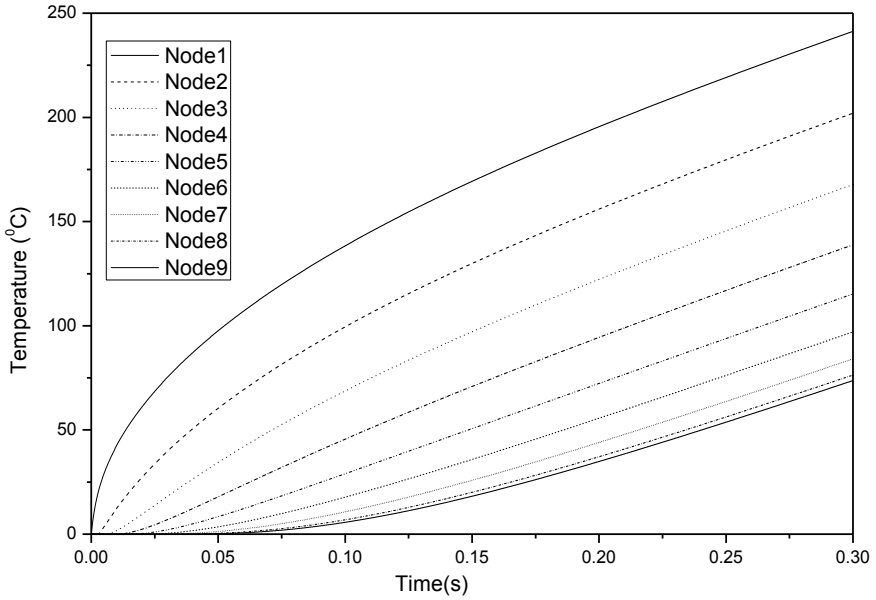

Fig.6.12 Temperature distribution of SUS304-Al_2O_3 FGM Simply Supported beam with convection at bottom for n=400 (L/h=100).

Temperature variations across the thickness of the beam, as shown in Fig.6.12 and calculated from Eq.(3.16), are extracted when a natural convective heat transfer coefficient of 100 W/m^{2}K is maintained. The temperature distribution across the thickness is similar as in the case of SS beam subjected to step heating on top surface and insulated on bottom surface. Due to presence of the convection on bottom surface, the surface temperature on the bottom layer is less as compared to insulated beam and varies exponentially with time as shown in Fig.6.13. The corresponding dynamic mid-

span deflection and thermal moment are illustrated in Fig.6.14 and Fig.6.15 respectively, and has similar characteristics of a beam subjected to step heating on one side and insulation on opposite side as examined in Fig.6.5 and Fig.6.6.

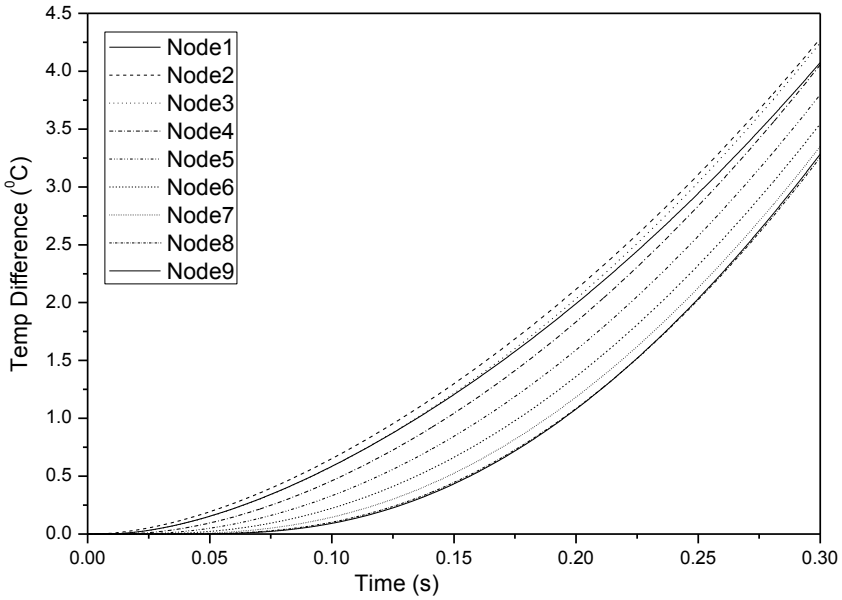

Fig.6.13 Difference in temperature for SUS304-Al_2O_3 FGM Simply Supported beam with insulation at bottom and convection at bottom for n=400 (L/h=100).

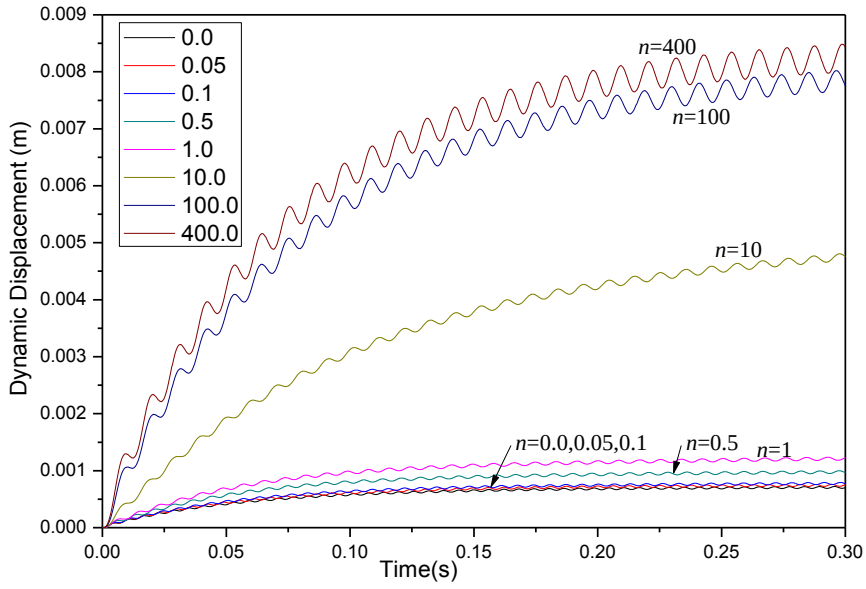

Fig.6.14 Dynamic mid-span deflection of simply supported FGM beam for L/h=100 with sudden heating on top surface and convection on bottom surface.

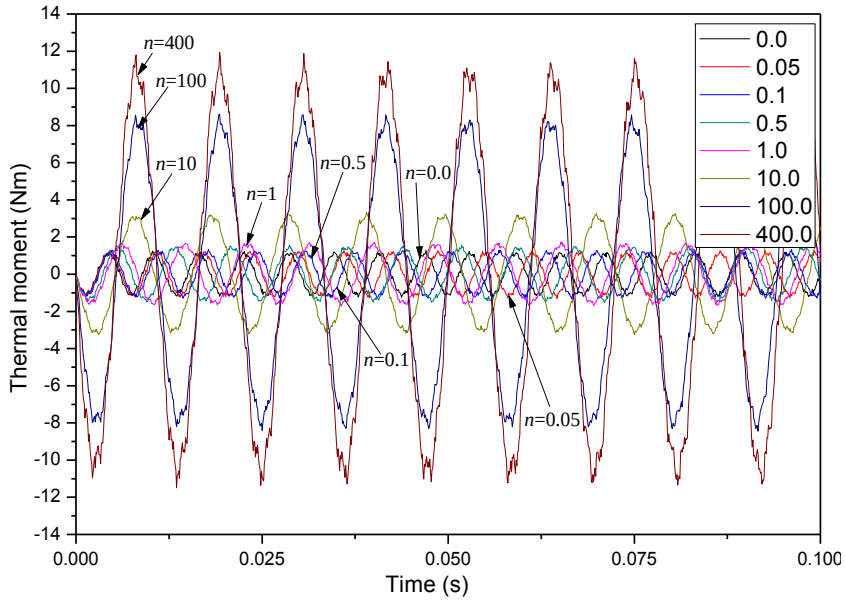

Fig.6.15 Dynamic mid-span thermal moment of simply supported FGM beam for *L/h*=100 with sudden heating on top surface and convection on bottom surface.

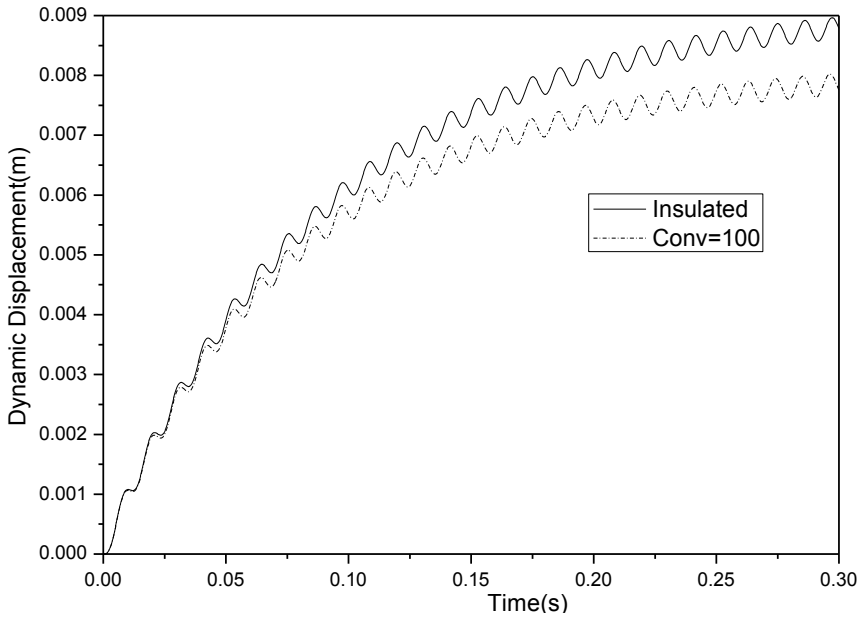

Fig.6.16 Comparison of simply supported beam dynamic mid span deflection for *n*=100 (insulated v/s convection).

Fig.6.16 shows the comparison of the dynamic mid span deflection for the simply supported SUS304-Al_2O_3 FGM beam for power law index of *n*=100, which means that beam is 99.99% metal rich. The top surface of the beam is subjected to step heat source

and bottom surface being (i) insulated and (ii) subjected to natural convective heat transfer coefficient of 100 W/m^2K. It is observed from the plot that during the initial time of the response, the difference in mid span deflection for both the cases is minimal. As the time progresses the beams experience larger static deflection as well as thermal oscillation. The mid span deflection for beam with bottom surface insulated is more than the one with convective heat loss due to higher value of thermal moment driving the vibrations. The difference in the static thermal deflection for the two cases is 1 mm close to the steady state at 300 ms.

6.3 SUMMARY

A linear theoretical analysis is presented on the thermally induced vibrations of FGM beams subjected to step heat input on top surface while the bottom surface is insulated or subjected to convection heat loss. The finite element FORTRAN computer program for FGM beam has been verified with the available literature for beams with simple support subjected to surface heating. Two functionally graded material combinations, aluminium-zirconia and stainless steel-aluminum oxide with temperature dependent and temperature independent material properties were considered for the study. Effect of heat loss by convective heat transfer is also studied for FGM beam subjected to step heat load.

CHAPTER - 7

RESULTS AND DISCUSSION - NONLINEAR FINITE ELEMENT ANALYSIS OF THIN FUNCTIONALLY GRADED MATERIAL BEAMS UNDER THERMAL LOADS

7.1 INTRODUCTION

Thermo-elastic response of the FGM beam is obtained using Newmark's method for linear and geometrically nonlinear formulation presented in Chapter 3. The elastic response of the FGM beam is discussed for various types of heat loads and structural boundary conditions. The study considers one surface of the beam subjected to heat load with opposite surface being thermally insulated. Considering the temperature dependency of material properties, 2-dimensional temperature distribution is obtained for various thermal loads and corresponding nonlinear results of the FGM beam in terms of time dependent deflection and displacement field are analysed. Effect of temperature dependent and temperature independent material properties on thermal deflection is also discussed. Parametric studies are conducted to examine the influences of the various involved parameters. The theoretical formulation for evaluation of stresses for FGM beam was discussed in Chapter 3. Stress analysis in SUS316-Al_2O_3 FGM beam subjected to various types of heat loads under different structural boundary conditions is also discussed in this chapter. The study considers one surface of the beam subjected to heat load with opposite surface being thermally insulated. Considering the temperature dependency of material properties, 2-dimensional temperature distribution is obtained for various thermal loads and corresponding nonlinear stresses are analysed.

7.2 NUMERICAL RESULTS AND DISCUSSION FOR NONLINEAR FORMULATION OF FGM BEAM SUBJECTED TO VARIOUS HEAT LOADS

A FORTRAN computer programme is written based on the formulation outlined in Chapter 4 to study the dynamic response of FGM beams. Numerical analyses are carried out for thin functionally graded material beams with various structural boundary conditions such as hinge-hinge (HH), clamp-pin (CP) and pin-pin (PP) to analyse the thermo-elastic response. First, we present results related to the verification of the geometrically nonlinear finite element code for analysis of FGM beam subjected to step heating. In the second part, the thermo-elastic response obtained by solving non-linear finite element equations for various thermal loads is presented and influence of structural boundary conditions and power law index is discussed. Parametric studies are also presented to study the effect of temperature dependent and temperature independent material properties, geometric nonlinearity and stiffness coefficients on thermal deflections.

7.2.1 Convergence for 2D thermal analysis

Table 7.1: Convergence of temperature for moving heat source for different mesh size.

Mesh size $(x \times z)$	Maximum temperature on top surface (^{0}C) at centre of beam
50 × 5	4.27747
50 × 6	4.67742
50 × 8	5.14621
50 × 10	5.36365
50 × 12	5.47161
50 × 15	5.55307
50 × 20	5.61253
75 × 10	6.32608
100 × 10	7.00809
125 × 10	7.49860
150 × 10	7.90439
200 × 10	8.49484
100 × 12	8.22919
150 × 12	8.49232

As a first endeavour, the study is carried out to find the number of layers required to achieve temperature convergence in z direction. The temperature is calculated for

moving heat load case. The number of layers considered for the study are 5 to 20 while number of elements in x direction were maintained as 50. In the second case, the number of layers were maintained constant and the number of elements in the x-direction were varied from 50 to 200 to study the convergence of temperature in x direction. The temperatures obtained for various mesh size using the 2D finite element computer programme is shown in Table 7.1. It is observed that increasing the number of elements in the x and z-directions leads to converged results. The convergence of non-linear transverse deflection was also studied and it was observed that a minimum of 60 elements are required in x direction to obtain converged results. Hence, a 2D mesh size of 150×12 (the number of elements along the x and z-directions, respectively) is sufficient to obtain acceptable results. Here-onwards unless otherwise specified, in generating the numerical results using the FEM for various heat loads, this mesh size has been used.

7.2.2 Verification problem, simply supported FGM beam subjected to step heating

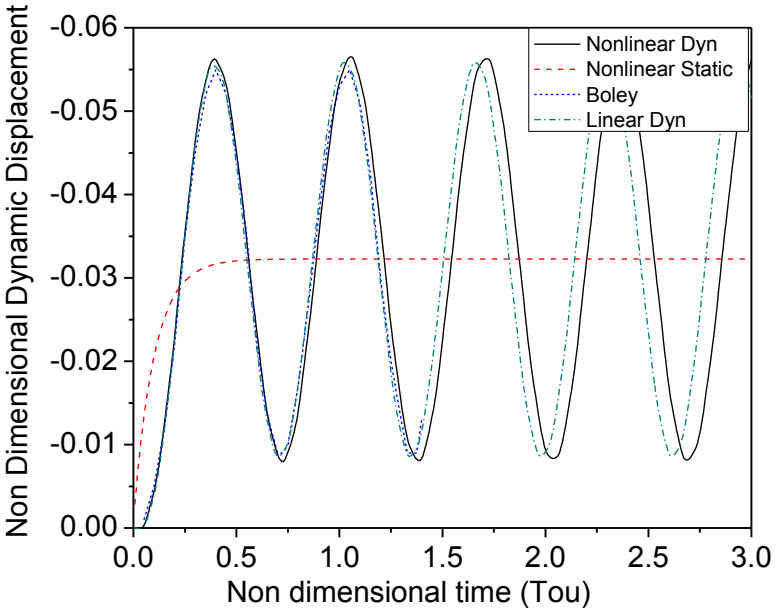

Fig.7.1 Non dimensional dynamic mid-span deflection of simply supported (H-H) beam.

The simply supported (HH) FGM beam problem discussed in section 6.2.1, Fig.6.2 has been revisited here and analysed using nonlinear FEM code and results are presented

in Fig.7.1. Dynamic response is obtained for time, t=0.085 s. When the power law index is set to n=0.0, FGM beam reduces to pure aluminium. Heat flux on the bottom surface is, Q=1.63×10^6 W/m^2. The properties are assumed to be independent of the temperature and results are evaluated considering ambient temperature of zero degree Celsius. The thermo-physical data for the Aluminium and beam dimensions are as referred from Boley (1956). As seen from Fig.7.1, and discussed in 6.2.1, it is found that the trends of the linear dynamic mid-span deflection are in good agreement while there is little shift for nonlinear dynamic mid-span deflection for HH beam. For nonlinear analysis, the shift is due to consideration of nonlinear geometry terms in the analysis.

Ghiasian et al. (2014) has presented numerical results on lateral vibration of SUS304-Si_3N_4 simply supported FGM beam having geometric parameters as length, $L = 100$ mm and height, $h = 1$ mm with power law index $n = 1.0$. First order shear deformation theory along with von-Kármán strain are used for the studies. A constant step temperature of 330K is applied on the top surface while bottom surface is insulated with free air stream temperature of 300K. Ghiasian et al. have used a 1-D heat conduction equation for temperature evaluation. For this particular problem, results on lateral vibration are obtained using present nonlinear thermal and structural code with 1-D and 2-D temperature distribution. The verification is illustrated in Fig.7.2. It is observed that the results obtained by Euler–Bernoulli theory with von-Kármán geometric nonlinearity using 1-D temperature distribution are in good agreement with the results obtained by Ghiasian et al. Referring to Fig.7.2(b), wherein the same problem has been attempted by using 2-D temperature distribution. The lateral displacements obtained using the second approach (using temperature distribution on transverse plane) agree reasonably well in terms of wavelength of the lateral displacements and amplitudes with respect to Ghiasian et al. The difference in the thermal deflection obtained using 1D temperature distribution and 2D temperature distribution is worth noting. As seen in Fig.7.2(b), the thermal deflection obtained using 2D temperature distribution are offset downwards from 0.0 to 0.01 s and from times 0.025 s and beyond the offset is upwards with respect to Ghiasian et al. (2014).

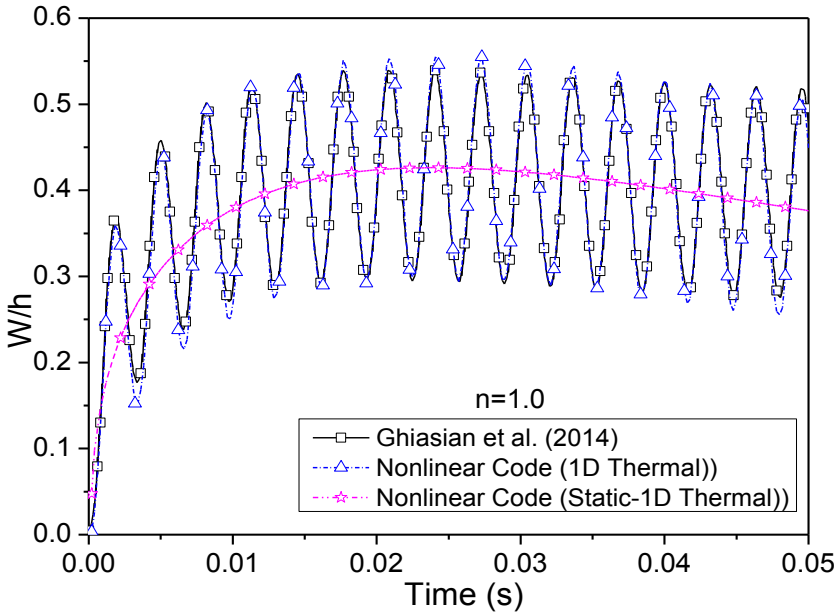

(a) 1-D heat conduction solution

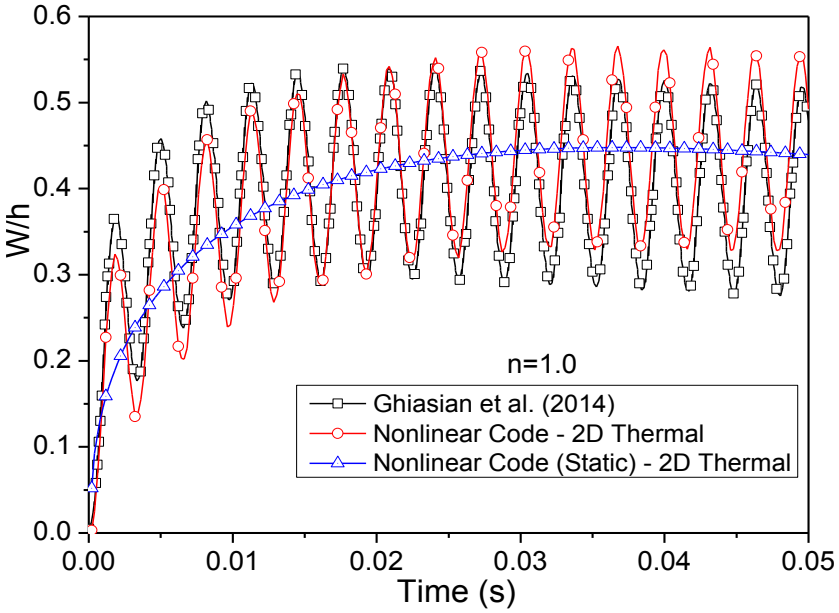

(b) 2-D heat conduction solution

Fig.7.2 Comparision of nonlinear thermo-elastic deflection for simply supported beam with step heating.

Fig.7.3 shows the corresponding temperature distribution with respect to time for FGM beam when subjected to step heating using 1-D and 2-D heat conduction equation for temperature evaluation. The temperature throughout the length of the beam for step heating is constant and gradually decreases from the surface which is exposed to heat toward the insulated surface. Also, it is observed from Fig.7.3 that as the time

progresses, the temperature of the beam gradually increases from reference temperature of 300 K to maximum. The temperature-time variation is more or less same based on the results obtained from the 1D and 2D heat conduction equation. The temperatures evaluated using the 2D heat conduction code and 1D heat conduction code differ slightly with a root mean square error of 1.696. Further, the temperature time gradient is more flat in the case of the 2D approach compared with that of the 1D heat conduction approach, see Fig.7.3, from times after 0.01 s.

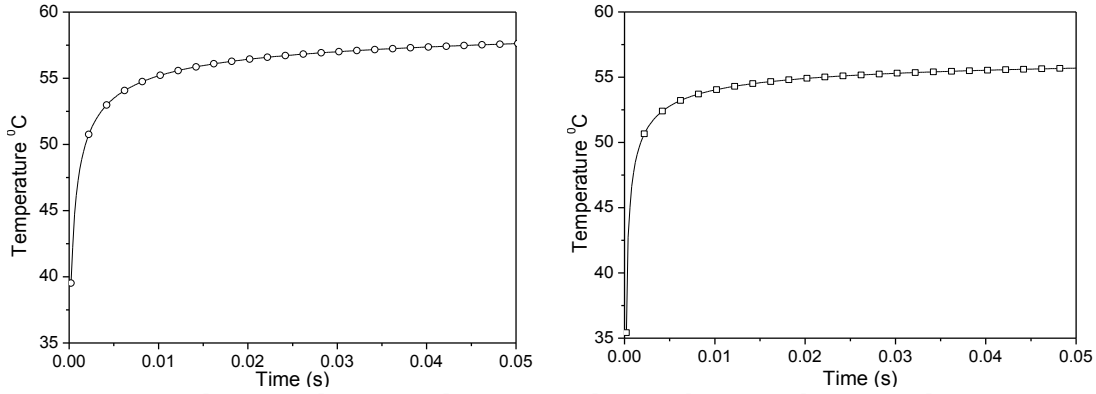

(a) 1-D heat conduction solution (b) 2-D heat conduction solution

Fig.7.3 Temperature distribution at centre with respect to time for FGM beam subjected to step heating.

7.2.3 Effect of material grading index and physical boundary conditions on nonlinear thermo-elastic vibrations of beams subjected to various heat loads

The material considered for the study is gradation of Stainless Steel and Aluminium Oxide (SUS316-Al_2O_3). The temperature dependent material properties for SUS316 and Al_2O_3 of the FGM systems, considered for computing the effective properties of the layers, are tabulated in Table 4.2. Initially the beam is considered to be free of any stresses at time $t = 0$ and temperature T_0. The beam is consider to undergo a sudden temperature rise due to step heat flux, moving line heat source, concentrated line heat source at centre and shock load. In case of step heating or shock load, since the constant heat is applied on entire surface of the beam, the temperature variation is only across the thickness of the beam and can be solved with one dimensional heat transfer problem

[Ghiasian et al. (2014)]. In case of moving line heat source or concentrated line heat source at centre, in addition to temperature variation across the thickness there is also temperature variation along the length of the beam and we need to solve a two dimensional heat transfer problem [Malekzadeh and Shojaee (2013, 2014)]. This type of heat sources are seen in laser cutting, heating of billet in furnace, surface hardening, flame hardening, plasma spraying, high velocity oxy-fuel spray, etc. The equations governing the conduction of heat in two dimensional co-ordinate is given by Eq.(3.10). To solve the Eq.(3.10) for specified boundary and initial conditions, the two dimensional four noded Lagrange rectangular finite element are used to discretise the domain. The heat load boundary condition on the ceramic rich surface, $z = h/2$ at time t_i is the prescribed heat flux q^* (see Eq.3.31) defined as follows,

Step heating: $q^* = 0$ for $t < 0$, $x = 0, L$ (7.1a)

$q^* = Q$ for $t \geq 0$, $x = 0, L$ (7.1b)

Shock heat: $q^* = 0$ for $t < 0$, $x = 0, L$ (7.2a)

$q^* = Q$ for $0 \leq t \leq t_{\max}/5$, $x = 0, L$ (7.2b)

$q^* = 0$ for $t > t_{\max}/5$, $x = 0, L$ (7.2c)

Moving line heat source: $q^* = 0$ at $t < 0$ (7.3a)

$q^* = Q$ for $t \geq 0$, $x = (t_i / t_{\max})\, L$ (7.3b)

Concentrated line heat source: $q^* = 0$ for $t < 0$, $x = L/2$ (7.4a)

$q^* = Q$ for $t \geq 0$, $x = L/2$ (7.4b)

whereas the surface $z = -h/2$ is considered to be insulated. $t_{\max}$ is the maximum time duration for which heat load is present. The maximum time in the present study varies from 0.025 s to 0.2 s. The heat loss from the side walls of the beam is also neglected. The temperature variation is assumed to happen only in the thickness direction and along the length of the beam. The results are evaluated considering ambient temperature of zero degree Celsius. The geometric dimensions of the beam are: $L = 0.1$ m and $h = 0.001$ m. Fig.7.4 shows the position of various heat source at time $t = 0.01$

s. At a given time a total heat load of 100 W is applied on the beam surface. In case of step and shock heating the total heat load is distributed discretely on the beam surface such that the sum of the discrete heat load is 100 W while for point and moving heat source the intensity of heat load is 100 W at a particular location on the beam.

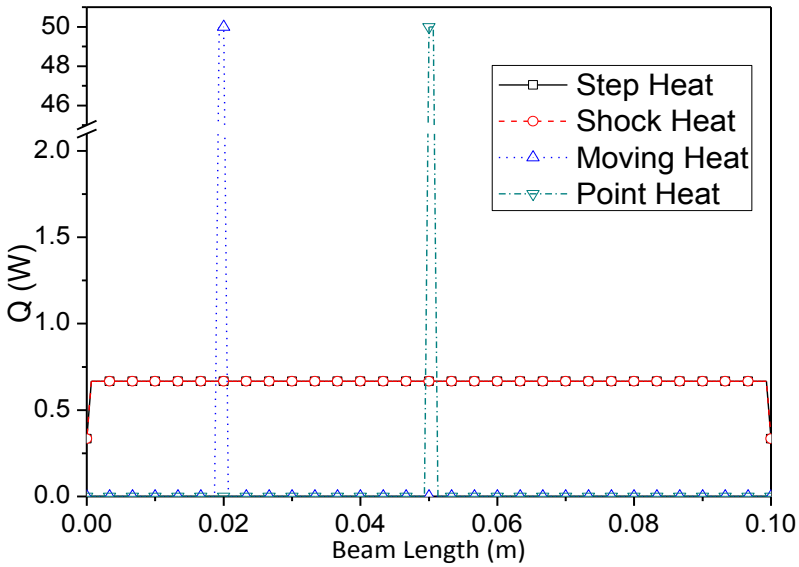

Fig.7.4 Different heat source condition at t=0.01s.

7.2.3.1 Step heating

The beam is subjected to step heating on bottom surface (Q=100 W) and insulated on the top surface. Fig.7.5 shows the dynamic mid span deflection for a pin-pin SUS316-Al_2O_3 FGM beam for various volume fractions of ceramic. The thermal deflections increases with time due to the step heat load as shown in Fig.7.5(a). Apart from thermal deflections the beam also oscillates. The ceramic rich beam (n = 400.0, 50.0, and 10.0) undergoes smaller magnitude of static deflections and deflections become steady within 10 ms whereas metal rich beams (n = 0.0, 0.1 and 1.0) exhibit higher value of static deflection, increasing gradually with time and deflection become steady after 50 ms.

The thermal moment as shown in Fig.7.5(b) for various power law index are the cause for thermal deflection. It is observed that the dynamic thermal moment is maximum for metal rich beam with n =0.0 and decrease as the power law index increase towards ceramic rich beam. The dynamic thermal moment pattern is similar to dynamic midspan

deflection with oscillating values of thermal moment about a mean value other than zero. The thermal oscillations, as the beam deflects also depends on the axial force due to the step heat load shown in Fig.7.6. For a beam with material distribution of ceramic and metal being linear i.e. power law index equal to 1.0, the axial force is maximum and tensile in nature. Axial force of compressive nature is induced in the metal rich beam while for ceramic rich beam the axial force is minimal.

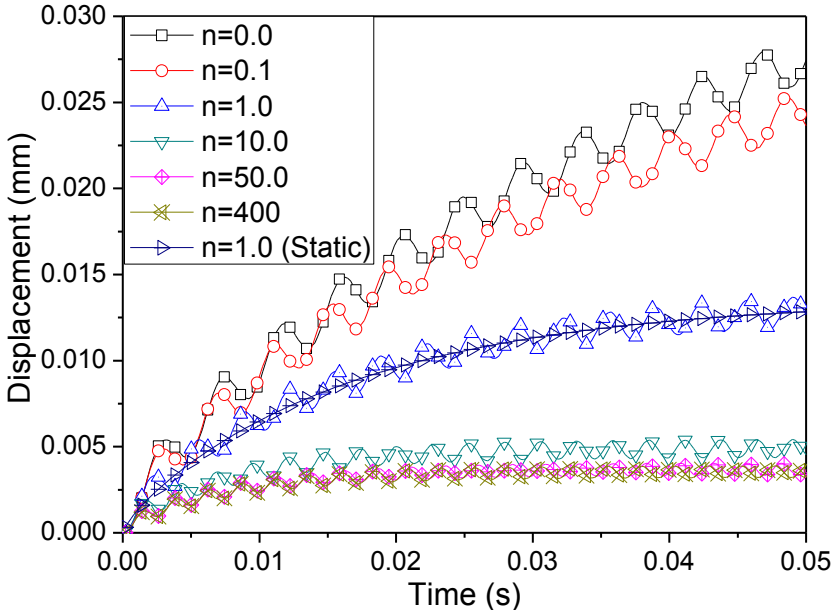

(a) Dynamic mid-span deflection

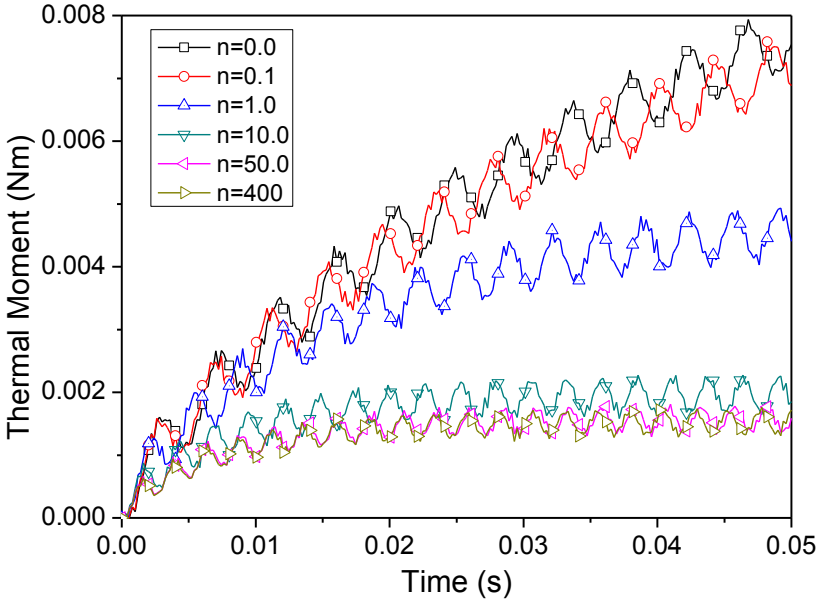

(b) Dynamic thermal moment

Fig.7.5 Pin-pin FGM beam subjected to step heating.

Fig.7.7(a) shows the dynamic mid-span deflection for HH FGM beam. Fig. 8.7(b) shows the mid-span dynamic thermal moment for HH beam and has similar characteristic and amplitude as of PP beam subjected to step heating as shown in Fig.7.5(b). Fig.7.8 shows the dynamic mid-span axial force for hinge-hinge FGM beam subjected to step heating. Since both the ends of the beam are free to move, hardly any axial force is induced in the HH beam at centre.

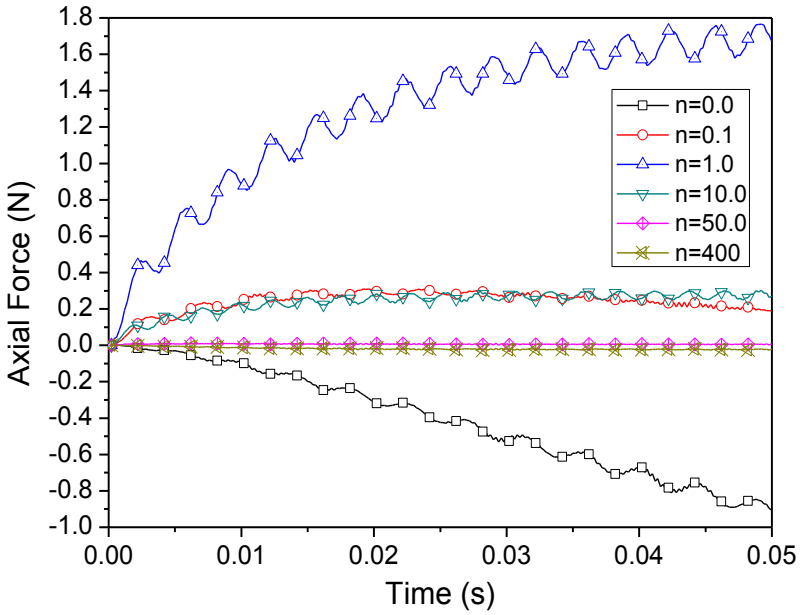

Fig.7.6 Dynamic mid-span axial force for pin-pin FGM beam subjected to step heating.

Fig.7.9(a) shows the dynamic mid-span deflection for CP FGM beam while Fig.7.9(b) shows the mid-span thermal moment. The dynamic mid-span thermal moment as seen from Fig.7.9(b) has similar characteristics of PP beam while the amplitude of the thermal moment is 0.25 times that of PP beam. Fig.7.10 shows the dynamic mid-span axial force for clamp-pin FGM beam subjected to step heating. The highest value of axial force is observed for power law index of 1.0 and reduces as power law index increases. It is observed that the PP and HH beams have similar deflection pattern whereas the maximum deflection of CP beam is 5 times smaller than PP and HH beam as clamped boundary condition at one end makes beam stiffer in case of CP boundary condition.

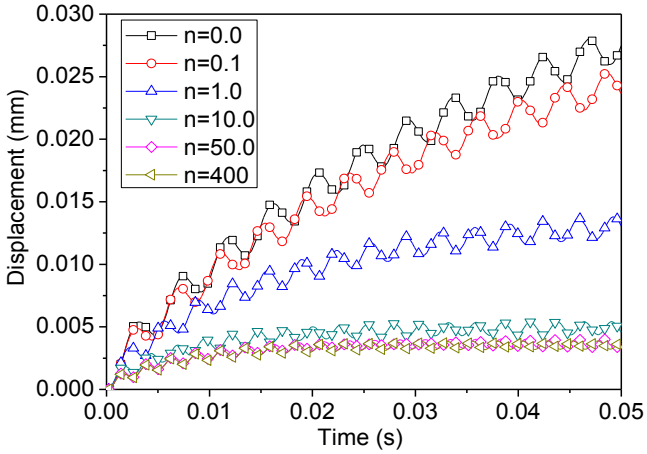

(a)

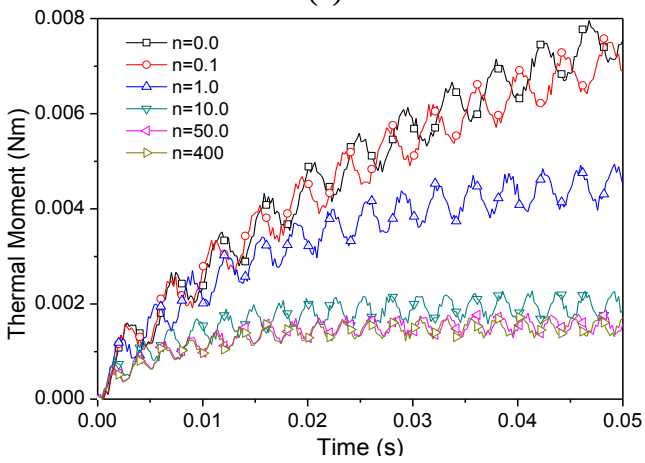

(b)

Fig.7.7 (a) Dynamic mid-span deflection (b) thermal moment for hinge-hinge FGM beam subjected to step heating.

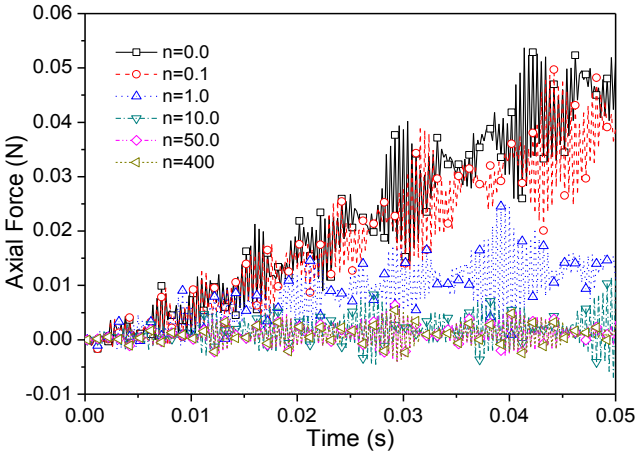

Fig.7.8 Dynamic mid-span axial force for hinge-hinge FGM beam subjected to step heating.

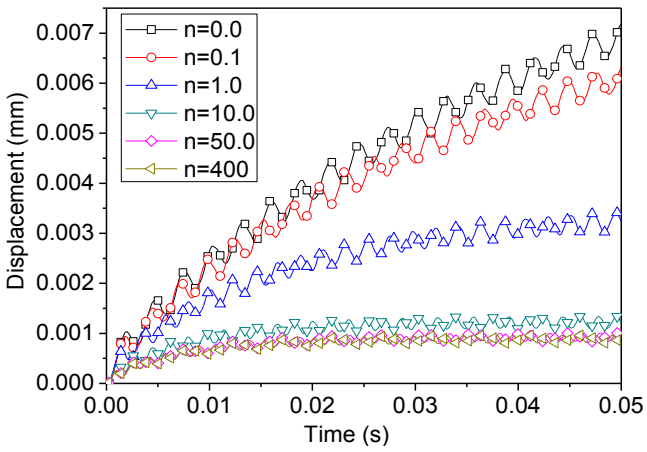

(a)

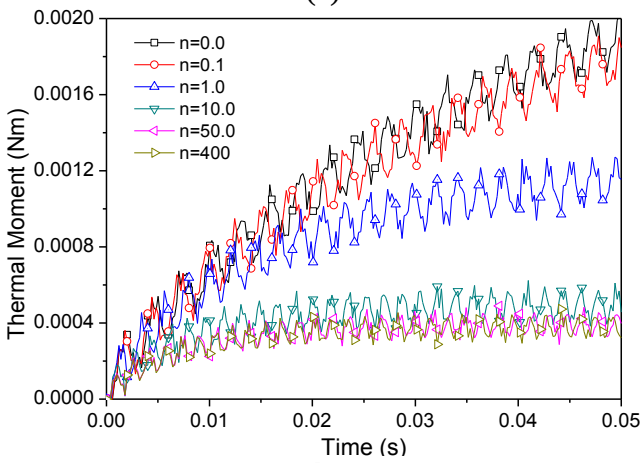

(b)

Fig.7.9 (a) Dynamic mid-span deflection (b) thermal moment for clamped-pin FGM beam subjected to step heating.

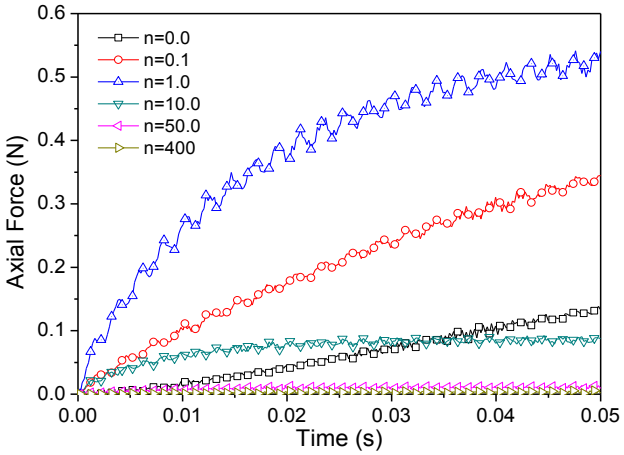

Fig.7.10 Dynamic mid-span axial force for clamp-pin FGM beam subjected to step heating.

7.2.3.2 Shock heat

The beam is subjected to shock heating on bottom/outer surface and insulated on the top surface. A total heat load of 100 W is applied on the entire beam surface for a very short time interval of 0.01 s. The temperature distribution and thermo-elastic response is studied for 0.05 s. Fig.7.11 shows the temperature variation with respect to time for the surface exposed to shock heating. During the time when the heat source is present, the temperature gradually increases to a maximum, similar to that found for step heat source and once the heat source is removed the temperature gradually decreases with respect to time. The time for maximum temperature rise of the FGM beam is independent of the power law index as seen in Fig.7.11 and the temperature rise decreases as the power law index increases.

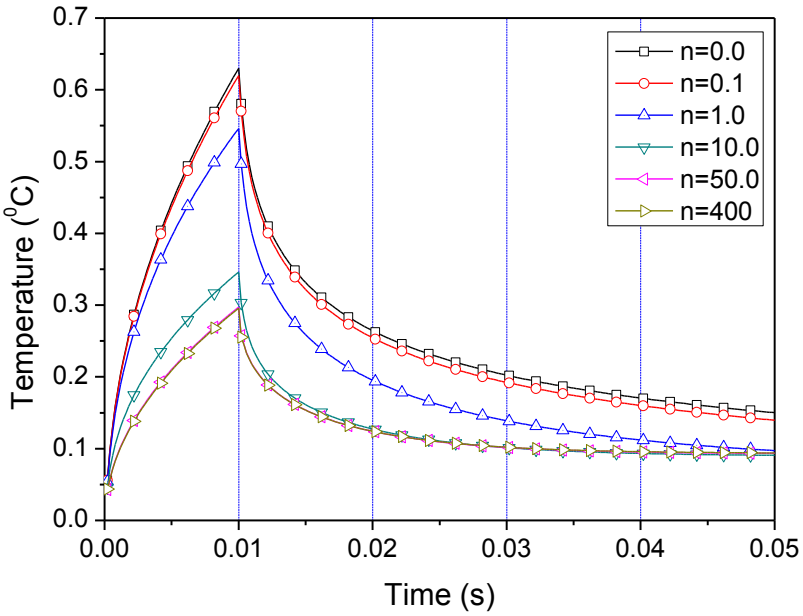

Fig.7.11 Temperature distribution at centre with respect to time for FGM beam subjected to shock heating.

It is seen from Fig.7.11 and Fig.7.12(a) that the maximum thermo-elastic deflection occurs at around 0.01 s when the temperature is maximum. The maximum deflection for FGM beams with n =0.0 and 0.1, occurs after 0.01 s and subsequently the displacement decline gradually. The thermal moment as shown in Fig.7.12(b) are the cause for thermal deflection. The thermal oscillations, as the beam deflects also depends on the axial force due to the step heat load shown in Fig.7.13. The maximum deflection for n =1.0, 10.0, 50.0 and 400, occurs before 0.01 s. The magnitude of the deflections

are higher for $n \leq 1.0$ and considerably low in magnitude for FGM beams with n >10.0. The amplitude of thermal deflection increases until the shock load is present, say approximately 0.01 s. Once the shock load is removed, the thermal deflection reduces gradually with oscillation for n =0.0, 0.1 and 10.0 and minimal or negligible oscillation are seen for n =1.0, 50.0 and 400. The thermal deflection gradually decreases as the temperature decreases with time and becomes steady at around 0.05 s with thermal oscillation. Similar phenomenon is observed for hinge-hinge SUS316-Al_2O_3 FGM beam as shown in Fig.7.14.

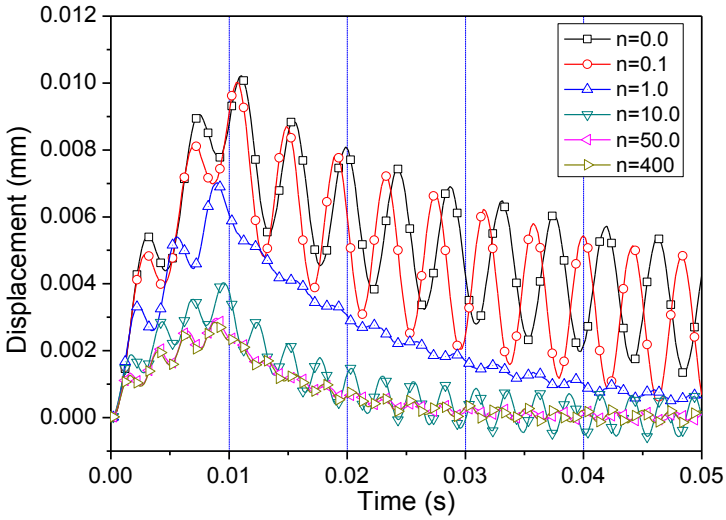

(a)

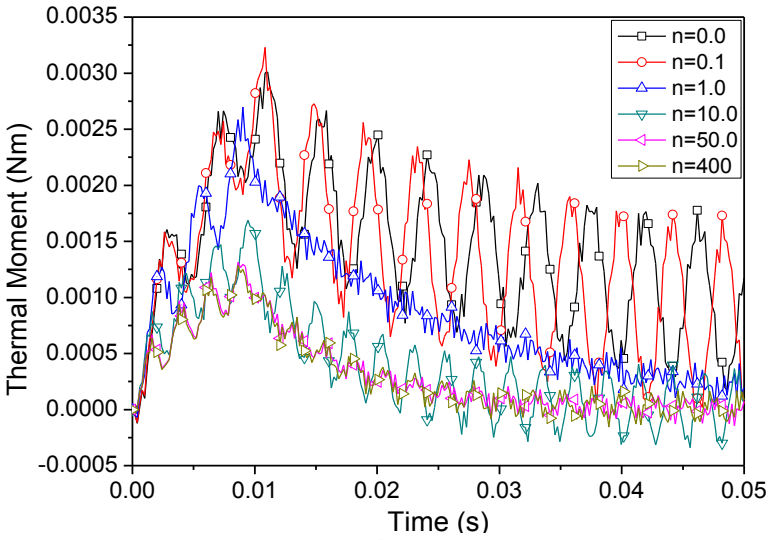

(b)

Fig.7.12 (a) Thermo-elastic mid-span deflection (b) dynamic thermal moment for pin-pin FGM beam subjected to shock heating.

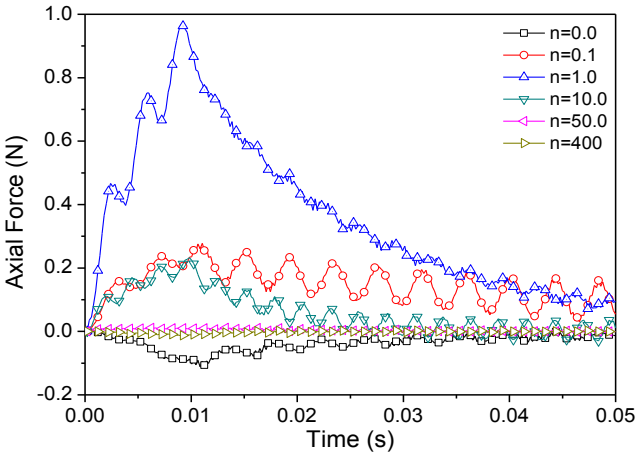

Fig.7.13 Dynamic mid-span axial force for pin-pin FGM beam subjected to shock heating.

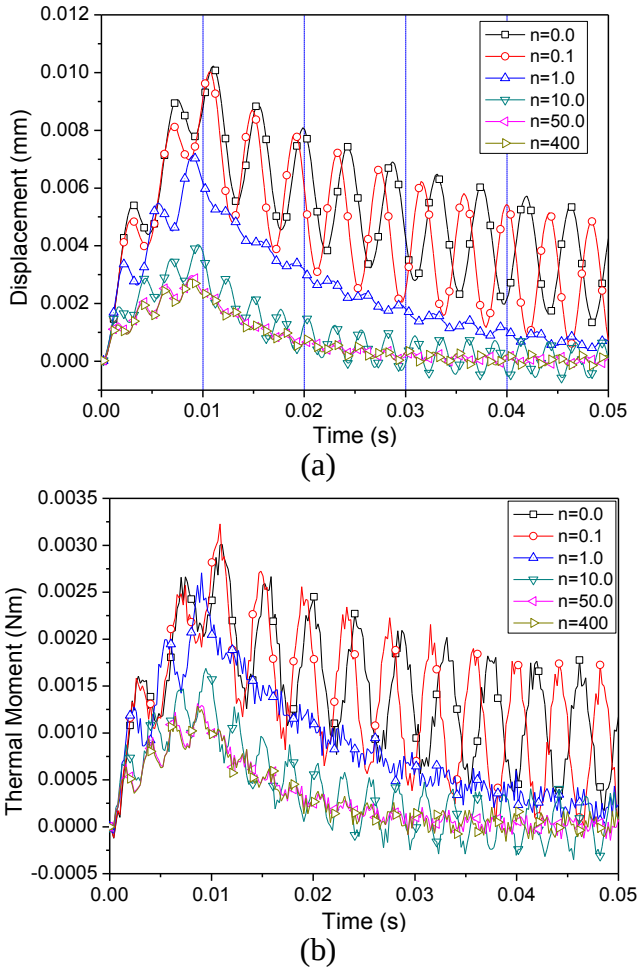

Fig.7.14 (a) Thermo-elastic mid-span deflection (b) Dynamic thermal moment for HH FGM beam subjected to shock heating.

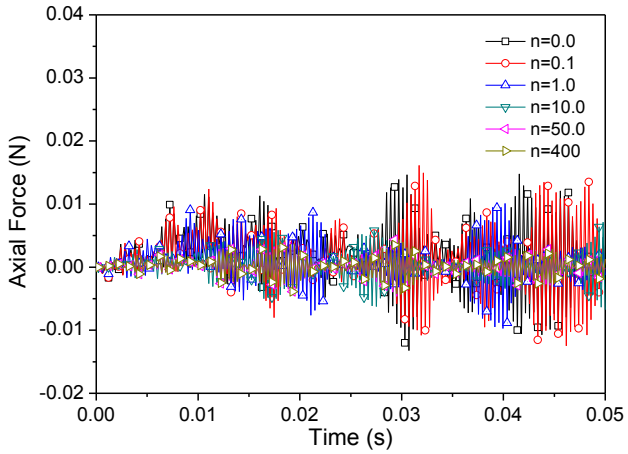

Fig.7.15 Dynamic mid-span axial force for HH FGM beam subjected to shock heating.

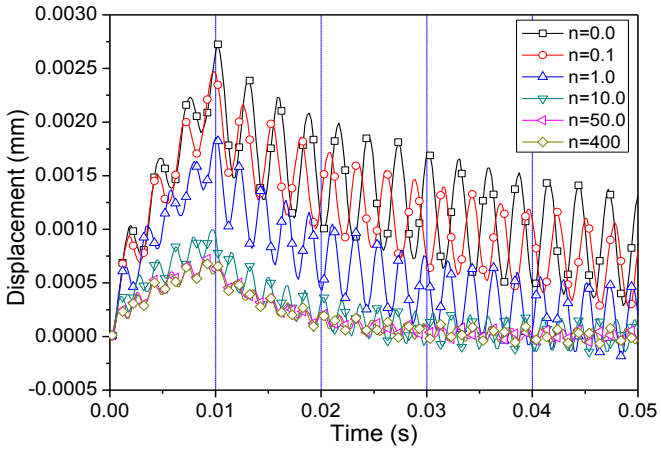

(a)

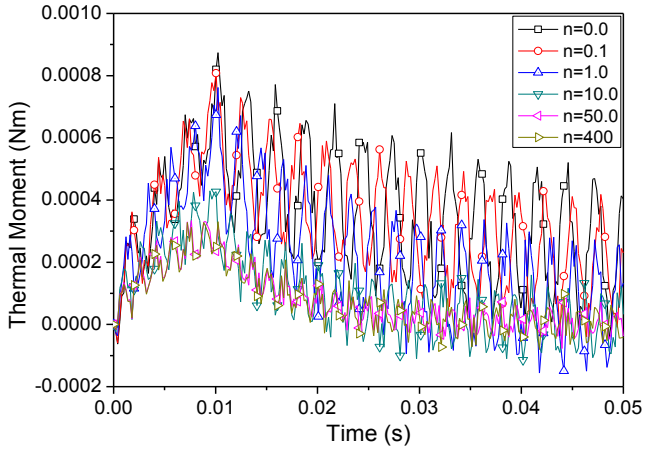

(b)

Fig.7.16 (a) Thermo-elastic mid-span deflection (b) Dynamic thermal moment for clamp-pin FGM beam subjected to shock heating.

The metal rich beam shows higher value of thermal deflection as compared to ceramic rich beam and have similar deflection pattern for both PP and HH beams. As HH beam is free to expand axially, hardly any axial force is seen acting on the HH beam as shown in Fig.7.15. Comparison shows that, the absolute value of thermo-elastic deflection of PP beam is marginally higher than HH beam which is due to axial constraints at both the ends for PP beam and higher axial force. As seen from Fig.7.16, the CP beam shows trends similar to PP and HH beam. The absolute value of thermo-elastic deflection for PP and HH beam is 4 times the absolute value of thermo-elastic deflection for CP beam. Irrespective of the power law index, the maximum deflection for CP beam occurs at 0.01 s when the heat source is removed. As seen from Fig.7.17, the axial force for CP beam shows trends similar to PP beam and is $1/4^{th}$ of the PP beam.

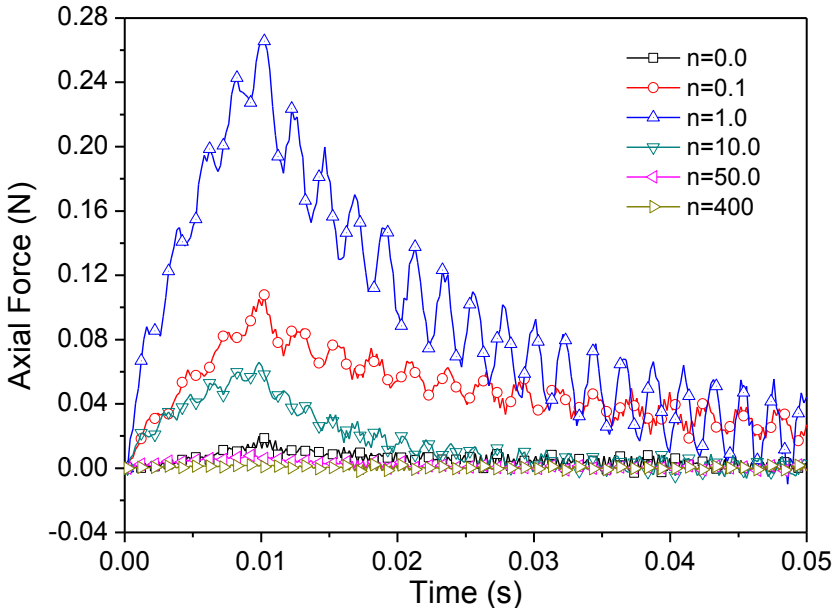

Fig.7.17 Dynamic mid-span axial force for clamp-pin FGM beam subjected to shock heating.

7.2.3.3 Concentrated line heat source at centre

The beam is subjected to concentrated line heat source of 100 W at the centre of the beam on bottom surface and insulated on the top surface. Line heat source has the meaning that the heat source is in the form of a line and spans the width of the beam, interchangeably referred to as point heat source in the present work. Fig.7.18(a) shows

the temperature distribution along the length of the beam for line heating (n =1.0) at t =0.05 s and Fig.7.18(b) shows the temperature variation with respect to time for the surface exposed to line heat source. The temperature at the centre of the beam rises and falls sharply, the profile resembling a spike. Locally the temperature shoots to a large magnitude. However temperature rise away from the heat source is minimal. From Fig.7.18(b), it is observed that as the time progresses, the temperature at centre of the beam gradually increases.

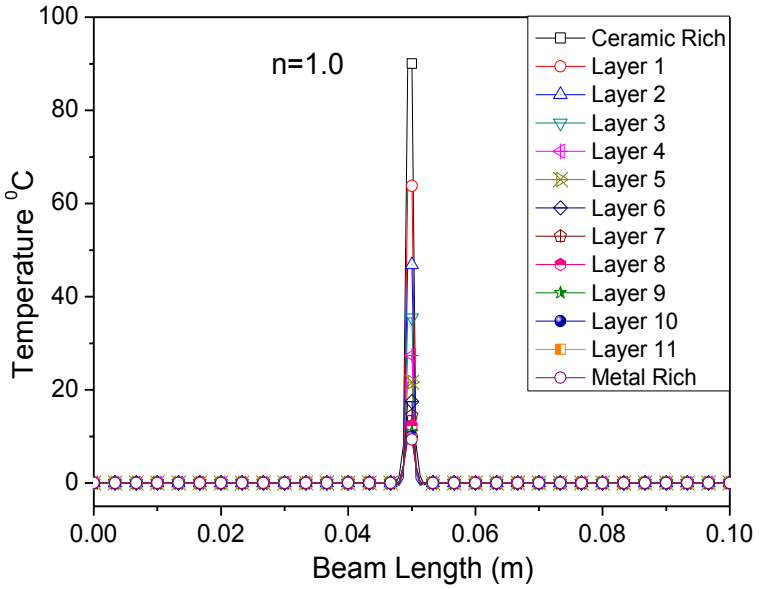

(a) along the length of beam

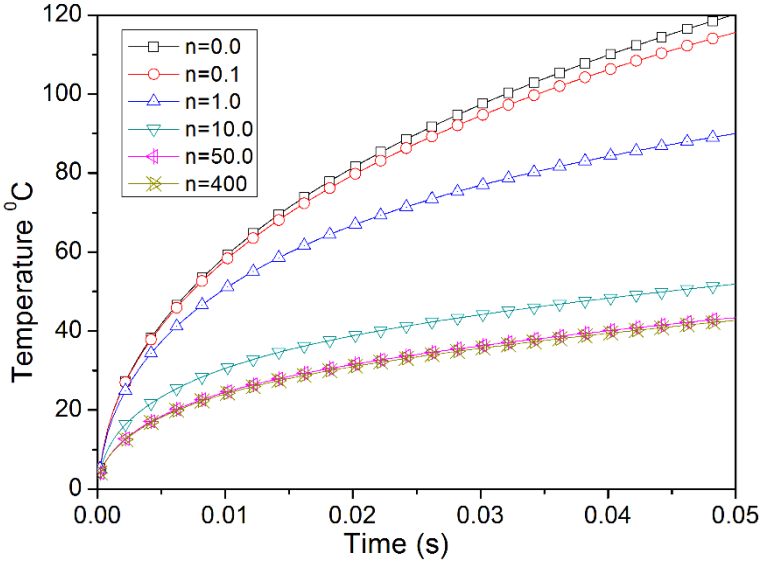

(b) with respect to time at mid point

Fig.7.18 Temperature distribution for FGM beam subjected to line heat source of 100 W at centre.

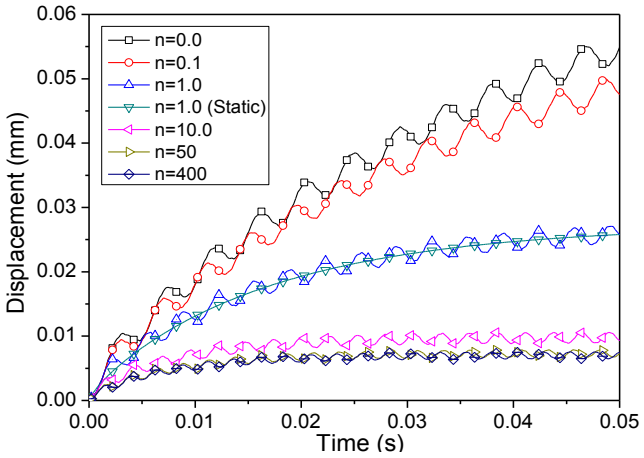

(a)

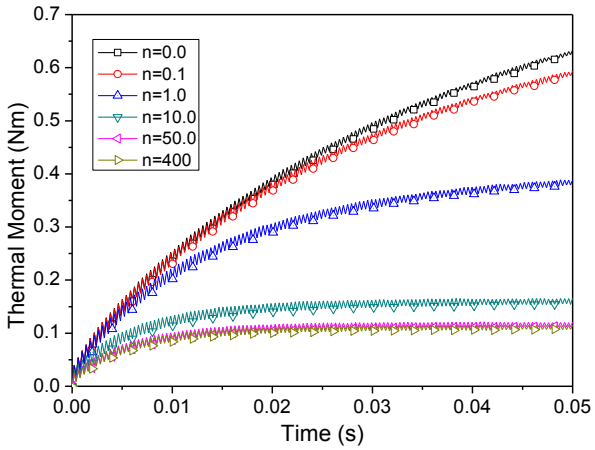

(b)

Fig.7.19 (a) Thermo-elastic mid-span deflection (b) Dynamic thermal moment for Pin-pin FGM beam subjected to concentrated line heat source at center.

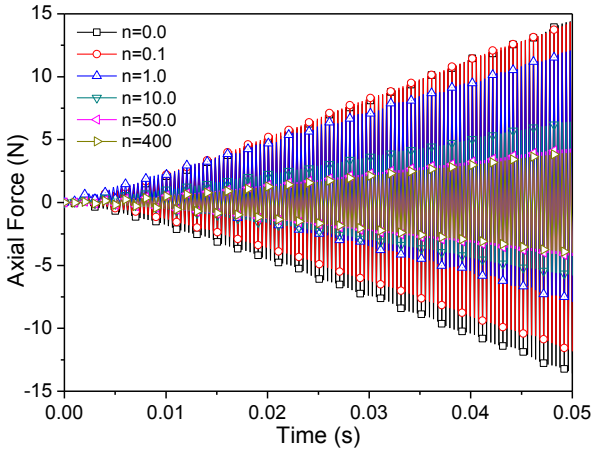

Fig.7.20 Dynamic mid-span axial force for pin-pin FGM beam subjected to concentrated line heat source at center.

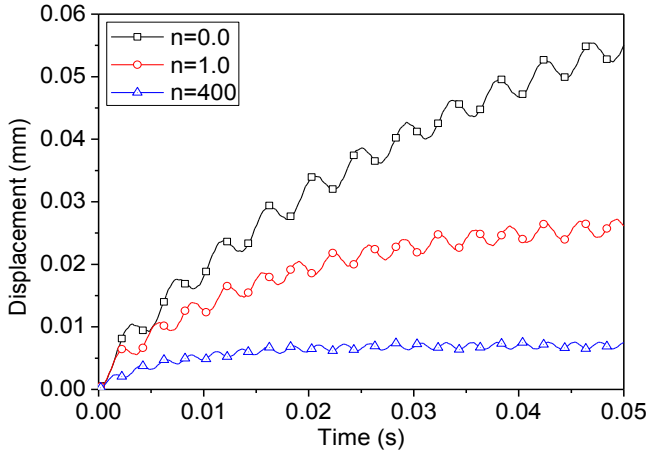

(a)

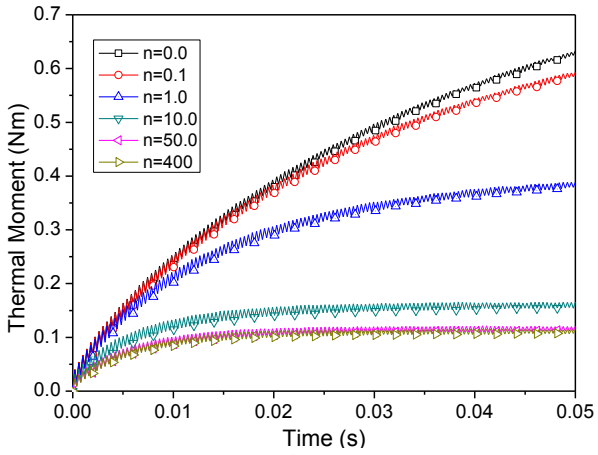

(b)

Fig.7.21 (a) Thermo-elastic mid-span deflection (b) Dynamic thermal moment for HH FGM beam subjected to concentrated line heat source at center.

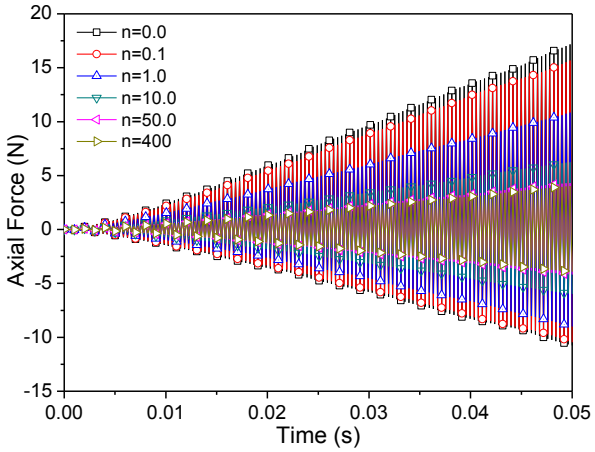

Fig.7.22 Dynamic mid-span axial force for HH FGM beam subjected to concentrated line heat source at center.

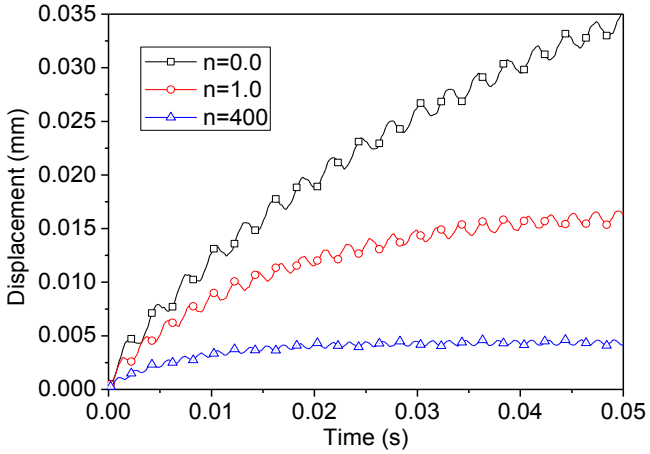

(a)

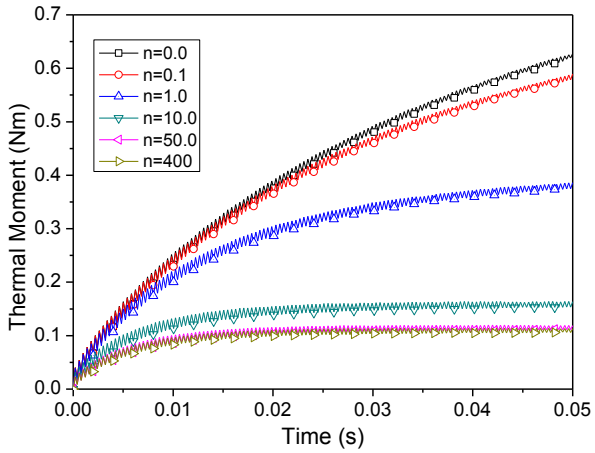

(b)

Fig.7.23 (a) Thermo-elastic mid-span deflection (b) Dynamic thermal moment for clamp-pin FGM beam subjected to concentrated line heat source at center.

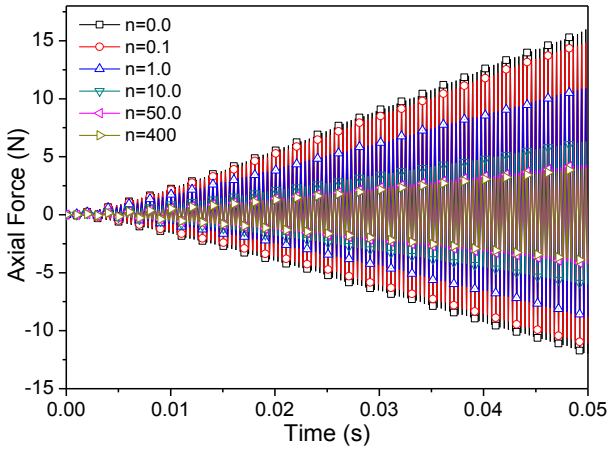

Fig.7.24 Dynamic mid-span axial force for clamp-pin FGM beam subjected to concentrated line heat source at center.

Fig.7.19(a) shows the thermo-elastic mid span deflection and Fig.7.19(b) shows dynamic thermal moment for a pin-pin SUS316-Al_2O_3 FGM beam for various power law index. It is seen from Fig.7.19(a) that the dynamic displacement increases initially from time t=0 and as time progresses, the beam oscillates with constant amplitude about static displacement. The thermal moment as shown in Fig.7.19(b) are the cause for thermal oscillation. The thermal oscillation also depend on the axial force due to concentrated heat load as shown in Fig.7.20. The trend of the static deflection for n =1.0 in Fig.7.19(a) is similar to the temperature profile as seen from Fig.7.18(b). The ceramic rich beam ($n = 400.0$, 50.0, and 10.0) undergoes smaller magnitude of static deflections and deflections becomes steady within 10 ms whereas metal rich beams ($n = 0.0$ and 0.1) exhibit higher value of static deflection, increasing gradually with time and deflection become steady after 50 ms. It is also observed from Fig.7.19(a) that the amplitude of the thermal oscillations about the mean static thermal deflection for ceramic rich beam is less whereas frequency of thermal oscillation is higher for metal rich beam. The temperature induced oscillations occur about the static thermal deflection irrespective of the volume fraction. Fig.7.21 and Fig.7.23 shows the thermo-elastic mid span deflection and dynamic thermal moment for a SUS316-Al_2O_3 FGM beam with HH and CP boundary conditions respectively for various volume fractions of ceramic. The corresponding axial force is shown in Fig.7.22 and Fig.7.24 respectively for HH and CP FGM beam. The thermo-elastic displacement has similar characteristics as of beam with PP boundary condition with absolute value of thermo-elastic deflection for HH equal to PP beam and CP beam having absolute value of thermo-elastic deflection equal to half that of beam with PP boundary condition.

7.2.3.4 Moving line heat source

The beam is subjected to a moving line heat source of 100 W on bottom surface and insulated on the top surface as shown in Fig.7.25. The study is carried out to analyse the effect of velocity of the moving heat source and structural boundary conditions on the thermo-elastic deflection of the beam.

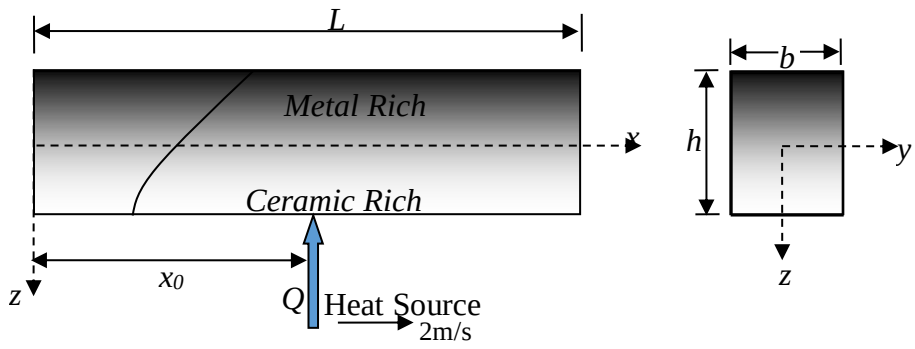

Fig.7.25 Geometry of typical FGM made of SUS316 and Al_2O_3 with moving heat source.

For heat source moving at velocity of 2m/s, Fig.7.26, Fig.7.27 and Fig.7.28 respectively, shows the temperature distribution at the centre, start-centre-end and across thickness of the PP beam. Depending on the location of the moving heat source along the beam, at the corresponding location a sharp temperature rise occurs as depicted in Fig.7.26 and Fig.7.27. For the moving heat source moving at 2 m/s, Fig.7.29(a) shows the thermo-elastic mid span deflection while Fig.7.29(b) shows dynamic thermal moment for a PP SUS316-Al_2O_3 FGM beam for various volume fractions of ceramic. The corresponding axial force is shown in Fig.7.30. For both PP and HH beams, referring to Fig.7.29(a) and Fig.7.31(a), the following observations are noted. The maximum deflection of the FGM beam depends on the power law index. As seen in Fig.7.31(a), for n =0.0, 1.0 and 400 the maximum deflection occurs at time 0.04 s, 0.033 s and 0.028 s respectively. The time for maximum deflection and time for maximum temperature rise at the centre of the beam do not coincide. Irrespective of the power law index, the maximum temperature at the centre of the beam occurs at 0.025 s (see Fig.7.26). Now referring to Fig.7.29(a), the maximum centre deflection for power law index n =0.0 to 400 occurs in the range 0.038 to 0.028 s respectively. This means that there is large time lag between maximum temperature rise at the centre of the beam and maximum centre deflection in case of metal rich beam and it is marginally small for ceramic rich beam. For both PP and HH beams, it is seen from Fig.7.29(a) and Fig.7.31(a) that the thermo-elastic deflection increases gradually with time, attains maximum value once the heat source crosses the centre of beam and then starts

decreasing with no thermal oscillations. This is due to the fact that, as the heat source moves beyond the centre of the beam, sufficient thermal moment is developed (refer Fig.7.29(b) and Fig.7.31(b)) which leads to higher thermal deflection. The metal rich beam shows thermal deflections 5 times higher than that of a ceramic rich beam.

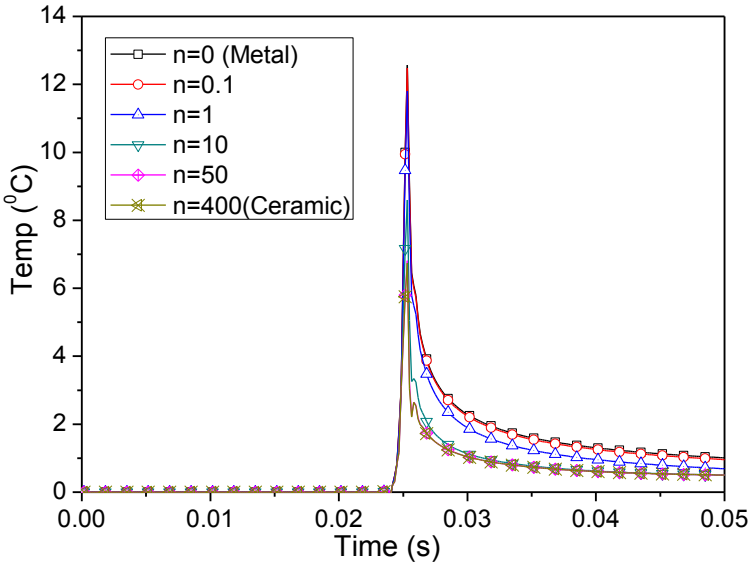

Fig.7.26 Temperature distribution at the centre of the pin-pin beam for various values of n at velocity of 2m/s.

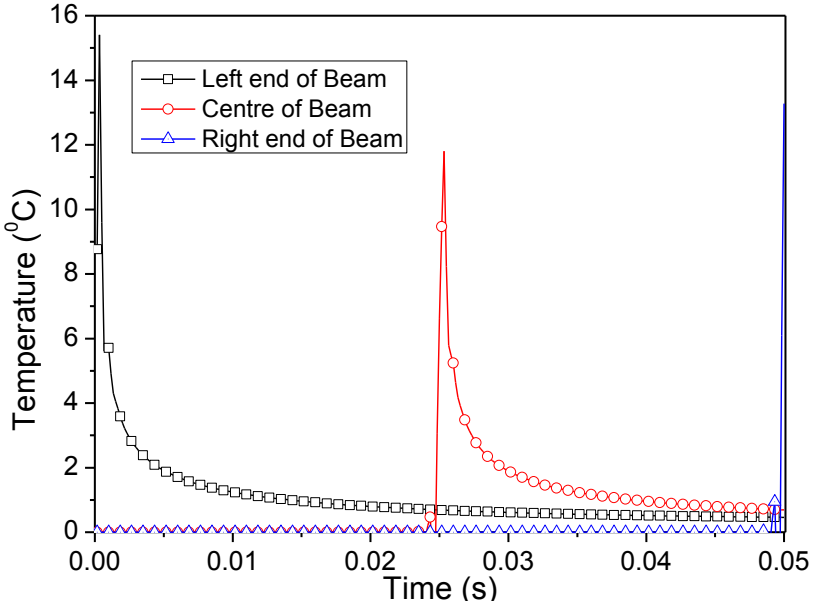

Fig.7.27 Temperature distribution at the start-centre-end of the pin-pin beam for $n=1$ at velocity of 2m/s.

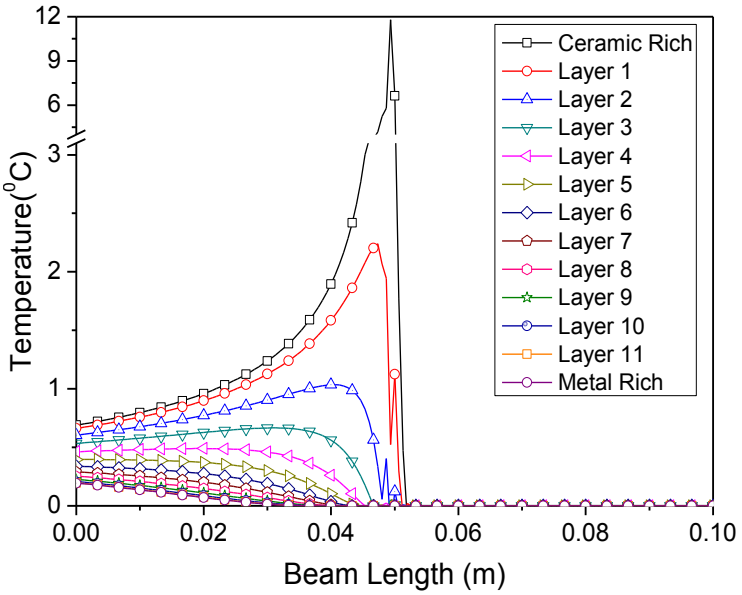

(a) moving heat source at center of beam at $t = 0.025$ s.

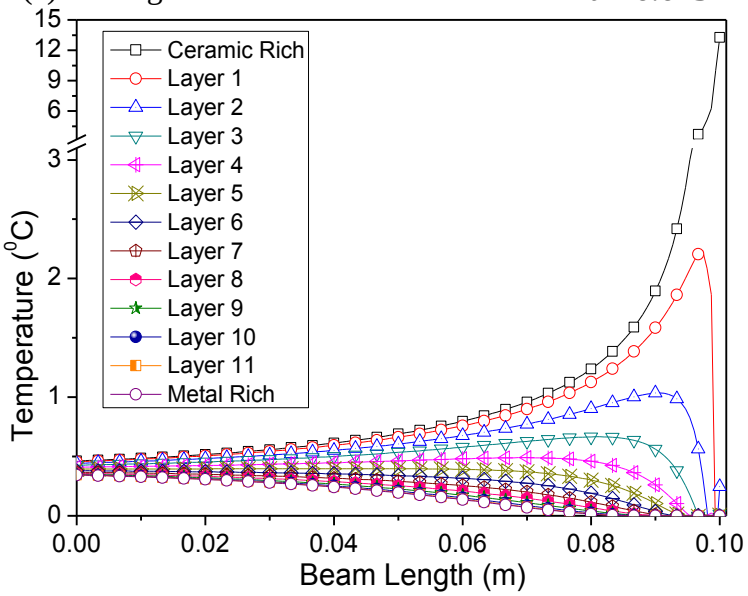

(b) moving heat source at the end of beam at $t = 0.05$ s.

Fig.7.28 Temperature distribution across thickness of the pin-pin beam for $n = 1$ at velocity of 2m/s.

Fig.7.30 and Fig.7.32 shows the axial force for PP and HH FGM beam subjected to moving heat source. Hardly any axial force is seen for the HH FGM beam as there are no end constraints for this beam. As seen from Fig.7.33(a), the CP beam shows reverse bending with thermal oscillations gradually increasing with time for quarter length of the beam and starts reducing further till it attains zero deflection at the centre. The deflections change their sign and follow similar pattern for the other half length of the

beam. The static deflection for CP beam shows the sinusoidal pattern. The corresponding dynamic thermal moment is shown in Fig.7.33(b) while axial force is shown in Fig.7.34. It is observed that the PP and HH beams have similar deflection pattern. Whereas the maximum deflection of CP beam is 1/3rd of PP and HH beam, because clamped boundary condition at left end makes the beam stiffer in case of CP boundary condition.

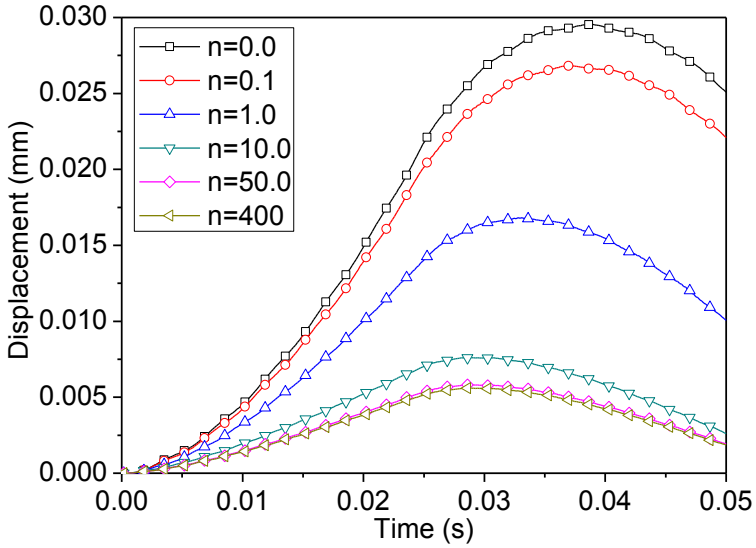

(a)

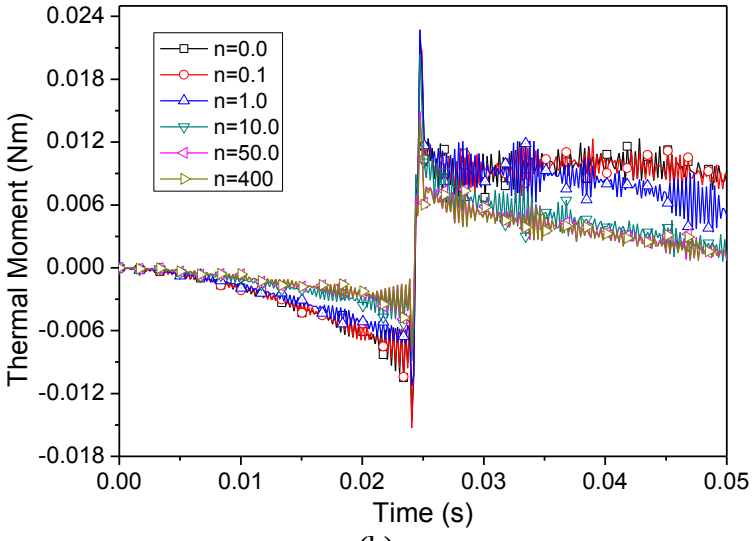

(b)

Fig.7.29 (a) Thermo-elastic deflection at centre (b) dynamic thermal moment for pin-pin FGM beam subjected to moving line heat source for various values of n at velocity of 2m/s.

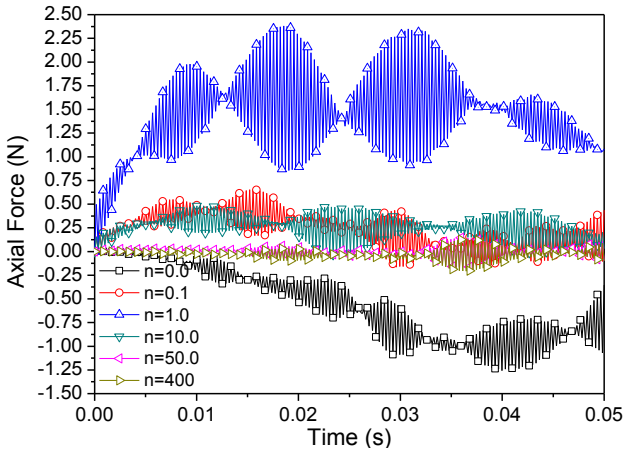

Fig.7.30 Dynamic mid-span axial force for pin-pin FGM beam subjected to moving line heat source.

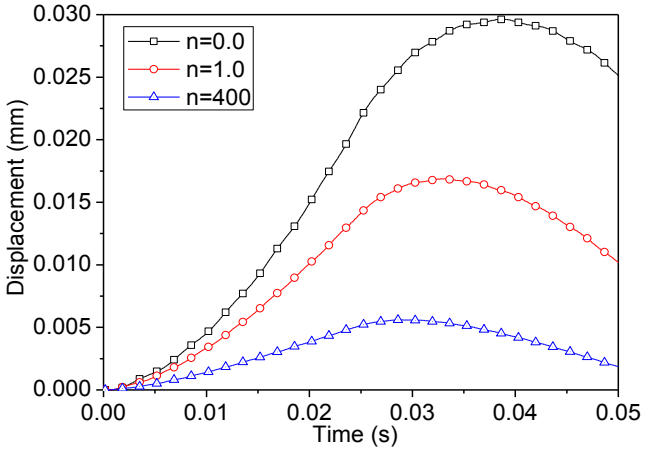

(a)

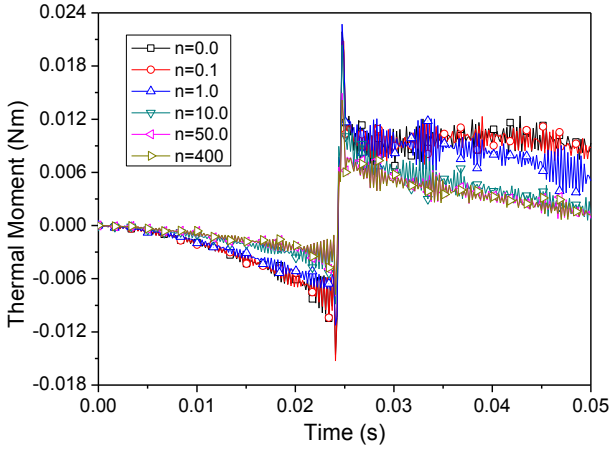

(b)

Fig.7.31 (a) Thermo-elastic deflection at centre (b) Dynamic thermal moment for hinge-hinge FGM beam subjected to moving line heat source for various values of n at velocity of 2m/s.

Fig.7.35 and Fig.7.36 shows the thermo-elastic deflection for various value of material grading index for heat source moving with velocity of 0.5m/s and 4m/s respectively. Fig.7.37 shows the comparison of thermo-elastic centre deflection of PP beam at different velocities of moving heat source while Fig.7.38 shows the corresponding temperature distribution of the bottom surface of the beam. The beam undergoes higher central thermal deflection when heat source moves with lower velocity and decreases as velocity of the heat source increases. This can be attributed to the fact that, as the velocity of the heat source increases, the time available for the heat source to induce heat in the beam is less and hence lower absolute temperature of the beam as seen from the Fig.7.38. In all the three cases it is observed that the deflection is maximum when the heat source has covered approximately 60% length of the beam. Fig.7.39 shows the thermo-elastic deflection for PP beam at different heat loads varying from 100 W to 1000 W. It is observed from the Fig.7.39 that as the heat load increases, the value of thermo-elastic deflection increases. Irrespective of the power law index, the beam does not undergo thermal oscillation even though the magnitude of heat source is increased.

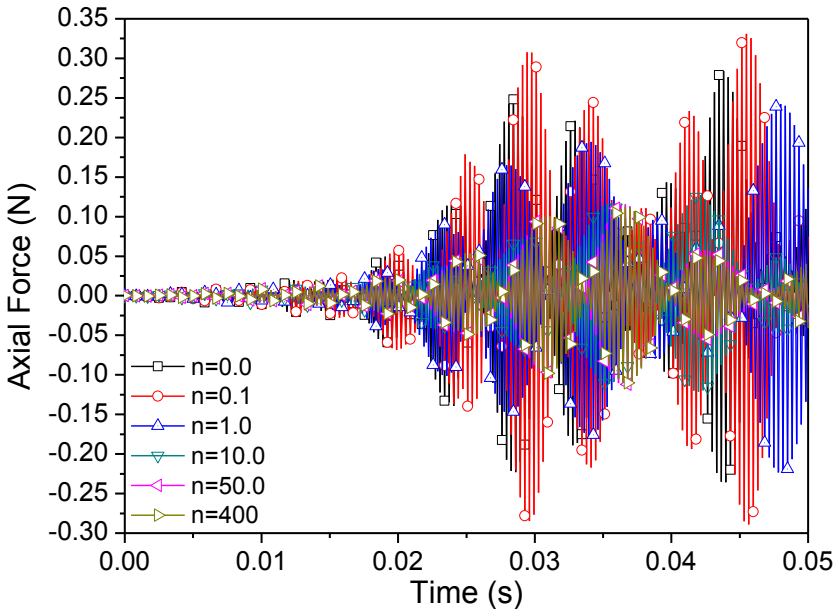

Fig.7.32 Dynamic mid-span axial force for hinge-hinge FGM beam subjected to moving line heat source.

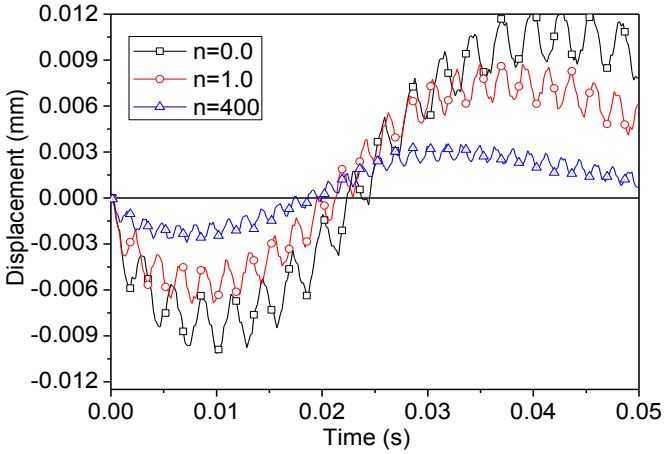

(a)

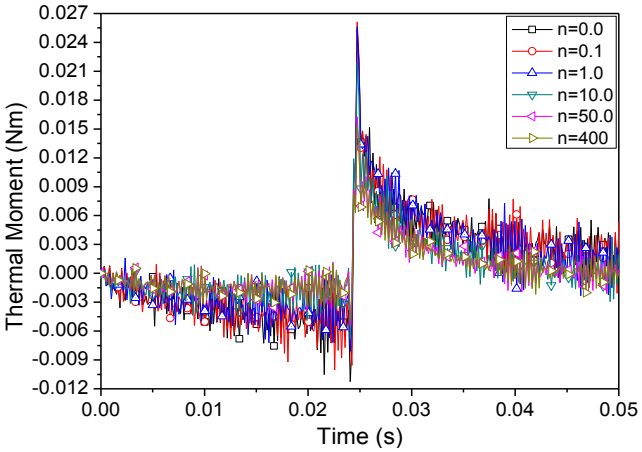

(b)

Fig.7.33 (a) Thermo-elastic deflection at centre (b) Dynamic thermal moment for clamp-pin FGM beam subjected to moving line heat source for various values of n at velocity of 2m/s.

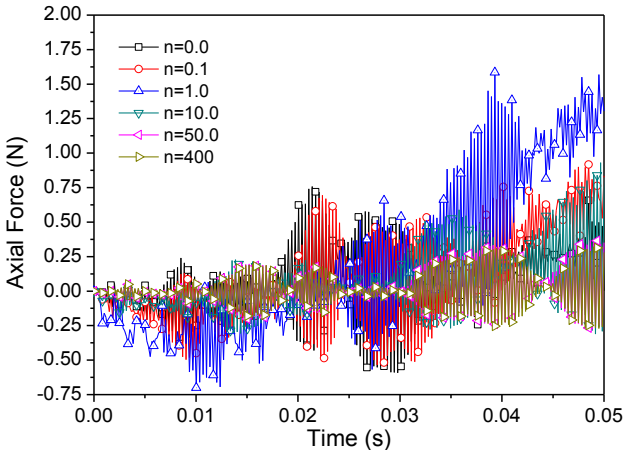

Fig.7.34 Dynamic mid-span axial force for clamp-pin FGM beam subjected to moving line heat source.

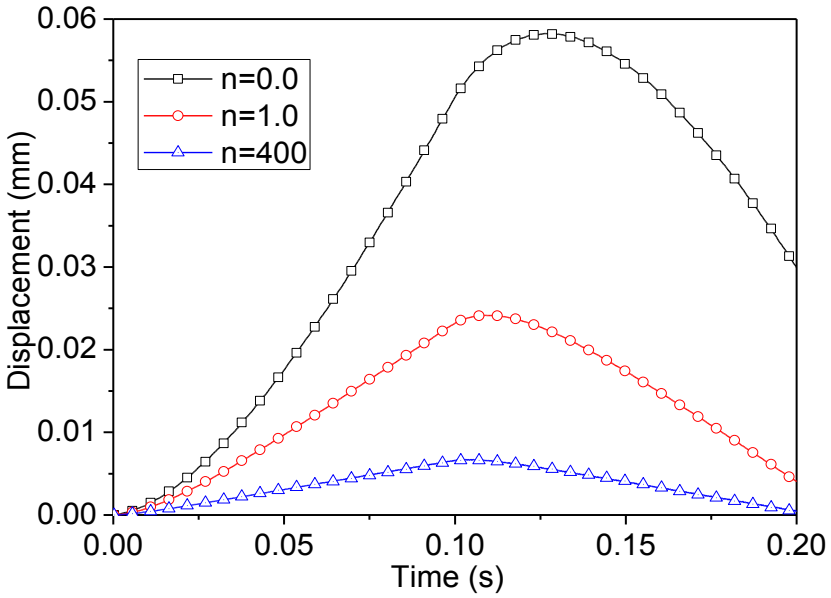

Fig.7.35 Thermo-elastic deflection at centre of pin-pin beam for various values of n at velocity of 0.5m/s.

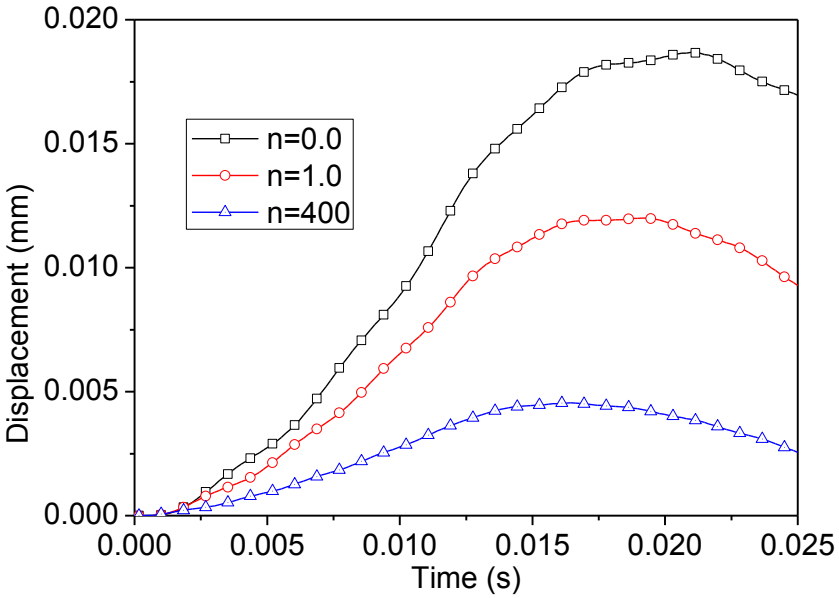

Fig.7.36 Thermo-elastic deflection at centre of pin-pin beam for various values of n at velocity at 4m/s.

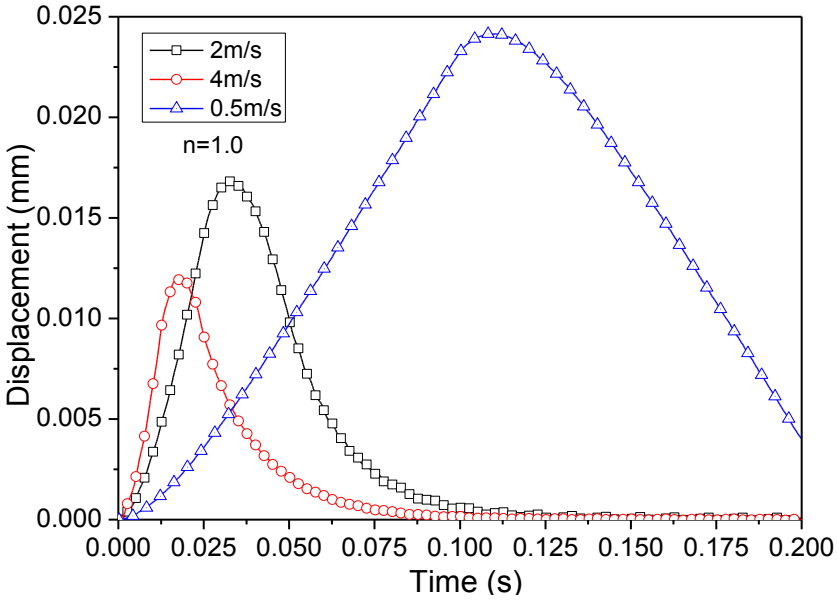

Fig.7.37 Thermo-elastic deflection at centre of pin-pin beam at different values of velocities of heat source.

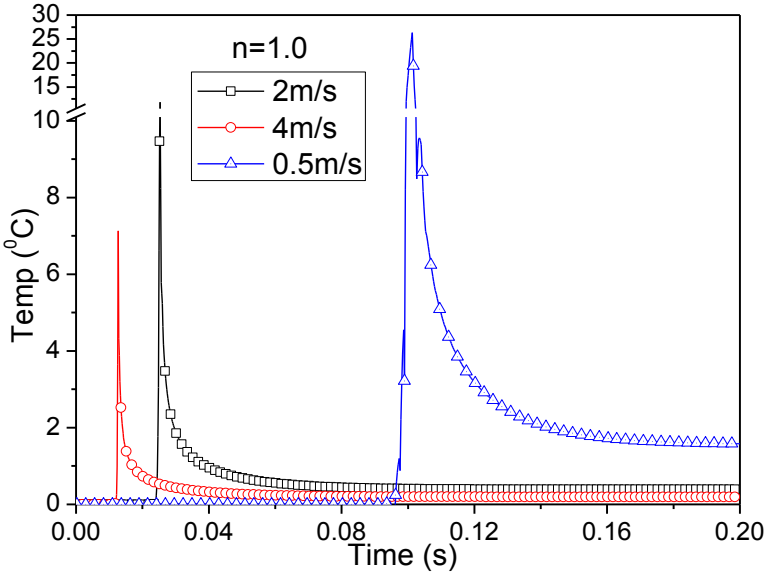

Fig.7.38 Temperature distribution at the centre of the pin-pin beam at different velocities of heat source.

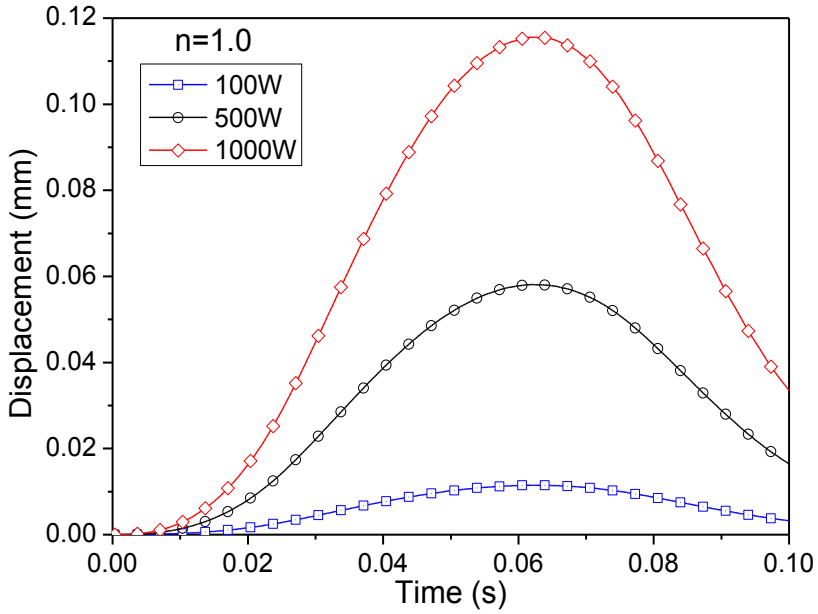

Fig.7.39 Thermo-elastic mid-span deflection for pin-pin FGM beam subjected to moving heat load of various magnitude at 2 m/s.

Fig.7.40 shows the comparison of central deflection of pin-pin beam at material grading index of 1.0 for various heat loads and the corresponding temperature distribution. It is seen from Fig.7.40(a) that, the step and point heat source have similar displacement pattern with thermo-elastic deflection oscillating about a mean static deflection increasing gradually with time and attains steady state after 0.05 s. The beam deflections are low when subjected to step heat load when compared to point heat source. The thermo-elastic deflection for step and shock heat load is same till the time heat source is present for shock load. The moving heat load causes deflection pattern such that displacement gradually increases with time without thermal oscillations. It is seen from Fig.7.40(b) that for step heat source the temperature along the length of the beam is constant while for shock load the temperature decreases gradually once the heat source is removed. For line heat source the beam experiences a peak in temperature at the centre for all the times. The temperature for moving heat source shows sudden peak at the location of the heat source.

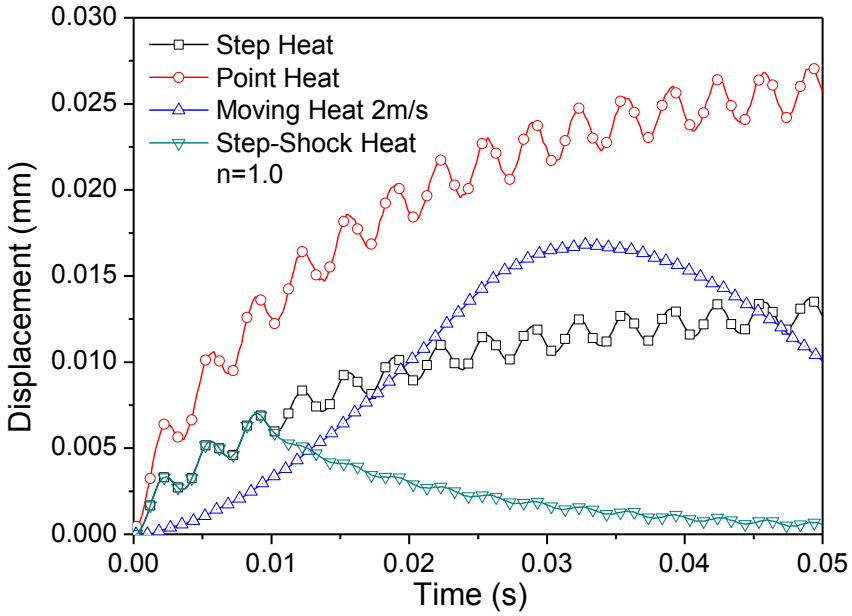

(a)

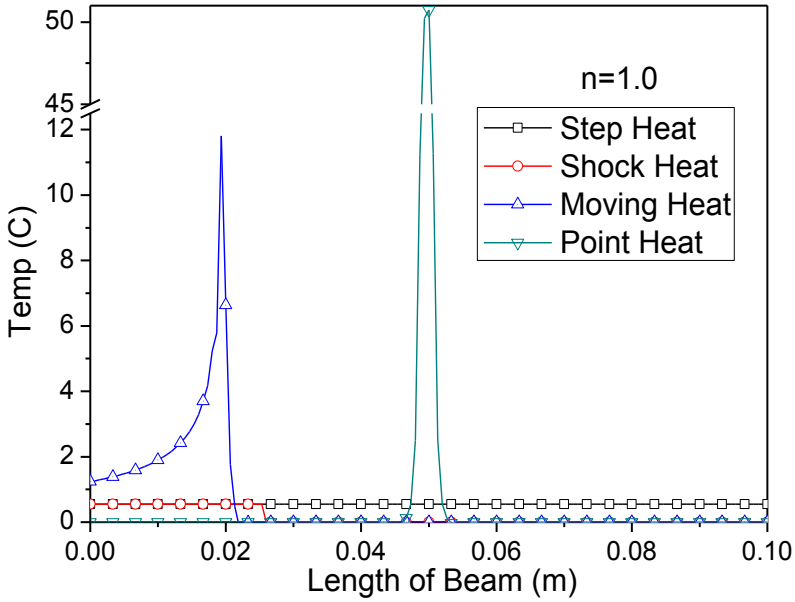

(b)

Fig.7.40 (a) Thermo-elastic mid-span deflection and (b) Temperature distribution for various heat source at 0.01 s for pin-pin boundary condition.

7.2.4 Beam moving under heat source

Typically the problem of moving beam or structure is seen in case of heat treatment of the components or surface hardening wherein the heat source which could be a furnace or the high temperature flame is stationary and the structure is fed in the furnace at constant velocity. The current problem considers a furnace with heat output of 100 W. The length of the furnace is considered to be equal to length of the beam. The beam moves from left to right with constant velocity of 2m/s as shown in Fig.7.41. Fig.7.42(a) shows the temperature distribution across the thickness of the beam for n =1.0 at 0.1 s and Fig.7.42(b) shows the temperature variation with respect to time for the surface exposed to heat source for n =1.0. The temperature distribution in Fig.7.42(a) is plotted when the beam has just moved out of the heat source as in Fig.7.41(a). It is seen from Fig.7.42(a) that the temperature along the length of the beam gradually increases from the left end to the right end where the heat source was present. A temperature gradient of around 0.4^0C is maintained by the beam. The temperature also decreases from the heat exposed surface to insulated surface. From Fig.7.42(b), if we consider the temperature profile for left end of the beam (0 m), it is observed that, as the time progresses, the temperature of the beam gradually increases to maximum at 0.05 s (corresponding to beam position (b) in Fig.7.41) and further gradually start decreasing to minimum as that end of the beam moves away from the heat source. Similar phenomenon is observed for other points on the beam.

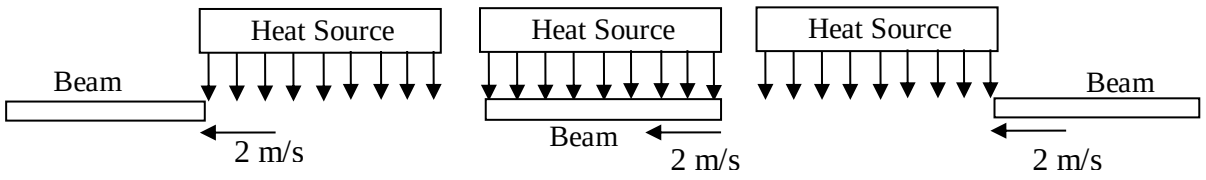

(a) t=0.1 s (b) t=0.05 s (c) t=0.0 s

Fig.7.41 Typical illustration of beam moving under heat source for surface treatment.

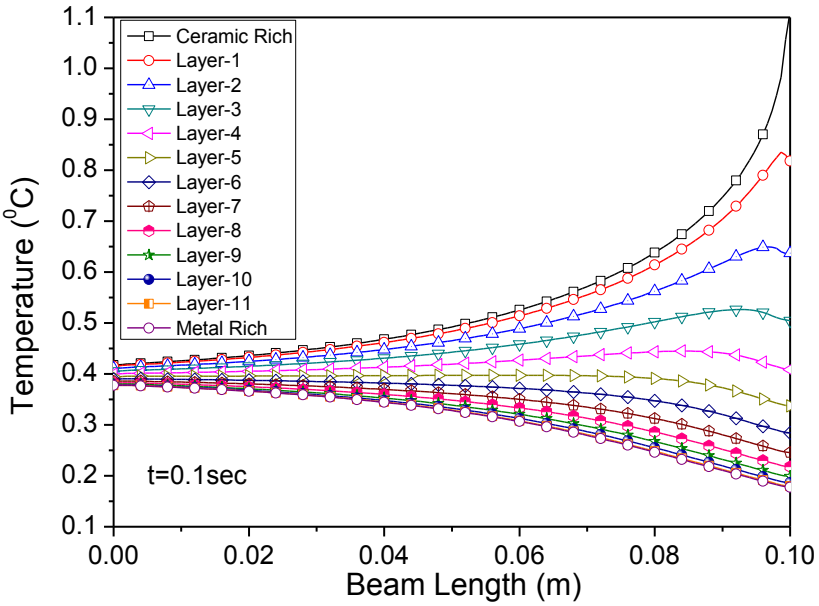

(a) across thickness of beam at t=0.1 s.

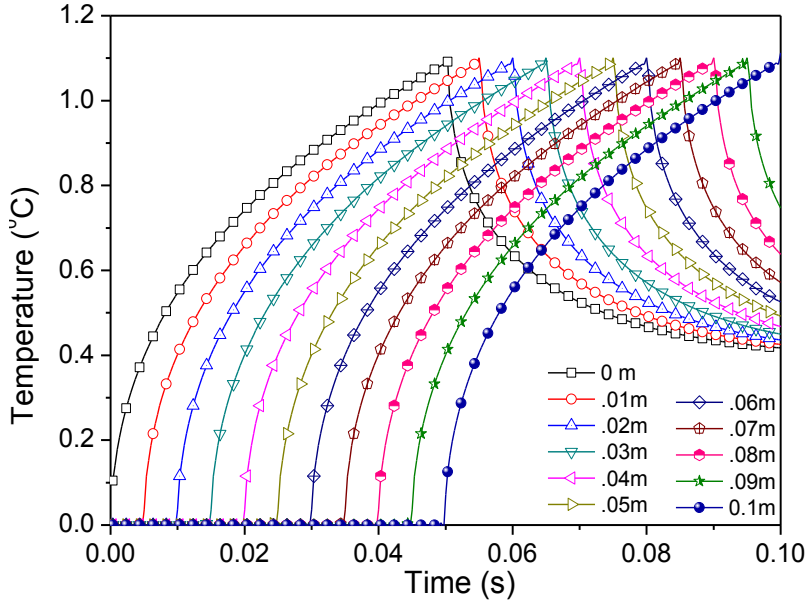

(b) with respect to time

Fig.7.42 Temperature distribution for FGM beam subjected to shock heat of 100 W for 0.1 s.

Fig.7.43 shows the thermo-elastic mid span deflection for a pin-pin SUS316-Al_2O_3 FGM beam for various volume fractions of ceramic. For n =1.0, it is seen from Fig.7.43 that as the temperature increases from 0 to maximum in Fig.7.42(b) (consider temperature profile at centre of the beam (0.05 m) as displacements are measured at centre), thermo-elastic displacement increases gradually with time, attains maximum at

around 0.65 s and then start decreasing with time till 0.1 s proportional to temperature gradient of the beam. Though the maximum temperature occurs at 0.075 s at centre of the beam, the maximum deflection occurs at 0.065 s much before the time required for maximum temperature rise. This is due to the reason that, it is not only the maximum temperature at the location where the displacements are measured is responsible for the deflection to occur but also the temperature gradient and thermal force in surrounding area. If we analyse critically, the maximum displacements occurs at time when the temperature is maximum at 0.04 m length of the beam. At this instance, the temperature difference between the centre of the beam (0.05 m) and 0.04 m and 0.06 m is 0.05^0C each while at 0.075 s where the temperature is maximum at centre of the beam, the temperature difference between the centre of the beam (0.05 m) and 0.04 m and 0.06 m is 0.35^0C and 0.05^0C respectively and hence lower thermo-elastic deflection. The beam does not undergo thermo-elastic oscillations and is independent of volume fraction of the beam. The metal rich beam shows higher value of thermo-elastic deflection as compared to ceramic rich beam and have similar deflection pattern for both PP and HH beams as shown in Fig.7.43 and Fig.7.45 respectively. The maximum thermo-elastic deflection occurs at different times for different volume fraction with least time of 0.55 s for ceramic rich beam to maximum time of 0.72 s for metal rich beam.

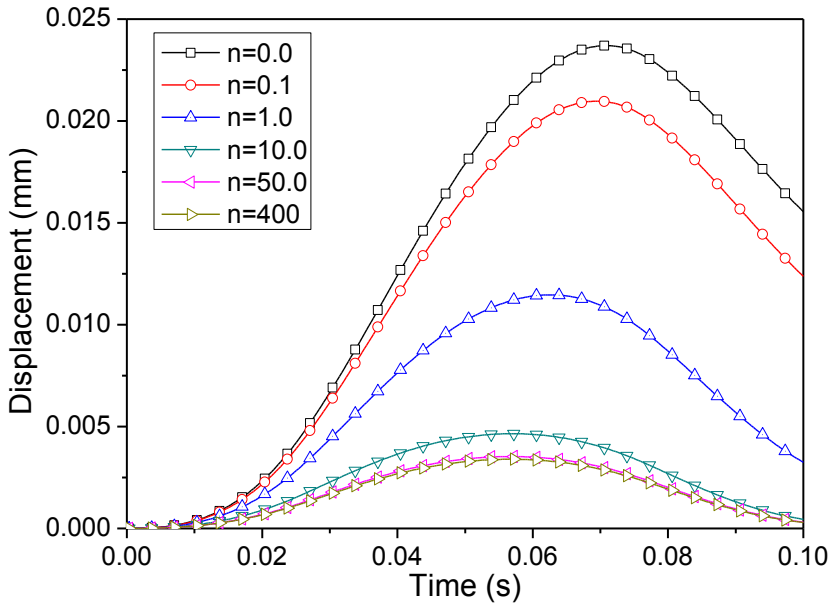

Fig.7.43 Thermo-elastic mid-span deflection for pin-pin FGM beam subjected to shock heating.

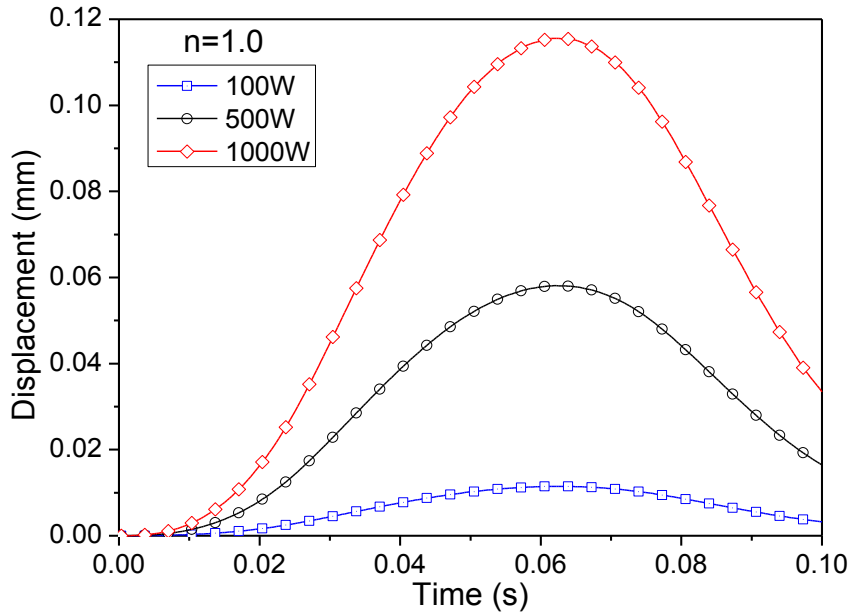

Fig.7.44 Thermo-elastic mid-span deflection for pin-pin FGM beam subjected to shock heating of various magnitude.

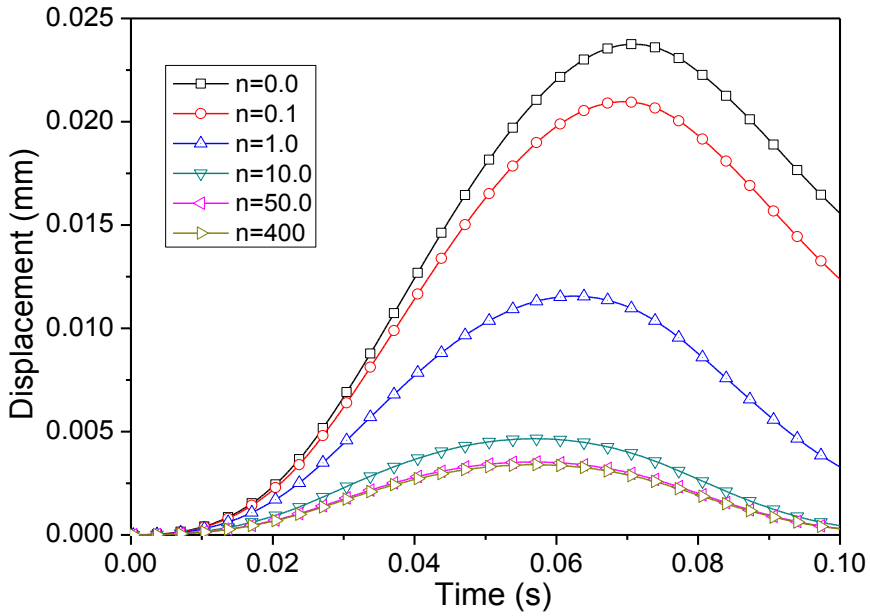

Fig.7.45 Thermo-elastic mid-span deflection for hinge-hinge FGM beam subjected to shock heating.

Fig.7.44 shows the thermo-elastic deflection for PP beam at different heat flux from 100 W to 1000 W. It is observed from the Fig.7.44 that as the heat flux increases, the value of thermo-elastic deflection increases. With increase in heat flux the beam does not undergo thermal oscillation and the same is true for beam when power law index is raised. Fig.7.46 shows thermo-elastic deflection for CP beam. It shows reverse bending for initial time up to 0.45 s and later starts gradually increasing with time till 0.75 s and the deflection slowly reduces once the heat source approaches towards the pin end of the beam. The absolute value of displacement for CP beam is less as compared to PP and HH beam.

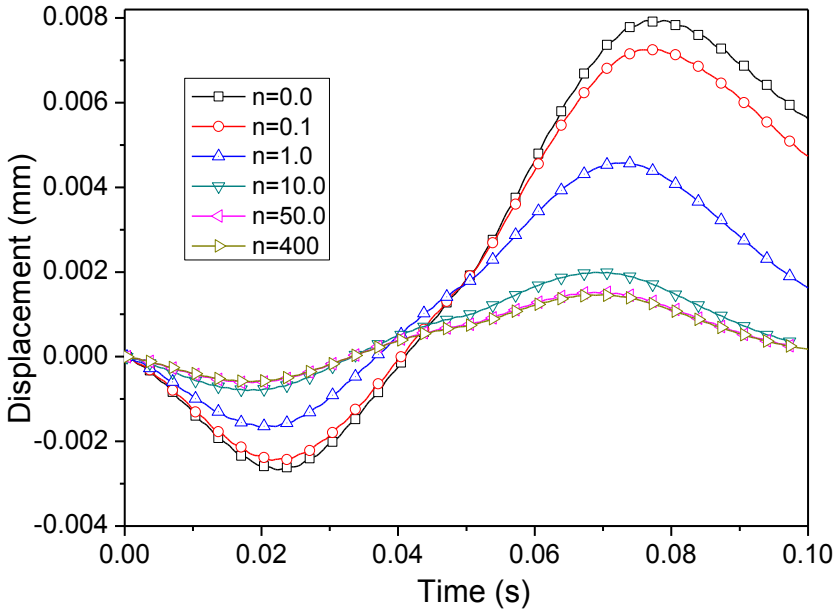

Fig.7.46 Thermo-elastic mid-span deflection for clamp-pin FGM beam subjected to shock heating.

7.2.5 Nonlinear displacement field of FGM beam for various heat loads

Studies have been carried out to understand the effect of material power law index, various structural boundary conditions and heat source on the displacement fields of the beam. Fig.7.47 shows effect of material power law index on the displacement field of FGM beam. It is observed from Fig.7.47(a) that metal rich beam shows higher axial displacements as compared to ceramic rich beam. This is attributed to the temperature coefficient of linear expansion of metal rich beam being approximately 1.8 to 1.9 times

more compared to ceramic rich beam (see Table 6.2) which gives rise to stretching/extension of beam.

Maximum axial displacement is observed at $1/4^{th}$ and $3/4^{th}$ of the beam length. This is due to the fact that both the ends of the beam are constrained from axial motion and due to symmetry, axial deflection is zero at the centre. The left hand support prevents the expansion in left direction and the axial strain is developed in the beam which gives rise to axial deflection which increases to a maximum at $1/4^{th}$ length of the beam. Similarly, right hand support prevents the expansion in right direction and the axial strain is developed in the right portion of the beam which gives rise to axial deflection which goes on increasing and becomes maximum at $3/4^{th}$ length of the beam. Thus, due to the end constrains on the beam, the axial deflection results in the point of inflection at the centre of the beam. Fig.7.47(b) shows the transverse displacements of the FGM beam wherein it is observed that metal rich beam deflects more than ceramic rich beam. This is because, bending rigidity of metal rich beam will be lesser compared to ceramic rich beam. Similar phenomenon is observed for the slope as shown in Fig.7.47(c) wherein slope of metal rich beam is more than ceramic rich beam. Fig.7.48 (a,b and c) shows the comparison of linear and nonlinear displacement field for pin-pin beam subjected to heat loads from 100 to 1000 W for power law index of n =1.0. It is to be noted that, as the heat load increases, the difference between axial and transverse displacements calculated using linear and nonlinear formulation increases. Similar is the case for the slope as shown in Fig.7.48(c).

Fig.7.49 shows the displacement field of FGM beam subjected to step heat load of 100 W for various structural boundary conditions at 0.05 s. It is observed from Fig.7.49(a) that as the CP and PP beam are constrained at both the end, the axial displacements at these ends is zero. For a hinge-hinge support, the axial motion of the beam is unconstrained. Accordingly from Fig.7.49(a), the axial displacement towards the support portion of the beam is large and the axial displacement at the centre is zero. The axial displacement for CP beam is maximum at the centre while it is zero for PP beam at centre.

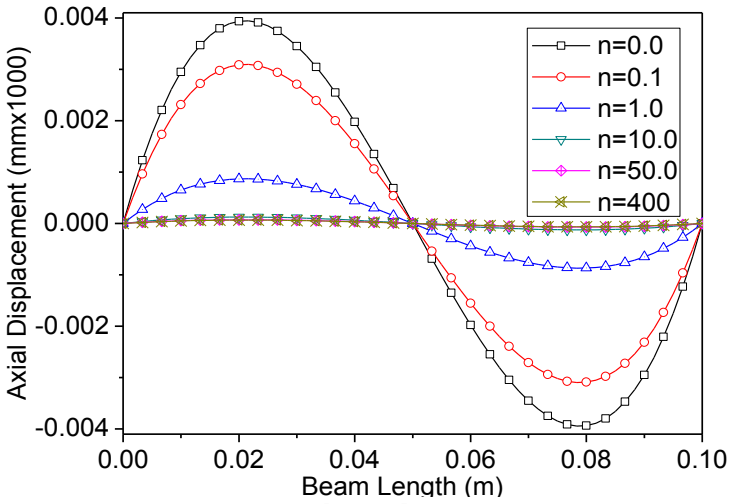

(a) Axial Displacement

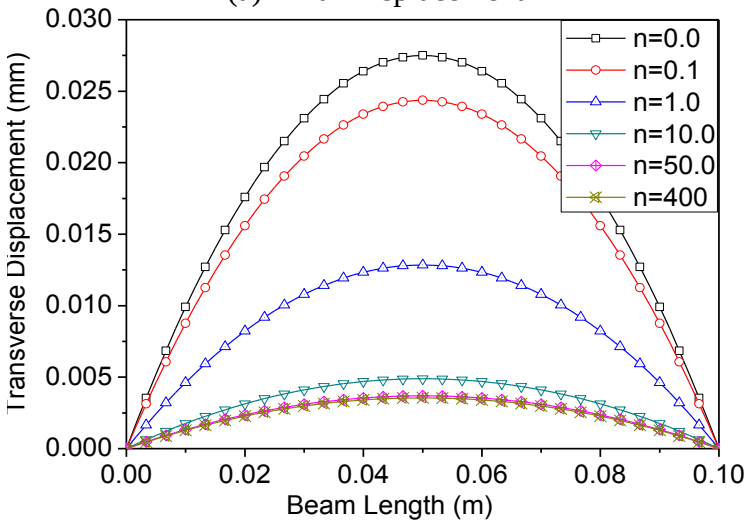

(b) Transverse Displacement

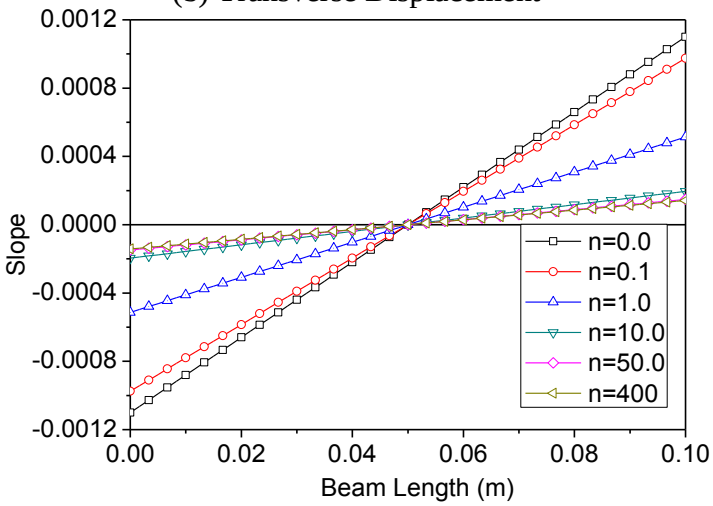

(c) Slope

Fig.7.47 Displacement field for pin-pin beam subjected to step heating of 100W (time=0.05 s).

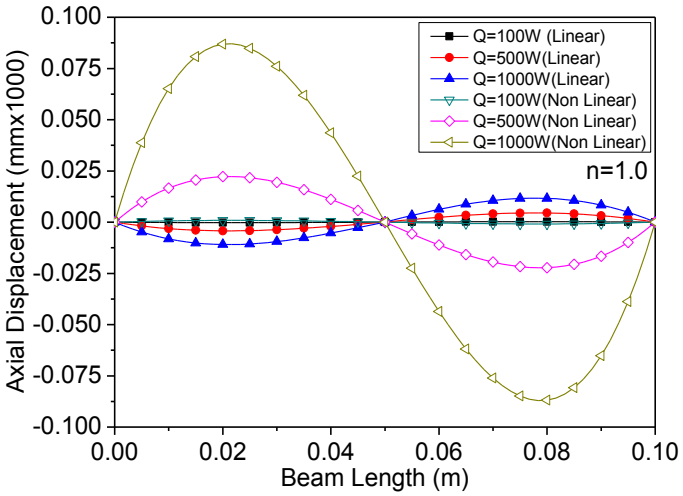

(a) Axial Displacement

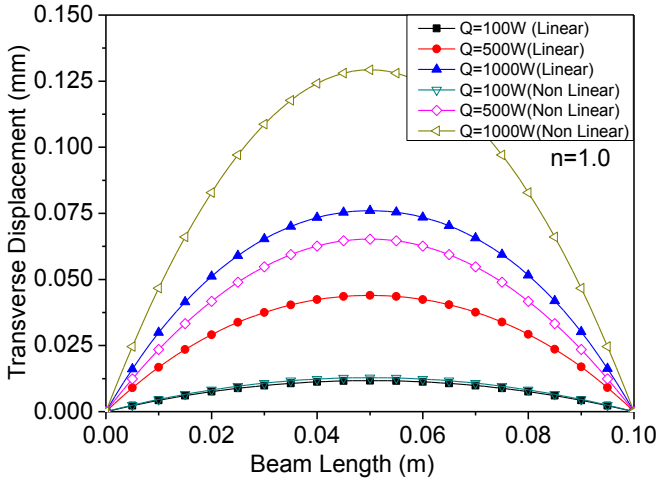

(b) Transverse Displacement

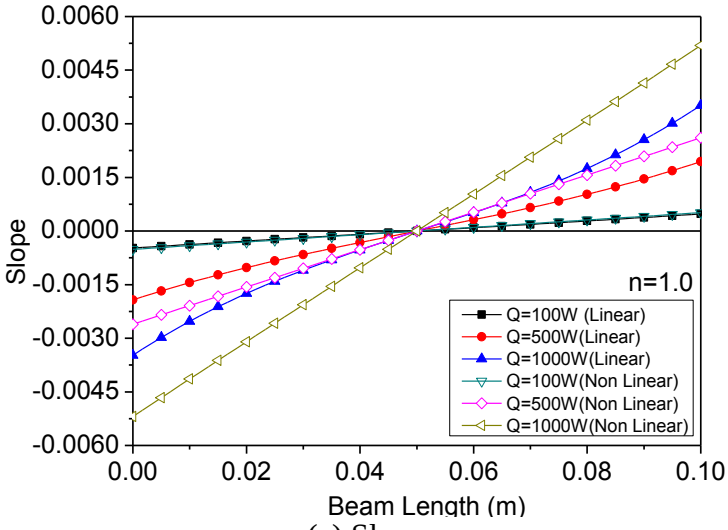

(c) Slope

Fig.7.48 Comparison of linear and nonlinear displacement field for pin-pin beam subjected to step heating for n=1.0 (time=0.05 s).

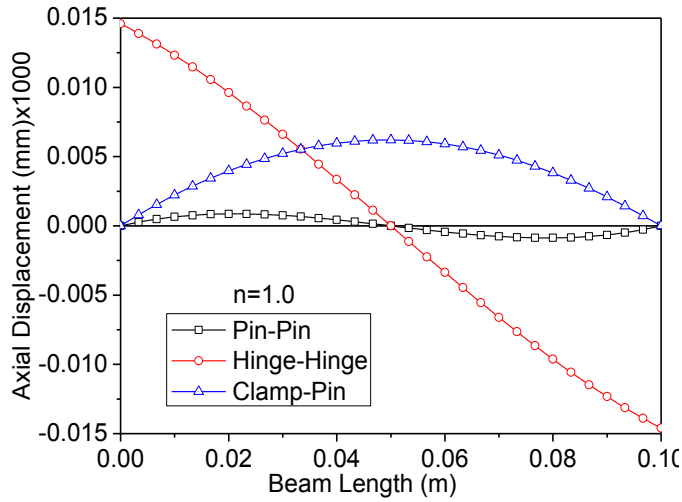

(a) Axial Displacement

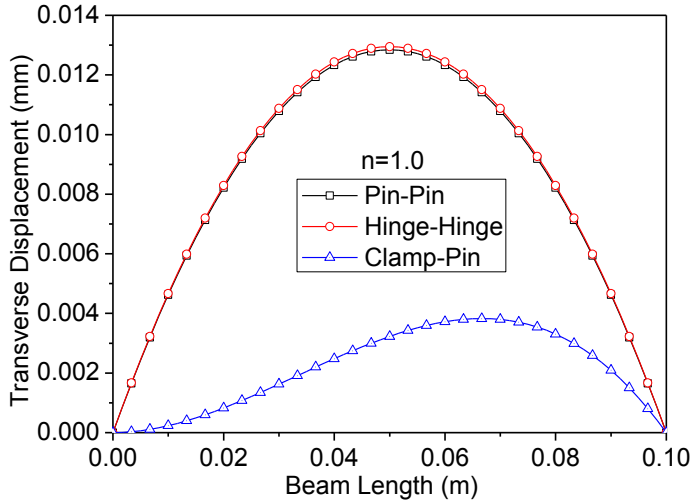

(b) Transverse Displacement

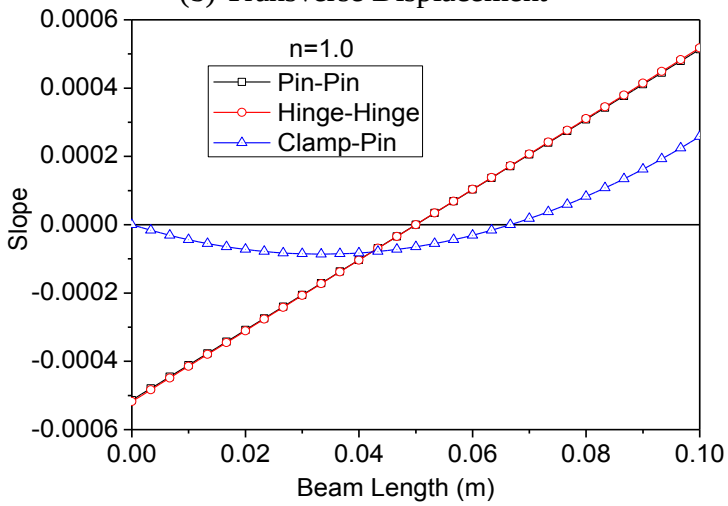

(c) Slope

Fig.7.49 Comparison of displacement field of FGM beam subjected to step heating of 100 W for various structural boundary conditions (time=0.05 s).

Fig.7.49(b) shows the transverse displacements of the FGM beam wherein it is observed that PP and HH beam shows maximum displacement at the centre while the displacements of the CP beam are 1/3rd of PP and HH beam due to fixed end constraint at clamped end. Closer examination reveals that, the centre displacements of HH beam are higher than PP beam by 0.85%. This is due to absence of axial constrain on a HH beam causing it to deflect more than PP beam which has axial restraints at the end. This is an advantage that using the nonlinear Euler–Bernoulli theory, effect of boundary conditions on the axial and transverse displacements are revealed by introducing nonlinear terms in axial, coupling and bending stiffness matrix as seen in Eq.(3.72). As seen from Fig.7.49(c), PP and HH beam shows maximum slope at both the end with zero slope at centre as per boundary conditions but for CP beam, the slope at the fixed end is zero with maximum slope at the pinned end.

Fig.7.50 shows the displacement field for pin-pin FGM beam subjected to various heat loads for n=1.0 at 0.05 s. It is observed from Fig.7.50(a) that, due to PP boundary condition, the axial displacement at both the ends and at the centre is zero for all the heat sources. The location where the line heat source is applied, the axial displacement shoot up sharply at the centre of the beam. Minimal axial displacement is observed for the step heat source. Similarly, for transverse displacement as shown in Fig.7.50(b), maximum displacement is observed in case of line heat source with least displacement in case of shock heat load which is also seen in Fig.7.50(a). The trend similar to axial displacement is seen for the slope as shown in Fig.7.50(c). There is sharp discontinuity in the axial, transverse deflection and slope of the FGM beam when it is subjected to line heat source as well as moving heat source. However, note the exception that, for moving heat source, the transverse displacement does not exhibit slope discontinuity but rather an asymmetric transverse deflection profile.

In case of FGM beam neutral plane does not coincide with centroidal plane. Therefore, the stretching and bending equations will be coupled. Bousahla et al. (2014) and Bourada et al. (2015) showed that there is no stretching-bending coupling in constitutive equations if the physical neutral surface is selected as reference surface.

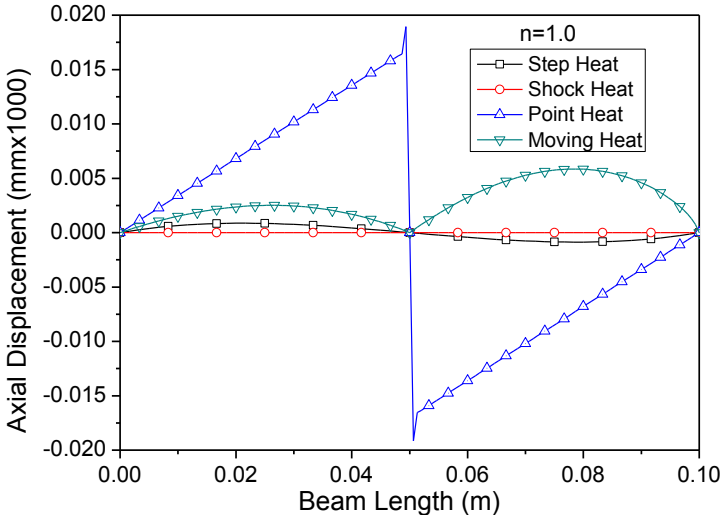

(a) Axial Displacement

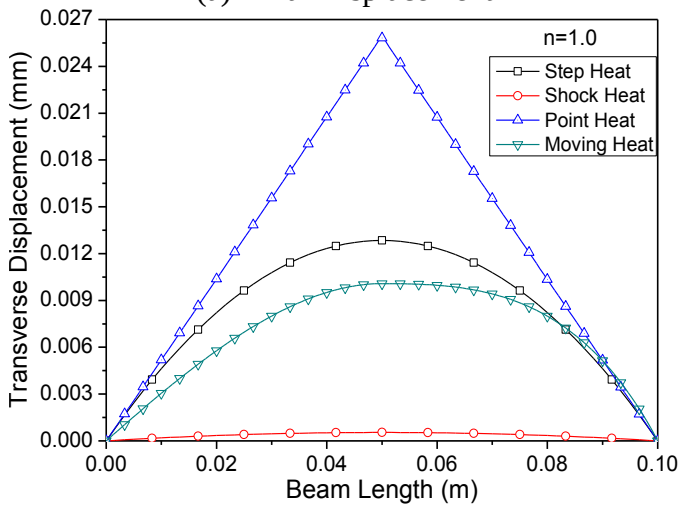

(b) Transverse Displacement

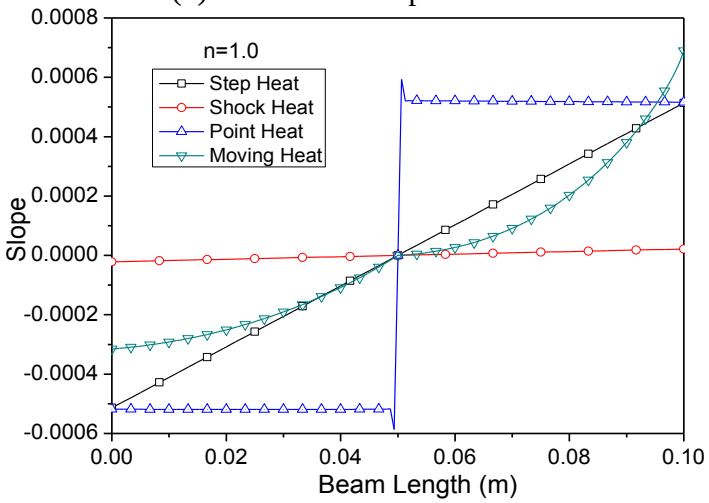

(c) Slope

Fig.7.50 Comparison of displacement field for pin-pin FGM beam subjected to various heat loads of 100 W for *n*=1.0 (time=0.05 s).

Fig.7.51 shows the location of the neutral plane for various values of power law index and corresponding axial displacement for PP beam subjected to step heating at time equal to 0.05 s. The value of the axial displacement is calculated at a distance of $L/4$ from left hand support where the axial displacement is maximum as seen from Fig.7.47(a) for PP beam. It is observed that there is a maximum shift of the neutral plane by 0.0325mm from centrodial axis for power law index of $n=1.0$. For fully metal and ceramic rich beam, as observed from Fig.7.51, the neutral plane is at the centrodial axis. Fig.7.52 shows the axial displacement across the thickness for PP beam subjected to step heating at time equal to 0.05 s for various values of power law index.

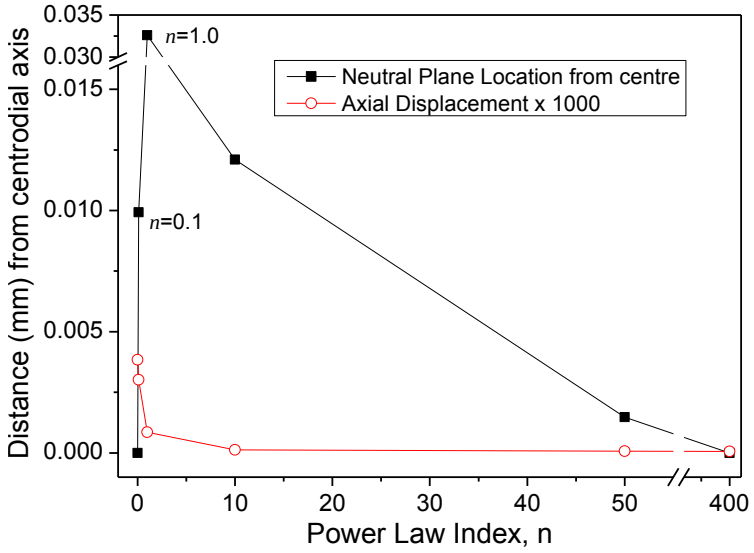

Fig.7.51 Location of the neutral plane for various values of power law index and corresponding axial displacement for pin-pin beam subjected to step heating (time=0.05 s).

It is observed from Fig.7.51 and Fig.7.52 that the maximum axial displacement is seen for metal rich beam with minimum displacement for ceramic rich beam. The metal rich beam shows axial displacement of 0.55 micron between top and bottom surface while for ceramic rich beam it is 0.071 micron. The axial displacement between top and bottom surface for beam with power law index, $n=1.0$, is 0.257 micron. It is observed that the axial displacement variation across the thickness is directly proportional to the slope of the beam. Fig.7.53 shows the effect of L/h ratio on the thermo-elastic vibration on HH beam subjected to step heating. It is observed that as the L/h ratio increases, the beam shows the higher thermal deflection. For L/h ratio of 60, 80 and

100, beam shows thermal deflection with oscillations while for moderate thick beam for L/h ratio of 40, beam shows thermal deflection without oscillation.

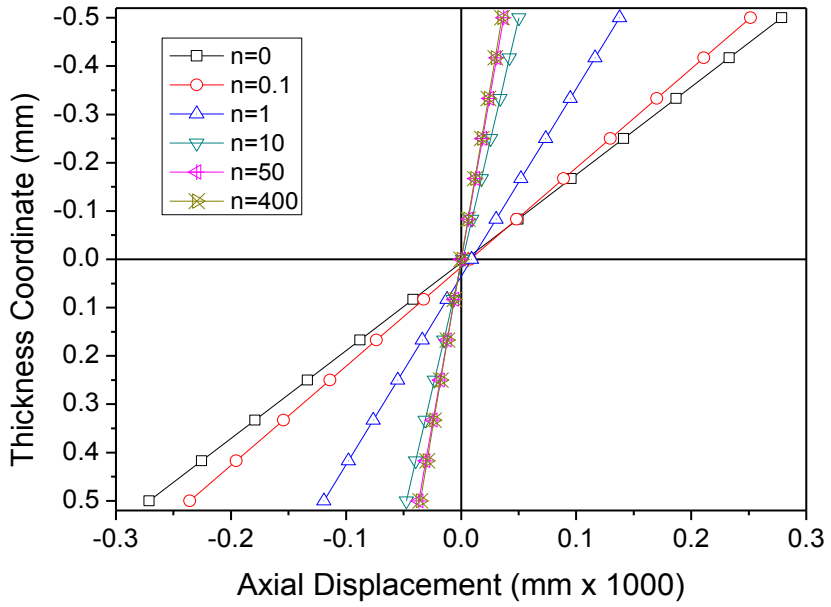

Fig.7.52 Axial displacement across the thickness for pin-pin beam subjected to step heating (time=0.05 s) for various values of power law index.

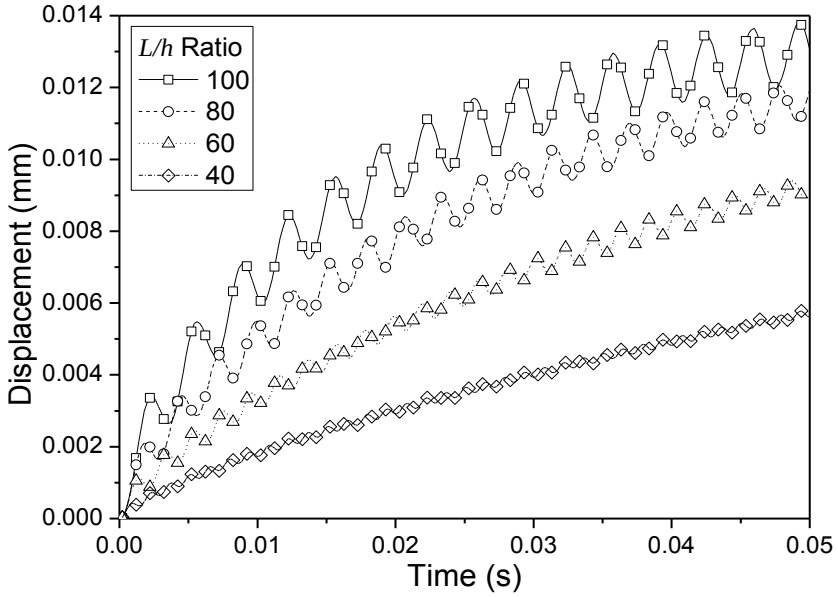

Fig.7.53 Effect of L/h ratio on the thermo-elastic vibration of hinge-hinge beam subjected to step heating

7.2.6 Thermal effect on mechanical properties of FGM Beams

The material considered for the study is gradation of Stainless Steel and Aluminium Oxide (SUS316-Al_2O_3). For this analysis, both temperature dependent and temperature independent material properties for SUS316 and Al_2O_3 are considered. Temperature independent material properties are considered at 0^0C (273K). The geometric dimensions of the beam are: $L = 0.1$ m and $h = 0.001$ m. At any time instance a total step heat load of 6000 W is applied on the beam surface. The temperature distribution across the thickness of the beam for various power law index n are shown in Fig.7.54. It is observed that the temperature gradient for metal rich beam is higher than the ceramic rich beam with top surface temperature being highest for metal rich beam.

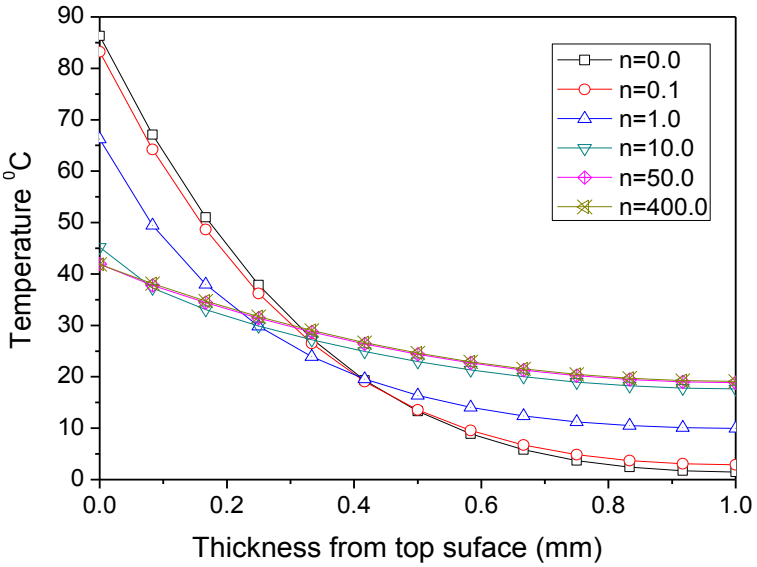

Fig.7.54 Temperature distribution through thickness of the beam due to step heat load of 6000 W.

Fig.7.55 shows Young's modulus, shear modulus, Poisson ratio and coefficient of thermal expansion for SUS316-Al_2O_3 FGM beam for various power law index. The material properties are calculated at time equal to 0.05 s. It is observed from the four plots, Fig.7.55(a,b,c,d), that the temperature coefficients of the material properties play an important role in deciding the value of the each material property.

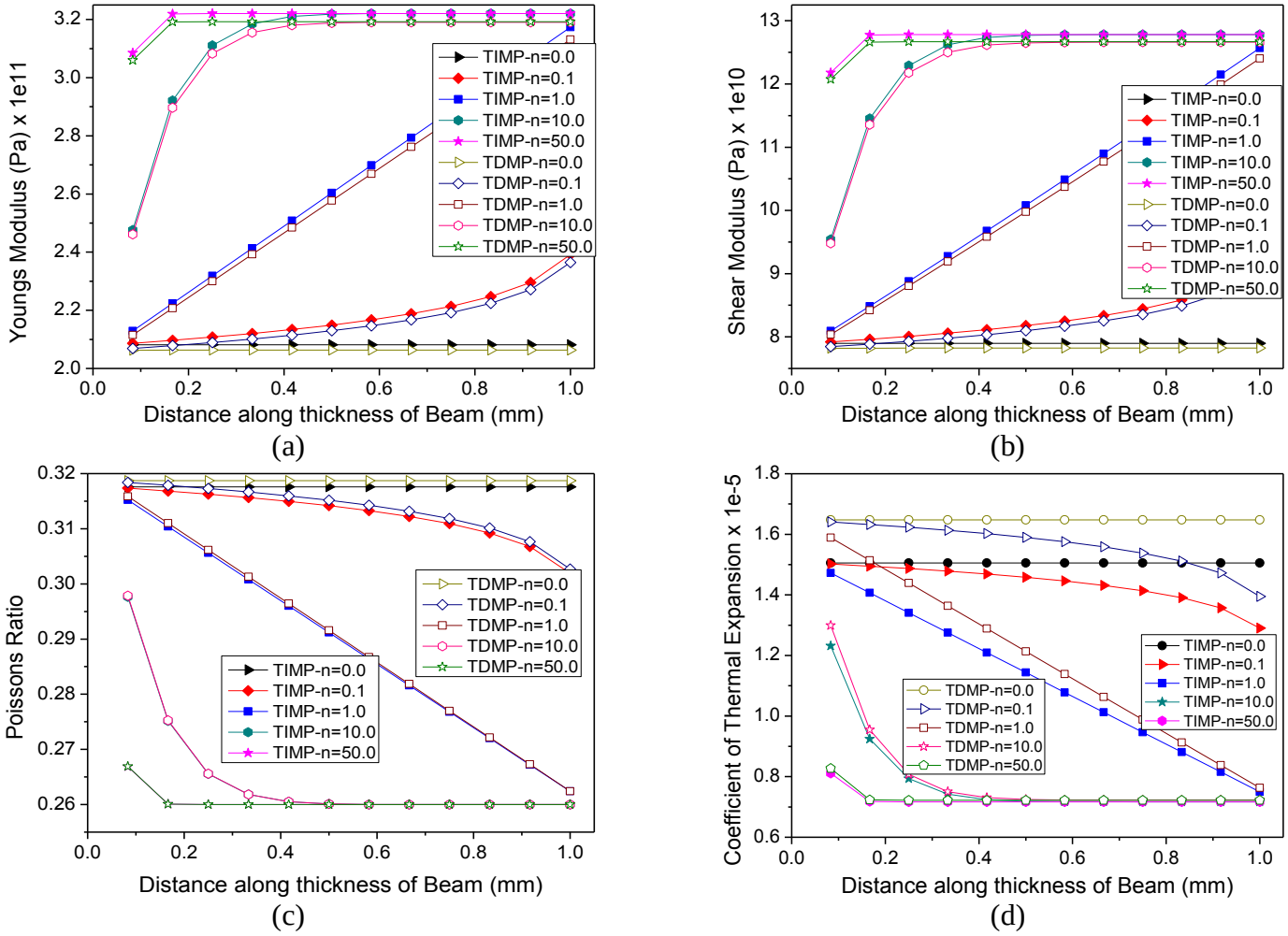

Fig.7.55 Material properties through thickness of the beam.

The material property of each layer varies with respect to the temperature of the corresponding FGM layer. It is observed that the temperature dependent Young's modulus and shear modulus are less than temperature independent property while temperature dependent Poisson ratio and coefficient of thermal expansion are more than temperature independent property. Since the material properties depend on temperature, the properties like extensional stiffness, A_{xx}, extensional – bending coupling stiffness, B_{xx}, and bending stiffness, D_{xx}, of the FGM beam in turn depend on the temperature profile as well as on the power-law index, n, of FGM beam. The variation of extensional stiffness, extensional-bending coupling stiffness and bending stiffness of the FGM beam across the thickness of the beam are shown in Fig.7.56(a), Fig.7.56(b) and Fig.7.56(c), respectively for different power-law index, n, considering temperature dependent material properties. In particular the extensional stiffness increase linearly across the thickness of the beam and is high for ceramic rich beam compared to metal rich beam.

The magnitude of the extensional-bending stiffness is minimum towards the center of the beam and increases to a maximum close to the top and bottom surface of the beam irrespective of the power law index. The bending stiffness are minimum in the top region of the beam which is dominated by metal composition. The bending stiffness increase gradually from the top surface, to approximately a quarter depth. Bending stiffness remains constant until the next half depth of the beam and later on bending stiffness increases to attain a maximum value at the bottom region of the beam, which is ceramic dominated.

Fig.7.57 shows the comparison of dynamic mid-span deflection for pin-pin FGM beam subjected to step heating with temperature dependent material properties (TDMP) and temperature independent material properties (TIMP) for various values of the power law index n. It is observed from Fig.7.57 that the dynamic mid span displacement for beam with TDMP is higher than the beam with TIMP, this observation is in line with results reported in Ghiasian et al. (2014) for case of thick FGM beam.

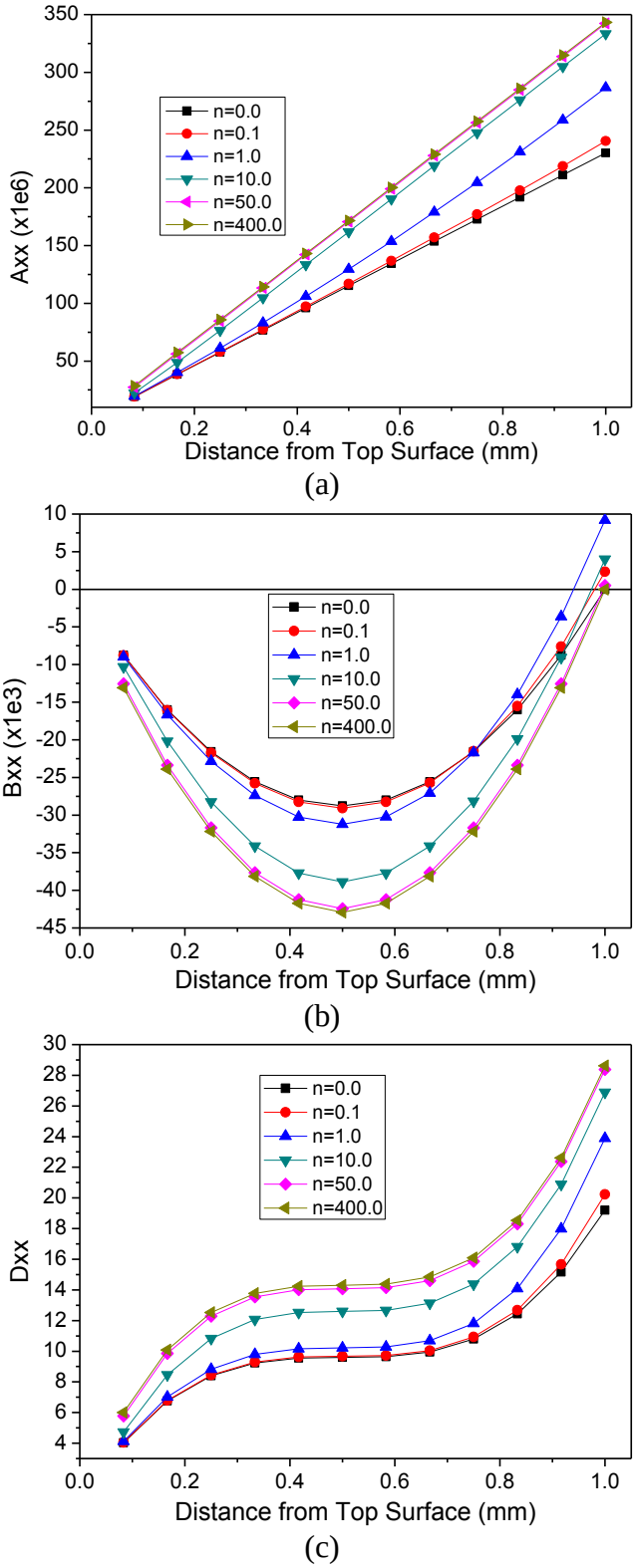

Fig.7.56 Extensional stiffness, extensional-bending coupling stiffness and bending stiffness of FGM beam for different power-law index, n .

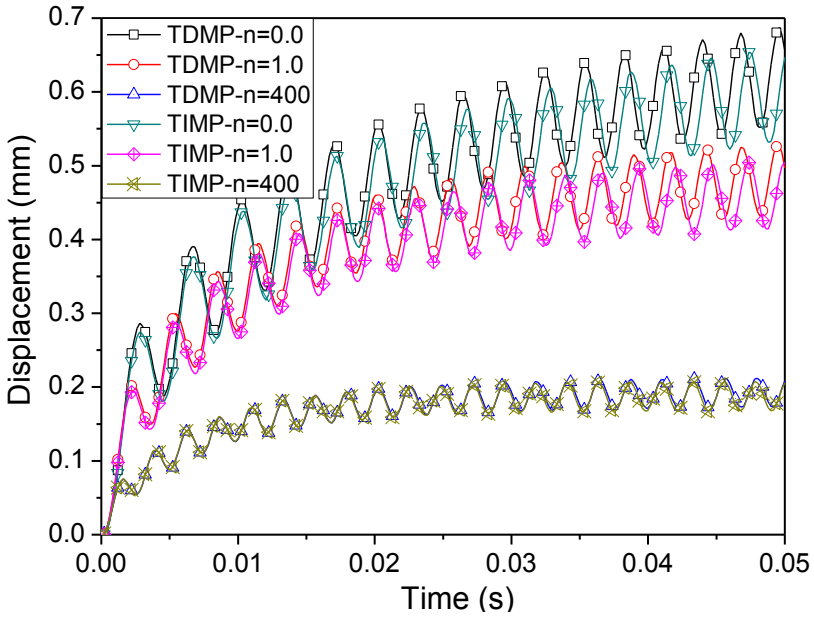

Fig.7.57 Comparison of dynamic mid-span deflection for pin-pin FGM beam subjected to step heating with TDMP and TIMP.

7.3 NONLINEAR STRESSES IN FGM BEAMS

The theoretical formulation for evaluation of stresses for FGM beam was discussed in Chapter 3. The evaluation of stresses in a stainless steel-aluminium oxide (SUS316-Al_2O_3) FGM beam with temperature dependent material properties is discussed in this section. The study considers one surface of the beam subjected to heat load with opposite surface being thermally insulated. Considering the temperature dependency of material properties, 2-dimensional temperature distribution is obtained for various thermal loads and corresponding nonlinear stresses are analysed. The geometric dimensions of the beam are: $L = 0.1$ m and $h = 0.001$ m. At a given time, a total step heat load of 100 W is applied on the beam surface while other surface is kept insulated. The temperature distribution across the thickness of the beam for various power law index n are shown in Fig.7.58 and the temperature distribution is similar to that in Fig.7.54.

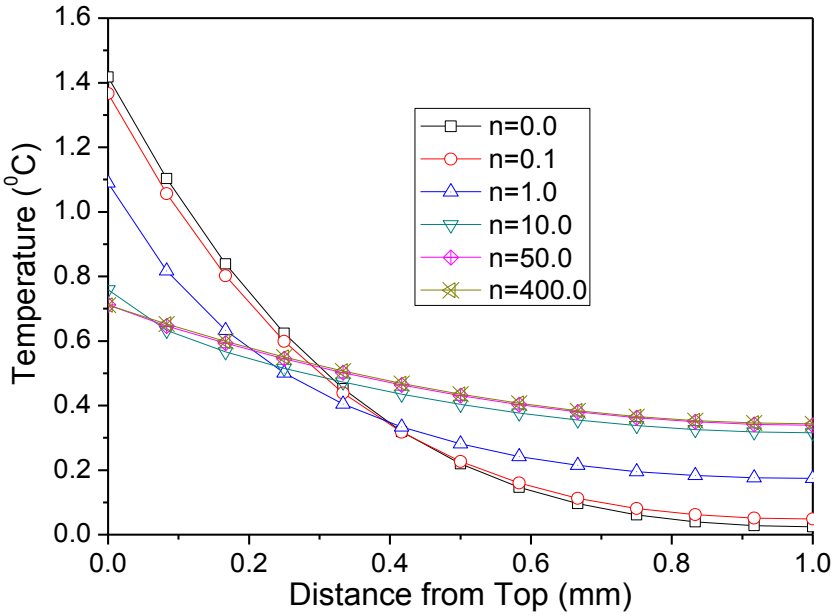

Fig.7.58 Temperature distribution through the thickness of the beam due to step heat load of 100 W.

7.3.1 Step heating

Fig.7.59 shows the dynamic thermal stress at the left end of a pin-pin FGM beam subjected to step heating for various power law index evaluated at centrodial or mid plane. Since the ends of the beam have constraint for axial movement, the maximum thermal stress is developed at the ends of the beam as shown in Fig.7.60. Referring to Fig.7.59, it is observed that the thermal stresses increases with time and are oscillatory in nature. The stresses are maximum for n =1.0, 0.1 and 10.0 respectively while for n =0, 50 and 400, the stresses are minimal or negligible. As seen from Fig.7.60, the stresses are compressive on the left end while they are of tensile nature on the right end. At the centre of the beam the stress is minimum due to symmetry of the applied boundary conditions for PP beam. Along the length of the beam, the stress increases to a maximum and decreases to zero. As shown in Fig.7.61 and Fig.7.62, the thermal stresses for HH beam shows similar pattern as for PP beam but the absolute value is higher by 1.33% than stresses for PP beam at 0.05 s.

Fig.7.63 shows the dynamic thermal stress at the left end of a clamped-pin FGM beam while Fig.7.64 shows stress along the length of the beam at the centroidal plane. Since the left end is clamped, hardly any stress is observed at this end of the beam. The right

end of the beam is constrained from axial movement, hence maximum thermal stress is observed at this end of the beam as shown in Fig.7.64. Negative stress is observed towards the clamp end of the beam while positive stress is seen towards the pin end. The stress is zero at 2/3rd length of the beam from clamp end.

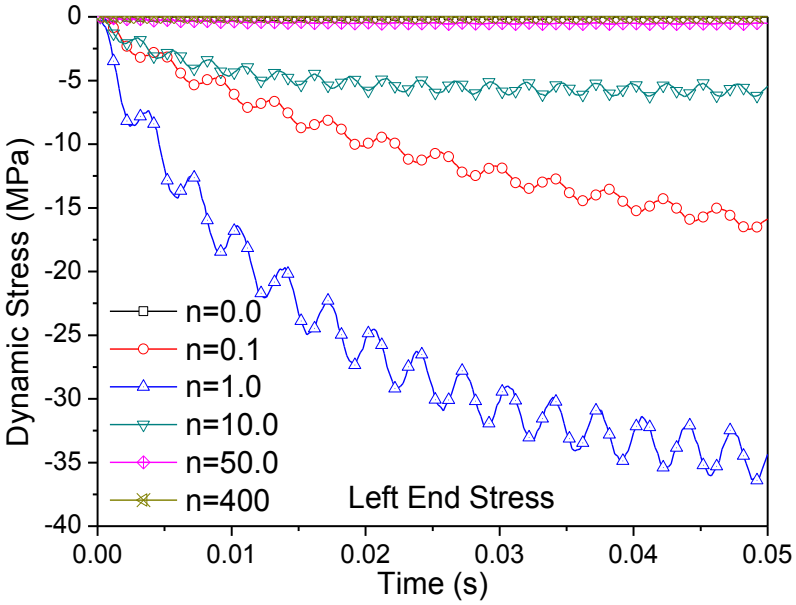

Fig.7.59 Dynamic thermal stress on left end of pin-pin FGM beam subjected to step heating.

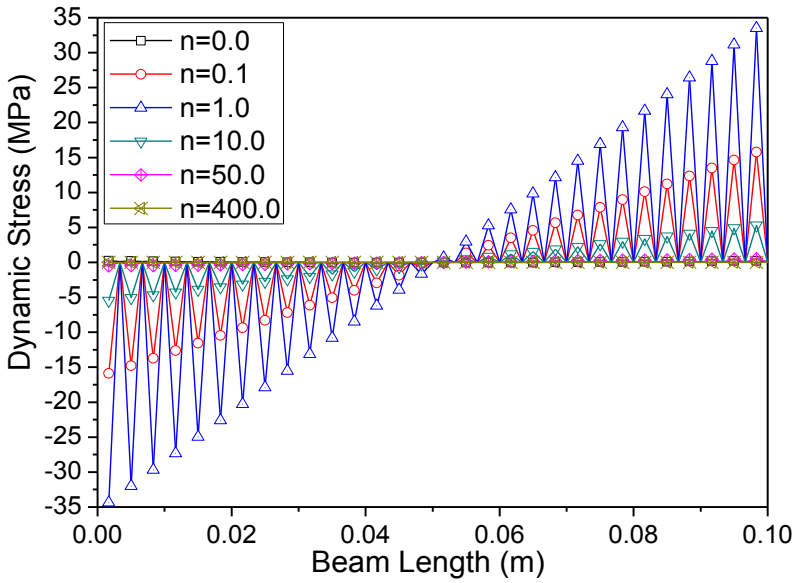

Fig.7.60 Dynamic thermal stress along the length of pin-pin FGM beam subjected to step heating at t=0.05 s.

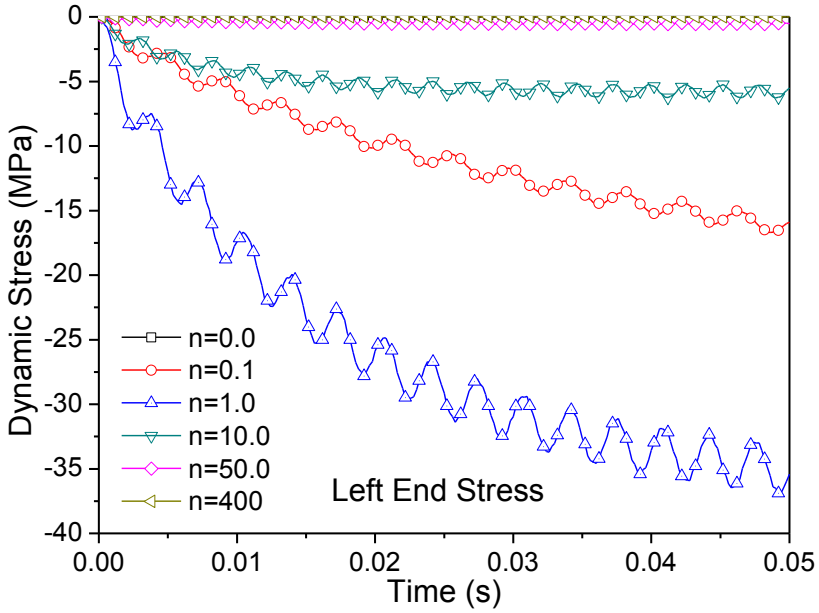

Fig.7.61 Dynamic thermal stress on left end of hinge-hinge FGM beam subjected to step heating.

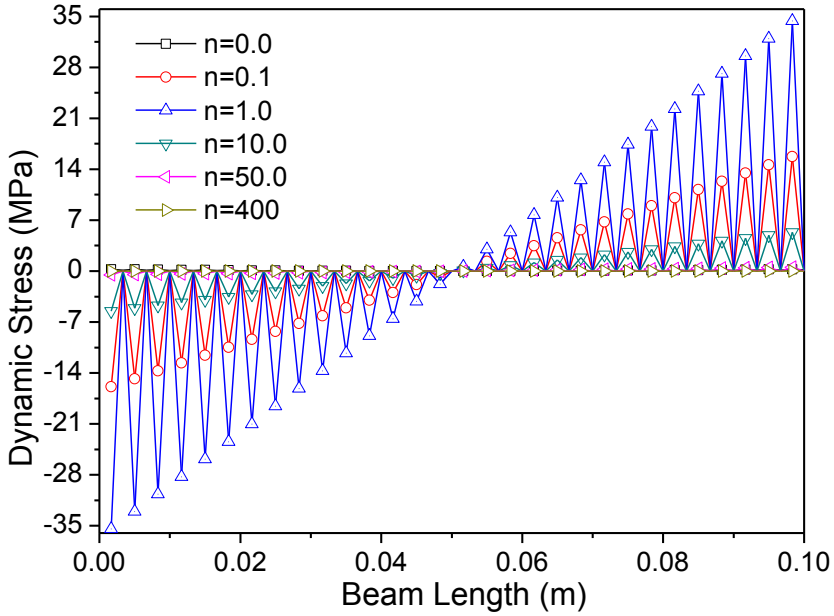

Fig.7.62 Dynamic thermal stress along the length of hinge-hinge FGM beam subjected to step heating at t=0.05 s.

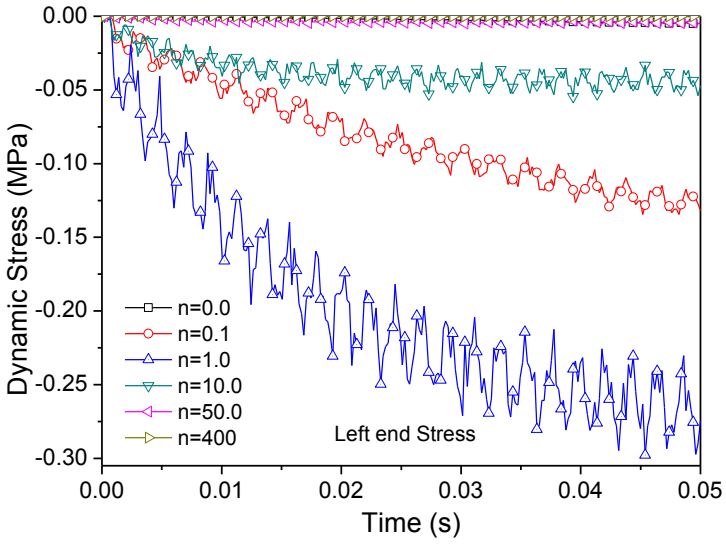

Fig.7.63 Dynamic thermal stress on left end of clamp-pin FGM beam subjected to step heating.

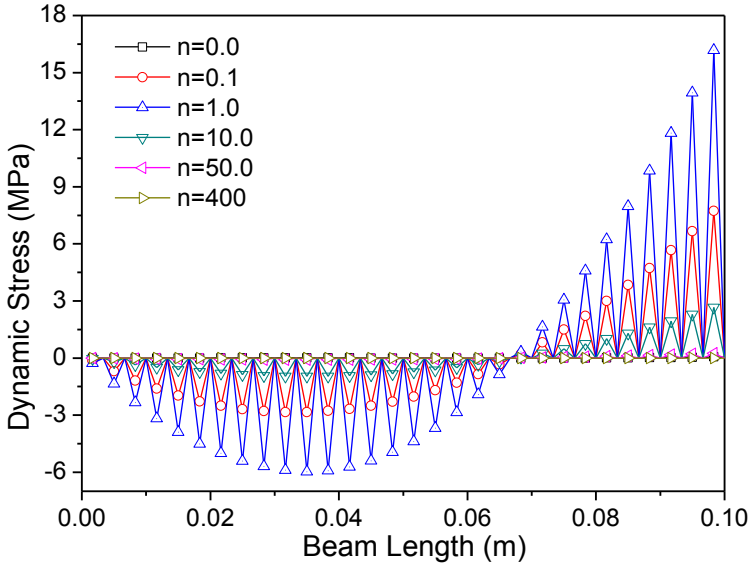

Fig.7.64 Dynamic thermal stress along the length of clamp-pin FGM beam subjected to step heating at t=0.05 s.

7.3.2 Shock heating

Fig.7.65 shows the dynamic thermal stress at the left end of a pin-pin FGM beam for various power law index when subjected to shock heat load for 0.01 s. During the time when heat source is present till 0.01 s as seen in Fig.7.65, the stress starts increasing gradually to maximum value similar to step heat source and once the heat source is removed, the stress strats to reduce gradually. The ends of the PP beam are constrained

from axial movement, hence the maximum thermal stress is observed at the ends of the beam as shown in Fig.7.66. Referring to Fig.7.11 and Fig.7.65, the maximum stress occurs at around 0.01 s when the temperature is maximum. $n=1$ shows the maximum value of the thermal stress.

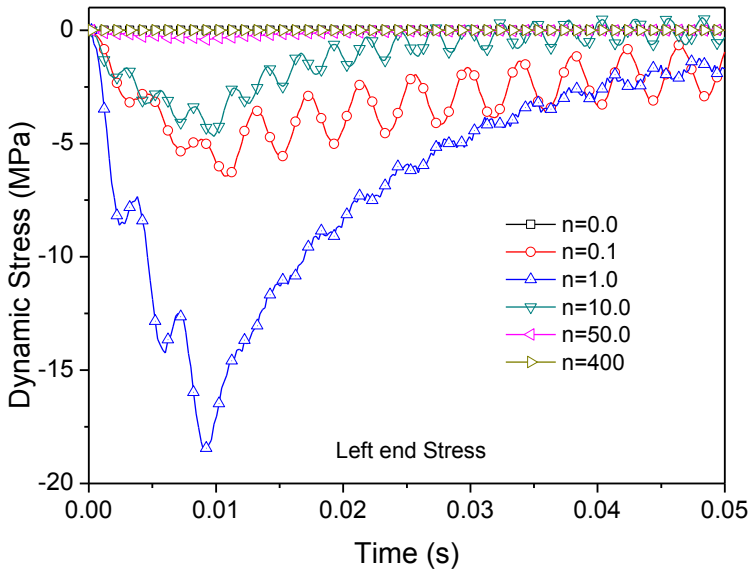

Fig.7.65 Dynamic thermal stress on left end of pin-pin FGM beam subjected to shock heating.

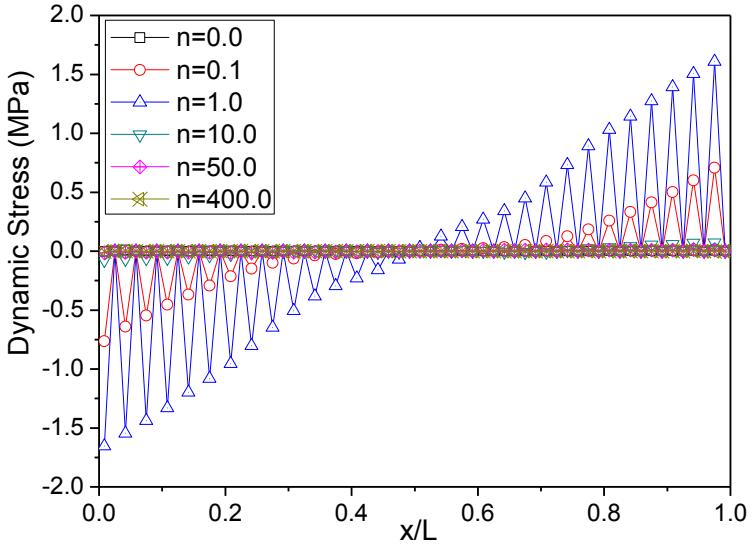

Fig.7.66 Dynamic thermal stress along the length of pin-pin FGM beam subjected to shock heating at t=0.05 s.

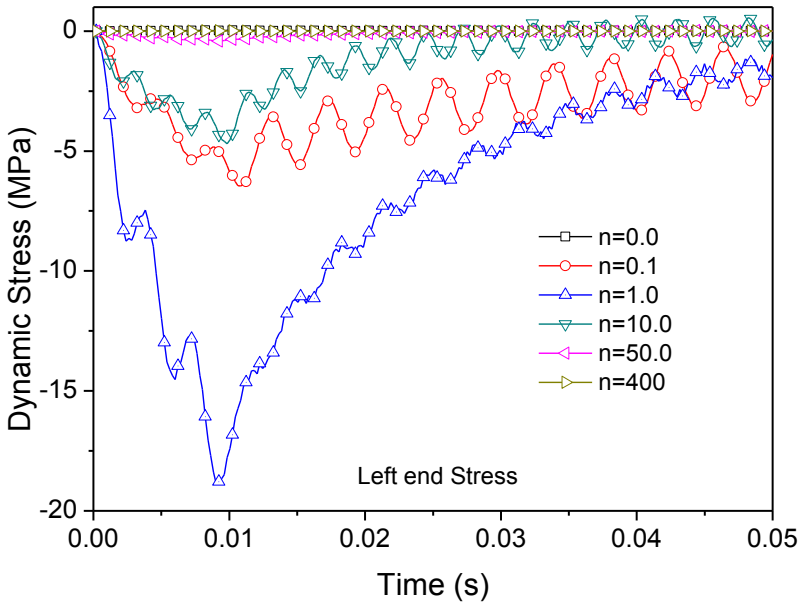

Fig.7.67 Dynamic thermal stress on left end of hinge-hinge FGM beam subjected to shock heating.

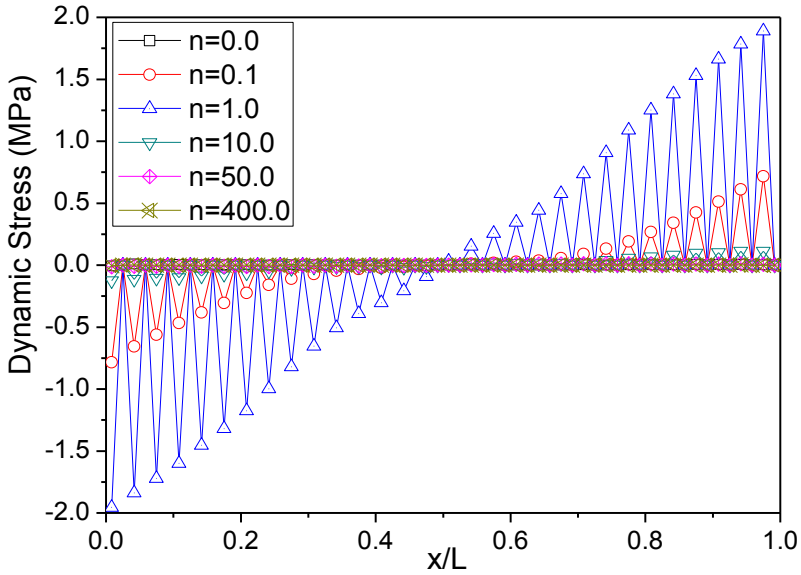

Fig.7.68 Dynamic thermal stress along the length of hinge-hinge FGM beam subjected to shock heating at t=0.05 s.

Due to symmetry of the applied boundary conditions for PP beam, the stresses developed at the centre of the beam are marginally small as seen from Fig.7.66. As shown in Fig.7.67 and Fig.7.68, the thermal stresses for hinge-hinge beam shows similar pattern as of a pin-pin beam but the stresses are higher by 1.52% than stresses for pin-pin beam at 0.01 s.

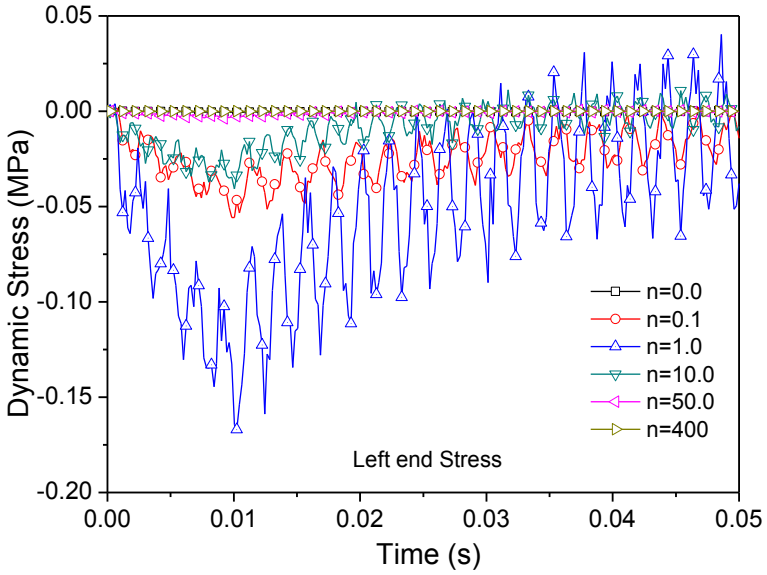

Fig.7.69 Dynamic thermal stress on left end of clamp-pin FGM beam subjected to shock heating.

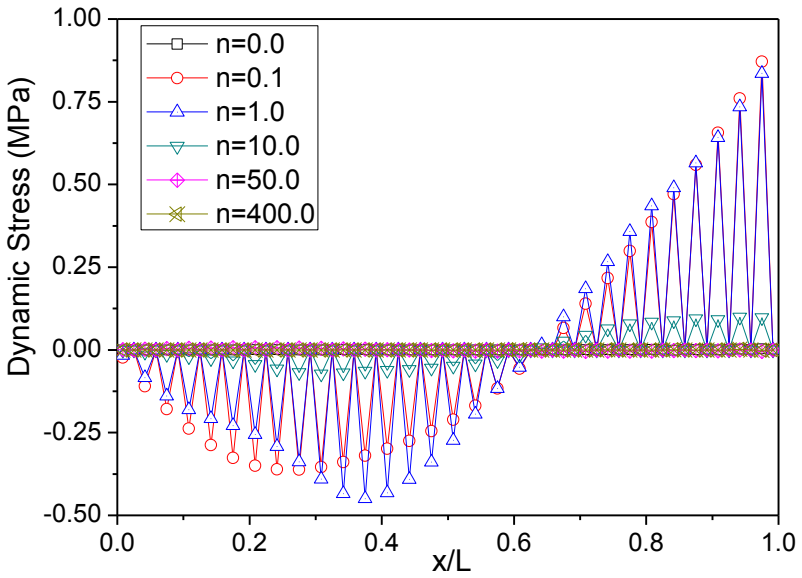

Fig.7.70 Dynamic thermal stress along the length of clamp-pin FGM beam subjected to shock heating at t=0.05 s.

Fig.7.69 shows the dynamic thermal stress at the left end of clamp-pin FGM beam while Fig.7.70 shows stress along the length of the beam. Since the left end is clamped, stresses are negligibly small at this end of the beam. The right end of the beam is constrained from axial movement, the maximum thermal stress is observed at this end of the beam as shown in Fig.7.70. Stress with negative sign is observed towards the

clamp end of the beam while positive stress is seen towards the pin end. The stress is zero at 2/3rd length of the beam from clamp end. The absolute value of stress observed in all the three cases is less than as observed for step heating as the heat source is present for only 0.01 s as against 0.05 s in case of step heat source.

Referring to Figs.9.2 to 9.13, it is observed that due to step and shock heat load, irrespective of the structural boundary condition, the stresses developed in metal rich and ceramic rich beam are less as compared to the stresses developed in the FGM with power law index n =1.0, 0.1 and 10.

7.3.3 Moving heat source

Fig.7.71 shows the dynamic thermal stress at the left end while Fig.7.72 shows dynamic thermal stress at the right end of a pin-pin FGM beam subjected to moving heat source for various power law index. As the heat source moves from left end to right end, the thermal stress starts increasing from zero to maximum and are oscillatory in nature. Referring to Figs.7.71 and 7.72, it is observed that the thermal stresses are maximum for metal rich and ceramic rich beam with n =0, 50 and 400 respectively while for FGM beam with n =0.1, 1.0 and 10, the stresses are minimal or negligible.

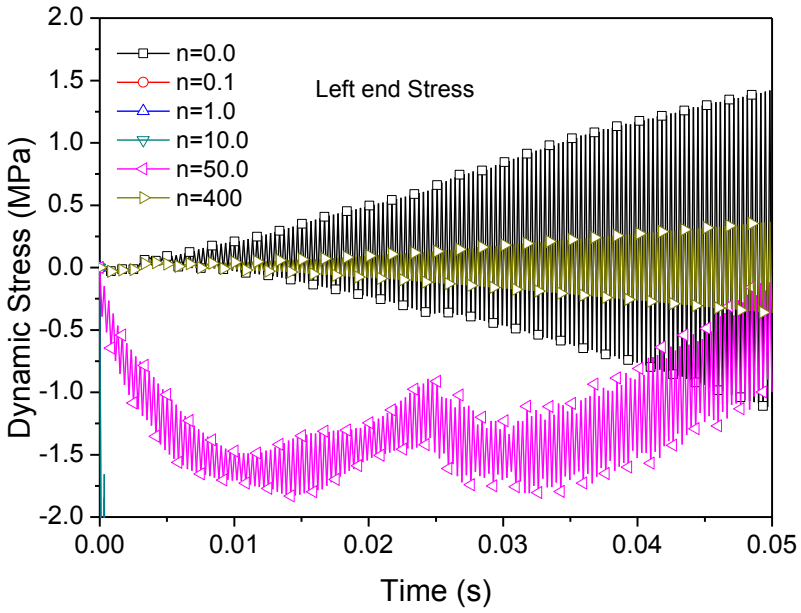

Fig.7.71 Dynamic thermal stress on left end of pin-pin FGM beam subjected to moving heat source.

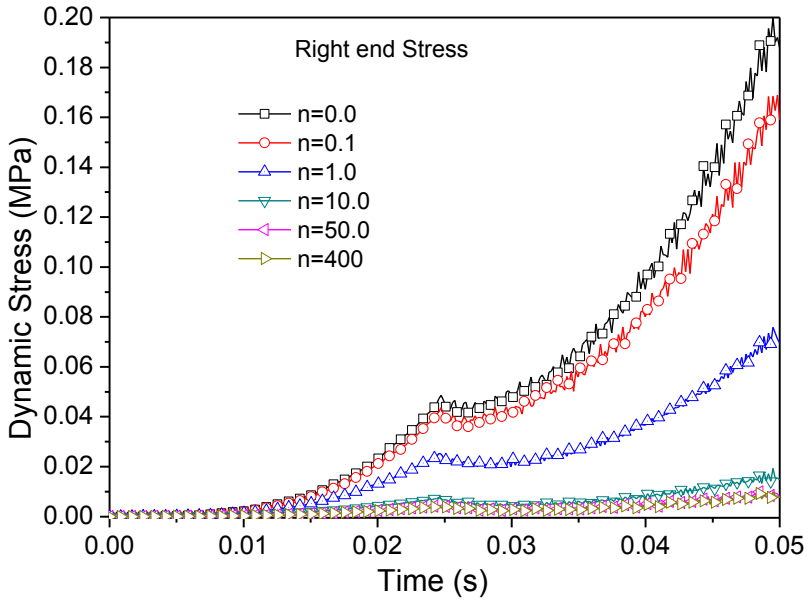

Fig.7.72 Dynamic thermal stress on right end of pin-pin FGM beam subjected to moving heat source.

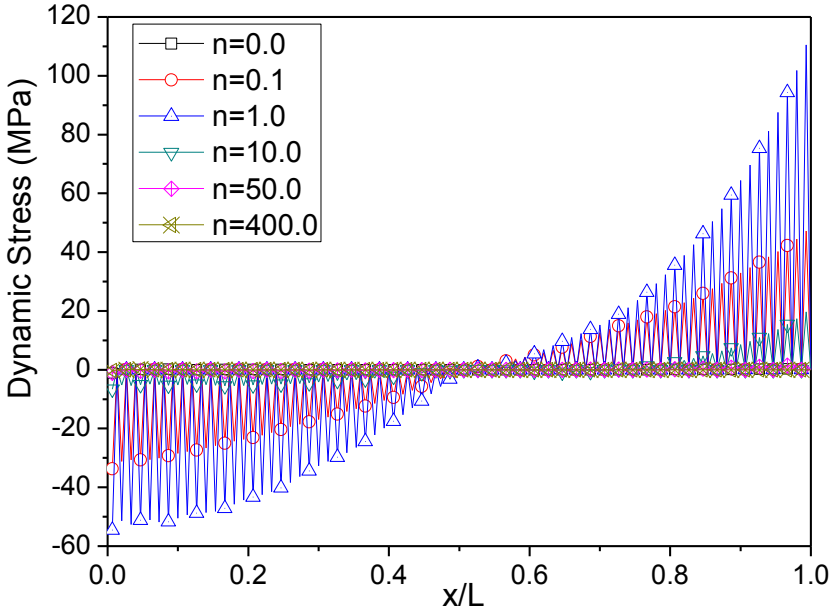

Fig.7.73 Dynamic thermal stress along the length of pin-pin FGM beam subjected to moving heat source at t=0.05 s.

Due to symmetry of the applied boundary conditions for pin-pin beam, stresses are minimum at the centre of the beam as seen from Fig.7.73. The stress is compressive on the left end while it tensile on the right end. The stress on the right end is approximately 2 times the stress on the left end as the heat source moves from left end to right end.

Results similar to pin-pin beam are seen for hinge-hinge beam subjected to moving heat load as shown in Fig.7.74, Fig.7.75 and Fig.7.76 with stress amplitude being higher by 1.48% for hinge-hinge beam.

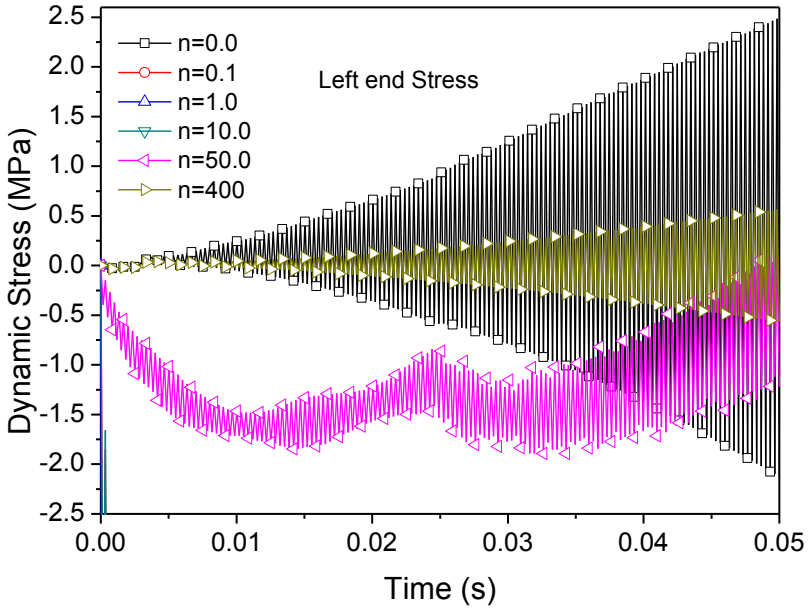

Fig.7.74 Dynamic thermal stress on left end of hinge-hinge FGM beam subjected to moving heat source.

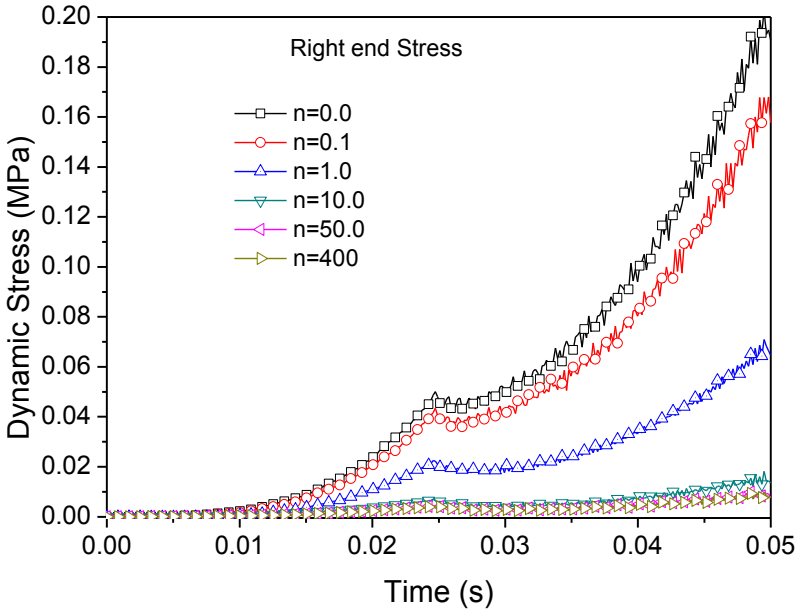

Fig.7.75 Dynamic thermal stress on right end of hinge-hinge FGM beam subjected to moving heat source.

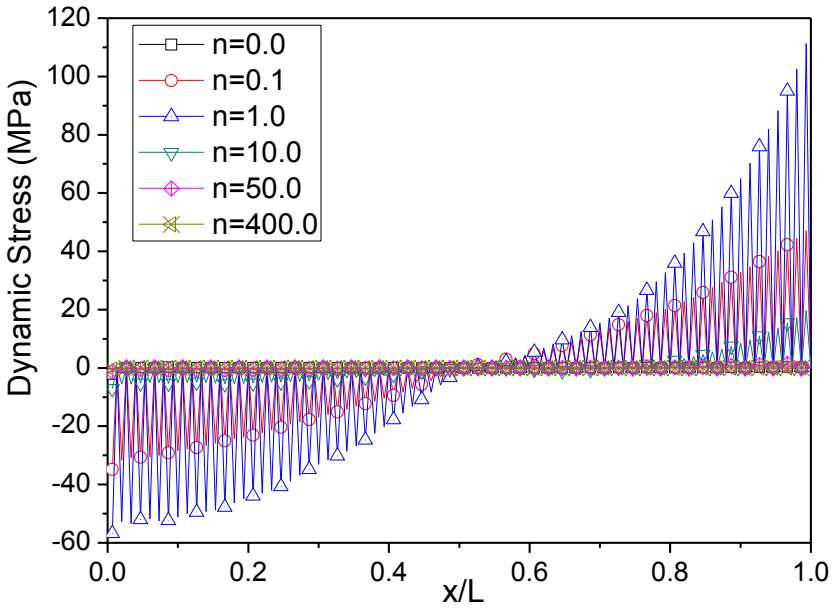

Fig.7.76 Dynamic thermal stress along the length of pin-pin FGM beam subjected to moving heat source at t=0.05 s.

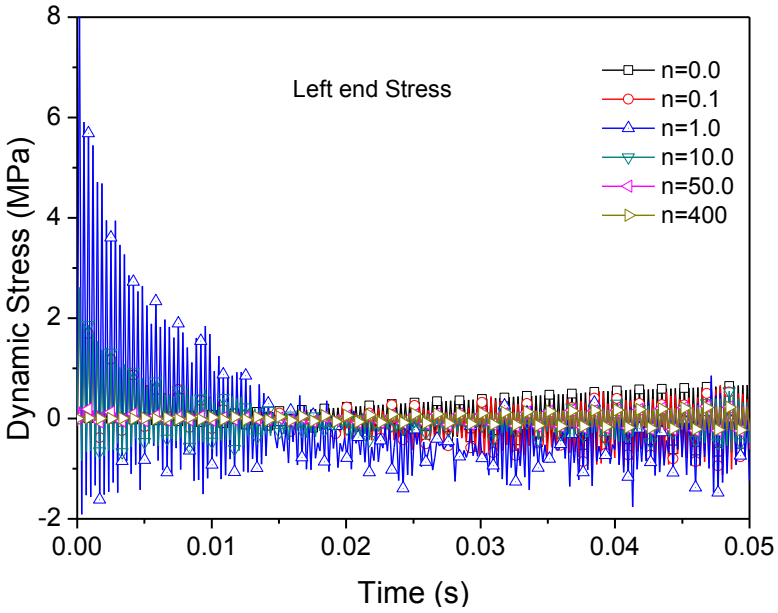

Fig.7.77 Dynamic thermal stress on left end of clamp-pin FGM beam subjected to moving heat source.

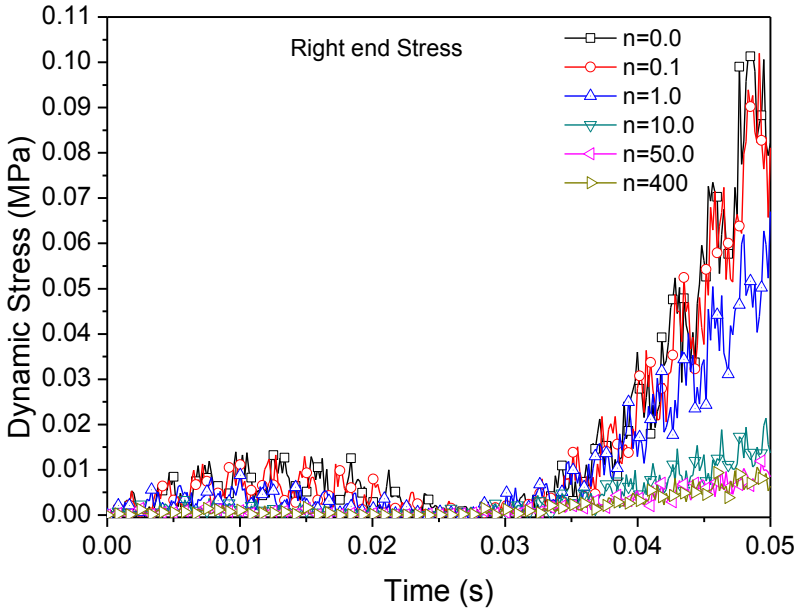

Fig.7.78 Dynamic thermal stress on right end of clamp-pin FGM beam subjected to moving heat source.

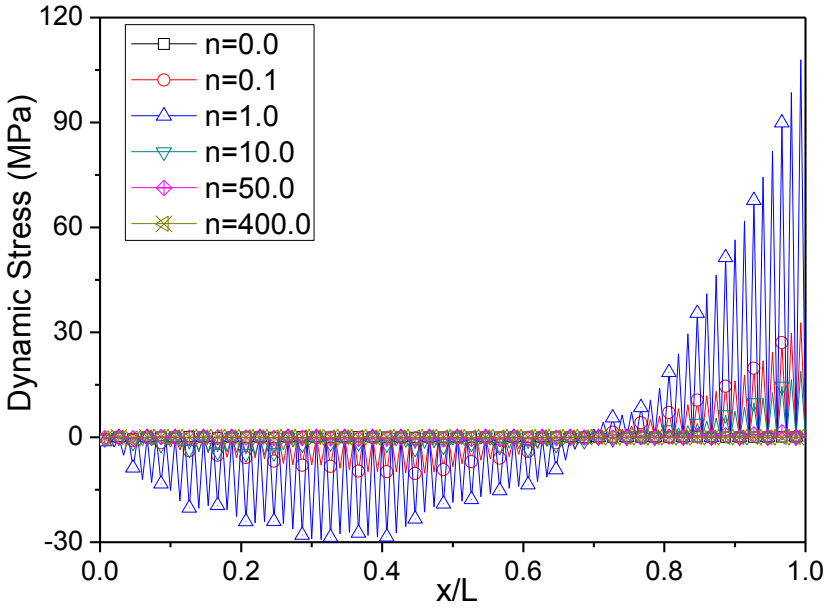

Fig.7.79 Dynamic thermal stress along the length of clamp-pin FGM beam subjected to moving heat source at t=0.05 s.

Fig.7.77 and Fig.7.78 shows the dynamic thermal stress at the left end and right end of a clamp-pin FGM beam respectively while Fig.7.79 shows stress along the length of the beam. Since the left end is clamped, minimal stresses are observed at this end of the beam while the magnitude of stress at the right end of the beam varies depending on

the power law index. Maximum stress is observed when the power law index, $n = 1.0$, as seen in Fig.7.79. Negative stress is observed towards the clamp end of the beam while positive stress is seen towards the pin end. The stress changes from being compressive to tensile at 2/3rd length of the beam. In case of moving heat load, for all the structural boundary conditions, the magnitude of the thermal stress is more than 2 times of the step and shock heat load.

7.3.4 Concentrated line heat source

Fig.7.80 shows the dynamic thermal stress at the left end of a pin-pin FGM beam subjected to line heat source for various power law index. Due to concentrated heat source, large magnitude thermal stresses are observed in the beam. The thermal stress increases with time and show oscillatory trend similar to stresses in step heat source. The magnitude of the stress remains constant for the left half of the beam and is compressive in nature while the stress in right half is tensile in nature as seen from Fig.7.81. The stress changes from compressive to tensile at the centre of the beam due to symmetry of the applied boundary conditions for pin-pin beam.

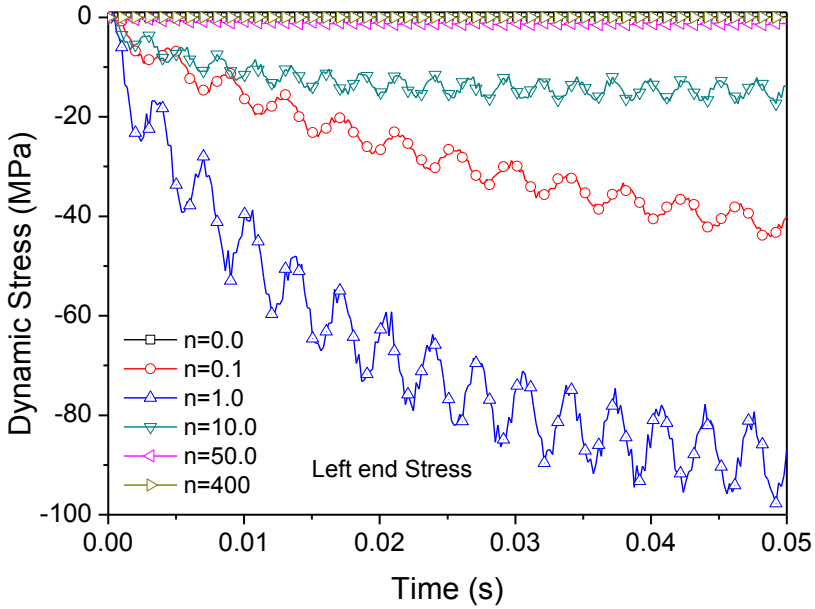

Fig.7.80 Dynamic thermal stress on left end of pin-pin FGM beam subjected to concentrated line heat source.

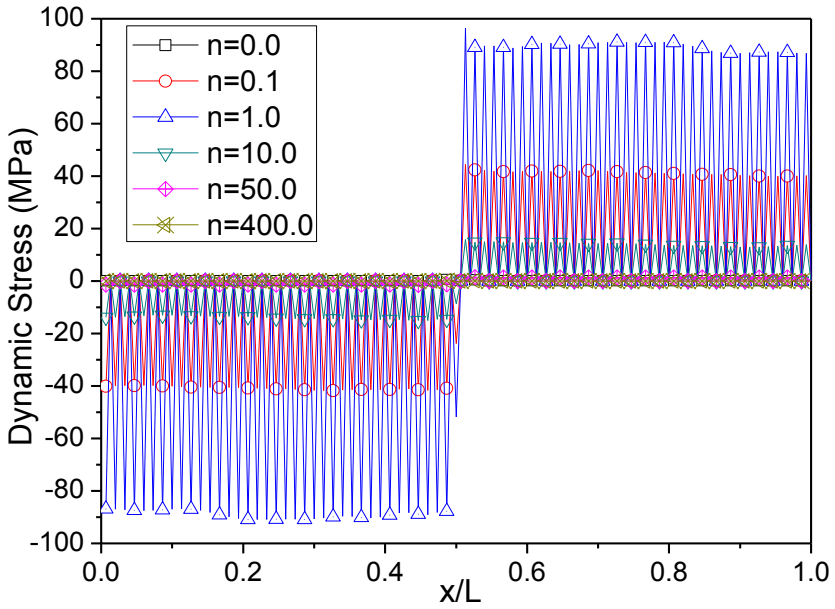

Fig.7.81 Dynamic thermal stress along the length of pin-pin FGM beam subjected to concentrated line heat source at t=0.05 s.

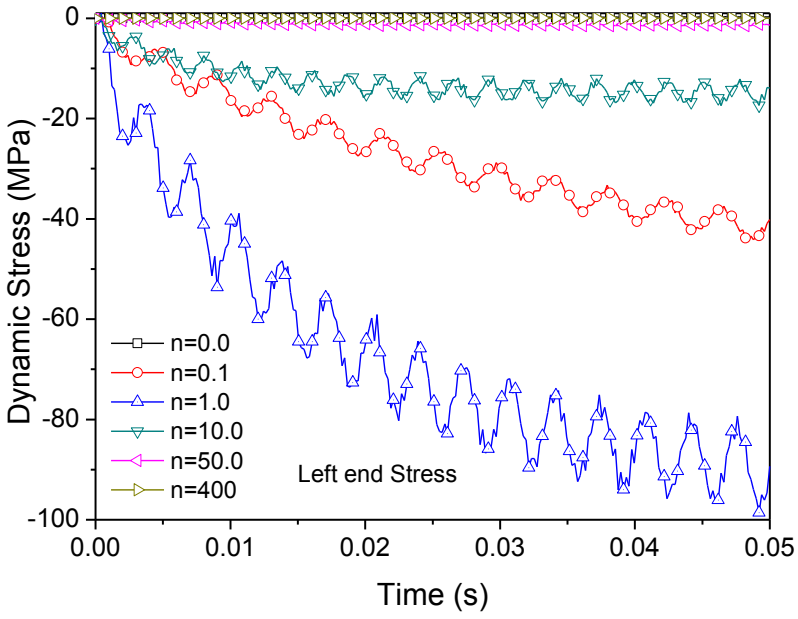

Fig.7.82 Dynamic thermal stress on left end of hinge-hinge FGM beam subjected to concentrated line heat source.

As shown in Fig.7.82 and Fig.7.83, the thermal stresses for hinge-hinge beam shows similar characteristics as for pin-pin beam. Fig.7.84 shows the dynamic thermal stress at left end for clamp-pin FGM beam while Fig.7.85 shows stress along the length of the beam. Since the left end is clamped, hardy any stress is observed at this end of the beam.

As the right end of the beam is constraint from any axial movement, the maximum thermal stress is observed at this end of the beam as shown in Fig.7.85. Maximum stress is observed for the beam with power law index, $n = 1.0$. In the region around clamp end, the stresses have a negative sign while positive stress is observed towards the pinned end. The stress changes from compressive to tensile at the centre of the beam.

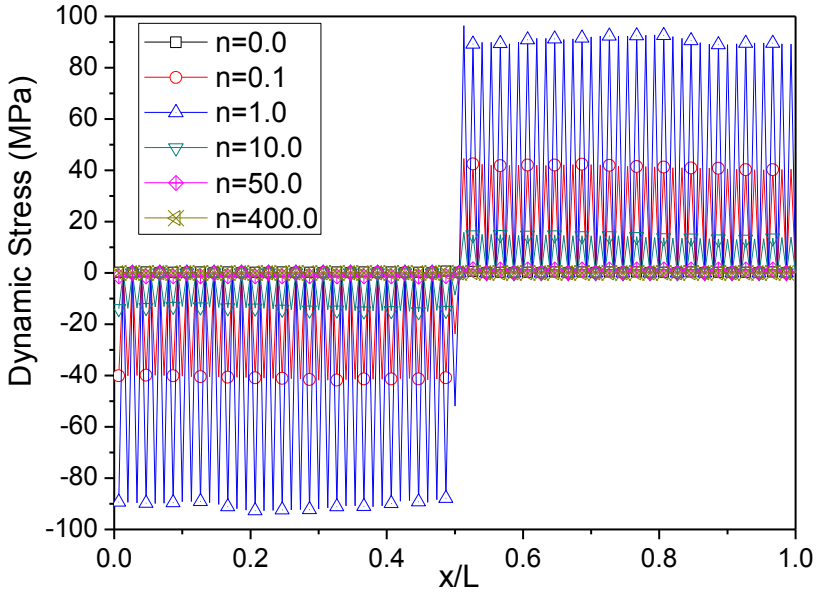

Fig.7.83 Dynamic thermal stress along the length of hinge-hinge FGM beam subjected to concentrated line heat source at *t*=0.05 s.

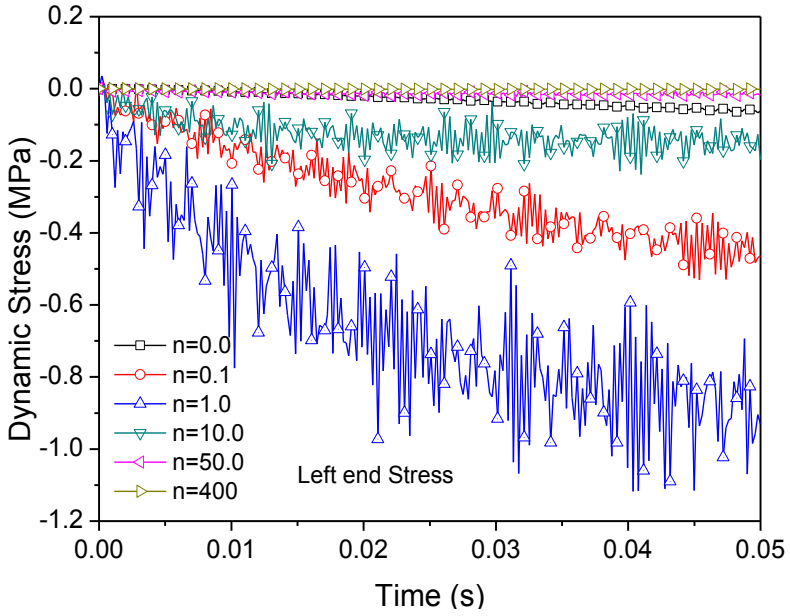

Fig.7.84 Dynamic thermal stress on left end of clamp-pin FGM beam subjected to concentrated line heat source.

In case of concentrated line heat source, irrespective of the applied structural boundary condition, minimal stress is observed for the metal rich and ceramic rich beam while maximum stress is observed for FGM beam with power law index of n =1.0, 0.1 and 10 respectively.

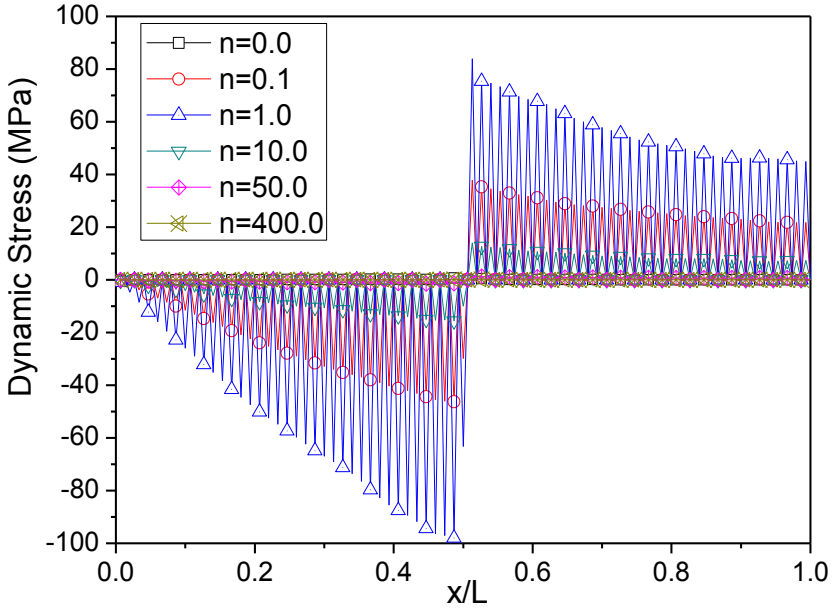

Fig.7.85 Dynamic thermal stress along the length of clamp-pin FGM beam subjected to concentrated line heat source at t=0.05 s.

7.4 SUMMARY

A nonlinear theoretical analysis has been carried out to predict the thermo-elastic response of layered FGM beams of SUS316-Al_2O_3 subjected to step heat, shock heat, concentrated line heat and moving line heat source under various structural boundary conditions. Due to heat loads like concentrated line and moving, evaluation of temperature on a transverse plane is more appropriate than evaluation of temperature across the thickness, hence a two dimensional finite element method is used. Parametric studies are performed to examine the effect of various influential parameters. Effect of TIMP and TDMP on thermal deflection has been also studied.

In the later part, the nonlinear stresses are evaluated for FGM beams of SUS316-Al_2O_3 subjected to step heat, shock heat, concentrated line heat and moving line heat source under various structural boundary conditions. The effect of structural boundary conditions and thermal loads is discussed in this chapter. It is observed that the stresses

in the hinge-hinge beam are marginally higher than pin-pin beam. For clamp-pin beam, irrespective of the heat load, the stress at the clamp end of the beam is minimum approaching to zero. The stresses in the left half of the beam are compressive while tensile stresses are observed on the right hand side. In case of clamp-pin beam, for all the heat loads, the stress changes its sign approximately at 2/3rd length of the beam from clamp end of the beam. The magnitude of the stress largly depends on the power law index, being highest for n =1.0. The stress magnitude is minimal or zero for pure ceramic and metal rich beams.

CHAPTER - 8

EXPERIMENTAL VALIDATION OF THERMAL ANALYSIS AND THERMO-ELASTIC DEFLECTION OF FUNCTIONALLY GRADED BEAMS

8.1 INTRODUCTION

Functionally Graded Material beam samples with multiple layers of metal-ceramic combination with their volume fractions varying from layer to layer were prepared for the experimental investigation as detailed in chapter 5. SUS316-Al_2O_3 FGM samples were prepared by thermal spray technique and Al-Al_2O_3 FGM samples were made by powder metallurgy process. Thermal analysis is carried out on both the FGM samples and results are validated with the results obtained using ANSYS for SUS316-Al_2O_3 FGM beam sample. Free vibration studies are carried out on the FGM beam samples under clamp free boundary condition with heat source at the clamp end. Thermal deflection study is also carried out for SUS316-Al_2O_3 FGM cantilever beam with heat source at clamp end. Theoretical model is also presented for the thermal deflection of SUS316-Al_2O_3 FGM beam.

8.2 TRANSIENT THERMAL ANALYSIS OF SUS316-AL_2O_3 FGM BEAM WITH HEAT SOURCE AT ONE END OF BEAM

This section discusses on experimental studies on the transient thermal analysis of SUS316-Al_2O_3 and Al- Al_2O_3 FGM beam. The results for SUS304-Al_2O_3 FGM beam are validated with the transient three dimensional heat transfer simulation using ANSYS R14.

8.2.1 Experimental setup for thermal analysis of FGM beam

Fig.8.1 shows the experimental setup for temperature evaluation of FGM beam. The heating coil is fixed at the free end of the beam with araldite. The rating of the heating element used is 10W. The other end of the beam is fixed in the clamp with heat insulators to avoid transfer of heat from beam to clamp. The beam with heating element attached at the end is kept in the closed box to avoid cooling by means of cross currents from outside air. The heat is supplied to the electric heater coil by means of 64V, 5A DC power supply (current × voltage gives the magnitude of heat flux). The temperature profile on the top surface of the beam is captured by means of thermal imaging camera, Testo-875 (refer APPENDIX II, section II.2 for more details of camera). The image is processed in "testo IRSoft" software. The temperature values at various locations on the beam can be extracted from the image using the software and can be imported to excel file for further processing. This data can be used for comparative analysis with ANSYS simulation results.

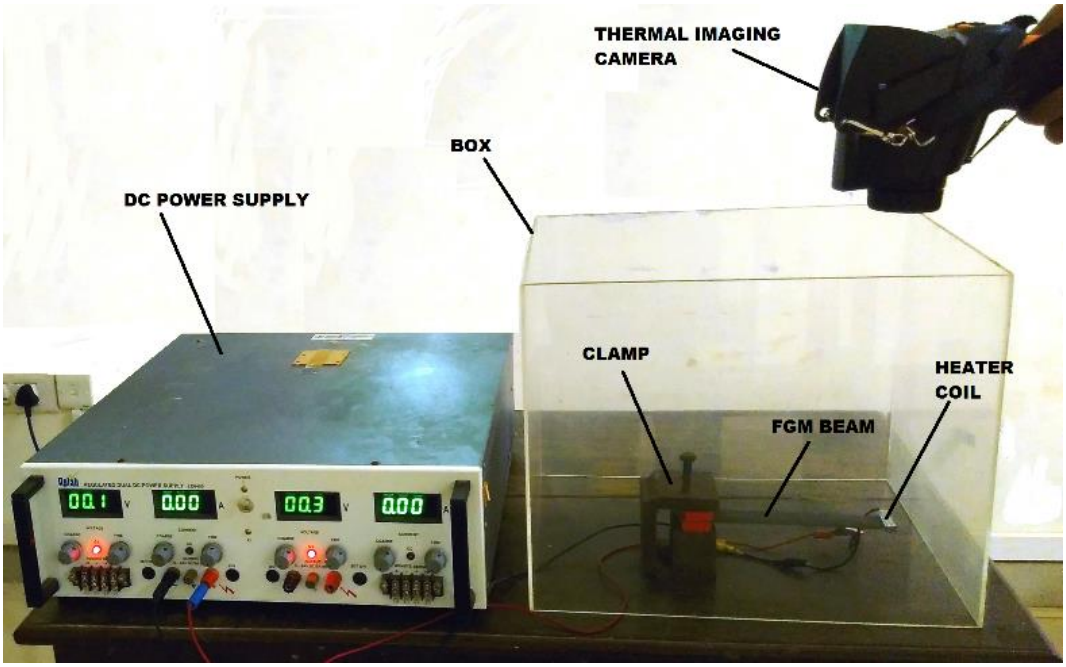

Fig.8.1 Experimental setup for thermal analysis of FGM beam.

8.2.2 Results and discussion on thermal analysis of SUS316-Al_2O_3 FGM beam

The transient thermal analysis of a thin SUS316-Al_2O_3 FGM beam with heating element located at free end of beam is carried out using ANSYS R14 considering temperature dependent material properties. The temperature distribution for SUS316-Al_2O_3 FGM beam has been validated using experimental study. Eight node brick element 'SOLID 70' with a single degree of freedom, temperature, at each node is used. It has a 3-D thermal conduction capability and can be used for 3-D, steady-state or transient thermal analysis. The size of the beam considered in the analysis is 162mm x 30mm x 0.84mm thick (SUS316-Al_2O_3 sample-5). The reference temperature assumed was 300 K. The beam is sweep meshed using hexahedron elements. The entire surface is divided into 81x15 grid and 7 layers across the thickness of the beam. The boundary and loading conditions are - heat flux of 3.24 W is applied at the end of the specimen (total area of heat application is 30x8 mm) for 300 s (5min) and the convective heat transfer coefficient of 20 W/m^{2}K is considered (Malik and Kadoli, 2005). Also it is assumed that volumetric heating is absent. The ANSYS simulation results are compared with experimental study. From Fig.8.2, it is observed that, as the time progresses, the temperature starts increasing at the end of the beam where heat source is present and diffuses in the surrounding area.

Fig.8.3 shows the experimental temperature variation along the length of the SUS316-Al_2O_3 FGM beam sample-5 from t=0 to 300 s. The temperature is highest at the location where the heat source is present. The temperature decreases along the length of the beam and away from the heat source. With time progressing, the temperature profile along the length of the beam also gradually decreases. Even after 300 s, the temperature away from the heat source is close to ambient. Table 8.1 presents the temperature obtained using experimental study and ANSYS near the heat source and 50mm away from the heat source. Maximum error of 17% is observed between the experimental study and ANSYS simulation results near the heat source while the maximum error 50mm away from heat source is 5.65%.

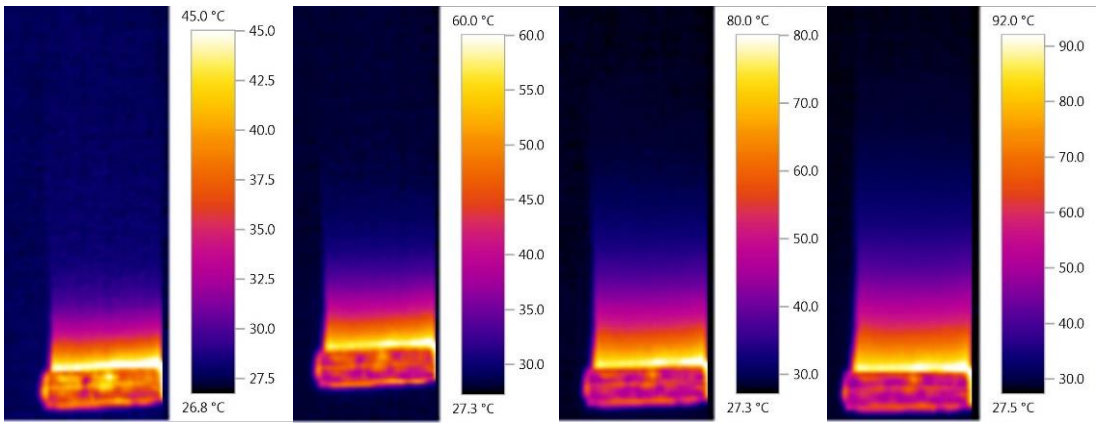

t=30 s *t*=60 s *t*=120 s *t*=180 s

(a) Experimental thermal plots (temperature in ^{0}C).

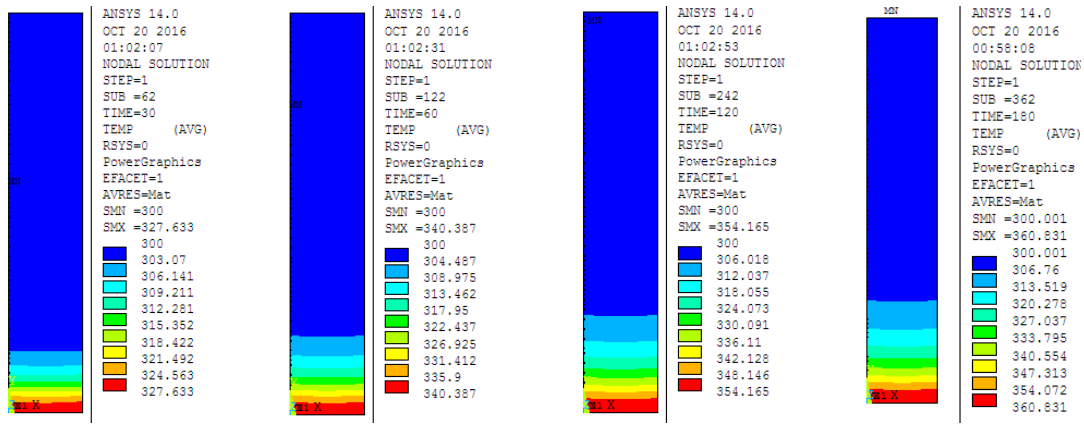

t=30 s *t*=60 s *t*=120 s *t*=180 s

(b) ANSYS-R14 thermal plots (temperature in K).

Fig.8.2 Temperature variation along the length of the beam from *t*=30 s to 180 s for SUS316-Al_2O_3 FGM sample-5.

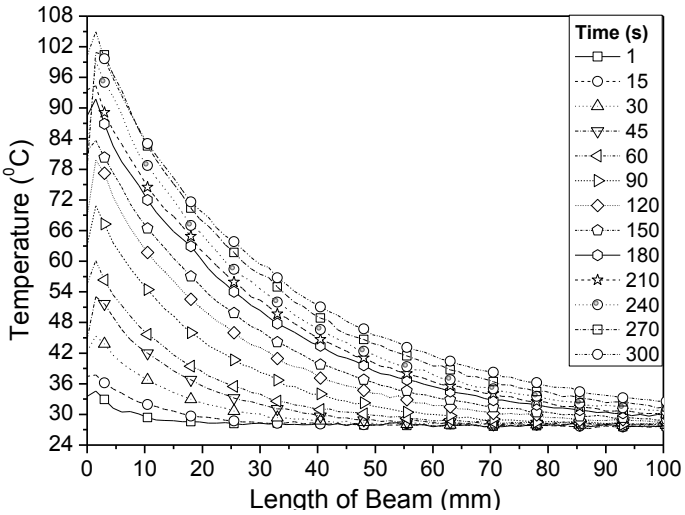

Fig.8.3 Experimental temperature variation along the length of the SUS316-Al_2O_3 FGM beam sample-5 from *t*=0 to 300 s.

Table 8.1 Temperature at different times for SUS316-Al_2O_3 FGM beam sample-5.

Time (s)	Temperature – Experimental (^{0}C)		Temperature - ANSYS - R14 (^{0}C)		% Error	
	1 mm from heat source	50 mm from heat source	1 mm from heat source	50 mm from heat source	1 mm from heat source	50 mm from heat source
30	42.7	27.9	50.03	28.54	-17.16	-2.28
60	54.85	28.4	60.66	29.24	-10.59	-2.97
120	74.95	30.1	72.14	30.01	3.75	0.30
180	84.75	32.1	77.69	32.07	8.33	0.09
240	93.6	33.8	80.52	32.36	13.98	4.27
300	97.7	36.4	81.98	34.34	16.09	5.65

8.2.3 Results and discussion on thermal analysis of Al-Al_2O_3 FGM beam

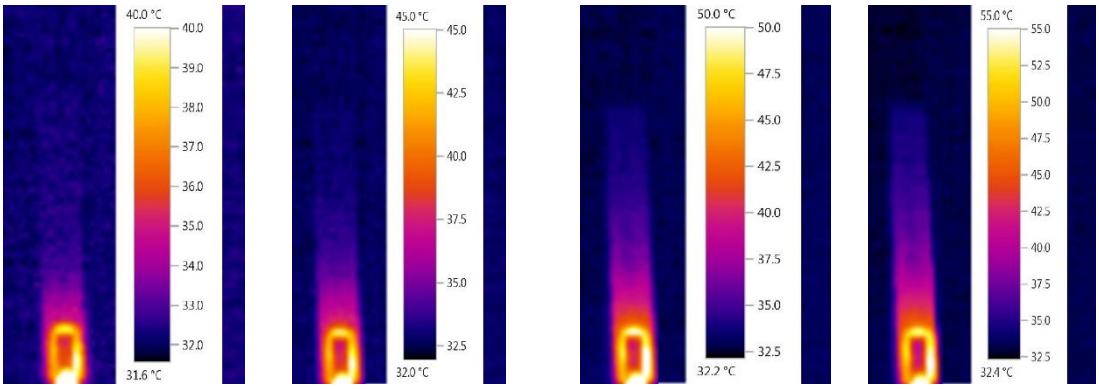

(a) Experimental thermal plots.

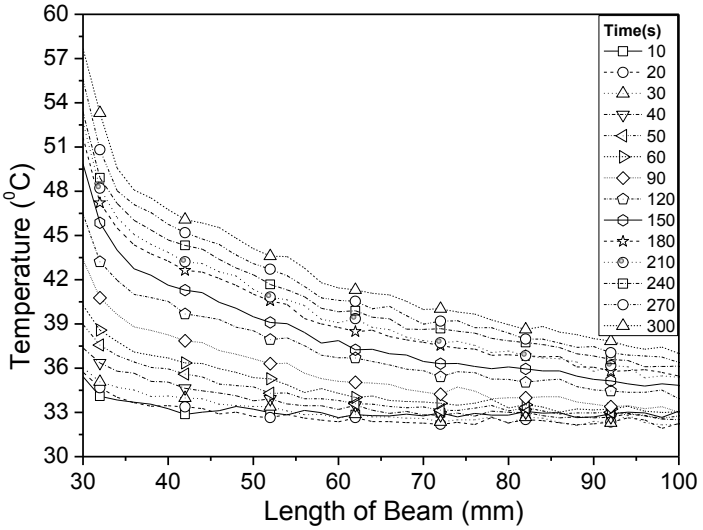

(b) Temperature variation along the length.

Fig.8.4 Experimental temperature variation along the length of the Al-Al_2O_3 FGM beam sample-20 from t=0 to 300 s.

Studies have also been carried out for Al-Al_2O_3 FGM beam sample-20 of size 150mm x 20mm x 2.49mm thick. Fig.8.4(a) shows the experimental thermal plots and Fig.8.4(b) shows the experimental temperature variation along the length of the beam from *t*=0 to 300 s. Results similar to SUS316-Al_2O_3 FGM beam are observed wherein the temperature gradually decreases to ambient from the end where heat source is present toward the other end. ANSYS thermal simulation is not carried out for this sample as temperature dependent material properties are not available for pure aluminium material to consider in the simulation.

8.3 THERMAL VIBRATION OF SUS316-AL_2O_3 FGM BEAM

Thermal vibration studies have been carried out on the SUS316-Al_2O_3 FGM beam sample under clamp free boundary condition. The heat is applied at clamp end using electric heating coil. The response of the 2 FGM beams and pure SUS316 beam are studied at various heat loads varying from 2.925 W to 23.9 W. Theoretical model is validated with experimental results for SUS316-Al_2O_3 FGM beam sample-1.

8.3.1 Experimental setup for thermal vibration of SUS316-Al_2O_3 FGM beam

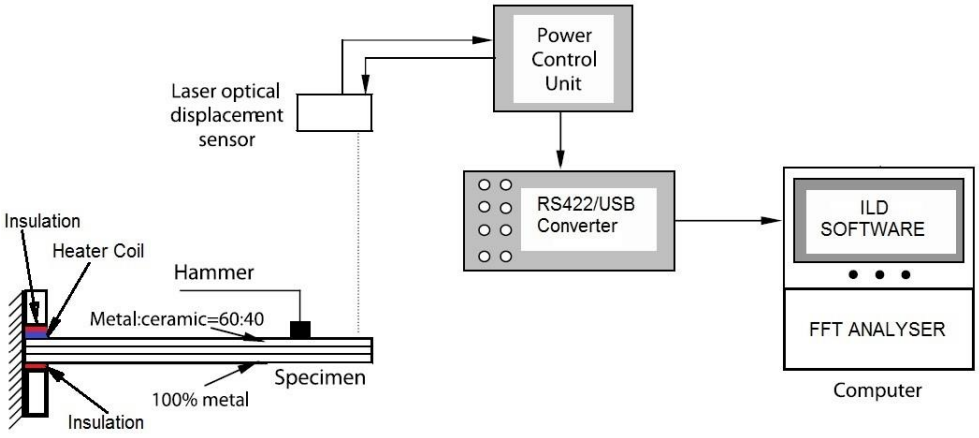

Fig.8.5 Schematic diagram of experimental set-up for thermal vibration.

The experimental setup is schematically shown in Fig.8.5 while Fig.8.6 shows the actual experimental setup to study vibration characteristics of the beam under heat load. The electric coil (30x20mm) is fixed at one end of the beam with araldite. The contact between the beam surface and clamp surface in the region where beam is held on to the

clamp is curtailed by wrapping insulators. Thus minimising the heat loss from the beam to the clamping parts. The entire assembly is fixed in the clamp support to simulate clamp free boundary condition. The beam with clamp support and heating element attached at the end is kept in the closed box to avoid cooling by means of cross currents from outside air. The heat is supplied to the electric heater coil by means of 64V, 5A DC power supply with maximum capacity of 320 W.

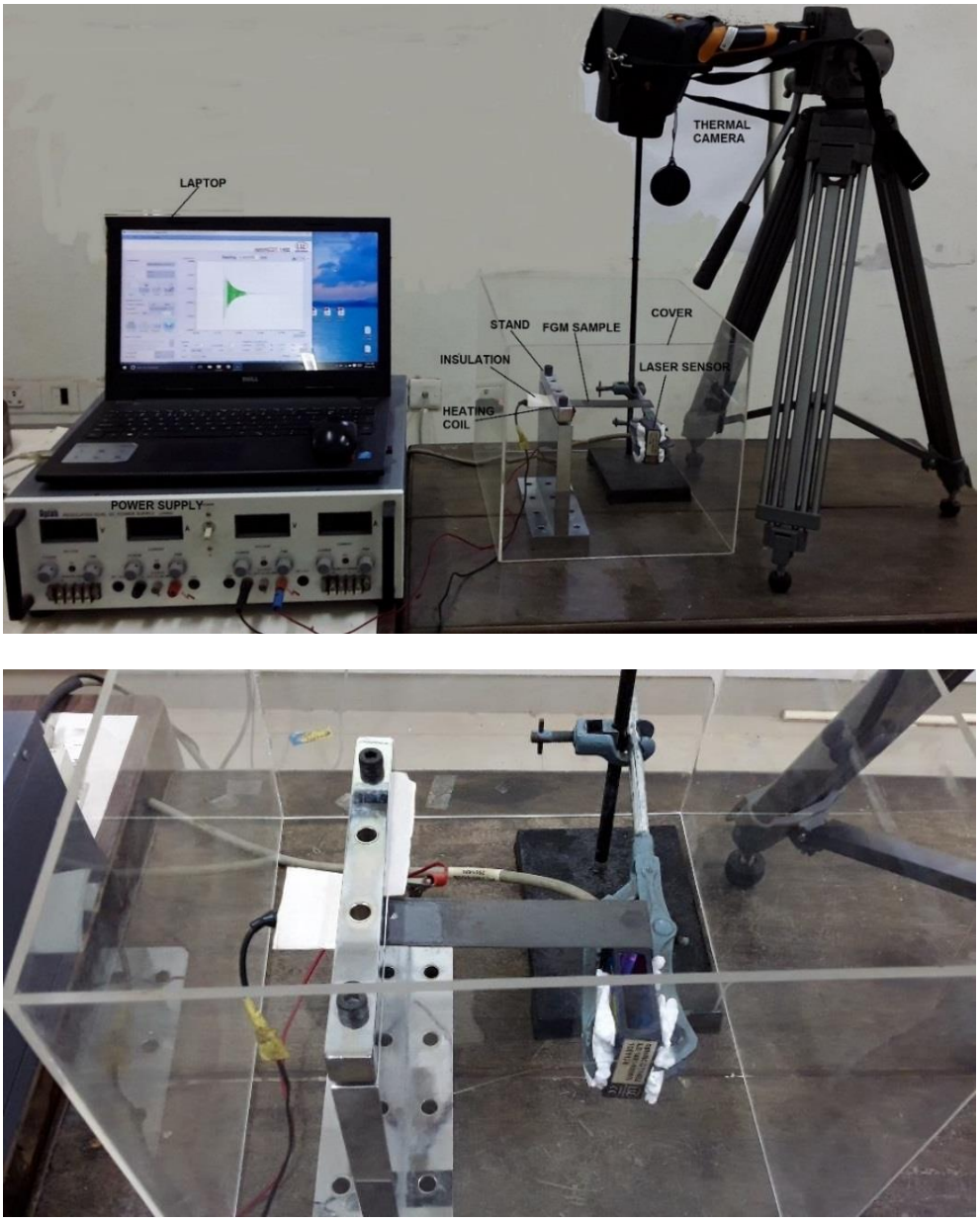

Fig.8.6 Experimental setup for thermal vibration analysis.

The temperature profile is captured from top by means of thermal imaging camera, Testo-875, as shown in Fig.8.6. The natural frequencies were measured for cantilever FG beam using the impact hammer testing method when the beam was heated by means of electric coil with DC power supply. The impulse is provided with an impact hammer with steel tip. The response was measured with laser optical displacement sensor. The signal from the laser sensor was acquired into a computer using ILD software. The FFT of the time domain response was computed using the data processing software, Origin Pro 8.0, to obtain the frequency response. The peak locations give the natural frequencies at various modes.

8.3.2 Results and discussion on thermal vibration of SUS316-Al_2O_3 FGM beam

A total heat of 23.9W is applied on the beam sample at the fixed end with 64V, 5A DC power supply for 5min to study the effect of heat load on vibration characteristics of the SUS316-Al_2O_3 FGM beam. Fig.8.7(a) show temperature variation along the length of beam at different time intervals while Fig.8.7(b) shows the temperature variation with respect to time at various points on beam for SUS316-Al_2O_3 FGM beam sample 1. It is observed from Fig.8.7(a) that the temperature is highest where the heat source is present and gradually decreases to ambient away from heat source towards the free end. Near the heat source, the temperature quickly increase to 85^0C within 1.5min and then starts increasing slowly to attain steady state temperature of approximately 89^0C for remaining 3.5min of study. The vibration amplitude were measured to study the effect of heat load on the natural frequency and thermal deflection of the FGM beam. The natural frequency of the beam without heat load is observed to be 49.73Hz. For the beam subjected to heat load and steady state temperature of 89^0C at around 300 s, frequency of the beam was measured as 48.622Hz. The corresponding damped vibration plot and natural frequency plot are shown in Fig.8.8. A drop in frequency of 2.23% is observed when the beam is heated for about 5min (300 s). Fig.8.9 gives the plot of frequency verses time with superimposed temperature profile taken near the heat source. This plot shows how the temperature effects the frequency of the FGM beam. It is observed that as the temperature of the beam increases, the natural frequency of the FGM beam decreases and starts stabilising as temperature starts attaining steady state at around 300s.

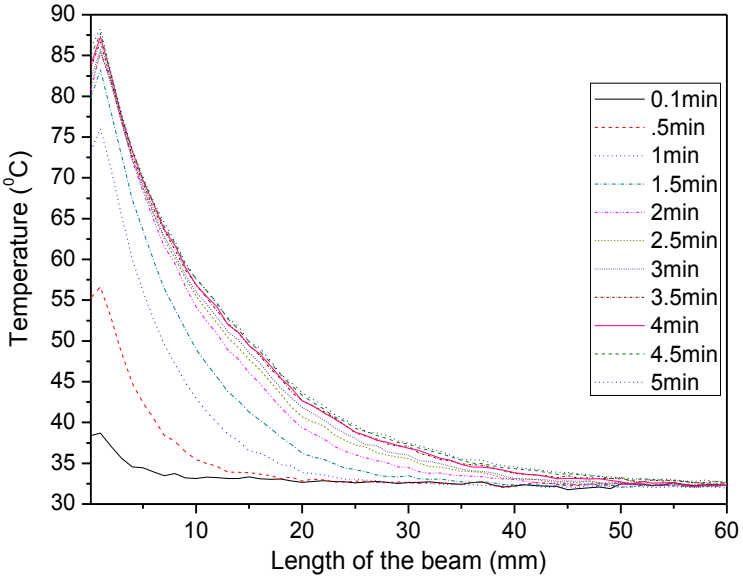

(a) Temperature variation along the length of beam at different time intervals.

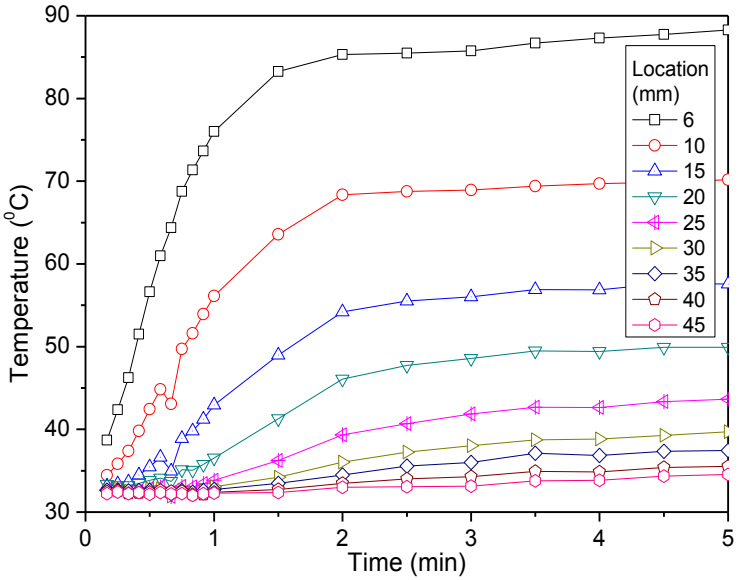

(b) Temperature variation with respect to time at various points on the beam.

Fig.8.7 Temperature distribution on SUS316-Al_2O_3 FGM beam sample-1.

Fig.8.10 show comparison of experimental and theoretical thermal deflection profile of SUS316-Al_2O_3 FGM beam Sample 1. A deflection of 0.6mm is observed in the beam when the beam reaches at around 89^0C. The deflection of the FGM beam is caused because of the thermal load without any external physical load. This thermal deflection occurs due to differential thermal expansion coefficients of SUS316 and Al_2O_3. It is observed that initially beam starts bending and within 60 s the stabilised deflection of

approximately equal to 0.6mm is observed. In yet another trial on SUS316-Al_2O_3 FGM beam sample 1, a total heat of 12.922 W is applied at the fixed end with 64V, 5A DC power supply for 5min. The ambient temperature was recorded as 31.9 ^{0}C. When steady state temperature is achieved at around 300 s, frequency of the beam was observed to be 48.8252 Hz. A drop in frequency was observed with respect to time when the beam is heated for about 5min. A deflection of 0.135mm is observed in the beam when the beam attains temperature of 64^{0}C. The detail result plots are available in APPENDIX-V, section V.1.1.

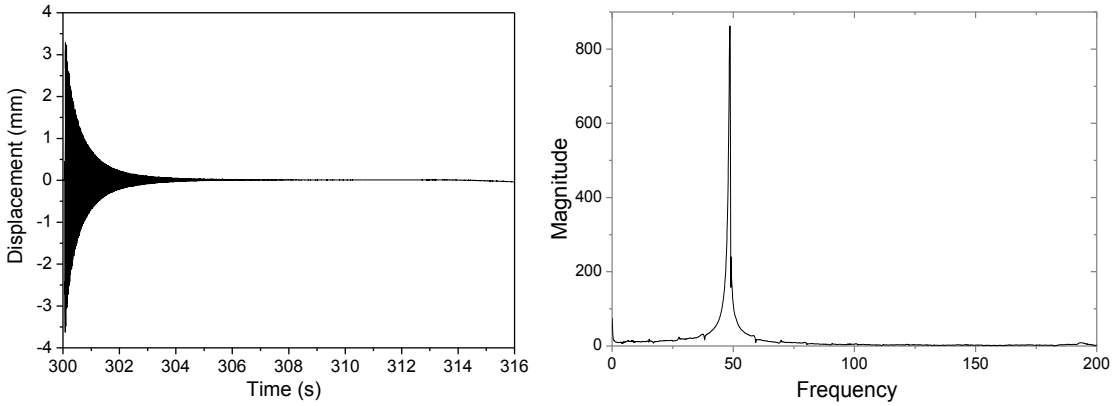

Fig.8.8 Natural frequency of three-layer SUS316-Al_2O_3 FGM beam sample 1 under cantilever boundary condition after 300 s is 48.622Hz.

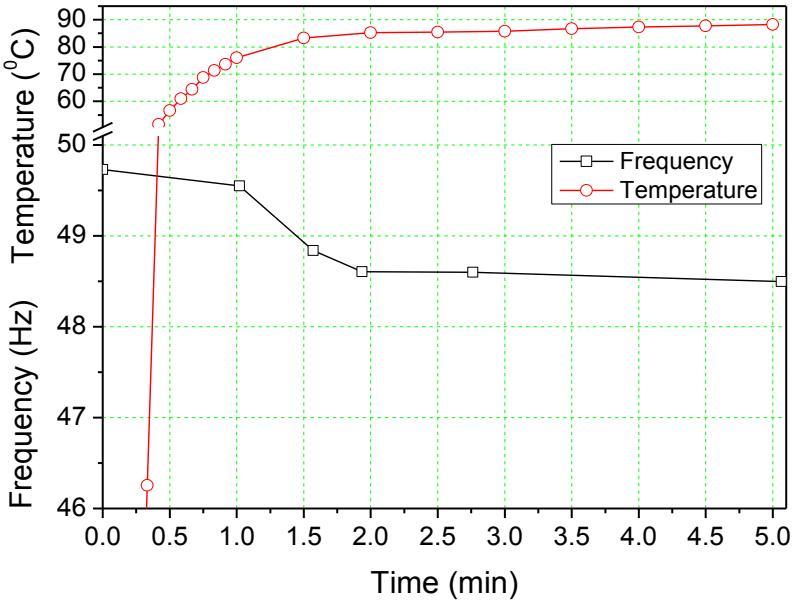

Fig.8.9 Frequency verses time and temperature verses time plot for SUS316-Al_2O_3 FGM beam sample 1.

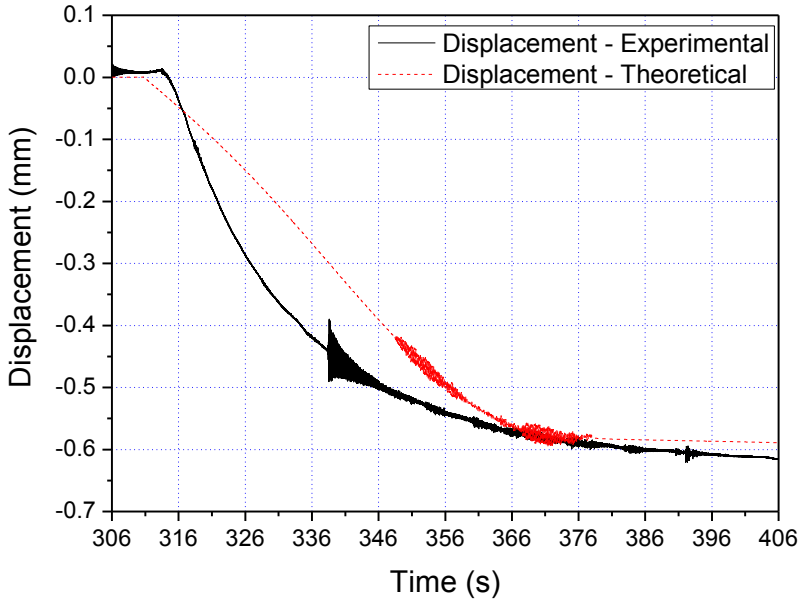

Fig.8.10 Comparision of theoretical and experimental thermal deflection profile of the SUS316-Al_2O_3 FGM beam sample 1 after t=306 s.

Similar studies have been carried out on pure SUS316 beam and SUS316-Al_2O_3 FGM beam sample 3. The temperature distribution, natural frequency, vibration response and thermal deflection plots are presented in APPENDIX-V. A heat load of 3.27 W was applied at the fixed end of SUS316-Al_2O_3 FGM beam sample 3 for 5 min. The deflection and frequency response characteristics similar to SUS316-Al_2O_3 FGM beam sample 1 were observed. After 5 min, a thermal deflection of 0.15mm was observed at the tip of the beam while the reduction in frequency was 0.36%. Similarly, for pure SUS316 beam, a heat load of 4.8075W was applied at the fixed end for 5min. Nither reduction in the frequency nor the thermal deflection were observed at the tip of the pure SUS316 beam. This concludes that varying thermal expansion coefficient between the top and the bottom layers of the FGM beam gives rise to thermal moment causing thermal deflection of the beam.

8.4 SUMMARY

The temperature distribution obtained using ANSYS has been validated using experimental study for SUS316-Al_2O_3 FGM beam sample. The temperature profile from ANSYS simulation results are in close comparison with the experimental results. The thermo-elastic response has been validate through experimental studies for

SUS316-Al_2O_3 FGM beam sample-1 when subjected to heat load at the fixed end of the beam. The experimental results are in close comparison with the theoretical results. Thermal deflection studies have also been attempted on SUS316-Al_2O_3 FGM beam sample-3 and pure SUS316 beam sample.

CHAPTER – 9

CONCLUSIONS AND SCOPE FOR FUTURE WORK

Thermal spray and powder metallurgy technique were used to fabricate stainless steel-alumina and aluminium-alumina FGM beams respectively. The various steps involved in the fabrication of the FGM beam samples using thermal spray and powder metallurgy processes were discussed. Microstructural studies of FGM powder mixtures and FGM beam samples reveal good interface between substrate and coating material with minor porosity for thermal spray sample and continuous gradation of the material for the samples prepared using powder metallurgy process. SEM-EDX analysis confirms the assumed element content in the Al-Al_2O_3 FGM and pure aluminium beam sample.

The experimental and theoretical studies have been carried out to predict the static bending and free vibration response of pure stainless steel, pure aluminium and layered FGM beams of SUS316-Al_2O_3 and Al- Al_2O_3 fabricated with plasma spray processes and powder metallurgy process respectively. The non-linear finite element FORTRAN program for FGM beam has been verified with the available literature for beams with pinned-pinned boundary conditions. From the study, the following general conclusions may be cited:

a) The theoretical and actual densities of SUS316-Al_2O_3 and Al-Al_2O_3 FGM and pure aluminium beam samples are compared and it is found that the difference in theoretical and actual densities is highest for Al-Al_2O_3 as compared to SUS316-Al_2O_3 FGM beam.
b) The accuracy of the theoretical model is established by comparing the static deflection and natural frequencies of clamped free and clamp-simple support FGM beams with experimental results. The comparison reveals that the

theoretical predictions match reasonably very well with experimental results for the three-layer SUS316-Al_2O_3 FGM beams with maximum errors of 12.91% for the deflection and 2.02 to 14.31 % for the fundamental frequency.

c) The error in the theoretical predictions for sample-2 is on the higher side, which may be due to lack of perfect bonding at the layer interfaces, variation in material properties being assumed and thickness of adjacent layer for the three-layer sample.

d) The third mode for SUS316-Al_2O_3 FGM beams sample 1 and 3 was observed to be a twisting mode. The fundamental frequency predicted by 3D solid element in ANSYS is very much close to the experimental frequency. Shear deformation theory should be used in order to establish the maximum accuracy of the theoretical model and to accurately predict higher modes.

e) In case of pure aluminium and Al-Al_2O_3 beam, error more than 50% for deflection and fundamental frequency was observed with respect to experimental results.

f) The error ranging from 11-23% was observed between actual and theoretical density of the pure aluminium and Al-Al_2O_3 FGM beam sample. The density evaluated using Archimedes principle was also found to be comparatively less than the theoretical density with an error of 7-10%. This concludes that the samples are porous.

g) The commonly used and accepted theoretical models on porosity effect available in the literature were used to obtain the theoretical results. Considering the porosity effect, 24-31% reduction in error was observed for pure aluminium beam while the error reduced by 13% for Al-Al_2O_3 FGM beam.

A theoretical analysis was presented on the thermally induced vibrations of FGM beams subjected to step heat input on top surface. The bottom surface was insulated or subjected to convection heat loss. The method has been verified for fully metallic aluminium beam (n=400) with the results given by Boley (1956). Fundamental non-dimensional frequencies have been verified with frequencies reported by Simsek and Kocaturk (2009) and Alshorbagy et al. (2011). Two functionally graded material combinations, aluminium-zirconia and stainless steel-aluminum oxide with

temperature dependent and temperature independent material properties were considered for the study. Some parametric studies are performed to examine the effect of various influential parameters. After accomplishing some parametric studies the following general conclusions may be cited:

a) Static thermal deflection and the associated thermal oscillations are dependent strongly on the elastic modulus of the FGM beam. FGM beam having low elastic modulus undergoes smaller magnitude of static thermal deflection with thermal oscillation superimposed and attains steady state faster.
b) The amplitude of the thermal oscillations for metal rich beam is higher as compared to ceramic rich beam; frequency of oscillations is less for metal rich beam and temperature induced oscillations occur with respect to the mean position.
c) Mid-span deflection for SS beam are four times of CS, and free end deflections for CF beam are four times of SS beam.
d) Metal-ceramic combination and power law index of the FGM beam greatly affects the vibration characteristics of the beam under thermal load.
e) The mid span deflection for beam with bottom surface insulated is more than the one with convective heat loss as the surface temperature on the bottom layer is less as compared to insulated beam and the difference varies exponentially with time.

The theoretical studies have been carried out to predict the thermo-elastic response of layered FGM beams of SUS316-Al_2O_3 subjected to shock heat, concentrated line heat and moving line heat source under various structural boundary conditions. Due to heat loads like concentrated line and moving, evaluation of temperature on a transverse plane is more appropriate than evaluation of temperature across the thickness, hence a two dimensional finite element method is used. The following general conclusions are recorded:

a) In case of shock heat load, the thermal deflections increases with time and the time for maximum deflection either leads or lags marginally with respect to the time for maximum temperature rise.

b) In case of step heating and concentrated line heat source, the thermo-elastic deflection increases with time irrespective of the power law index and structural boundary conditions on the beam.
c) In case of moving heat source, higher the velocity of heat source, lower is the deflection. The time for maximum deflection depends on the power law index, being maximum for metal rich beam compared to ceramic rich beam.
d) The study confirms that the inclusion of geometric non-linear terms in the analysis is essential when heat load increases.
e) The stresses due to thermal load depends on the power law index and their magnitude increases with increase in thermal load. Design of FGM beams under thermal environment becomes crucial since large thermal loads can result in stresses exceeding the yield stress.

Thermal analysis is carried out on SUS316-Al_2O_3 and Al-Al_2O_3 FGM beam with heat source at one end. The temperature distribution is simulated using ANSYS and is validated with the experimental results. The temperature is highest at the location where the heat source is present and decreases along the length of the beam away from the heat source. An error of 17% is observed near the heat source while the maximum error 5.65% is observed 50mm away from heat source. The effect of heat load on vibration and thermal deflection characteristics of the SUS316-Al_2O_3 FGM beam is studied under clamp free boundary condition with heat applied at clamp end. The response of the 2 FGM beams and pure SUS316 beam are studied at various heat loads varying from 2.925 W to 23.9 W. It is observed that as the temperature of the beam increases, the natural frequency of the FGM beam decreases and starts stabilising as temperature starts attaining steady state. Thermal deflection are observed in case of SUS316-Al_2O_3 FGM beam once the beam attains steady state temperature at around 300 s. Theoretical thermal deflection is validated with experimental results for SUS316-Al_2O_3 FGM beam sample-1. This concludes that varying thermal expansion coefficient between the top and the bottom layers of the FGM beam gives rise to thermal moment causing thermal deflection of the beam.

The present theoretical model can be very well used for solution of non-linear thermo-elastic problem for various thermal and structural loads and boundary conditions.

Similar studies can be attempted for design of structural components for atmospheric re-entry vehicles.

SCOPE FOR FUTURE WORK

a. The parameters used to fabricate Al-Al_2O_3 FGM beam samples by powder metallurgy process need be tailored to get better FGM samples.
b. The free vibration and static deflection studies need to be conducted for different structural boundary conditions on Al and Al-Al_2O_3 beam samples.
c. Further experimental studies need to be carried out on thermal vibration of the SUS316-Al_2O_3 and Al-Al_2O_3 beams.
d. Mechanical testing is required to be carried out to evaluate the Young's modulus value for pure aluminium and FGM beam samples prepared using powder metallurgy process to have results close to the experimental results.
e. New theoretical model need to be developed to account for porosity in the samples prepared using powder metallurgy process.
f. The nonlinear theoretical model can be used to study other material combinations and to be extended for Timoshenko beam theory.

REFERENCES

Alshorbagy, A.E., Eltaher, M.A. and Mahmoud, F.F. (2011). "Free vibration characteristics of a functionally graded beam by finite element method." *Applied Mathematical Modelling,* 35, 412–425.

Alshorbagy, A.E. (2013). "Temperature effects on the vibration characteristics of a functionally graded thick beam." *Ain Shams Engineering Journal*, 4(3), 455-464.

Amabili, M. and Carra, S. (2009). "Thermal effects on geometrically nonlinear vibrations of rectangular plates with fixed edges." *Journal of Sound and Vibration*, 321, 936–954.

Amsellem, O., Borit, F., Guipont, V., Jeandin, M. and Pauchet, F. (2007). "A composite approach to Al2O3 based plasma-sprayed coatings." *Proceedings of the 20th International conference on surface modification technologies*, 25-29 Sep 2006, Vienne, Austria. *ASM International*: 30-34.

Anandrao, S.K., Gupta, R.K., Ramachandran, P. and Rao, G.V. (2012). "Free Vibration Analysis of Functionally Graded Beams." *Defence Science Journal,* 62(3), 139-146.

Anandrao, S.K., Gupta, R.K., Ramachandran, P. and Rao, G.V. (2013). "Thermal Buckling and Free Vibration Analysis of Heated Functionally Graded Material Beams." *Defence Science Journal*, 63(3), 315-322.

Arbind, A., Reddy, J.N. (2013). "Nonlinear analysis of functionally graded microstructure-dependent beams." *Composite Structures*, 98: 272-281.

Asmani, M., Kermel, C., Leriche, A. and Ourak, M. (2001). "Influence of porosity on Young's modulus and Poisson's ratio in alumina ceramics*." Journal of the European Ceramic Society,* 21, 1081-1086.

Baker, J.G. (1933). ''Self Induced Vibrations.'' *Trans. ASME,* 55, 5–13.

Bachschmid, N., Pennacchi, P. and Vania, A. (2007). "Thermally induced vibrations due to rub in real rotors." *Journal of Sound and Vibration,* 299(4-5), 683–719.

Beam, R.M. (1969). ‘‘On the Phenomenon of Thermoelastic Instability (Thermal Flutter) of Booms with Open Cross Section.’’ *NASA* TN D-5222.

Bennoun, M., Houari, M.S.A. and Tounsi, A. (2016). “A novel five variable refined plate theory for vibration analysis of functionally graded sandwich plates.” *Mechanics of Advanced Materials and Structures*, 23(4), 423-431.

Belabed, Z., Houari, M.S.A. Tounsi, A., Mahmoud, S.R. and Anwar Bég, O. (2014). “An efficient and simple higher order shear and normal deformation theory for functionally graded material (FGM) plates.” *Composites: Part B*, 60, 274-283.

Bhattacharyya, M., Kumar, A.N. and Kapuria, S. (2008). “Synthesis and characterization of Al/SiC and Ni/Al2O3 functionally graded materials.” *Materials Science and Engineering A*, 487, 524–535.

Birman, V. and Byrd, L.W. (2007). “Modeling and Analysis of Functionally Graded Materials and Structures.” *ASME Trans. J. Appl. Mech. Reviews*, 60, 195–216.

Blandino, J.R. and Thornton, E.A. (2001). “Thermally Induced Vibration of an Internally Heated Beam.” - *ASME Journal of Vibration and Acoustics*, 123, 67-75.

Boccaccini, D.N. and Boccaccini, A.R. (1997). “Dependence of ultrasonic velocity on porosity and pore shape in sintered materials.” Journal of Nondestructive Evaluation, 16(4), 187-192.

Boley, B.A. (1956). ‘‘Thermally Induced Vibrations of Beams.’’ *J. Aeronaut. Sci.*, 23, 179–181.

Boley, B.A. and Barber, A.D. (1957). “Dynamic Response of Beams and Plates to Rapid Heating.” *Journal of Applied Mechanics*, 24, 413-416.

Boley, B.A. (1972). “Approximate Analysis of Thermally Induced Vibrations of Beams and Plates.” *Journal of Applied Mechanics*, 39, 212-216.

Bourada, M., Kaci, A., Houari, M.S.A. and Tounsi, A. (2015). “A new simple shear and normal deformations theory for functionally graded beams.” *Steel and Composite Structures*, 18(2), 409-423.

Bousahla, A.A., Houari, M.S.A., Tounsi, A. and Adda Bedia, E.A. (2014). "A novel higher order shear and normal deformation theory based on neutral surface position for bending analysis of advanced composite plates." *Int. J. Computat. Method*, 11(6), 1350082.

Bouderba, B., Houari, M.S.A. and Tounsi, A. (2013). "Thermomechanical bending response of FGM thick plates resting on Winkler–Pasternak elastic foundations." *Steel and Composite Structures*, 14(1), 85-104.

Cao, G. Chen, X. and Kysar, J.W. (2005). "Thermal vibration and apparent thermal contraction of single-walled carbon nanotubes." *Journal of the Mechanics and Physics of Solids*, 54(6), 1206–1236.

Chakraborty, A., Gopalakrishnan, S. and Reddy, J.N. (2003). "A new beam finite element for the analysis of functionally graded materials." *International Journal of Mechanical Sciences*, 45:519-539.

Chang, W.P and Wan S.M. (1986). "Thermomechanically Coupled Non-Linear Vibration of Plates." *International Journal of Non-Linear Mechanics*, 21(5), 375-389.

Chang, J.S., Wang, J.H. and Tsai, T.Z. (1992). "Thermally induced vibration of thin laminated plates by finite element method." *Computers and Structures*, 42 (1), 117-128.

Chi, S.H. and Chung, Y.L. (2006). "Mechanical Behavior of Functionally Graded Material Plates Under Transverse Load, Part I: Analysis." *Int. J. Solids Struct*., 43, 3657–3674.

Chen, C.S., Lin, C.Y. and Chien, R.D. (2011). "Thermally induced buckling of functionally graded hybrid composite plates." *International Journal of Mechanical Sciences*, 53, 51–58.

Cinefra, M., Carrera, E., Della Croce, L. and Chinosi, C. (2012). "Refined shell elements for the analysis of functionally graded structures." *Composite Structures*, 94, 415-422.

Ctibor, P., Ageorges, H., Neufuss, K. and Zahalka, F. (2009). "Composite Coatings of Alumina-based Ceramics and Stainless Steel Manufactured by Plasma Spraying." *Materials Science,* 15(2): 108-114.

Das, S. (1983). "Vibration of Polygonal Plates Due to Thermal Shock", *Journal of Sound and Vibration*, 89(4), 471-476.

Deschilder, M., Eslami, H. and Zhao, Y. (2006). "Nonlinear Static Analysis of a Beam Made of Functionally Graded Material." *47th AIAA/ASME/ASCE/AHS/ASC Structures, Structural Dynamics, and Materials Conference*, Newport, Rhode Island.

Dogan, V. (2013). "Nonlinear vibration of FGM plates under random excitation." *Composite Structures*, 95, 366–374.

Erdemir, A., Canakci, A. and Varol, T. (2015). "Microstructural characterization and mechanical properties of functionally graded Al2024/SiC composites prepared by powder metallurgy techniques." *Trans. Nonferrous Met. Soc. China*, 25, 3569−3577.

Ghiasian, S.E., Kiani, Y. and Eslami, M.R. (2014). "Non-linear rapid heating of FGM beams." *International Journal of Non-Linear Mechanics,* 67: 74-84.

Ghiasian, S.E., Kiani, Y. and Eslami, M.R. (2015). "Nonlinear thermal dynamic buckling of FGM beams." *European Journal of Mechanics A/Solids*, 54, 232-242.

Gu, Y.W., Khor, K.A., Fu, Y.Q. and Wang, Y. (1997). "Functionally graded ZrOz-NiCrA1Y coatings prepared by plasma spraying using pre-mixed spheroidized powders." *Surface and Coatings Technology*, 96: 305-312.

Gulick, D.W. and Thornton, E.A. (1995). "Thermally-Induced Vibrations of a Spinning Spacecraft Boom." *Acta Astronautica,* 36(3), 163-176.

Gupta, A. and Talha, M. (2015). "Recent development in modeling and analysis of functionally graded materials and structures." *Progress in Aerospace Sciences*, 79, 1-14.

Hamid, A., Houari, M.S.A., Mahmoud, S.R. and Tounsi, A. (2015). "A sinusoidal plate theory with 5-unknowns and stretching effect for thermomechanical bending of functionally graded sandwich plates." *Steel and Composite Structures,* 18(1), 235-253.

Hebali, H., Tounsi, A., Houari, M.S.A., Bessaim, A. and Adda Bedia, E.A. (2014). "A new quasi-3D hyperbolic shear deformation theory for the static and free vibration analysis of functionally graded plates." *ASCE J. Engineering Mechanics*, 140, 374-383.

Heshmati, M. and Yas, M.H. (2013). "Dynamic analysis of functionally graded multi-walled carbon nanotube-polystyrene nanocomposite beams subjected to multi-moving loads." *Materials and Design*, 49, 894–904.

Hong, C.C. and Jane, K.C. (2003). "Shear Deformation in Thermal Vibration Analysis of Laminated Plates by the GDQ Method." *Int. J. Mech. Sci*., 45, 21–36.

Hong, C.C., Liao, H.W., Lee L.T., Ke, J.B. and Jane K.C. (2005). "Thermally induced vibration of a thermal sleeve with the GDQ method." *International Journal of Mechanical Sciences*, 47, 1789-1806.

Hong, C.C. (2009). "Rapid Heating Induced Vibration of a Laminated Shell with the GDQ Method." *The Open Mechanics J.*, 3, 1–5.

Huang, X.L. and Shen, H.S. (2004). "Nonlinear vibration and dynamic response of functionally graded plates in thermal environments." *International Journal of Solids and Structures*, 41: 2403-2427.

Johnston, J.D. and Thornton, E.A. (1996). ''Thermal Response of Radiantly Heated Spinning Spacecraft Booms.'' *Journal of Thermophysics and Heat Transfer*, 10, 60–68.

Johnston, J.D. and Thornton, E.A. (2000). "Thermally induced Dynamics of Setallite Solar Panels." *Journal of Spacecraft and Rockets*, 37(5).

Kapuria, S., Bhattacharyya, M. and Kumar, A.N. (2008). "Bending and free vibration response of layered functionally graded beams: A theoretical model and its experimental validation." *Composite Structures*, 82: 390-402.

Kadoli, R., Akhtar, K. and Ganesan, N. (2008). "Static analysis of functionally graded beams using higher order shear deformation theory." *Applied Mathematical Modelling*, 32, 2509-2525.

Kidawa-Kukla, J. (1997). “Vibration of a Beam Induced By Harmonic Motion of a Heat Source.” *Journal of Sound and Vibration*, 205(2), 213-222.

Kidawa-Kukla, J. (2003). “Application of the Green functions to the problem of the thermally induced vibration of a beam.” *Journal of Sound and Vibration*, 262, 865–876.

Ke, L.L., Yang, J. and Kitipornchai, S. (2010). “An analytical study on the nonlinear vibration of functionally graded beams.” *Meccanica*, 45, 743–752.

Kien, N.D., Thom, T.T., Gan, B.S. and Tuyen, B.V. (2016). “Influences of dynamic moving forces on the functionally graded porus-nonuniform beams.” *International Journal of Engineering and Technology Innovation*, vol. 6(3), 173-189.

Kiani, Y. and Eslami, M.R. (2013). “Thermomechanical Buckling of Temperature dependent FGM Beams.” *Latin American Journal of Solid and Structures*, 10, 223 – 246.

Kovacik, J. (1999). “Correlation between Young’s modulus and porosity in porous materials.” *Journal of Materials Science Letters*, 18, 1007-1010.

Kraus H. (1966). “Thermally induced vibrations of thin nonshallow spherical shells.” *AIAA Journal*, 4, 500-505.

Lambros, J., Narayanaswamy, A., Santare, M.H. and Anlas, G. (1999). “Manufacture and Testing of a Functionality Graded Material.” *ASME J. Eng. Mater. Technol.*, 121, 488–493.

Lee, Y.Y., Zhao, X. and Reddy, J.N. (2010). “Postbuckling analysis of functionally graded plates subject to compressive and thermal loads.” *Computer Methods in Applied Mechanics and Engineering*, 199, 1645–1653.

Li, C.J. and Sun, B. (2003). "Microstructure and property of Al2O3 coating microplasma-sprayed using a novel hollow cathode torch", *Materials Letters*, 58, 179–183.

Manolis and Beskos. (1981). “Thermally induced vibrations of Beam structures.” *Computer methods in Applied Mechanics and Engineering*, 21, 337-355.

Murozono, M. and Thornton, E. A. (1998). ‘‘Buckling and Quasistatic Thermal-Sructural Response of an Asymmetric Rolled-Up Solar Array.’’ *Journal of Spacecrafts and Rockets*, 35, 147–155.

Malik, P. and Kadoli, R. (2005). “Transient Heat Transfer in Vertical Hollow Tube – A Theoretical and Experimental Study”, National Conference, README’05 held at P.A. College of Engineering, Mangalore, Dec’1-3, 2005.

Malik, P., Kadoli, R. and Ganesan, N. (2007). “Effect of boundary conditions and convection on thermally induced motion of beams subjected to internal heating.” *Journal of Zhejiang University SCIENCE A*, 8(7), 1044-1052.

Mahamood, R.M., Akinlabi, E.T. Shukla, M. and Pityana, S. 2012. “Functionally Graded Material: An Overview.” *Proceedings of the World Congress on Engineering 2012 Vol III, WCE 2012, 4-6, London, U.K.*

Malekzadeh, P. and Shojaee, S.A. (2013). “Dynamic response of functionally graded plates under moving heat source.” *Composites: Part B*, 44, 295–303.

Malekzadeh, P. and Shojaee, S.A. (2014). “Dynamic response of functionally graded beams under moving heat source.” *Journal of Vibration and Control*, Vol. 20(6) 803–814.

Mahi, A., Adda Bedia, E.A., Tounsi, A. and Mechab, I. (2010). “An analytical method for temperature-dependent free vibration analysis of functionally graded beams with general boundary conditions.” *Composite Structures*, 92, 1877–1887.

Mahi, A., Adda Bedia, E.A, and Tounsi, A. (2015). “A new hyperbolic shear deformation theory for bending and free vibration analysis of isotropic, functionally graded, sandwich and laminated composite plates.” *Applied Mathematical Modelling*, 39, 2489-2508.

Meziane, M.A.A., Abdelaziz, H.H. and Tounsi, A. (2014). “An efficient and simple refined theory for buckling and free vibration of exponentially graded sandwich plates under various boundary conditions.” *Journal of Sandwich Structures and Materials*, 16(3), 293-318.

Na, K.S. and Kim, J.H. (2006). “Thermal postbuckling investigations of functionally graded plates using 3-D finite element method.” *Finite Elements in Analysis and Design*, 42, 749–756.

Naebe, M. and Shirvanimoghaddam, K. (2016). “Functionally graded materials: A review of fabrication and properties.” *Applied Materials Today*, 5, 223-245.

Navazi, H.M. and Haddadpour, H. (2007). “Aero-thermoelastic stability of functionally graded plates.” *Composite Structures*, 80, 580–587.

Naj, R., Sabzikar, B.M. and Eslami, M.R. (2008). “Thermal and mechanical instability of functionally graded truncated conical shells.” *Thin-Walled Structures,* 46, 65-78.

Nemat-Alla, M. (2003). “Reduction of thermal stresses by developing two dimensional functionally graded materials.” *International Journal of Solids and Structures,* 40, 7339-7356.

Nguyen, T. K., Sab, K. and Bonnet, G. (2008). “First-Order Shear Deformation Plate Models for Functionally Graded Materials.” *Composite Structures*, 83, 25–36.

Ootao, Y. and Tanigawa Y. (2005). “Transient analysis of multilayered magneto-electro-thermoelastic strip due to nonuniform heat supply.”, *Composite Structures*, 68, 471–480.

Pandey, S. and Pradyumna, S. (2017). “A finite element formulation for thermally induced vibrations of functionally graded material sandwich plates and shell panels.” *Composite Structures,* 160, 877–886.

Phani, K.K. and Niyogi, S.K. (1987). “Young's modulus of porous brittle solids.” *Journal of Materials Science*, 22, 257-263.

Pradhan, K. K. and Chakraverty, S. (2013). “Free Vibration of Euler and Timoshenko Functionally Graded Beams by Rayleigh-Ritz Method.” *Composites Part B: Engineering*, (51), 175–184.

Praveen, G.N. and Reddy, J.N. (1998). “Non Linear Thermoelastic Analysis of Functionally Graded Ceramic Metal Plates.”, *International Journal of Solids and Structures*, 35-33, 4457-4476.

Qatu, M.S., Sullivan, R.W. and Wanga, W. (2010). “Recent research advances on the dynamic analysis of composite shells: 2000–2009.” *Composite Structures*, 93, 14-31.

Reddy, J.N. and Chin, C.D. (1998). “Thermomechanical analysis of functionally graded cylinders and plates.” *Journal of Thermal Stresses*, 21(6), 593-626.

Reddy, J.N. and Cheng, Z.Q. (2001). “Three-dimensional thermomechanical deformations of functionally graded rectangular plates.” *Eur. J. Mech. A/Solids*, 20, 841–855.

Reddy, J.N. (2011). “Microstructure-dependent couple stress theories of functionally graded beams.” *Journal of Mechanics and Physics of Solids*, 59: 2382-2399.

Stroud, R.C. and Mayers J. (1971). “Dynamic Response of Rapidly Heated Plate Elements.” *AIAA Journal*, 9(1), 76-83.

Seibert, A.G. and Rice, J. S. (1973). “Coupled Thermally Induced Vibrations of Beams.” *AIAA Journal*, 7(7), 1033-1035.

Sankar, B. V. (2001). “An elasticity solution for functionally graded beams.” *Composite Science and Technology*, 61, 689-696.

Sankar, B.V. and Tzeng, J.T. (2002). “Thermal stresses in functionally graded beams.” *AIAA Journal*, 40(6), 1228-1232.

Shen, H.S. (2007). “Nonlinear thermal bending response of FGM plates due to heat conduction.” *Composites: Part B*, 38, 201–215.

Sohn, K.J. and Kim, J.H. (2008). “Structural stability of functionally graded panels subjected to aero-thermal loads.” *Composite Structures*, 82, 317–325.

Sina, S.A., Navazi, H.M. and Haddadpour, H. (2009). “An analytical method for free vibration analysis of functionally graded beams.” *Materials and Design*, 30, 741–747.

Simsek, M. and Kocatürk T. (2009). “Free and forced vibration of a functionally graded beam subjected to a concentrated moving harmonic load.” *Composite Structures*, 90, 465–473.

Sadowski, T., Ataya, S. and Nakonieczny, K. (2009). “Thermal analysis of layered FGM cylindrical plates subjected to sudden cooling process at one side – Comparison

of two applied methods for problem solution." *Computational Materials Science*, 45, 624‑632.

Sepiani, H.A., Rastgoo, A., Ebrahimi, F. and Ghorbanpour, A.A. (2010). "Vibration and buckling analysis of two-layered functionally graded cylindrical shell, considering the effects of transverse shear and rotary inertia." *Materials and Design*, 31, 1063-1069.

Sheng, G.G. and Wang, X. (2013). "An analytical study of the non-linear vibrations of functionally graded cylindrical shells subjected to thermal and axial loads." *Composite Structures*, 97, 261‑268.

Shen, H.S. and Wang, Z.X. (2014). "Nonlinear analysis of shear deformable FGM beams resting on elastic foundations in thermal environments." *International Journal of Mechanical Sciences*, 81: 195-206.

Shen, H.S. (2002). "Nonlinear bending response of functionally graded plates subjected to transverse loads and in thermal environments." *International Journal of Mechanical Sciences*, 44: 561-584.

Shooshtari, A. and Rafiee, M. (2011). "Nonlinear forced vibration analysis of clamped functionally graded beams." *Acta Mech*, 221, 23–38.

Simsek, M., Kocaturk, T. and Akbas, S.D. (2013). "Static bending of a functionally graded microscale Timoshenko beam based on the modified couple stress theory." *Composite Structures*, 95, 740-747.

Simsek, M. (2016). "Buckling of Timoshenko beams composed of two-dimensional functionally graded material (2D-FGM) having different boundary conditions." *Composite Structures*, 149, 304–314.

Sobczak, J.J. and Drenchev, L. (2013). "Metallic Functionally Graded Materials: A Specific Class of Advanced Composites", *Journal of Materials Science & Technology*, 29(4), 297-316.

Sun, Y., Li, S.R. and Batra, R.C. (2016). "Thermal buckling and post-buckling of FGM Timoshenko beams on nonlinear elastic foundation." *Journal of Thermal Stresses*, 39(1), 11–26.

Thai, H.T. and Vo, T.P. (2012). “Bending and free vibration of functionally graded beams using various higher-order shear deformation beam theories.” *International Journal of Mechanical Sciences*, 62, 57-66.

Thornton, E.A. and Foster, R.S. (1992). ‘‘Dynamic Response of Rapidly Heated Space Structures.’’ *Computational Nonlinear Mechanics in Aerospace Engineering, S.N. Alturi, ed., Vol. 146, Progress in Astronautics and Aeronautics, AIAA, Washington, DC,* 451–477.

Thornton, E.A. and Kim, Y.A. (1993). ‘‘Thermally Induced Bending Vibrations of a Flexible Rolled-Up Solar Array.’’ *Journal of Spacecrafts and Rockets*, 30, 438– 448.

Thornton, E.A., Gulick, D.W. and Chini, G. (1995). “Thermally induced vibrations of a self shadowed split blanket solar array.” *Journal of Spacecraft and Rockets*, 32(2), 302-311.

Tran, T.Q.N., Lee, H.P. and Lim S.P. (2007). “Structural intensity analysis of thin laminated composite plates subjected to thermally induced vibration.” *Composite Structures*, 78, 70–83

Tornabene, F. (2009). “Free vibration analysis of functionally graded conical, cylindrical shell and annular plate structures with a four-parameter power-law distribution.” *Computer Methods in Applied Mechanics and Engineering*, 198, 2911-2935.

Tounsi, A., Houari, M.S.A., Benyoucef, S. and Adda Bedia, E.A. (2013). “A refined trigonometric shear deformation theory for thermoelastic bending of functionally graded sandwich plates.” *Aerospace Sci. Tech.*, 24, 209-220.

Tounsi, A., Houari, M.S.A. and Bessaim, A. (2016). “A new 3-unknowns non-polynomial plate theory for buckling and vibration of functionally graded sandwich plate.” *Struct. Eng. Mech., Int. J.*, 60(4), 547-565.

Taeprasartsit, S. (2015). “Nonlinear free vibration of thin functionally graded beams using the finite element method.” *Journal of Vibration and Control*, 21(1), 29-46.

Woo, J. and Meguid, S.A. (2001). “Non Linear Analysis of Functionally Graded Plates and Shallow Shells.” *International Journal of Solids and Structures*, 38, 7409-7421.

Wang, B.L., Mai, Y.W. and Zhang, X.H. (2004). "Thermal shock resistance of functionally graded materials." *Acta Materialia*, 52, 4961–4972.

Wang, Y. and Wu, D. (2016). Thermal effect on the dynamic response of axially functionally graded beam subjected to a moving harmonic load, *Acta Astronautica*, 127, 171–181.

Wattanasakulpong, N., Gangadhara, P. and Kelly, D. (2011). "Thermal buckling and elastic vibration of third-order shear deformable functionally graded beams." *International Journal of Mechanical Sciences*, 53, 734–743.

Wattanasakulpong, N., Gangadhara, P. B., Kelly, D. W. and Hoffman, M. (2012), "Free vibration analysis of layered functionally graded beams with experimental validation." *Materials and Design*, 36, 182–190.

Wattanasakulpong, N. and Ungbhakorn, V. (2014). "Linear and nonlinear vibration analysis of elastically restrained ends FGM beams with porosities." *Aerospace Science and Technology*, 32, 111–120.

Yahia, S.A., Atmane, H.A., Houari, M.S.A. and Tounsi, A. (2015). "Wave propagation in functionally graded plates with porosities using various higher-order shear deformation plate theories." *Structural Engineering and Mechanics*, 53(6), 1143-1165.

Yang, J., Kitipornchai, S. and Liew, K.M. (2003). "Large amplitude vibration of thermo-electro-mechanically stressed FGM laminated plates." *Comput. Methods Appl. Mech. Engrg.*, 192, 3861–3885.

Yang, J., Liew, K.M., Wu, Y.F. and Kitipornchai, S. (2006). "Thermo-mechanical post-buckling of FGM cylindrical panels with temperature-dependent properties." *International Journal of Solids and Structures*, 43, 307–324.

Yang, J. and Shen, H.S. (2003). "Nonlinear bending analysis of shear deformable functionally graded plates subjected to thermo-mechanical loads under various boundary conditions." *Composites: Part B*, 34: 103-115.

Yang, J. and Huang, X.L. (2007). "Nonlinear transient response of functionally graded plates with general imperfections in thermal environments." *Comput. Methods Appl. Mech. Engrg.*, 196, 2619–2630.

Yu, Y.Y. (1969). "Thermally induced vibrations and flutter of a flexible boom." *Journal of Spacecrafts and Rockets*, 6(8), 902-910.

Zhao, X., Lee, Y.Y. and Liew, K.M. (2009). "Mechanical and thermal buckling analysis of functionally graded plates." *Composite Structures*, 90, 161–171.

Zhang, W., Hao, Y.X. and Yang, J. (2012). "Nonlinear dynamics of FGM circular cylindrical shell with clamped-clamped edges." *Composite Structures*, 94, 1075-1086.

Zhang, J. and Kobayashi, A. (2005). "Corrosion resistance of Al2O3+ZrO2 composite coatings sprayed on stainless steel substrates", *Transactions of JWRI*, 34(2), 17-22.

Zidi, M., Tounsi, A., Houari, M.S.A. and Bég, O. (2014). "Bending analysis of FGM plates under hygro-thermo-mechanical loading using a four variable refined plate theory." *Aerospace Sci. Tech*., 34, 24-34.

Zhua, J., Lai, Z., Yin, Z., Jeon, J. and Lee, S, (2001). "Fabrication of ZrO2–NiCr functionally graded material by powder metallurgy." *Materials Chemistry and Physics*, 68, 130–135.

Books

Bathe, K.J. (1996). *Finite Element Procedures*, 1st Edition, Prentice Hall, New Jersey.

Carslaw, H.S. and Jaeger, J.C. (1959). *Conduction of Heat in Solids*, Second Edition, Clarendon Press, Oxford.

Desai, C.S. and Abel, J.F. (1972). *Introduction to the Finite Element Method*, Van Nostrand Reinhold Co., New York.

Incropera, F.P. and DeWitt, D.P. (2002). *Fundamentals of Heat and Mass Transfer*, Fifth Edition, John Wiley and Sons, 399-414.

Lewis, R.W., Nithiarasu, P. and Seetharumu, K.N. (2004). *Fundamentals of Finite Element Method for Heat and Fluid Flow*, John Wiley and Sons Ltd, England.

Logan, D.L. (2002). *A First Course in the Finite Element Method*, Third Edition, Brooks/Cole, Thomson Learning, USA, 571-573.

Reddy, J.N. (2003). *An introduction to the Finite Element Analysis*, Second Edition, Tata McGrow-Hill.

Reddy, J.N. (2004). *An Introduction to Nonlinear Finite Element Analysis*, Oxford University Press, Oxford, UK.

Segerlind, L.J. (2004). *Applied Finite Analysis, Second Edition*, John Wiley and Sons.

Timoshenko, S. and Woinowsky-Krieger, S. (1959). *Theory of Plates and Shells*, 2nd Ed., McGraw-Hill Co., Inc., New York.

Web-online

Atmospheric Plasma Spray Solutions – Issue 5 – October 2014, www.oerlikon.com/metco

An Introduction to Thermal Spray – Issue 6 – July 2016, www.oerlikon.com/metco

Liu, J. "Processes for sintering aluminum and aluminum alloy components." http://www.google.com/patents/US7517492, Google Patents (2009).

APPENDIX – I

Table I.1 Different materials, their chemical composition and applications for selecting material for die fabrication.

Sl. No.	Material Grade	Chemical composition in %								Typical applications
		C	Si	Mn	Cr	Ni	V	Co	Mo	
1	AISI A2	0.95-1.05	0.5 max	1.0 max	4.75-5.50	0.3 max	0.15-0.5	-	0.9-1.4	Large blanking dies, forming dies
2	AISI D2	1.40-1.60	0.6 max	0.6 max	11.0-13.0	0.3 max	1.10 max	1.0 max	0.7-1.20	Blanking dies, forming dies, extrusion dies
3	AISI D2 (available with supplier)	1.70 max	0.30 max	0.30 max	12.0 max	-	0.10 max	-	0.60 max	Forming dies, Punches

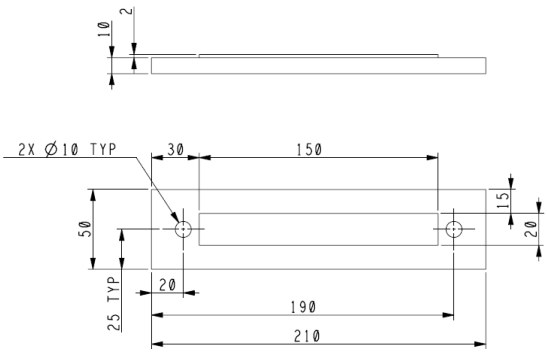

(a) Base

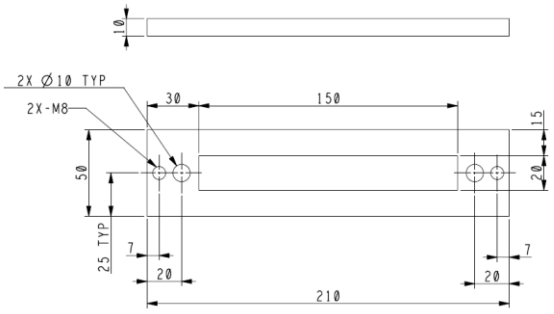

(b) Mid

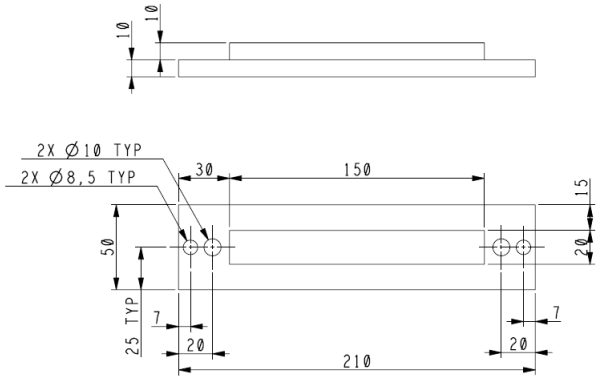

(c) Punch

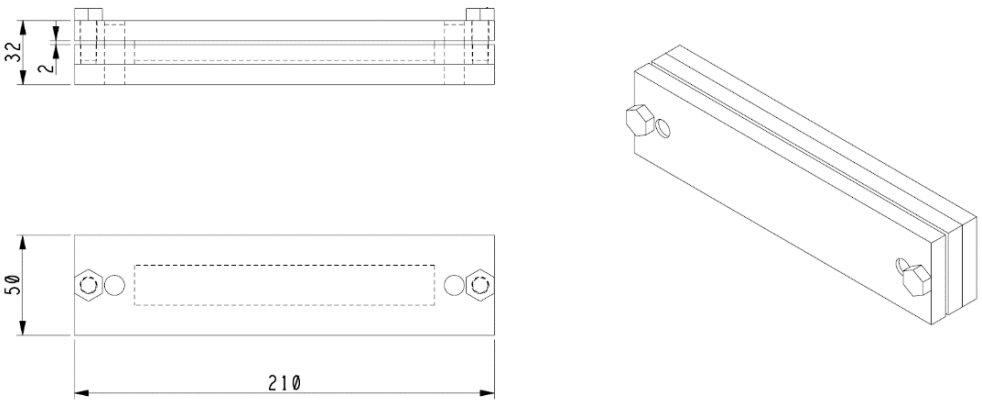

(d) Assemble view

Fig.I.1 Schematic 2D drawing of the die components and die assembly.

Table I.2 Volume fraction details, thickness and photographs of various physical sample.

Sample #	Layer #	Vc %	Sample Photo	Average Thickness (mm)
FG#1	1	50		
	2	10		
	3	1.25		
	4	0		
	5	0		
FG#2	1	50		
	2	10		
	3	1.25		
	4	0		
	5	0		
FG#3	1	50		
	2	10		
	3	1.25		
	4	0		
	5	0		
FG#4	1	20		2.986
	2	1.25		
	3	0		
	4	0		
	5	0		
FG#5	1	20		
	2	1.25		
	3	0		
	4	0		
	5	0		
FG#6	1	20		
	2	1.25		
	3	0		
	4	0		
	5	0		
FG#7	1	20	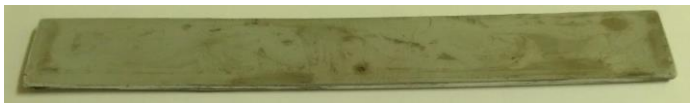	
	2	1.25		
	3	0		
	4	0		
	5	0		
FG#8	1	20		2.986
	2	1.25		
	3	0		
	4	0		
	5	0		
FG#9	1	10		2.54
	2	5		
	3	1.25		
	4	0		
	5	0		
FG#10	1	10	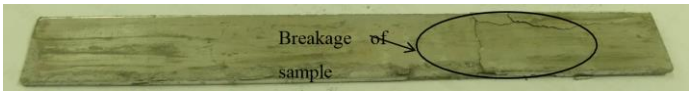	2.994
	2	5		
	3	1.25		
	4	0		
	5	0		

FG#11	1	10	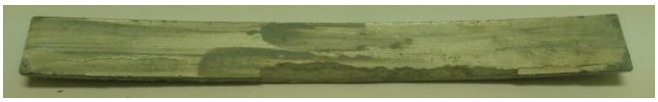	3.016
	2	5		
	3	1.25		
	4	0		
	5	0		
FG#12	1	10		
	2	5		
	3	2.5		
	4	1.25		
	5	0		
FG#13	1	10		2.332
	2	5		
	3	2.5		
	4	1.25		
	5	0		
FG#14	1	10		
	2	5		
	3	2.5		
	4	1.25		
	5	0		
FG#15	1	10		2.548
	2	5		
	3	2.5		
	4	1.25		
	5	0		
FG#16	1	10		2.568
	2	5		
	3	2.5		
	4	1.25		
	5	0		
FG#17	1	10		
	2	5		
	3	2.5		
	4	1.25		
	5	0		
FG#18	1	10		2.584
	2	5		
	3	2.5		
	4	1.25		
	5	0		
FG#19	1	10		2.476
	2	5		
	3	2.5		
	4	1.25		
	5	0		
FG#20	1			2.49
	2			
	3			
	4			
	5			

Al#1			2.826
Al#2			2.408
Al#3			2.428
Al#4		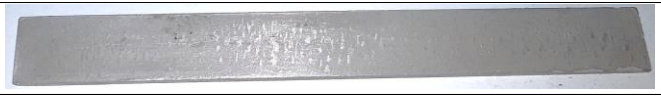	2.364

APPENDIX – II

II.1 Experimental setup to measure transverse deflection and free vibration frequency of FGM beams

a. Introduction

The experimental setup to find out the free vibration natural frequency of beams is described in this APPENDIX. Important accesories for experimental setup like laser displacement sensor, RS422/USB converter, ILD1402 DAQ software, FFT analyser, impact hammer and mounting arrangement are explained in detail in this APPENDIX. At the end of this APPENDIX, procedure for measuring the free vibration natural frequency and transverse deflection of the beam sample is explained in detail.

b. Experimental setup to conduct free vibration test of FGM beams

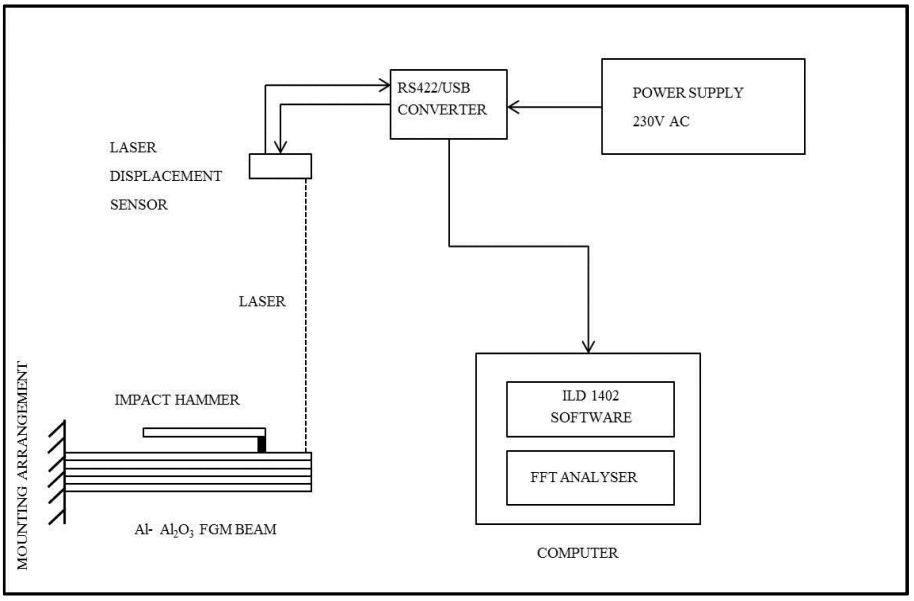

Fig.II.1 Schematic diagram of experimental setup to measure free vibration natural frequency of beams in clamped – free condition.

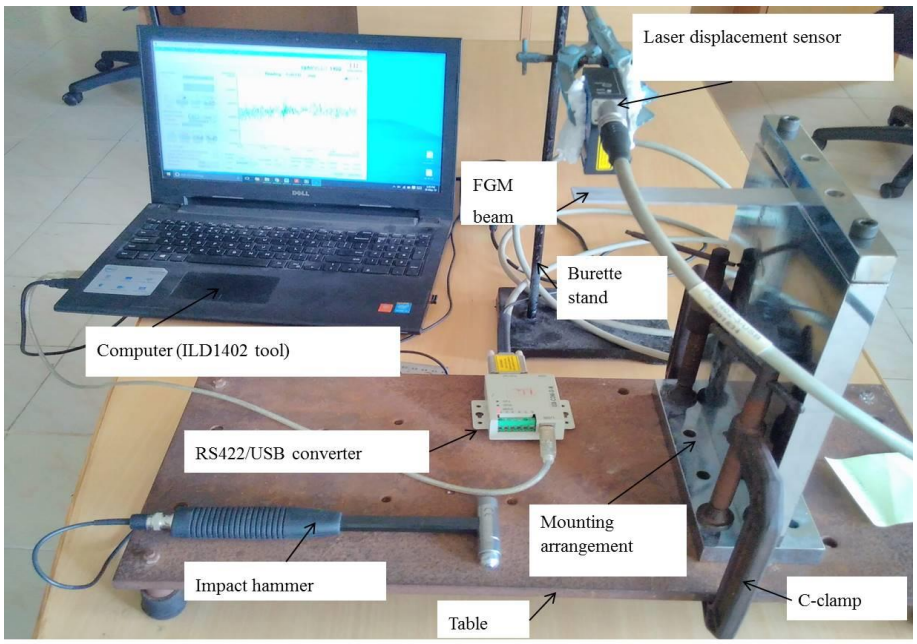

Fig.II.2 Actual test setup to measure free vibration natural frequency of beams in clamped – free condition.

Free vibration experiment is performed on the beams prepared by thermal spray and powder metallurgy process. Schematic diagram of experimental setup for measuring free vibration natural frequency of beams in clamped – free boundary condition is shown in the Fig.II.1.

The experimental setup consists of mounting arrangement, beam sample, impact hammer, laser displacement sensor, RS422 / USB converter, computer (ILD1402 DAQ software and FFT analyser). Actual test setup to measure free vibration natural frequency of beams in clamped – free condition is shown in Fig.II.2.

Each component of the experimental setup is explained in detail in the following sections.

c. Mounting arrangement for beam.

It is a rigid stand used to hold the FGM beam sample at one end restricting the movement. Two C – clamps are used to hold the mounting arrangement rigidly to the table. The beam sample is kept between top and bottom part of the mounting arrangement and two allen bolts are used to tighten the top part with the bottom part of the mounting arrangement as shown in the Fig.II.3.

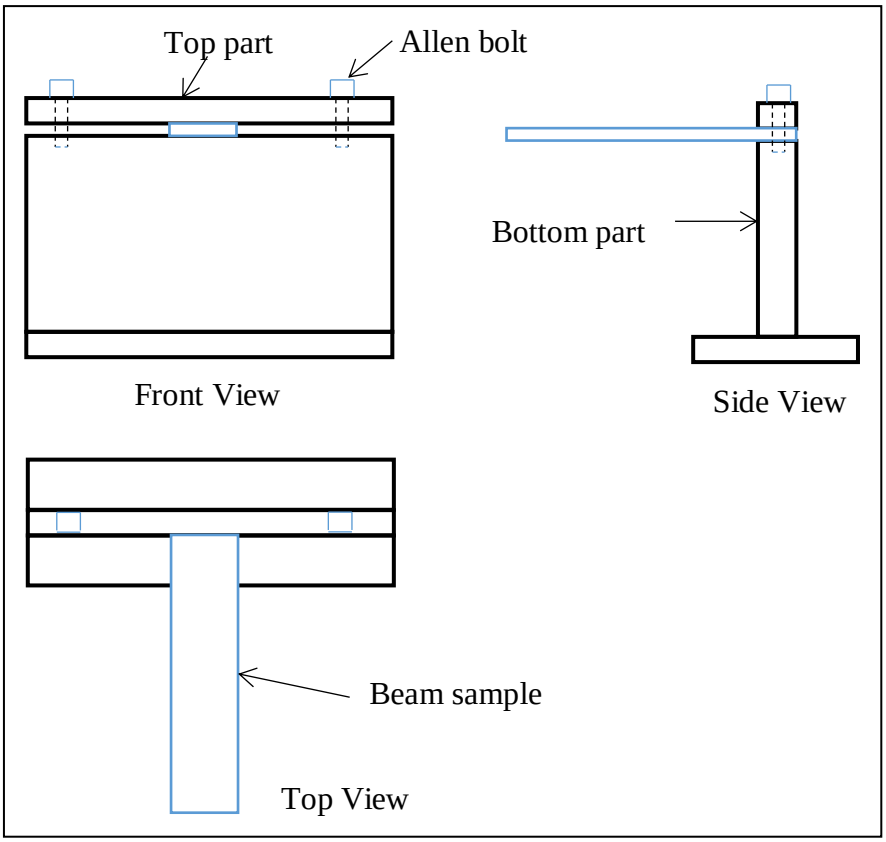

Fig.II.3 Schematic representation of mounting of beam sample in the mounting arrangement.

d. Impact hammer

Impact hammer is used to give initial stimulus during free vibration experiment to find the natural frequency of the beam sample. In present experiment, stimulus (force) is given by using PCB piezotronics (model no. 086C03) impact hammer which is shown in the Fig.II.4. The technical specifications of PCB piezotronics make impact hammer is given in the Table II.1.

Fig.II.4 PCB piezotronics make impact hammer.

Table II.1 Technical specifications of PCB piezotronics make impact hammer (Source: product manual, PCB piezotronics)

Make	PCB piezotronics
Model no.	086C03
Sensitivity (±15%)	2.25 mV/N
Measurement range	±2224N
Resonant frequency	≥22 kHz
Nonlinearity	≤1%
Sensing element	Quartz
Sealing	Epoxy
Hammer mass	0.16 kg
Head diameter	1.57 cm
Tip diameter	0.63 cm
Hammer length	21.6 cm
Electrical connection position	Bottom of handle
Extender mass weight	75 gm
Electrical connector	BNC jack
Excitation voltage	20 to 30V DC
Constant current excitation	2 to 20 mA
Output impedance	<100 ohms
Output bias voltage	8 to 14V DC

e. Laser displacement sensor

It is a laser sensor with integrated digital signal processor which is used to measure displacement, distance and position. The displacement at a particular point in the beam is measured by a micro epsilon make optoNCDT 1402 laser displacement sensor. Fig.II.5 shows micro epsilon make optoNCDT 1402 laser displacement sensor.

The sensor works by using a semiconductor laser with a wavelength of 670 nm. The maximum optical power of laser is ≤ 1 mW (Instruction manual, optoNCDT 1402). Table II.2 gives the technical specifications of optoNCDT 1402 laser displacement sensor.

Fig.II.5 Micro epsilon make laser displacement sensor (model: optoNCDT 1402-10).

Table II.2 Technical specifications of optoNCDT 1402 laser displacement sensor (Source: instruction manual, optoNCDT 1402).

Make	Micro epsilon
Model	optoNCDT 1402-10
Measurement range	0-10 mm
Resolution	Max. 1 µm
Measuring rate	1 kHz
Supply	24V DC /50 mA
Output	Digital, RS422
Operating temperature	0 to 50° C

Functional principle

The sensor uses the principle of optical triangulation to measure distance from an object without touching it. In this principle, visible point of light is projected on the target surface. The diffuse element of the light reflected from the surface is imaged by a receiver element which is positioned at an angle to the axis of the laser light, on to a high sensitive resolution element, charge- coupled device (CCD). The controller computes the measured value of distance from the CCD array. A closed loop feedback control assists the sensor to measure against various surfaces (Instruction manual, optoNCDT 1402).

A LED is provided on the sensor which is used to indicate different states as mentioned below,

Green – measuring object within the measurement range.

Yellow – midrange.

Red – poor target or out of range.

f. RS422 / USB converter

Fig.II.6 RS422/USB converter (micro epsilon make).

The RSS 422/USB converter transforms the digital signal acquired from a laser displacement sensor into a USB data packet. The sensor and the converter are connected through the RS 422 interface of the converter. Data output is done through USB interface. This data output is acquired using ILD1402 software via RS422/USB converter by connecting USB cable to the port provided in the computer (www.micro-epsilon.com). Fig.II.6 shows the micro epsilon make RS422/USB converter.

g. ILD1402 DAQ software

ILD 1402 (version 3.3.1) is a software tool to configure the optoNCDT 1402 laser displacement sensor. The output data from the sensor can be obtained by data acquisition through RS422 / USB converter. All the settings can be done conveniently via an user interface window on the computer. Fig.II.7 shows the user interface window of ILD 1402 software module. Initial configuration need to be done by selecting the com port where USB cable from RS422/USB converter is connected to computer. Interface, port and baud rate should be selected for configuring the ILD1402 DAQ tool initially before starting the experiment.

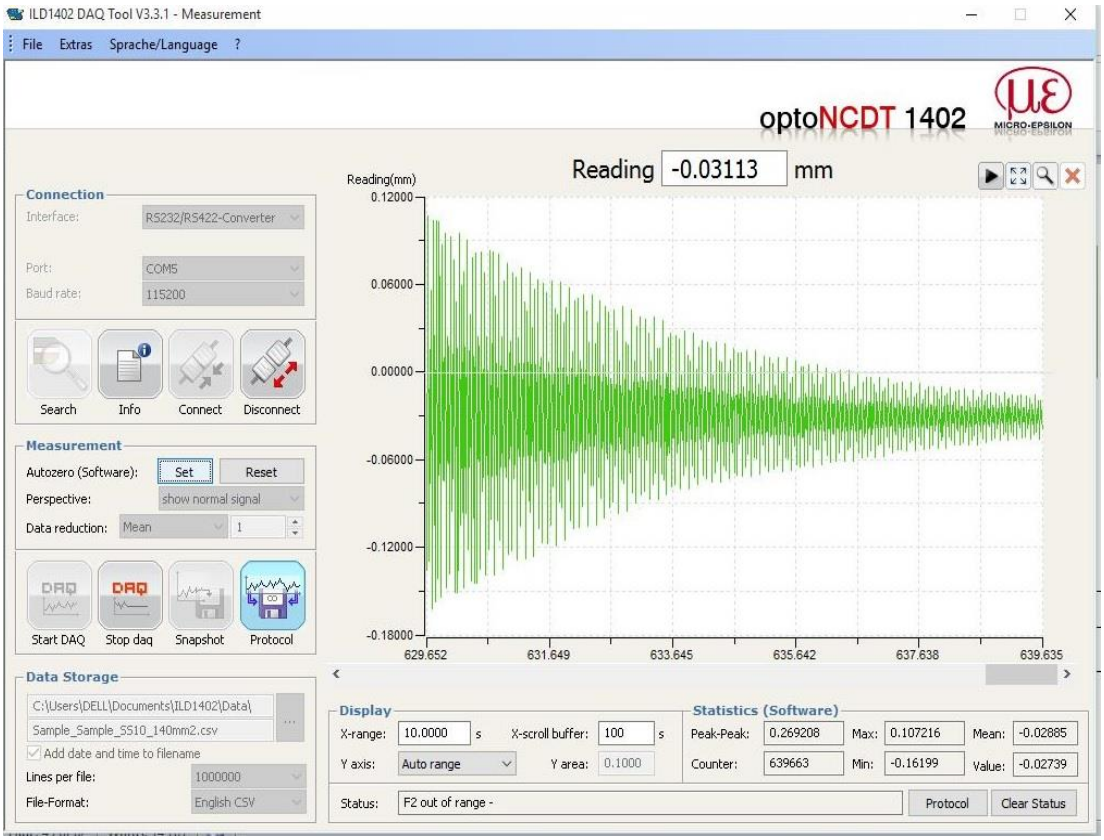

Fig.II.7 User interface window of ILD 1402 DAQ tool.

h. FFT analyser

Origin pro 8 software package is used to analyze the data obtained from the ILD 1402 tool. The output obtained from the ILD 1402 sensor gives the displacement values over a period of time. Fast Fourier Transform (FFT) analyser tool in origin pro 8 converts the time domain signal into frequency domain signal. It provides information such as magnitude, amplitude, phase, real, imaginary, power density of frequency domain signal. From the FFT analyser window required plots can be selected. It also provides the preview option to view the selected plots. Fig.II.8 shows the FFT analyser tool dialogue box of origin pro 8 software.

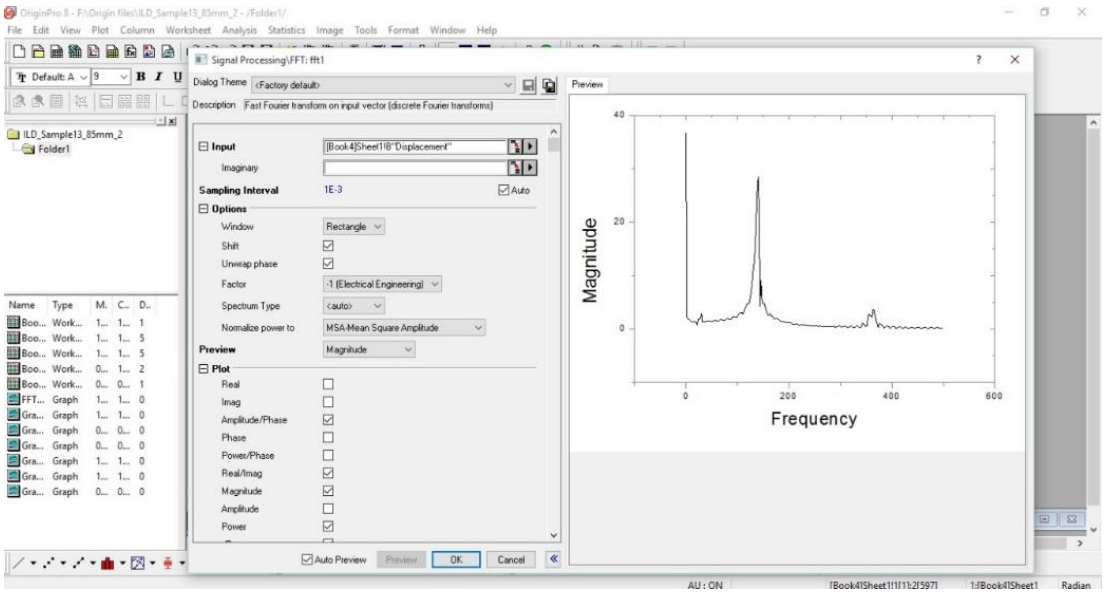

Fig.II.8 FFT analyser tool dialogue box of origin pro 8 software.

i. Accelerometer - 8730A (Kistler)

Small, 1.9 gram weight general purpose accelerometer is used for vibration measurements in wide range of applications. Available with an integral 5-40 UNC mounting stud (Type 8730AE500: M3), this light weight hermetically sealed accelerometer features a wide

frequency response.

• Low impedance voltage mode

• Quartz shear sensing element

• Ultra-low base strain sensitivity

• Minimal thermal transient response

• Ground isolated version available

• Conforming to CE

Description

The light weight, Type 8730A… accelerometer series uses Kistler's uniquely designed K-Shear quartz sensing element. Operating in the shear mode with precisely cut quartz plates, allows the accelerometers to exhibit ultra low sensitivity to thermal transients,

base strain and transverse motion. Housed in a hermetically sealed titanium case, the quartz sensing elements afford excellent long-term stability that ensures repeatable and accurate measurements. The mounting and size details of the accelerometer are given in Fig.II.9 while the technical data is presented in Table II.3.

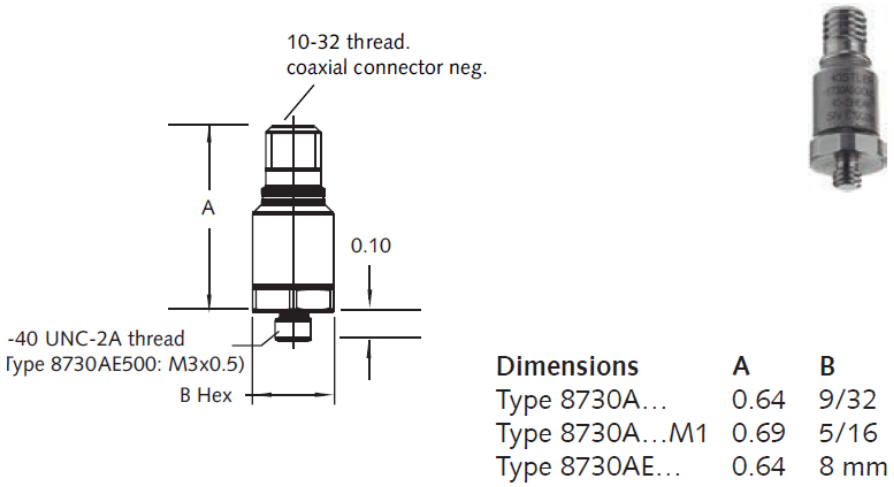

Dimensions	A	B
Type 8730A…	0.64	9/32
Type 8730A…M1	0.69	5/16
Type 8730AE…	0.64	8 mm

Fig.II.9 Geometry and mounting details of the accelerometer.

The standard Type 8730A… and the low temperature 8730A500M8 accelerometer weighs only 1.9 grams while the M1 version which is slightly larger and "off-ground" weighs 2.5 grams. Internal microelectronic Piezotron® signal conditioning circuit converts the charge developed in the quartz element as a result of the accelerometer being subjected to a vibration, into a useable high level voltage signal at a low impedance output. The low impedance output provides high immunity to noise and insensitivity to cable motion. Kistler's design allows the use of rugged, low cost coaxial cable between the accelerometer and power/readout equipment. Where minimum cable and connector weight are desirable, Type 1761B… general purpose cable is recommended.

Table II.3 Technical Data for Type 8730A accelerometer.

Specification	Unit	Type 8730A500
Acceleration range	g	±500
Acceleration limit	gpk	±1 000
Transverse acceleration limit	gpk	±1 000
Threshold (noise μVrms), nom.	grms	0.01 (130)
Type 8730A ... M1, M8	grms	0.02 (200)
Sensitivity, ±10 %	mV/g	10
Resonant frequency mounted, nom.	kHz	76
Frequency response, ±5 %	Hz	2 … 10 000
Type 8730A ... M1	Hz	2 ... 7 000
Amplitude non-linearity	%FSO	±1
Time constant, nom.	s	0.5
Transverse sensitivity nom. (max. 3)	%	1.5

j. Procedure to measure free vibration natural frequency of beam samples.

1. Mounting arrangement is placed on the table and two C-clamps are used to hold the mounting arrangement rigidly to the table.
2. The FGM beam sample is taken and one end of the beam is placed between the top part and bottom part of the mounting arrangement. By tightening the two allen bolts, one end of the beam is fixed to the mounting arrangement and the other end is free.
3. A 12-pin female connector cable from RS422/USB converter is connected to corresponding 12-pin male connector of ILD1402 laser sensor. The power input is given to the laser through RS422/USB converter by connecting the power cable to 230V AC power supply. The USB cable is used to connect RS422/USB converter to the computer.
4. Burette stand is used to hold the laser sensor tightly above the free end of the beam sample such that the laser impinges on the beam sample when sensor is switched on.
5. Power supply is switched on and LED on the laser displacement sensor glows. The height of the burette holder is adjusted such that the LED turns green which indicate

that the object is within the measuring range. If the LED turns red, it indicates that the object is out of range. Once the LED turns green, the burette holder is fixed in that position.

6. Position of laser displacement sensor is adjusted such that laser light falls on the free end of the FGM beam sample.
7. Computer is switched on and displacement reading is taken by running the ILD1402 DAQ software. Initial configuration is done by selecting the com port where USB cable from RS422/USB converter is connected to the computer. Interface, port and baud rate should be selected for configuring the ILD1402 DAQ tool initially before starting the experiment.
8. Once the configuration of ILD1402 DAQ tool is completed, the display window shows variation of displacement over the time.
9. Before starting the experiment, directory where the data file should be saved is chosen. A new file name can be given at the place provided in the dialogue box.
10. Once the directory and file name is chosen, 'Protocol' option available in the user interface window of ILD1402 DAQ tool is clicked which stores the data from start of the data acquisition to end of the data acquisition.
11. 'Start DAQ' and 'Stop DAQ' are provided on the user interface window of ILD1402 DAQ tool to start the data acquisition and end the data acquisition from the laser sensor respectively.
12. Experiment is started by selecting the 'Start DAQ' option on the user interface window and 'Set autozero' option is selected to make the initial displacement value to zero.
13. Initial impact force is applied on the beam sample near the fixed end by the impact hammer during free vibration experiment.
14. The displacement of free end of the clamped-free beam with respect to time is acquired using ILD1402 data acquisition tool.
15. The experiment is repeated by applying impact force at different time intervals so that data for different trials is obtained.
16. 'Stop DAQ' option is selected from the user interface window of ILD1402 DAQ tool to stop the experiment.

17. The data acquired from ILD1402 DAQ tool is saved in .csv format in the specified file and in the specified directory.
18. The free vibration data is analysed by importing it to the Origin pro 8 software. A new project is created in the origin software and the data is imported to a new work book. The data is plotted using the graph plotting tools in origin which gives variation of displacement over a period of time.
19. The required data points are selected and saved in a work book. This work book is selected for analysis using signal processing FFT toolbox of origin software.
20. When signal processing FFT is selected, a dialogue box will appear where required plots can be selected. Preview option is also available to view the required plots. The required plots such as magnitude v/s frequency and amplitude v/s frequency are selected. The FFT analysis is completed by selecting option 'Ok' in the signal processing FFT dialogue box.
21. The plots selected along with the respective data will appear in the workbook. The magnitude v/s frequency plot is selected and analysed to find out the free vibration natural frequency of the beam sample. The frequency corresponding to maximum magnitude in the magnitude v/s frequency plot gives the free vibration natural frequency of the beam sample.
22. The experiment is repeated for different beam samples to find out their respective free vibration natural frequencies.

k. Procedure to measure transverse deflection of beam samples.

1. Mounting arrangement is placed on the table and two C-clamps are used to hold the mounting arrangement rigidly to the table.
2. The beam sample is taken and one end of the beam is placed between the top part and bottom part of the mounting arrangement. By tightening the two allen bolts one end of the beam is fixed to the mounting arrangement and the other end is free.
3. A weighing pan is fixed at the free end of the beam to support weights.
4. A 12-pin female connector cable from RS422/USB converter is connected to corresponding 12-pin male connector of ILD1402 laser sensor. The power input is given to the laser through RS422/USB converter by connecting the power cable to

230V AC power supply. The USB cable is used to connect RS422/USB converter to the computer.

5. Burette stand is used to hold the laser sensor tightly above the free end of the beam sample such that the laser impinges on the beam sample when sensor is switched on.
6. Power supply is switched on and LED on the laser displacement sensor glows. The height of the burette holder is adjusted such that the LED turns green which indicate that the object is within the measuring range. If the LED turns red, it indicates that the object is out of range. Once the LED turns green, the burette holder is fixed in that position.
7. Position of laser displacement sensor is adjusted such that laser light falls on the free end of the FGM beam sample.
8. Computer is switched on and displacement reading is taken by running the ILD1402 DAQ software. Initial configuration is done by selecting the com port where USB cable from RS422/USB converter is connected to the computer. Interface, port and baud rate should be selected for configuring the ILD1402 DAQ tool initially before starting the experiment.
9. Once the configuration of ILD1402 DAQ tool is completed, the display window shows variation of displacement over the time.
10. Before starting the experiment, directory where the data file should be saved is chosen. A new file name can be given at the place provided in the dialogue box.
11. Once the directory and file name is chosen, 'Protocol' option available in the user interface window of ILD1402 DAQ tool is clicked which stores the data from start of the data acquisition to end of the data acquisition.
12. 'Start DAQ' and 'Stop DAQ' are provided on the user interface window of ILD1402 DAQ tool to start the data acquisition and end the data acquisition from the laser sensor respectively.
13. Experiment is started by selecting the 'Start DAQ' option on the user interface window and 'Set autozero' option is selected to make the initial displacement value to zero.
14. The beam is loaded at the free end by weights of varying magnitude from 50g-200g

by placing weights in the pan.

15. The displacement of free end of the clamped-free beam with is acquired using ILD1402 data acquisition tool.
16. 2 min waiting time is given for beam to stabilize under load so that the average deflection value can be recorded.
17. The weight is removed from the pan and again 2 min time is given for the beam to come back to zero position.
18. 3 trials each are carried out with the particular weight and data for different trials is recorded.
19. 'Stop DAQ' option is selected from the user interface window of ILD1402 DAQ tool to stop the experiment at each time the weight is being changed.
20. The data acquired from ILD1402 DAQ tool is saved in .csv format in the specified file and in the specified directory.
21. The data is tabulated in origin software and displacement v/s load graph is plotted for 3 different trials.
22. The experiment is repeated for different magnitude of weights, typically, 50, 70, 100, 130, 150 and 200g.
23. The experiment is repeated for different beam samples to find out their respective transverse deflection profile.

II.2 Thermal imaging camera – Testo 875

The testo 875 is a handy and robust thermal imager. Typical areas of application are:

• Building inspection (heating, ventilation and air conditioning trade, company technicians, engineering offices, experts): Energy evaluation of buildings

• Preventative maintenance (servicing): Mechanical and electrical inspection of systems and machines

• Production monitoring (quality assurance): Monitoring production processes.

The details of the instrument are as follows:

Measuring

Characteristic	Values
Temperature range (can be changed)	-20 - 100 °C/0 - 280°C (-4 - 212 °F/32 - 536°F)
Accuracy	±2 °C (±3.6 °F) or ±2 % of reading (whichever is the greater)
Reproducibility	±1 °C (±1.8 °F) or ±1 % (whichever is the greater)
Measuring point minimum diameter	Standard lens: 10 mm at 1 m Telephoto lens: 3 mm at 1 m
On-time (time to image)	30 s
Measuring functions	Standard measurement (1-point), Cold-/ Hotspot testo 875-2: Display of the surface moisture distribution via manual entry of the dewpoint
Compensation for reflected temperature	manual
Setting emissivity	0.01 - 1.00

Fig.II.10 Details of thermal imaging camera.

The temperature profile on the top surface of the beam is captured by means of thermal imaging camera, Testo-875. The image is processed in “testo IRSoft” software. The temperature values at various locations on the beam can be extracted from the image using the software and can be imported to excel file for further processing.

APPENDIX – III

III.1 Free vibration plots for SUS316-Al2O3 FGM beam

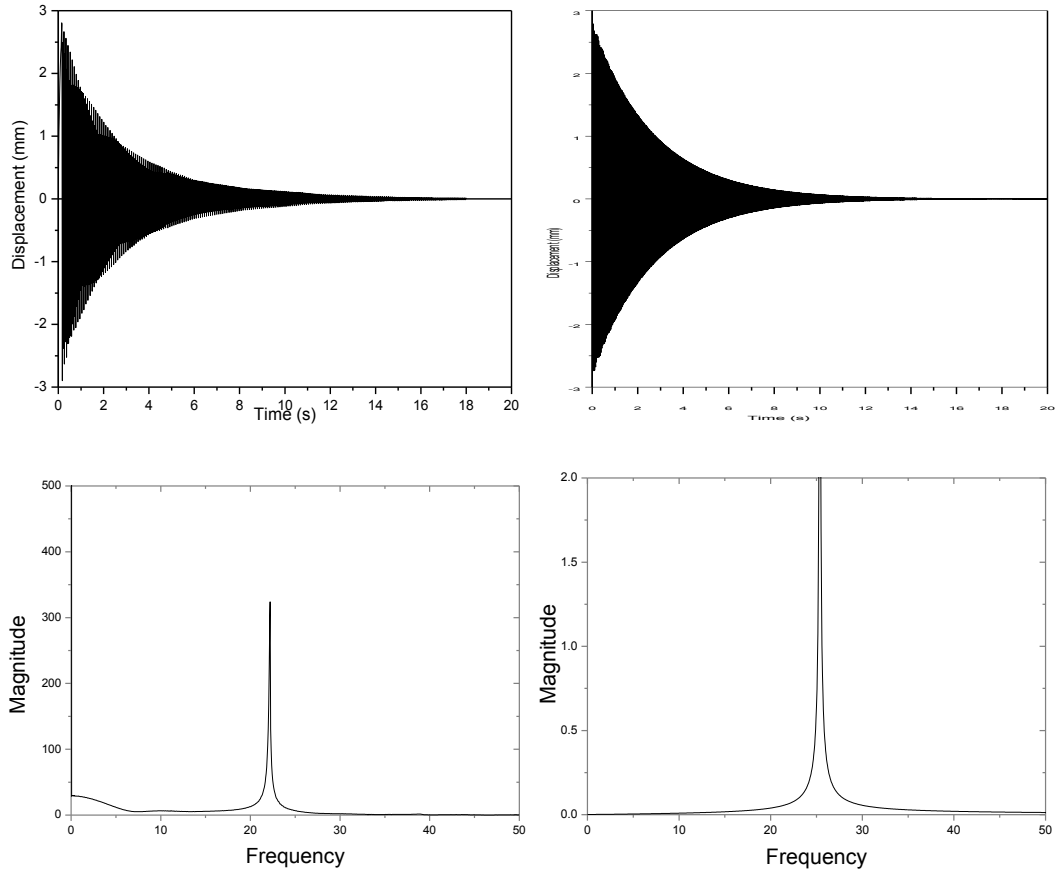

Experimental - 22.209 Hz (b) Theoretical - 25.349Hz

Fig.III.1 Natural frequencies of three-layer SUS316/Al_2O_3 FGM beams under cantilever boundary condition – Sample 2.

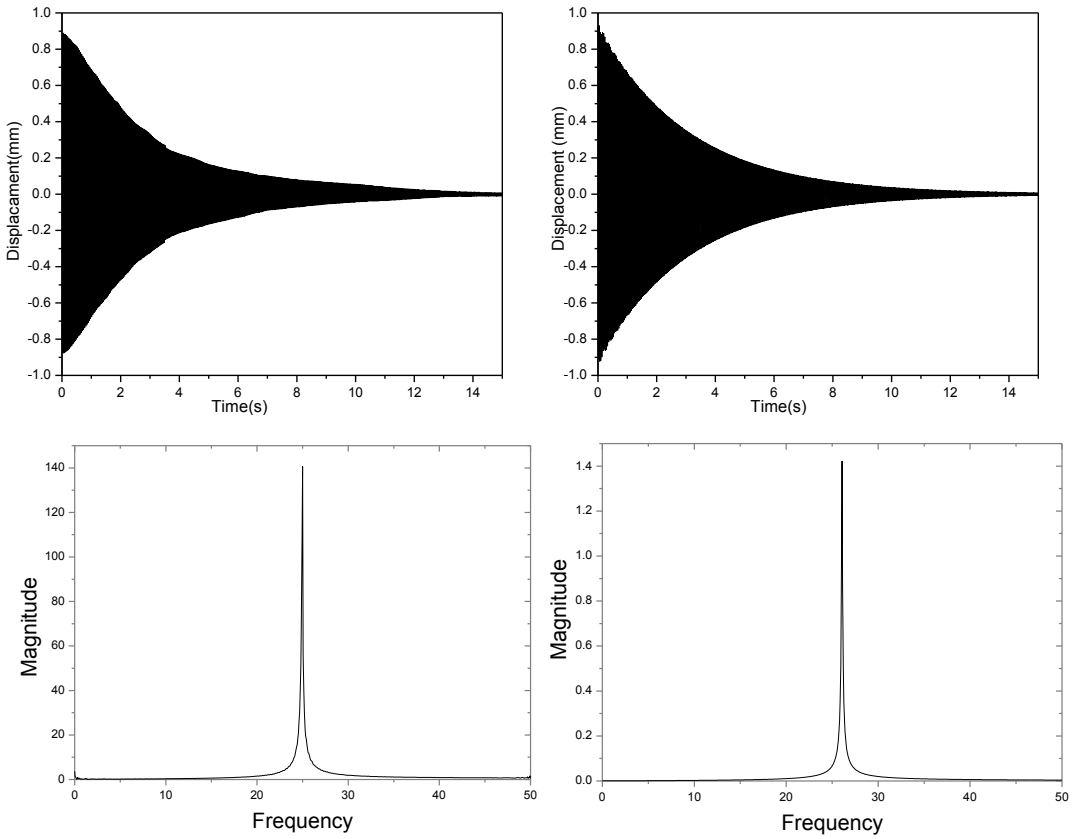

Experimental - 25.003 Hz (b) Theoretical - 26.066Hz

Fig.III.2 Natural frequencies of three-layer SUS316/Al_2O_3 FGM beams under cantilever boundary condition – Sample 3.

III.2 Free vibration plots for Al-Al2O3 FGM beam

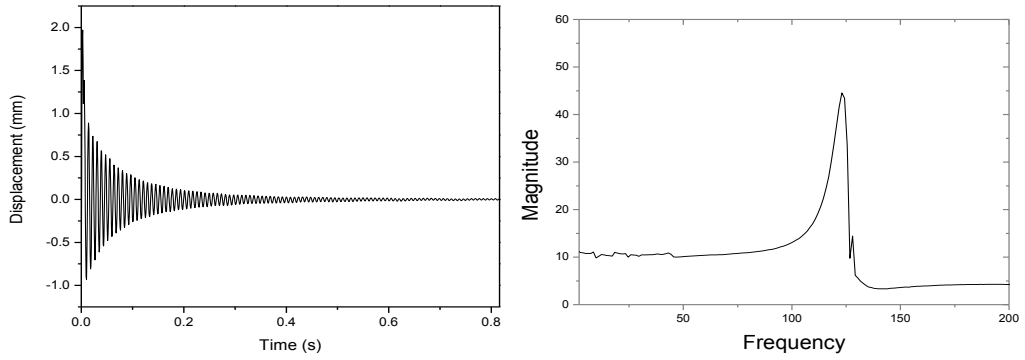

(a) (b)

Fig.III.3 (a) Displacement versus time and (b) magnitude versus frequency plots for Al-Al_2O_3 FGM beam sample 8 in clamped-free boundary condition.

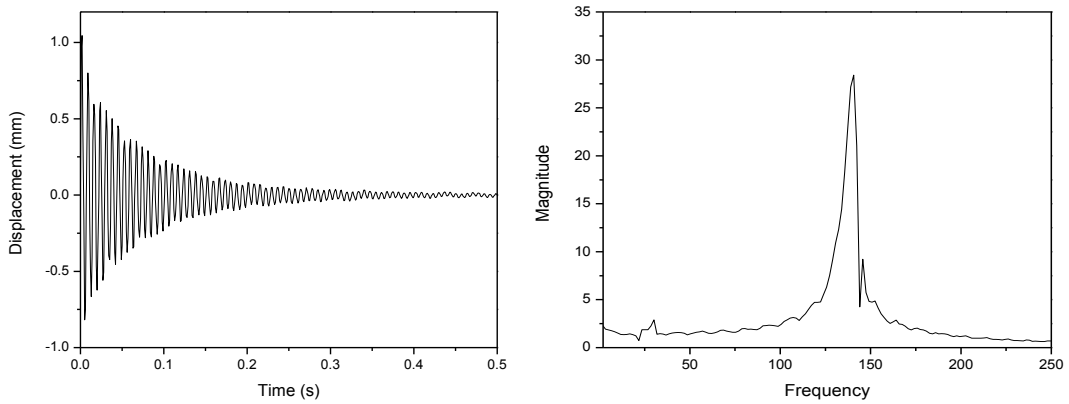

(a) (b)

Fig.III.4 (a) Displacement versus time and (b) magnitude versus frequency plots for Al-Al_2O_3 FGM beam sample 13 in clamped-free boundary condition.

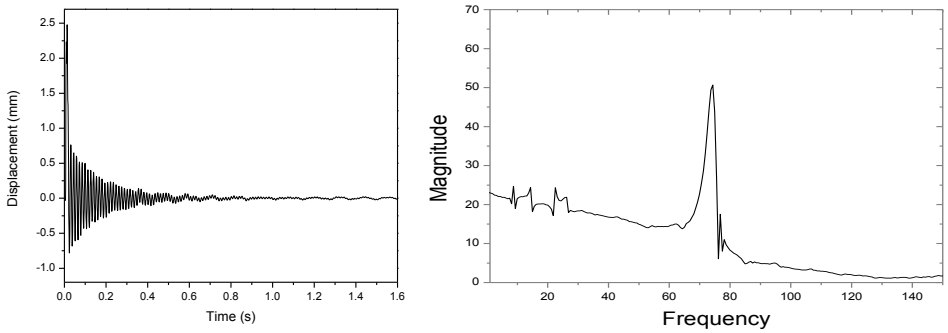

(a) (b)

Fig.III.5 (a) Displacement versus time and (b) magnitude versus frequency plots for Al-Al_2O_3 FGM beam sample 15 in clamped-free boundary condition.

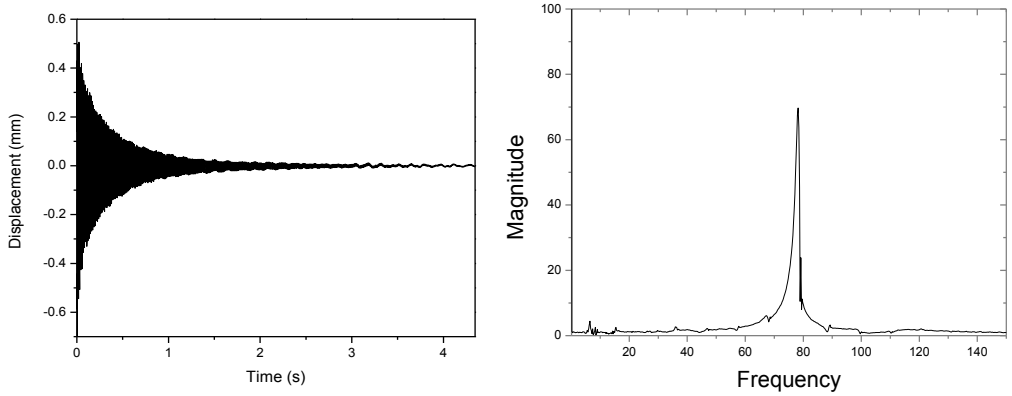

(a) (b)

Fig.III.6 (a) Displacement versus time and (b) magnitude versus frequency plots for Al-Al_2O_3 FGM beam sample 18 in clamped-free boundary condition.

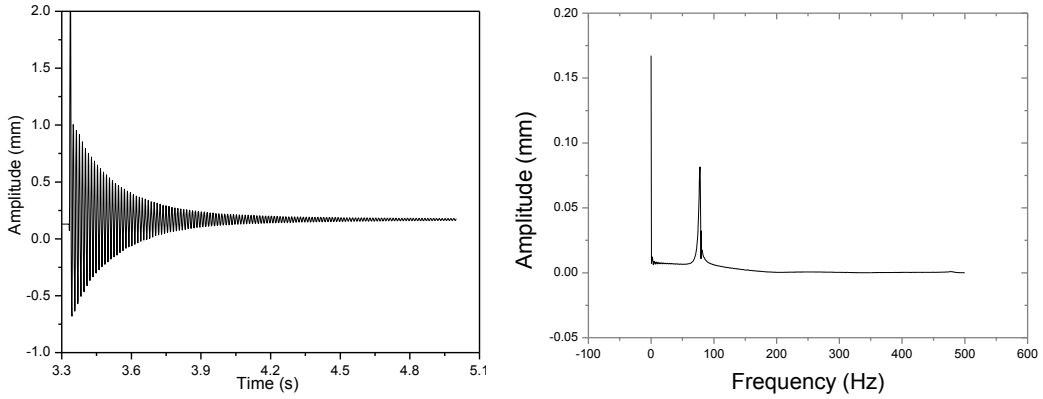

(a) (b)

Fig.III.7 (a) Displacement versus time and (b) magnitude versus frequency plots for Al-Al_2O_3 FGM beam sample 19 in clamped-free boundary condition.

III.3 Free vibration plots for pure Al beam

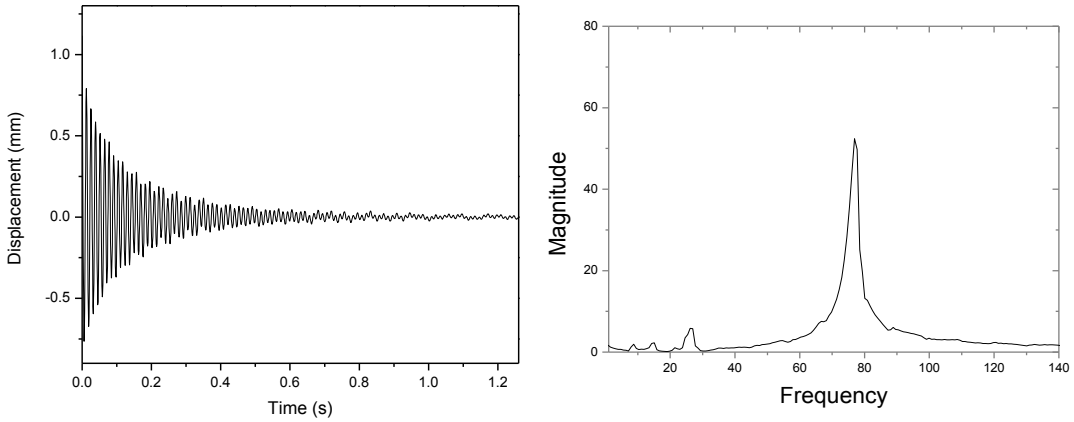

(a) (b)

Fig.III.8 Displacement versus time and magnitude versus frequency plots for pure Al beam sample 2 in clamped-free boundary condition.

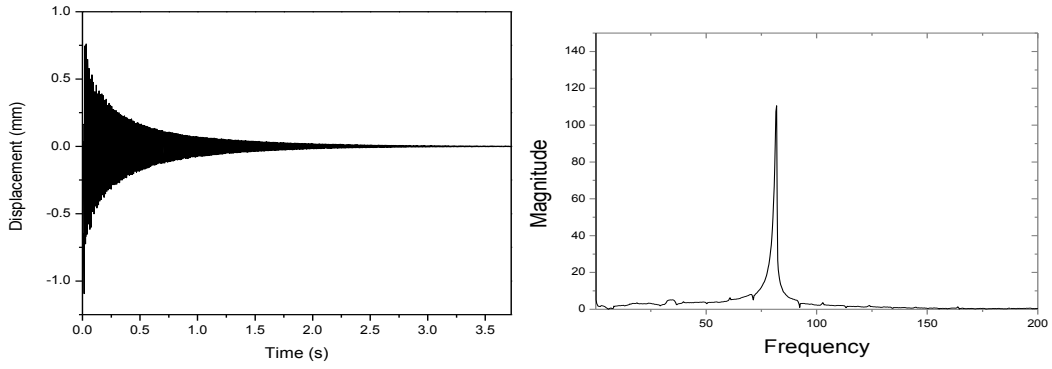

(a) (b)

Fig.III.9 Displacement versus time and magnitude versus frequency plots for pure Al beam sample 3 in clamped-free boundary condition.

APPENDIX-IV

IV.1 The convergence against the number of element along the axial direction of beam

FEM code was run for 6, 10, 20 and 40 number of elements along the axial direction of the beam. There is no variation in the displacement values for 20 and 40 elements. The variation between 10 and 20 elements is for 30% of the data, but the variation is only in the fifth decimal digit for a maximum value of 0.00001. The variation between 6 and 10 axial elements is around 0.00001 to 0.00003. Hence, considering the computation time, 10 number of elements are considered in the axial direction. The sample plot of the readings is shown in Fig.IV.1 and sample data is presented in Table IV.1.

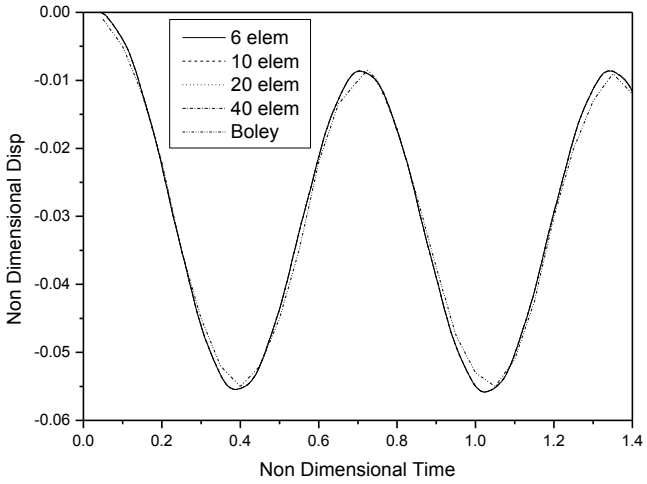

Fig.IV.1 Convergence study for number of elements in axial direction for FGM beam

Table IV.1 Sample data for axial convergence plot in Fig.IV.1.

	Number of elements in axial direction			
Non-Dim Time, τ	6-Element	10-Element	20-Element	40-Element
0.36507	-0.05474	-0.05474	-0.05474	-0.05474
0.36868	-0.05495	-0.05497	-0.05498	-0.05498
0.3723	-0.05512	-0.05514	-0.05515	-0.05515
0.37591	-0.05525	-0.05528	-0.05527	-0.05527
0.37953	-0.05535	-0.05536	-0.05537	-0.05537
0.38314	-0.05543	-0.05541	-0.05542	-0.05542
0.38676	-0.05545	-0.05544	-0.05544	-0.05544
0.39037	-0.05544	-0.05545	-0.05544	-0.05544
0.39399	-0.05539	-0.05543	-0.05543	-0.05543
0.39760	-0.05533	-0.05537	-0.05538	-0.05538

APPENDIX-V

V.1 Results and discussion on thermal vibration of beams – additional trials

V.1.1 SUS316-Al2O3 FGM beam sample – 1 (trial 2)

A total heat of 12.922 W is applied on the SUS316-Al_2O_3 FG beam sample 1 at the fixed end with 64V, 5A DC power supply for 5min. At the time of experiment, the ambient temperature was recorded as 31.9 ^{0}C. The free length of the beam for study was 130mm. Fig.V.1(a) show temperature variation along the length of beam at different time intervals while Fig.V.1(b) shows the temperature variation with respect to time at various points on beam for SUS316-Al_2O_3 FG beam sample 1.

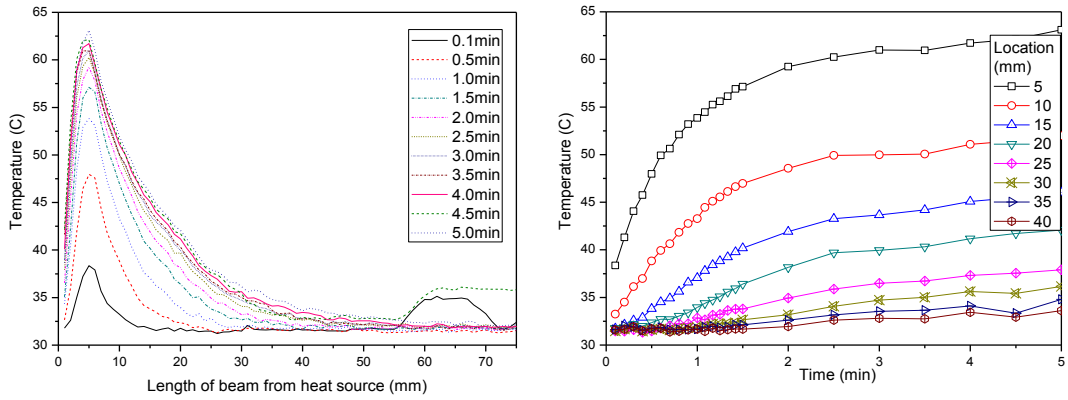

(a) (b)

Fig.V.1 Temperature distribution on SUS316-Al_2O_3 FGM beam (sample-1-trial 2) (a) temperature variation along the length of beam at different time intervals (b) temperature variation with respect to time at various points on the beam

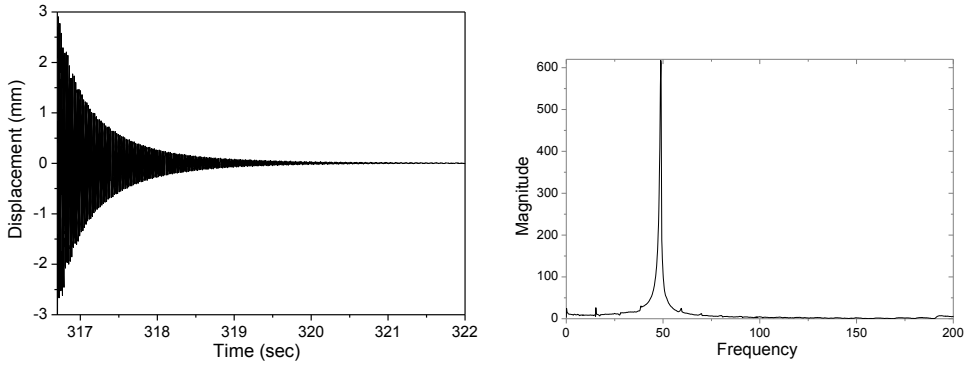

(a) (b)

Fig.V.2 (a) Displacement versus time and (b) magnitude versus frequency plots for three-layer SUS316-Al_2O_3 FGM beam sample 1 (trial 2) under cantilever boundary condition after 300 s.

When steady state temperature is achieved at around 300 s, frequency of the beam was observed to be 48.8252 Hz. The corresponding damped vibration plot and natural

frequency plot are shown in Fig.V.2. A drop in frequency is observed with respect to time when the beam is heated for about 5min. The details are presented in Table V.1. Fig.V.3 show experimental thermal deflection profile of SUS316-Al_2O_3 FGM beam Sample 1 (trial 2). A deflection of 0.135mm is observed in the beam when the beam attains temperature of 64^0C.

Table V.1 Details of reduction in frequency with time for SUS316-Al_2O_3 FGM beam sample 1 – trial 2.

Time (s)	Frequency (Hz)
23.35	49.57143
50.87	49.20000
79.86	49.11765
106.59	48.99456
136.61	48.93542
166.77	48.88346
316.70	48.82520

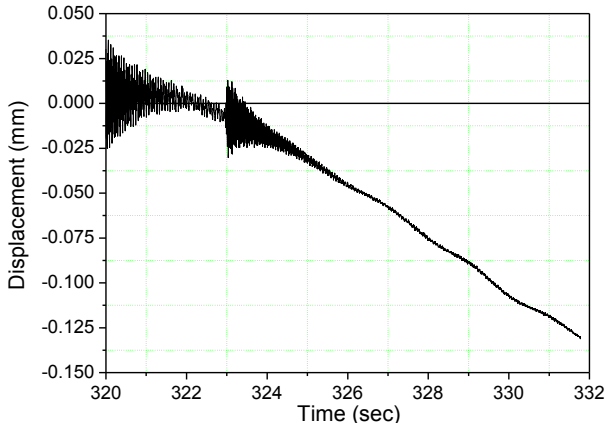

Fig.V.3 Thermal deflection profile of the SUS316-Al_2O_3 FGM beam sample 1 after t=320 s.

V.1.2 SUS316-Al2O3 FGM beam sample – 3 (trial 1)

A total heat of 2.925W is applied on the SUS316-Al_2O_3 FG beam sample 3 at the fixed end with 64V, 5A DC power supply for 5min. At the time of experiment, the ambient temperature was recorded as 30.6 ^{0}C. The free length of the beam for study was 172 mm. Fig.V.4(a) show temperature variation along the length of beam at different time intervals while Fig.V.4(b) shows the temperature variation with respect to time at various points on beam for SUS316-Al_2O_3 FG beam sample 3.

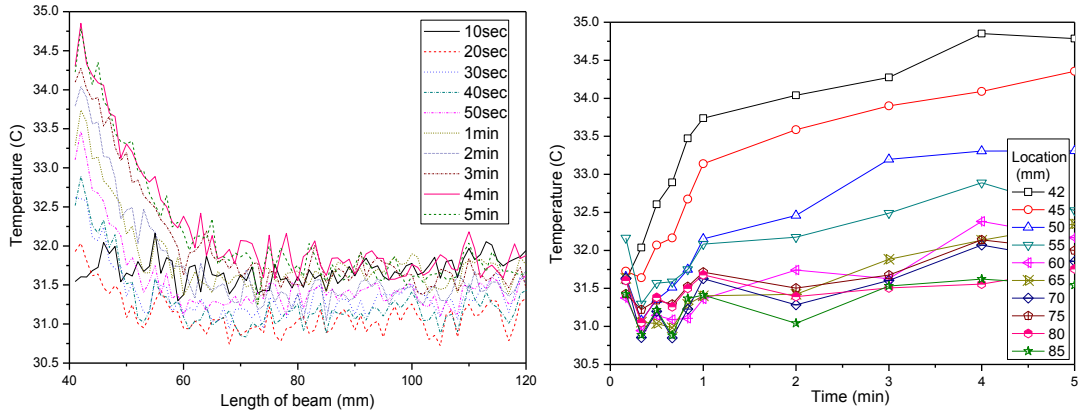

(a) (b)

Fig.V.4 Temperature distribution on SUS316-Al_2O_3 FGM beam (sample-3-trial 1) (a) temperature variation along the length of beam at different time intervals (b) temperature variation with respect to time at various points on the beam.

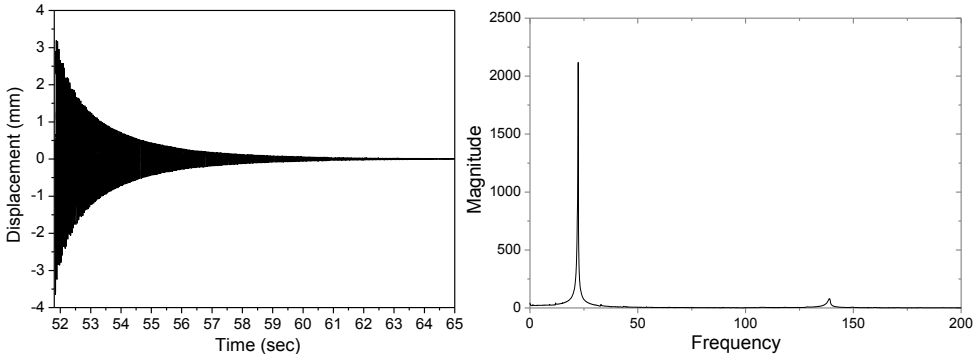

(a) (b)

Fig.V.5 (a) Displacement versus time and (b) magnitude versus frequency plots for three-layer SUS316-Al_2O_3 FGM beam sample 3 (trial 1) under cantilever boundary condition after 50 s.

When steady state temperature is achieved at around 300 s, frequency of the beam was observed to be 22.36228 Hz. The damped vibration plot and natural frequency plot at 51.83 s are shown in Fig.V.5. No much drop in frequency is observed with respect to time when the beam is heated for about 5min as the magnitude of heat of load was very low. The details are presented in Table V.2.

Table V.2 Details of reduction in frequency with time for SUS316-Al_2O_3 FGM beam sample 3 – trial 1.

Time (s)	Frequency (Hz)
27.88	22.42052
51.83	22.34679
81.70	22.37717
11.04	22.36742
140.74	22.36643
170.56	22.40911
323.65	22.36228

V.1.3 SUS316-Al2O3 FGM beam sample – 3 (trial 2)

A total heat of 3.27 W is applied on the SUS316-Al_2O_3 FG beam sample 3 at the fixed end with 64V, 5A DC power supply for 5min. Fig.V.6(a) show temperature variation along the length of beam at different time intervals while Fig.V.6(b) shows the temperature variation with respect to time at various points on beam for SUS316-Al_2O_3 FG beam sample 3. When beam attains steady temperature at around 300 s, frequency of the beam was observed to be 22.29624 Hz. The damped vibration plot and natural frequency plot at 37.52 s are shown in Fig.V.7. No much drop in frequency is observed with respect to time when the beam is heated for about 5min as the magnitude of heat load was very low. The details of time and frequency are presented in Table V.3.

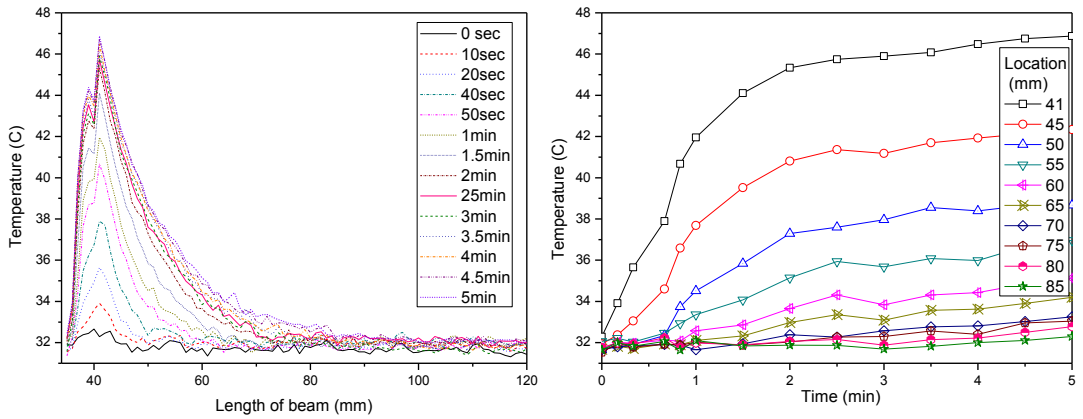

(a) (b)

Fig.V.6 Temperature distribution on SUS316-Al_2O_3 FGM beam (sample-3-trial 2) (a) temperature variation along the length of beam at different time intervals (b) temperature variation with respect to time at various points on the beam.

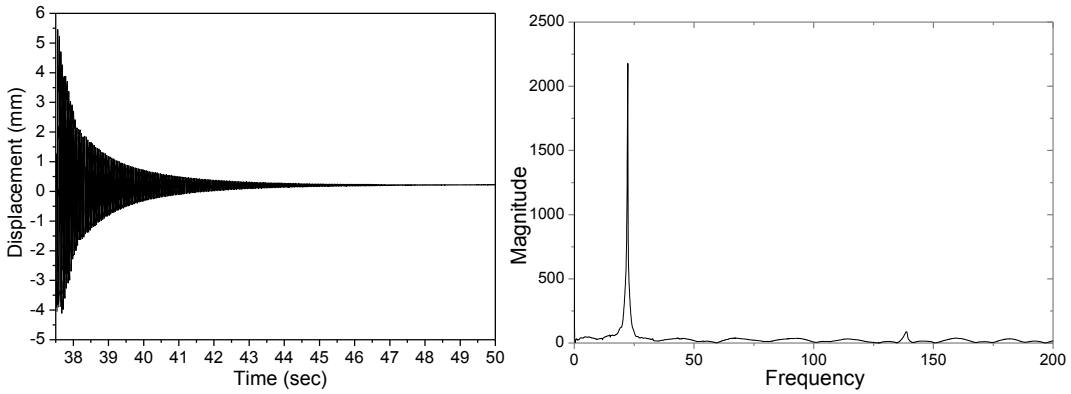

(a) (b)

Fig.V.7 (a) Displacement versus time and (b) magnitude versus frequency plots for three-layer SUS316/Al_2O_3 FGM beams under cantilever boundary condition – Sample 3.

Table V.3 Details of reduction in frequency with time for SUS316-Al_2O_3 FGM beam sample 3 – trial 2.

Time (s)	Frequency (Hz)
37.52	22.33333
68.52	22.29281
98.30	22.30579
136.13	22.26667
158.08	22.23399
310.29	22.29624
381.30	22.25293

V.1.4 Commercially available pure SUS316 beam sample

A total heat of 4.8075 W is applied on the commercially available pure SUS316 beam sample at the fixed end with 64V, 5A DC power supply for 5min. The free length of the beam used for study was 140 mm. Fig.V.8(a) show temperature variation along the length of beam at different time intervals while Fig.V.8(b) shows the temperature variation with respect to time at various points on beam. Nither reduction in the frequency nor the thermal deflection were observed at the tip of the pure SUS316 beam. The damped vibration plot and natural frequency plot at 252 s are shown in Fig.V.9.

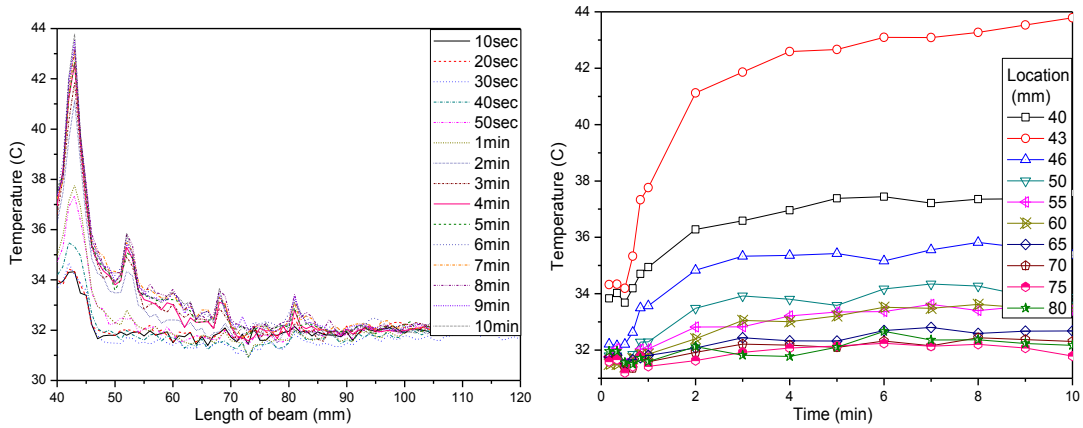

(a) (b)

Fig.V.8 Temperature distribution on SUS316 beam (sample-9) (a) temperature variation along the length of beam at different time intervals (b) temperature variation with respect to time at various points on the beam.

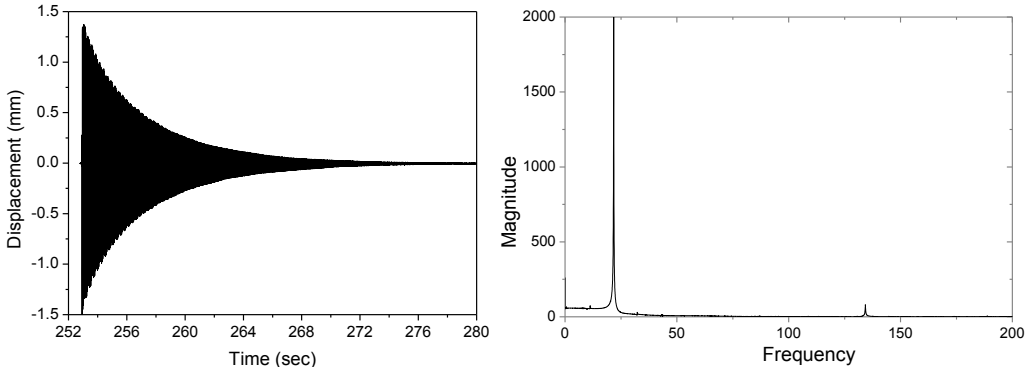

(a) (b)

Fig.V.9 (a) Displacement versus time and (b) magnitude versus frequency plots for pure SUS316 beam (sample 9) under cantilever boundary condition.

BIODATA

NAME:	PRAVIN VITHAL MALIK
DATE OF BIRTH:	13 DEC 1980
ADDRESS:	H.NO:553, KARWALWADA, KUDNE, SANQUELIM, GOA, 403505.
QUALIFICATION:	B. E. MECHANICAL (GOA UNIVERSITY)
	M.TECH – ADVANCE MANUFACTURING ENGINEERING (NATIONAL INSTITUTE OF TECHNOLOGY KARNATAKA SURATHKAL)

LIST OF PUBLICATIONS

JOURNAL PAPERS

1. Malik P, Kadoli R, Thermal induced motion of functionally graded beams subjected to surface heating, *Ain Shams Eng J* (2015), http://dx.doi.org/10.1016/j.asej.2015.10.010
2. Malik P, Kadoli R, Nonlinear bending and free vibration response of SUS316-Al_2O_3 functionally graded plasma sprayed beams: theoretical and experimental study, *Journal of Vibration and Control*, 1–14, (2016), DOI: 10.1177/1077546316659422.
3. Malik P, Kadoli R, Thermo-elastic response of SUS316-Al_2O_3 functionally graded beams under various heat loads (April 2017), *International Journal of Mechanical Sciences*), http://dx.doi.org/10.1016/j.ijmecsci.2017.04.014.

INTERNATIONAL CONFERENCE

4. Jagadish P, Malik P, Kadoli R, Sharnappa J, Bending and free vibration studies on layered Al-Al_2O_3 functionally graded beam prepared using powder metallurgy process, ICAMES-17, P E S College of Engineering, Mandya-571401, Karnataka, India. April' 21-22' 2017.